Accretion Disk-Corona connection in Active Galactic Nuclei

A Thesis
Submitted for the Degree of

Doctor of Philosophy

in

The Department of Physics,
Pondicherry University,
Puducherry - 605 014, India

by

Indrani Pal
Indian Institute of Astrophysics,
Bangalore - 560 034, India

June 2023

Accretion Disk-Corona connection in Active Galactic Nuclei

Indrani Pal
Indian Institute of Astrophysics

Indian Institute of Astrophysics
Bangalore - 560 034, India

Title of the thesis	:	**Accretion Disk-Corona connection in Active Galactic Nuclei**
Name of the author	:	**Indrani Pal**
Address	:	Indian Institute of Astrophysics II Block, Koramangala Bangalore - 560 034, India
Email	:	indrani.pal@iiap.res.in
Name of the supervisor	:	**Prof. C. S. Stalin**
Address	:	Indian Institute of Astrophysics II Block, Koramangala Bangalore - 560 034, India
Email	:	stalin@iiap.res.in

Declaration of Authorship

I hereby declare that the matter contained in this thesis is the result of the investigations carried out by me at the Indian Institute of Astrophysics, Bangalore, under the supervision of **Prof. C. S. Stalin**. This work has not been submitted for awarding any other degree, diploma, associateship, fellowship, etc., of any other University or Institute.

Indrani Pal
Ph.D. Scholar, IIA,
Bangalore-560034, India

Date : 23 June, 2023

Certificate

This is to certify that the thesis entitled **"Accretion Disk-Corona connection in Active Galactic Nuclei"** submitted to Pondicherry University by Ms. Indrani Pal for the award of the degree of Doctor of Philosophy, is based on the results of the investigations carried out by her under my supervision and guidance, at the Indian Institute of Astrophysics. This thesis has not been submitted for the award of any other degree, diploma, associateship, fellowship, etc. of any other University or Institute.

C. S. Stalin
Thesis Supervisor,
Indian Institute of Astrophysics,
Bangalore-560034, India

Date : 23 June, 2023

List of Publications

1. **Indrani Pal**, Anju A., Sreehari Harikesh, Gitika Rameshan, C. S. Stalin & Stefano Marchesi; *On the properties of corona in Seyfert 1 galaxies*; **2023**, (Submitted)

2. **Indrani Pal**, C. S. Stalin, Rwitika Chatterjee, Vivek K. Agrawal; *X-ray polarization observations of IC 4329A with IXPE: Constraining the geometry of the X-ray corona*; **2023**, J Astrophys Astron (2023) 44, 87

3. **Indrani Pal** & C. S. Stalin; *Search for coronal temperature variation in Seyfert galaxies* **2023**, Monthly Notices of the Royal Astronomical Society (2023) 518, 2529

4. **Indrani Pal**, C. S. Stalin, Michael Parker, Vivek K. Agrawal & Stefano Marchesi; *X-ray spectral and timing analysis of the Compton Thick Seyfert 2 galaxy NGC 1068*; **2022**, Monthly Notices of the Royal Astronomical Society (2022) 517, 3341

5. **Indrani Pal**, C. S. Stalin, Labani Mallick & Priyanka Rani; *NuSTAR spectral analysis of three Seyfert galaxies: NGC 3227, NGC 5548 and MR 2251-178*; **2022**, *Astronomy & Astrophysics* (2022) 662A, 78

6. * Suvendu Rakshit, Malte Schramm, C. S. Stalin, I. Tanaka, Vaidehi S. Paliya, **Indrani Pal**, Jari Kotilainen, Jaejin Shin; *TXS 1206+549: a new γ-ray-detected narrow-line Seyfert 1 galaxy at redshift 1.34?*; **2021**, *MNRAS Letters* (2021) 504, L22

7. * Amit Kumar Mandal, Suvendu Rakshit, C. S. Stalin, Dominika Wylezalek, Markus Kissler-Patig, Ram Sagar, Blesson Mathew, S. Muneer, **Indrani Pal**; *Dust reverberation mapping of Z229-15*; **2021**, *Monthly Notices of the Royal Astronomical Society* (2021) 501, 3905

*Not included in this thesis

Presentations

1. Oral presentation in the "National conference on REcent Trends in the study of Compact Objects (RETCO-V): Theory and Observation" at Kodaikanal Solar Observatory from 3rd to 5th April 2023.

2. Presented a poster with a three minutes flash talk in the "Indian Institute of Astrophysics in-house symposium" at IIA Bangalore main campus from 30th to 31st March 2023.

3. Oral presentation in "Committee on Space Research (COSPAR) 44th Scientific Assembly" in Athens, Greece, from 16th to 24th July 2022.

4. Presented a poster in "*NuSTAR* Science Meeting 2022: Ten Years of High-Energy Universe in Focus" in Cagliari, Italy, from 20th to 22nd June 2022.

5. Presented a poster in the "40th Meeting of The Astronomical Society of India (ASI)" held at IIT Roorkee from 25th to 29th March 2022.

6. Attended a workshop on "Accretion processes around black holes and the emergence of AGN jets" on 25th March 2022 in the "40th Meeting of The Astronomical Society of India (ASI)" held at IIT Roorkee.

7. Presented a poster at the "38th Meeting of The Astronomical Society of India" at the Indian Institute of Science Education & Research (IISER) Tirupati, Transit Campus from 13th to 17th February 2020.

8. Attended a workshop on "Broadband X-ray polarization of Compact Object" on 13th February 2020 at the "38th Meeting of The Astronomical Society of India" held at the Indian Institute of Science Education & Research (IISER) Tirupati.

9. Participated in a conference on "Transient Astronomy", organised by Space Astronomy Group, U R Rao Satellite Centre, Bengaluru, from 11th to 12th November 2019.

10. Presented a poster at "4th National Conference on Recent Trends in the Study of Compact objects: Theory and Observation (RETCO – IV)" at IUCAA Pune, from 17th to 20th, 2019.

Acknowledgements

First and foremost, I would like to express my sincere gratitude to my thesis advisor, Prof. C. S. Stalin, for his continuous support throughout my PhD journey. I appreciate his perseverance, inspiration, enthusiasm, and immense knowledge. I am fortunate to have had a mentor who provided help and guidance whenever needed.

My sincere thanks go to my collaborators, Dr Vivek K. Agrawal, Ms Rwitika Chatterjee, Dr Sreehari Harikesh, Dr Labani Mallick, Dr Stefano Marchesi, Dr Michael Parker, Dr Suvendu Rakshit, Dr Priyanka Rani and Dr Claudio Ricci. Working with them and discussing research ideas with such brilliant minds was a pleasure. A special thanks go to my senior, Dr Amit Kumar Mandal, for his assistance and guidance with my pre-PhD project work. I am grateful to Dr Keith A. Arnaud, Dr Gulab Dewangan, Dr Javier A. Garcia, Dr Arghajit Jana, Ms Kristína Kallová, Dr Santanu Mondal, Dr Giorgio Matt, Dr Ranjeev Misra, Dr Markus Kissler-Patig, Dr Katja Pottschmidt, Mr Jayadev Pradeep and Dr Andrzej Zdziarski for helpful discussion and electronic communication. I thank my doctoral committee members, Dr Sudhanshu Barway and Prof. Alok Sharan, for their comments and suggestions on my thesis plan during the course of the doctoral committee meetings.

I am grateful to my parents, Mr Narayan Pal and Mrs Rupa Pal, for their constant support and encouragement that helped me stay motivated during my PhD journey. I am in a great debt of gratitude to them for their constant faith in me, which has greatly aided me in maintaining my composure over many difficult circumstances. I also thank my little sister Ms Chandrani Pal for always inspiring me with her insightful thoughts about life during our late-night conversations. I thank my grandfather, Mr Shanti Gopal Biswas, for being there with me in every important affair of my academic career.

I can not thank my loving husband, Dr Subhojit Roy, enough for his constant support and encouragement over the past few years. He always inspired me to think outside the box. Discussing several physics problems with him since our college days always motivated me and helped me stay focused throughout my educational journey.

I could not have undertaken this journey away from home without my friends at IIA. A big thanks to all my friends, Anirban, Deepthi, Sioree, Sonith, Fazlu, Swastik, Athira, Bharat, Anohita and Renu, for making my stay joyful and comfortable at Bhaskara. I sincerely thank my group mates, Dr Bhoomika Rajpoot, Ms Kshama Kurian, Ms Aratrika Dey and Ms Payel Nandi, for the useful physics discussion during the group meetings. I am also thankful to all my seniors and juniors at IIA. Lastly, I thank all the faculty, academic, non-academic and library personnel at IIA for their assistance and support. I also thank the staff at Bhaskara Guest House for maintaining a nice and research-friendly environment for the researchers. At IIA, I have crossed paths with many incredible people and made friendships that will last a lifetime, and I will always be grateful for that.

–Indrani

Data usage

This thesis has made use of the publicly available data from *NuSTAR*, *XMM-Newton* and *IXPE*. The *NuSTAR* data is available in the *NuSTAR* science archive (https://heasarc.gsfc.nasa.gov/docs/nustar/nustar_archive.html) for public use. The data from the spacecraft *XMM-Newton* is available for the public at the *XMM-Newton* science archive (http://nxsa.esac.esa.int). The IXPE data used in this thesis are publicly available in the HEASARC database (https://heasarc.gsfc.nasa.gov/docs/ixpe/archive/).

This thesis is dedicated to

my uncle, the late Janardan Paul

and

grandma, the late Anima Biswas,

who would have been most happy

to see it

Abstract

Active Galactic Nuclei (AGN), amongst the most luminous sources in the Universe (L = 10^{42} − 10^{46} erg s^{-1}), emit radiation over the entire electromagnetic band. Though AGN are known to be powered by the accretion of matter onto their central supermassive black holes (SMBHs), the detailed structure of the accretion flow onto the central engine is still unclear. The emission of high energy radiation (X-rays and γ-rays) from the central part of the galaxy is one of the most distinguishable features of AGN from the normal galaxy. It is commonly believed that in the radio-quiet class of AGN, a compact region composed of energetic plasma situated in the vicinity of the central engine is responsible for the emission of the observed X-ray continuum and is known as the corona. Despite a growing number of studies of AGN in X-ray waveband, the physical nature, geometry and position of the corona are still unknown quantities. In my thesis, the work is directed to investigate the physical properties of the corona through broad band X-ray spectral analysis of the radio-quiet category of AGN. The systemic and detailed study was carried out using the hard X-ray data from the *Nuclear Spectroscopic Telescope Array* (*NuSTAR*) in the 3−79 keV energy band. Owing to its high sensitivity at hard X-ray energies (>10 keV) *NuSTAR* enabled the examination of the key features of the X-ray spectrum and to put constraints on the measurement of several physical properties of the corona (such as coronal temperature, optical depth etc.), which is one of the most important goals of this thesis.

The first study presented in this thesis concentrates on constraining the nature of the X-ray corona in Seyfert 1 galaxies. With this aim, a sample of 130 type 1 sources with a count rate greater than 0.1 was collected from *NuSTAR* Master Catalogue between August 2013 and May 2022. A uniform analysis of the 130 sources was carried out using the phenomenological model to estimate the high

energy turnover observed in the hard X-ray *NuSTAR* spectra of the sources. To constrain the physical parameters of the corona, further analysis was carried out using different physically motivated models in 48 sources, for which the high energy cut-off could be constrained. To understand the nature of the corona, possible correlations between various properties of the corona obtained from the physical model fits to the observed spectra and between various coronal parameters and physical properties of the sources, such as Eddington ratio and black hole mass etc., were investigated.

In addition to finding the temperature of the corona in about four dozen Seyfert 1 galaxies via a homogeneous analysis, this thesis also investigated the coronal temperature variation and the possible reasons behind such variation observed in Seyfert 1 sources. From the *NuSTAR* Master catalogue, 21 sources with good signal-to-noise ratio (count rate > 0.1) data with multiple epochs of observations were selected to carry out a systematic spectral analysis of the X-ray spectra in the 3−79 keV band. From fitting physical models to the data for 72 epochs of 21 sources, the coronal temperature could be constrained in most of the observations, a few of which are found for the first time. Among the 21 sources, the variation in the temperature of the corona was ascertained at a 90% confidence level in two sources, namely, NGC 3227 and MCG+08-11-011. In MCG+08-11-011, analysing the epochs in which we could constrain the temperature of the source, a "hotter-when-brighter" trend was noticed. The spectra of the source followed a "hotter-when-softer" nature with the reflection fraction, and the optical depth of the corona diminishing with the temperature of the corona. All these observations point to changes in the coronal geometry as a reason behind the variation in the coronal temperature of MCG+08-11-011. In NGC 3227, we found no notable correlation of kT_e, Γ or R with flux, while a significant negative relation is found between τ and kT_e. This could be due to more than one physical process at work in the source responsible for the observed change in kT_e.

In addition to the investigation of the coronal properties in Seyfert 1 type AGN, the thesis also investigated the timing and spectral properties of the Compton Thick Seyfert 2 AGN NGC 1068 observed using *NuSTAR* and *XMM-Newton*. For the first time, the coronal temperature was calculated for the source. The variation of the corona temperature was also checked between the epochs. The data analysed in this work comprised of (a) eight epochs of observations with *NuSTAR* carried out during the period December 2012 to November 2017, and (b) six epochs of observations with *XMM-Newton* carried out during July 2000 to February 2015. From timing analysis of the *NuSTAR* observations, the source did not show any variations in the soft band. However, on examination of the flux at energies beyond 20 keV, during August 2014 and August 2017, the source was brighter by about 20% and 30%, respectively, compared to the mean flux of the three 2012 *NuSTAR* observations as in agreement with the results found in the literature. From an analysis of the *XMM-Newton* data, no variation in the hard band (2−4 keV) was found between epochs and within epochs. In the soft band (0.2−2 keV), while the source was found to be not variable within epochs, it was found to be brighter in the epoch B (observation ID: 60002030004) relative to the epoch A (observation ID: 60002030002). By fitting physical models, the temperature of the corona was found to range between $8.46^{+0.39}_{-0.66}$ keV and $9.13^{+0.63}_{-0.98}$ keV with no detection of variation in the temperature of the corona in NGC 1068.

From physical model fits to the observed spectra for several AGN, the thesis was able to find the temperature of the corona in many AGN, as well as the variation in the temperature of the corona in two sources, namely, NGC 3227 and MCG+08-11-011. However, from spectral analysis alone, it is not possible to distinguish between different coronal geometries. X-ray polarimetric observations could yield the needed measurements to constrain the geometry of the X-ray-emitting corona in AGN. As of the writing of the thesis, the *Imaging X-ray Polarimetry Explorer IXPE*, launched on December 9, 2021, and sensitive in the 2−8 keV band, has observed four radio-quiet AGN. The final part of the thesis reports the first time

measurement of X-ray polarization in the radio-quiet Seyfert 1 galaxy IC 4329A. The first-time measurement of the X-ray polarization in IC 4329A argues against a spherical lamp post geometry, however, favouring a conical-shaped corona in IC 4329A. The thesis finally ends with possible future work that needs to be undertaken to understand the central regions of AGN.

Contents

List of Figures

List of Tables

Abbreviations

SMBH	**S**upar **M**assive **B**lack **H**ole
NuSTAR	**N**uclear **S**pectroscopic **T**elescope **A**rray
XMM	**X**-ray **M**ulti **M**irror
EPIC	**E**uropean **P**hoton **I**maging **C**amera
IXPE	**I**maging **X**-ray **P**olarimetry **E**xplorer
FWHM	**F**ull **W**idth at **H**alf **M**aximum
LLS	**L**inear **L**east **S**quares
ISCO	**I**nnermost **S**table **C**ircular **O**rbit
S/N	**S**ignal−**t**o−**N**oise **R**atio
PCC	**P**earson's **C**orrelation **C**oefficient
NHPNC	**N**ull **H**ypothesis **P**robability for **N**o **C**orrelation
CGRO	**C**ompton **G**amma **R**ay **O**bservatory
INTEGRAL	**INTE**rnational **G**amma-**R**ay **A**strophysics **L**aboratory
BAT	**B**urst **A**lert **T**elescope
ASCA	**A**dvanced **S**atellite for **C**osmology and **A**strophysics
CCD	**C**harge **C**oupled **D**evice
ARF	**A**uxiliary **R**esponse **F**ile
RMF	**R**esponse **M**atrix **F**ile
FPMA	**F**ocal **P**lane **M**odule **A**
FPMB	**F**ocal **P**lane **M**odule **B**

Chapter 1

Introduction

1.1 Active Galactic Nuclei (AGN)

AGN are the highly luminous ($\sim 10^{42} - 10^{48}$ erg s^{-1}) central region of galaxies. They are assumed to be powered by the accretion of the infalling matter onto their central supermassive black holes (SMBHs) with masses of $\sim 10^{6} - 10^{10}\ M_{\odot}$ (Lynden-Bell 1969; Shakura & Sunyaev 1973; Rees 1984; Antonucci 1993; Urry & Padovani 1995). The observed optical, ultra−violet (UV) radiation from these accretion-powered systems is believed to originate from the standard optically thick, geometrically thin accretion disk (Shields 1978; Malkan & Sargent 1982; Sun & Malkan 1989) that surrounds the SMBHs. AGN produce varied radiation across the full electromagnetic spectrum, from radio to $\gamma - rays$ (Wagner & Witzel 1995).

1.2 A brief historical introduction to AGN

The history of AGN started in 1908 when E.A. Fath first obtained the optical spectrum of NGC 1068 at the Lick observatory (Fath 1909). While observing the "spiral nabulae", he found both bright emission and absorption lines in the spectrum of NGC 1068. Later the result was confirmed by V. M. Slipher, who first observed that these lines were resolvable, having widths of a few hundred kilometres per second (Slipher 1917). The optical spectra of a few of these galaxies were first systematically examined by Carl Seyfert in 1943 (Seyfert 1943). He reported the existence of nuclear emission lines in their spectra, and this study led to the coining of the word "Seyfert galaxies".

Substantive development in radio astronomy in the 1950s led to the discovery of many radio sources with several radio surveys, such as the third Cambridge survey at 158 MHz (Edge et al. 1959). During a lunar occultation event in 1963, Hazard et al. (1963) accurately defined the position of a bright quasar, namely 3C 273. The same year, Schmidt (1963) made a significant discovery by identifying redshifted emission lines in the optical spectra of 3C 273. These redshifted lines are the immediate proof of the Hubble expansion of the Universe. These kinds of extragalactic objects with enormous luminosity were soon excluded from the class of stellar objects and became known as "quasi-stellar objects" (QSOs). Two years later, Sandage et al. (1965) discovered a population of radio-quiet quasars which exhibited the presence of strong UV excess in their spectra.

1.3 Anatomy of AGN

According to the standard working model, different components of AGN are centred around the central engine, which consists of a SMBH surrounded by a geometrically thin accretion disk (Shakura & Sunyaev 1973). The schematic diagram of the anatomy for radio-loud AGN is shown in Fig. 1.1. The main components of the AGN are discussed in brief below:

SMBH: The centre of all AGN hosts a SMBH with masses (M_{BH}) of the order of $10^6 - 10^{10}$ $M_\odot$. From several observational shreds of evidence, it is now commonly accepted that the accretion of infalling material onto the SMBH in the centre powers AGN. (Salpeter 1964; Lynden-Bell 1969; Shakura & Sunyaev 1973; Rees 1984; Ho 2008). Although the central part of the nuclei is unresolved, from the time scale of flux variation, the size of the emitting region in AGN could be restricted.

Accretion disk: The infalling material onto the SMBH forms an accretion disk. In order to maintain the angular momentum conservation law, the matter could not fall directly into the SMBH; rather, it forms a geometrically thin accretion disk around the SMBH (Shakura & Sunyaev 1973). The gravitational energy of the matter is thus converted into thermal energy and gives rise to the black body radiation of temperature around $10^4 - 10^5$ K. The accretion disk is estimated to be typically 0.001 pc in size.

Corona: The corona is thought to be the source of the X-ray emission from AGN. The X-ray variability timescale measurement indicates that the corona is a compact region with a size scale of $3 - 10R_G$ (Fabian et al. 2015). It is commonly believed that the corona consists of hot plasma of temperature in the order of $10^8 - 10^9$ K, situated close to the vicinity of the SMBH. The optical-UV photons from the accretion disk get Compton up-scattered by the hot plasma in the corona,

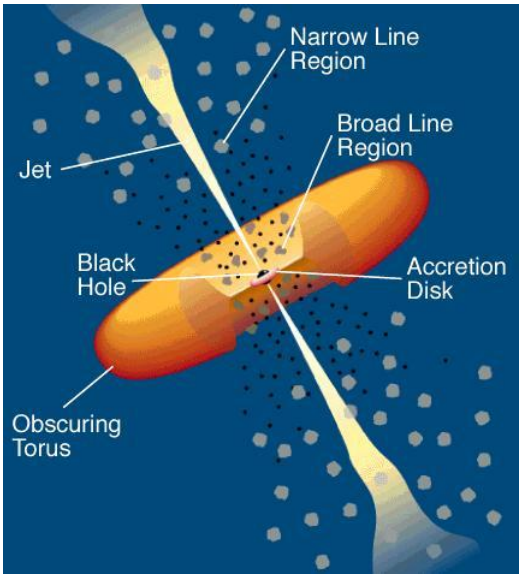

FIGURE 1.1: The radio-loud AGN paradigm is depicted in a schematic graphic taken from Urry & Padovani (1995).

producing the X-ray continuum. Despite many studies for many years, the nature, position and geometry of the X-ray emitting AGN corona are still debated.

Broad-line region (BLR): The BLR is responsible for the origin of the observed broad emission lines in the spectra of AGN. It is situated at around 0.01 pc from the central SMBH. This region is composed of high-density partially ionized gas. The continuum emission gets reprocessed in the region and appears as broad emission lines with widths that range from 500 kms^{-1} to 10^4 kms^{-1} with a typical value of around 5000 kms^{-1}.

Dusty torus: This is an optically thick region of dusty gas. It obscures the radiation originating from the central engine. Depending on the viewing angle of this obscured dusty torus AGN are classified into type 1 and 2 classes. The thick dust absorbs the AGN radiation and re-radiates it in the infrared (IR) regime. The radial distance of this region ranges from $\sim$ 0.1 to 10 pc.

Narrow-line region (NLR): This is the only AGN component which can be spatially resolved in the optical band. This region is composed of low-density gas

leading to many forbidden emission lines that are not collisionally suppressed. The full with at half maximum (FWHM) of the narrow lines that originate from the NLR ranges from 200 kms^{-1} to 900 kms^{-1}. NLR is a bi-conical extended region at around $10^4 - 10^5$ pc from the central SMBH.

Relativistic jets: Highly energetic and collimated outflow of particles forms the relativistic jets that are ejected perpendicular to the accretion disk. The jets can either have a continuous appearance or contain knotty regions. In the radio-loud AGN, the high energy X-rays and γ-rays are emitted due to non-thermal emission via synchrotron mechanisms and inverse-Compton processes. The relativistic jets can extend from parsec to several hundreds of kpc scale.

1.4 Classification of AGN

The primary division between AGN is based on the power of the relativistic jets hosted by the AGN, which determines the relative strength of the radio emission from them. The radio-quiet category of AGN (85% of the total AGN population) emits weaker radiation in the radio band than the radio-loud category (15% of the total population). Usually, the classification between radio-quiet and radio-loud classes of AGN is based on the ratio between the flux density in the radio band at 5 GHz to the optical B-band flux density at 4400 Å (R = F_R/F_O; Urry & Padovani 1995). Based on the radio loudness parameter, Kellermann et al. (1989) first introduced the classification between these two categories of AGN in the Palomar Bright Quasar Survey. The radio-quiet and radio-loud AGN classes were separated into two categories: radio-quiet with $R \sim 0.1 - 1$ and radio-loud with $R \sim 10 - 1000$. Radio-quiet objects were further classified into two subclasses; (a) Seyfert galaxies and (b) radio-quiet quasars. On the other hand, the radio-loud objects were classified as (a) blazars, (b) radio galaxies etc.

1.4.1 Radio-quiet AGN

Based on the source luminosities, the two subclasses of the radio-quiet AGN were categorised. The lower-luminosity Seyfert galaxies have an absolute magnitude of $M_B > -23$ in the B band. Quasars, on the other side, have the highest AGN luminosity ($M_B < -23$) (Schmidt & Green 1983).

Seyfert galaxies: This type of galaxy has broad emission lines in its spectrum. Khachikian & Weedman (1974) first distinguished the Seyfert galaxies based on the presence of the permitted emission lines. In the Seyfert 1 type AGN spectra, both broad permitted and narrow forbidden emission lines are present. Type 1 class of AGN could be further divided into Type 1.2, 1.5, 1.8, and 1.9 based on the strength of the emission lines in their optical spectra. In the optical spectra of Type 2 Seyfert galaxies, only narrow emission lines are present. In both Type 1 and Type 2 categories, in addition to the emission lines, absorption lines are also present. A unique subclass of Seyfert galaxies are Narrow Line Seyfert 1 galaxies (NLSy1). (Osterbrock & Pogge 1985) with FWHM($H\beta$) < 2000 kms^{-1}. In the optical spectra of NLSy1 galaxies, relatively weaker [OIII] lines are present with O[III]/$H\beta$ lesser than 3. This subclass of Seyfert galaxies often shows strong optical Fe II lines. Additionally, they exhibit a high accretion rate and a relatively smaller mass of the central black hole ($\sim 10^6 - 10^8$ M$_\odot$, Grupe et al. 2010).

Quasars: Quasars are the luminous counterparts to Seyfert galaxies, with the bolometric luminosity of about 10^{44} to 10^{47} ergs^{-1}. Their host galaxies are hardly resolved, with features of stellar absorption from the host galaxies being very feeble.

1.4.2 Radio-loud AGN

Radio-loud objects are categorised in the following two classes:

Blazars: The relativistic jets of Blazars are pointed close to the line of sight to the observer. They emit over the entire accessible electromagnetic spectrum and also show flux variations across wavelengths. In addition to flux variations, they also show large optical polarization and polarization variability. Flat spectrum radio quasars (FSRQs) and BL Lac objects (BL Lacs) are further classifications for blazars. FSRQs have strong emission lines in their spectra, whereas BL Lacs have featureless spectra or weak emission lines with an equivalent width lesser than 5Å.

Radio galaxies: Similar to the Seyfert classifications, radio galaxies could also be divided into two categories; (a) Broad-Line Radio Galaxies (BLRGs) and (b) Narrow-Line Radio Galaxies (NLRGs). In the optical spectra of BLRGs, both broad and narrow emission lines are present, wherein the optical spectra of NLRGs show only the narrow emission lines. The radio galaxies are further divided into Fanaroff-Riley Type I (FRI) and Type II (FRII) radio galaxies on the basis of the power at 178 MHz (Fanaroff & Riley 1974).

1.5 AGN unification model

According to the unified model of AGN (Antonucci 1993; Urry & Padovani 1995), the observed differences between the different classes of AGN are attributed to orientation effect, where the SMBH and torus are viewed at different angles along the line of sight of the observer's. In this unified model, there are various components of AGN as outlined in Section 1.3. The unified model of AGN is shown in

Fig. 1.1. This model classifies the Seyfert category of AGN into two types, Seyfert type 1 and type 2 galaxies, on the basis of the orientation of the viewing angle. According to this model, the observational difference between these two classes of galaxies is explained due to the inclination of the line of sight concerning the dusty torus. Seyfert 1 galaxies are those that are viewed at lower inclination angles, and Seyfert 2 galaxies are viewed at a higher inclination, with the central region in them completely blocked by the dusty molecular torus that surrounds the BLR. The detection of hidden BLR was first reported in NGC 1068, which forms the discovery of the first Type 2 AGN. This was based on spectro-polarimetric observations that revealed the presence of broad polarized emission lines (Antonucci & Miller 1985). X-ray observations also provide evidence of the obscuring dusty torus in AGN (Awaki et al. 1991) with large column densities seen in type 2 Seyfert galaxies.

In radio-loud objects, the unification scheme is built mainly based on the orientation of the relativistic jets. The BL-Lac objects are now identified as the low-luminosity FRI-type radio galaxies, viewed at an inclination angle lesser than 10 degrees (Urry & Padovani 1995). Thus the emission from the BL-Lac objects is expected to be Doppler-boosted (Blandford & Königl 1979). In the case of FSRQs, the relativistic jets are mostly aligned to the line of sight at angles larger than that of BL-Lacs.

1.6 The Corona of AGN

Corona, a crucial component of AGN, causes the detected X-ray emission. The observed X-ray emission from the nuclear region of the radio-quiet category of AGN is believed to be produced by the inverse Compton scattering process caused by the interaction of the seed optical/UV photons from the accretion disk with the

thermal plasma in a hot ($10^8 - 10^9$ K) region called the corona that is situated close to the accretion disk (Haardt & Maraschi 1991; Haardt et al. 1994). The accretion disk reprocesses this X-ray continuum, resulting in the reflection hump at roughly 15−30 keV and the broad FeKα line at 6.4 keV (George & Fabian 1991; Matt et al. 1993a). Soft excess between 0.1−2 keV is ubiquitously observed in Type I AGN (Magdziarz et al. 1998; Fabian et al. 2002; Crummy et al. 2006; Bianchi et al. 2009; Gliozzi & Williams 2020), although the physical origin of this component remains highly debated, different analyses showed that a two-temperature Comptonization process explains such a component either from an observational (Jin et al. 2012; Porquet et al. 2018; Petrucci et al. 2018; Middei et al. 2020; Matzeu et al. 2020) or theoretical (Różańska et al. 2015; Petrucci et al. 2020; Ballantyne & Xiang 2020; Ballantyne 2020) point of view. Analysis of these spectral features (reflection, FeKα line, soft excess) will help provide strong constraints on the X-ray emitting region. From X-ray reverberation studies (Fabian et al. 2009; Zoghbi et al. 2012), AGN corona is assumed to be a compact region situated in the vicinity of the accretion disk, mostly within 3 to 10 R_G, where R_G means the gravitational radius, and it is explained as, $R_G = GM_{BH}/c^2$, here M_{BH} is the mass of the SMBH, and G is the gravitational constant. However, there are strong debates concerning coronal geometry. The lamp post is one such possibility, but other models also exist (Haardt et al. 1994; Done et al. 2012; Petrucci et al. 2013).

The shape of the observable X-ray continuum can be depicted by a power law with a cut-off (E_{cut}), and the shape of the AGN spectra depends on the optical depth (τ), the temperature of the coronal plasma (kT_e), seed photon temperature and the viewing angle. From a study of the Seyfert galaxy NGC 5548, Petrucci et al. (2000) showed the existence of an approximate relation between E_{cut} and kT_e as $E_{cut} = 2-3\ kT_e$. On analysis of a few Seyfert galaxies, according to Petrucci et al. (2001), for an optically thin corona with $\tau < 1$; $E_{cut} \sim 2\ kT_e$, while for an optically thick corona with $\tau > 1$; $E_{cut} \sim 3\ kT_e$. However, by fitting Comptonized spectra simulated using a range of τ and kT_e, Mao et al. (2019), showed that the typically

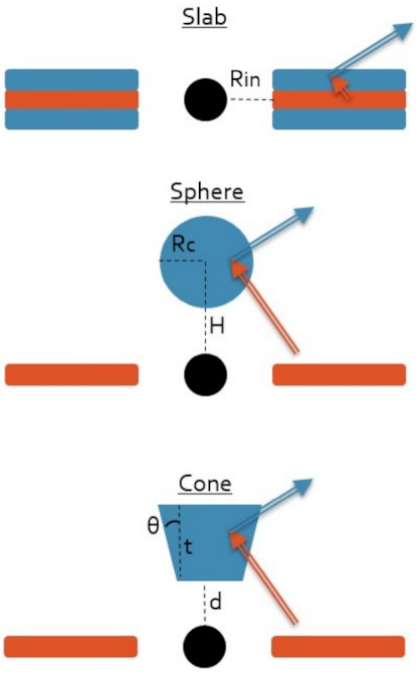

FIGURE 1.2: Different coronal geometry. Credit: Ursini et al. (2022).

adopted relation of $E_{cut} = 2-3\ kT_e$ is not justifiable for all values of τ and kT_e, instead valid for only low values of τ and kT_e.

Observations from high energy X-ray missions such as CGRO (Zdziarski et al. 2000; Johnson et al. 1997), BeppoSAX (Nicastro et al. 2000; Dadina 2007), INTEGRAL (Malizia et al. 2014; Lubiński et al. 2010, 2016; Ricci et al. 2011), Swift-BAT (Vasudevan et al. 2013; Ricci et al. 2017); and Suzaku (Tazaki et al. 2011) showed that the corona in Seyfert galaxies has a wide range of temperature with E_{cut} ranging from $50 - 500$ keV. However, observations from those missions are limited to bright and nearby sources. Thus, it is very clear that many efforts were put to measure E_{cut} in several AGN. However, a major transformation in the studies of the Comptonization spectrum of AGN to determine E_{cut} from an epoch of observation happened after the launch of the *Nuclear Spectroscopic Telescope Array* (*NuSTAR*; Harrison et al. 2013) in the year 2012, due to its extensive $3-79$ keV spectral coverage and good sensitivity beyond 10 keV. Since the launch of *NuSTAR*, E_{cut} values were obtained for many AGN (Fabian et al. 2017; Tortosa

et al. 2018; Rani & Stalin 2018a,b; Rani et al. 2019; Lanzuisi et al. 2019; Baloković et al. 2020; Reeves et al. 2021; Kang et al. 2021a).

1.6.1 Does the coronal temperature vary?

In less than half a dozen sources, there are reports of variation in E_{cut}, pointing to variation in kT_e. For example, in seven sources, namely MCG-5-23-16 (Zoghbi et al. 2017), 3C 382 (Ballantyne et al. 2014), NGC 4593 (Ursini et al. 2016), NGC 5548 (Ursini et al. 2015), Mrk 335 (Keek & Ballantyne 2016), NGC 3227 and SWIFT J2127.4+5654 (Kang et al. 2021a) variations in E_{cut} values are available in the literature. Recently, from a reanalysis of the *NuSTAR* spectra of five sources using a model-independent approach, (Zhang et al. 2018) confirmed the E_{cut} variation in three of the five sources, namely 3C 382, NGC 5548 and Mrk 335. Most of these inferences were based on variations in E_{cut} obtained from phenomenological model fits to the data. However, to know changes in kT_e, it is imperative to fit physical models to the data because it is known recently that the relation $E_{cut} = 2-3\ kT_e$ does not always hold true (Mao et al. 2019). Though E_{cut} is known to vary, we do not yet know the causes for its variation. Despite that, it is necessary to increase the number of sources that show variation in the temperature of the corona. This is now achievable owing to the multiple epochs of observation available on a adequate number of AGN in the *NuSTAR* archives.

The origin of the corona in AGN as well as its geometry, is currently not known. According to our current knowledge of the shape of the corona, it is believed that the corona could have (a) spherical lamp post geometry situated above the black hole (Wilkins & Fabian 2012), (b) conical geometry if the corona can consitute the base of the relativistic jets of AGN (Markoff et al. 2005) or (c) a slab geometry sandwiching the accretion disk (Haardt & Maraschi 1993). The different coronal geometries are shown in Figure 1.2. In spite of the technological advancements over

the last decade, particularly after the launch of *NuSTAR*, there has been tremendous progress in the efforts to understand the central regions of AGN through timing and broadband spectral analysis. Irrespective of this, our knowledge of the corona of AGN is limited. This thesis aims to address this issue.

1.7 Motivation of the thesis

The objectives of the thesis are outlined below

1. **What is the temperature of the corona?** Till the last few years, our knowledge of the temperature of the corona in AGN has been based on phenomenological fits to the observed spectra to a large extent. This thesis aims to overcome this limitation by aiming to ascertain the temperature of the corona in a large sample of AGN using the physical model fits to the observed X-ray spectra.

2. **Does the temperature of the corona vary with time?** Making use of the multi-epoch data available on a few AGN, the thesis aims to find evidence for variation in the temperature of the corona and try to pinpoint the reasons behind the variation by studying its relation to various coronal and physical properties of AGN.

3. **What is the geometry of the corona?** From the spectral analysis of AGN, it is difficult to distinguish between coronal geometries. X-ray polarimetry is an effective tool to examine the geometry of AGN, and this is now possible with the launch of the *Imaging X-ray Polarimeter* (*IXPE*) on December 9, 2021. X-ray polarimetric analysis of a radio-quiet AGN, IC 4329A, is aimed in this thesis to constrain the geometry of the corona.

1.8 Outline of the thesis

This Ph.D. thesis aims to characterise the X-ray corona in radio-quiet Seyfert galaxies. The outline of various chapters in this thesis is given below

1. In Chapter 1, we give an overview of AGN, its various components and the X-ray corona in AGN.

2. In Chapter 2, we describe the (a) selection of Seyfert 1 galaxies for characterising the temperature of their X-ray corona and (b) the selection of sources for investigating variation in the temperature of the corona. The details of observation and data reduction are also described in this Chapter.

3. In Chapter 3, we describe in detail our efforts to characterise the temperature of the corona in a sample of Seyfert 1 galaxies. For our sample of 130 Seyfert 1 galaxies, we could constrain E_{cut} in 75 and kT_e in 48 sources. From detailed analysis, we conclude that the coronal X-ray emission in our sample of sources seems to originate in a thermal plasma.

4. In Chapter 4, we discuss our results on characterising variation in the temperature of the corona in Seyfert 1 galaxies. From a careful analysis of a total of 72 spectra for 21 sources, we could unambiguously find variation in the temperature of the corona in two sources, namely NGC 3227 and MCG+08-11-011. We found evidence for both the "hotter-when-brighter" and "cooler-when-brighter" trend in our sample of sources that showed kT_e variation. Thus the observed relation between the temperature of the corona and the source brightness is found to be different among sources.

5. In Chapter 5, we carried out spectral and timing analysis of the Seyfert 2 AGN, NGC 1068. From timing analysis of data from *NuSTAR*, we found the source not to show variations in the soft band; however, at energies beyond 20 keV, the source showed flux variations. From the physical model

fits to the observed spectra, we characterised the temperature of the corona. However, we found no variation in the temperature of the corona

6. In Chapter 6, we present our results on X-ray polarimetric observations of a Seyfert 1 AGN, IC 4329 A. X-ray polarimetry is a powerful tool to probe the geometry of the X-ray corona. In this thesis, we characterised the polarimetric properties of the X-ray corona in IC 4329A for the first time. From *IXPE* observations, from the model-independent approach, we found a polarisation degree of 3.7% $\pm$ 1.5% in the 2$-$8 keV band. From spectro-polarimetric analysis, we found a similar degree of polarisation of 4.8% $\pm$ 2.2%. Based on the observed moderate value of the degree of polarization, we argue for a conical shape geometry for the corona in IC 4329A.

7. In Chapter 7, we provide a summary of the thesis work, where we essentially highlight the important results obtained in this thesis and also put forward some ideas for investigation in the future.

Chapter 2

Observation, selection of sample and reduction of data

2.1 Observation and selection of sample

2.1.1 Sample for the determination of coronal temperature

Our sample of sources for the determination of coronal temperature was selected from the *NuSTAR* Master Catalog. From this catalogue, we looked into the publicly available data for Seyfert galaxies during the period between August 2013 and May 2022. Of these, we found a total of 850 Seyfert galaxies. We selected only Seyfert 1 galaxies with a net count rate greater than 0.1 in the $3-79$ keV energy range to have a sufficiently good S/N spectrum for model fitting. Adopting the criteria, we found 130 Seyfert 1 galaxies covering the redshift interval of 0.002

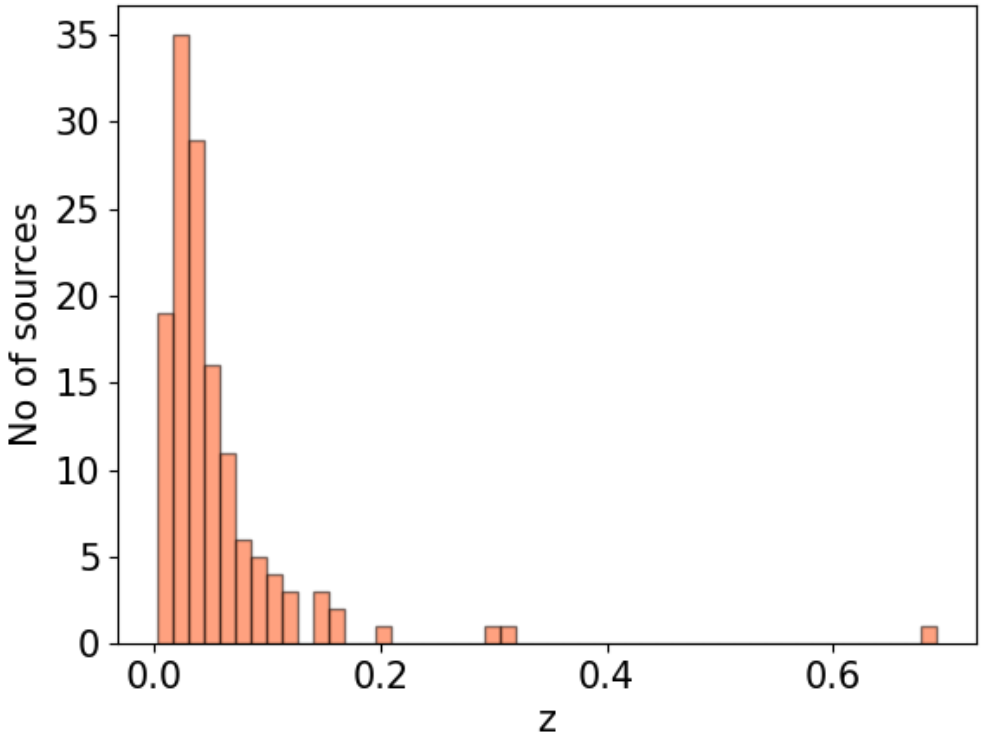

FIGURE 2.1: The redshift distribution.

$< z <$ 0.692. The full list of the Seyfert 1 galaxies and their *NuSTAR* observational details are given in Table 2.1. We show in Fig. 2.1 the distribution of their redshifts.

2.1.2 Sample for coronal temperature variation

Of the source given in Table 2.1, we selected only those sources that have E_{cut} measurement from our model fitting along with more than one epoch of observations. This led us to a final sample of 24 sources. Of these, we excluded three sources, namely Ark 564, SWIFT J12127.4+5654 and 3C 382, for which there are reports in the literature on the variation in E_{cut}/kT_e. So, in this thesis, we analyzed 21

sources with 72 epochs of observations. The details of these 21 sources and the data available on those sources are depicted in Table 2.2.

TABLE 2.1: Information on the sources investigated to determine kT_e. The pillars are (1) the source's name, (2) RA (h:m:s), (3) DEC (d:m:s), (4) redshift (z), (5) type of the source, (6) observation ID (7) net count rate for the FPMA spectrum and (8) exposure time in sec. Some of the information, including the right ascension (α_{2000}), declination (δ_{2000}), z and type of source, are from SIMBAD.

Source	α_{2000}	δ_{2000}	z	Type	OBSID	counts/sec	Exposure
NGC 3516	11 06 47.46	+72 34 07.29	0.009	Sy1.5	60002042004	0.17	72088
MRK 590	02 14 33.56	−00 46 00.18	0.026	Sy1.2	80502630002	0.33	68123
MRK 79	07 42 32.82	+49 48 34.78	0.022	Sy1.2	60601010002	0.58	65805
IGRJ19378-0617	19 37 33.02	−06 13 04.80	0.01	Sy1.0	60101003002	0.52	65521
ARK 120	05 16 11.40	−00 08 59.15	0.03	Sy1.0	60001044004	0.99	65453
MRK 817	14 36 22.08	+58 47 39.39	0.158	Sy1.5	60601007002	0.21	135300
HE1136−2304	11 38 51.00	−23 21 35.34	0.027	Sy	80002031003	0.26	63565
Fairall 51	18 44 53.98	−62 21 52.87	0.014	Sy1.0	60402014002	0.24	63532
MKN 6	06 52 12.33	+74 25 37.12	0.019	Sy1.5	60102044002	0.21	62472
MRK 279	13 53 03.43	+69 18 29.41	0.031	Sy1.5	60601011004	0.16	200632
NGC 4151	12 10 32.57	+39 24 21.06	0.003	Sy1.5	60001111005	6.27	61528
UGC06728	11 45 15.94	+79 40 53.37	0.067	Sy1.2	60160450002	0.14	22615
NGC 4051	12 03 09.61	+44 31 52.68	0.002	Sy1.5	60401009002	0.43	311139
MRK 915	22 36 46.49	−12 32 42.88	0.024	Sy1.0	60002060004	0.17	54249
MRK 359	01 27 32.52	+19 10 43.83	0.017	Sy1.5	60402021002	0.15	52526
3C 111	04 18 21.27	+38 01 35.80	0.05	Sy1.0	60202061004	0.74	49361
NGC 5548	14 17 59.54	+25 08 12.60	0.016	Sy1.5	60002044006	0.99	51460

Continued

Table 2.1 – Following the previous page

Source	α_{2000}	δ_{2000}	z	Type	OBSID	counts/sec	Exposure
MRK 335	00 06 19.53	+20 12 10.61	0.025	Sy1.2	60001041005	0.17	93022
IRAS F12397+3333	12 42 10.60	+33 17 02.66	0.044	Sy1.0	60501007002	0.16	48709
3C 390.3	18 42 08.99	+79 46 17.12	0.06	Sy1.0	60001082003	1.03	47557
ESO 323−G077	13 06 26.12	−40 24 52.59	0.015	Sy1.2	60202021006	0.13	43403
NGC 3783	11 39 01.71	−37 44 19.00	0.009	Sy1.0	60101110002	1.11	41265
ESO 511−G030	14 19 22.40	−26 38 41.13	0.022	Sy1.0	60502035008	0.12	41807
2MASXJ10523297+1036205	10 52 32.97	+10 36 19.99	0.088	Sy1.0	60160414002	0.12	40696
NGC 5506	14:13:14.89	−03:12:27.28	0.006	Sy1.9	60501015002	1.39	61384
MRK 813	14 27 25.05	+19 49 52.26	0.111	Sy1.0	60160583002	0.21	24562
PG0052+251	00 54 52.11	+25 25 38.98	0.155	Sy1.2	60661001002	0.13	24392
IGRJ21247+5058	21 24 39.40	+50 58 25.00	0.02	Sy1.0	60301005002	2.61	40338
2MASXJ15295830−1300397	15 29 58.33	−13 00 39.78	0.104	Sy1.0	60160617002	0.15	24227
MRK 376	07 14 15.08	+45 41 55.90	0.056	Sy1.5	60160288002	0.12	24174
MCG+08-11-011	05:54:53.61	+46:26:21.61	0.020	Sy1.5	60201027002	1.23	97921
ESO 209−G012	08 01 57.97	−49 46 42.39	0.04	Sy1.5	60160315002	0.29	23715
MR 2251−178	22 54 05.88	−17 34 55.40	0.064	Sy1.0	90601637002	0.55	23620
MRK 841	15 04 01.19	+10 26 15.78	0.036	Sy1.5	60101023002	0.44	23419
RBS0295	02 14 37.40	−64 30 05.06	0.074	Sy1.0	60061021002	0.13	23366
NGC 4593	12 39 39.44	−05 20 39.03	0.008	Sy1.0	60001149002	0.63	23317
MCG-06-30-15	13 35 53.76	−34 17 44.16	0.008	Sy1.2	60001047005	0.8	23267

Continued

Table 2.1 – Following the previous page

Source	α_{2000}	δ_{2000}	z	Type	OBSID	counts/sec	Exposure
HE 1143−1810	11 45 40.46	−18 27 14.96	0.033	Sy1.0	60302002006	0.69	23096
H1821+643	18 21 57.21	+64 20 36.22	0.297	Sy1.0	60160683002	0.37	22173
MRK 1148	00 51 54.76	+17 25 58.50	0.064	Sy1.0	60160028002	0.5	22087
CGCG229−015	19 05 25.94	+42 27 39.76	0.028	Sy1.0	60160705002	0.13	21992
HE0103−3447	01 05 46.72	−34 31 44.09	0.057	Sy1.0	60160038002	0.22	21986
IGRJ14552−5133	14 55 17.51	−51 34 15.18	0.016	Sy1.0	60401022002	0.23	100942
2MASXJ19380437−5109497	19 38 04.39	−51 09 49.38	0.04	Sy1.0	60160716002	0.24	21830
2MASSJ17485512−3254521	17 48 55.13	−32 54 52.10	0.02	Sy1.0	60160677002	0.27	21801
MRK 1044	02 30 05.52	−08 59 53.20	0.016	Sy1.0	60401005002	0.22	267078
UGC 3478	06 32 47.17	+63 40 25.28	0.013	Sy1.2	60061068002	0.13	21680
MRK 704	09 18 25.99	+16 18 19.63	0.029	Sy1.5	60061090002	0.27	21524
2MASXJ18470283-7831494	18 47 02.69	−78 31 49.60	0.074	Sy1.0	60160699002	0.22	21505
2MASXJ21192912+3332566	21 19 29.12	+33 32 56.67	0.051	Sy1.5	60061358002	0.23	21483
1H1934-063	19 37 33.02	−06 13 04.80	0.01	Sy1.0	60101003002	0.52	65521
NGC 0985	02 34 37.88	−08 47 17.02	0.043	Sy1.0	60761008002	0.39	21326
NGC 7469	23 03 15.67	+08 52 25.28	0.017	Sy1.2	60101001002	0.75	21579
MRK 110	09 25 12.84	+52 17 10.38	0.036	Sy1.0	60201025002	0.98	184563
1H 0419-577	04 26 00.71	−57 12 01.76	0.104	Sy1.0	60101039002	0.4	169462
Mrk 509	20 44 09.75	−10 43 24.72	0.034	Sy1.5	60101043002	1.19	165885
IC 4329A	13 49 19.26	−30 18 34.21	0.016	Sy1.2	60001045002	2.61	162390

Continued

Table 2.1 – Following the previous page

Source	α_{2000}	δ_{2000}	z	Type	OBSID	counts/sec	Exposure
PG0026+129	00 29 13.70	+13 16 03.94	0.142	Sy1.0	60663003002	0.19	147374
3C 120	04 33 11.09	+05 21 15.61	0.034	Sy1.0	60001042003	1.31	127716
MRK 1383	14 29 06.57	+01 17 06.15	0.086	Sy1.0	60501049002	0.18	95955
KUG 1208+386	12 10 44.27	+38 20 10.19	0.023	Sy1.0	60061225002	0.15	31761
ESO 031−G008	03 07 35.34	−72 50 02.50	0.028	Sy1.0	60160141002	0.19	31655
SDSSJ104326.47+110524.2	10 43 26.47	+11 05 24.26	0.047	Sy1.0	60376004002	0.13	31062
MRK 1393	15 08 53.95	−00 11 49.00	0.054	Sy1.5	60376005002	0.21	30816
IRAS 05589+2828	06 02 10.47	+28 28 19.40	0.033	Sy1.0	60061062002	0.78	29276
ESO 025−G002	18 54 40.26	−78 53 54.10	0.029	Sy1.0	60160700002	0.24	27978
VII ZW 653	16 25 25.95	+85 29 41.69	0.063	Sy1.0	60160639002	0.14	27580
MRK 279	13 53 03.45	+69 18 29.57	0.03	Sy1.5	60601011004	0.16	200632
MCG-01-30-041	11 52 38.16	−05 12 25.27	0.019	Sy1.8	60061216002	0.15	26904
MRK 290	15 35 52.40	+57 54 09.51	0.03	Sy1.0	60061266004	0.2	26348
IGRJ17476-2253	17 47 29.72	−22 52 44.90	0.047	Sy1.0	60463061002	0.19	26097
GRS 1734-292	17 37 28.38	−29 08 02.11	0.021	Sy1.0	60301010002	0.15	26020
2MASS J1830231+731310	18 30 23.16	+73 13 10.71	0.123	Sy1.0	60464150002	0.16	26019
3C 382	18 35 03.38	+32 41 46.85	0.058	Sy1.0	60001084002	0.82	82583
2E1739.1-1210	17 41 55.25	−12 11 56.58	0.037	Sy1.2	60160670002	0.3	21366
MCG+05-40-026	17 01 07.77	+29 24 24.58	0.036	Sy1.0	60061276002	0.12	21000
MRK 520	22 00 41.35	+10 33 08.03	0.027	Sy1.0	60160774002	0.29	20902

Continued

Table 2.1 – Following the previous page

Source	α_{2000}	δ_{2000}	z	Type	OBSID	counts/sec	Exposure
IGR14488-4008	14 48 50.00	−40 08 00.00	0.123	Sy	60463049002	0.17	20300
6dFJ1254564-265702	12 54 56.37	−26 57 02.10	0.059	Sy1.0	60363001002	0.14	20296
2MASXJ1802473-145454	18 02 47.30	−14 54 55.00	0.035	Sy1.0	60160680002	0.59	19958
3C 380	18 29 31.78	+48 44 46.16	0.692	Sy1.0	60160690002	0.13	19610
IRAS04392-2713	04 41 22.53	−27 08 19.33	0.084	Sy1.0	60160201002	0.19	19553
2MASXJ12313717-4758019	12 31 37.14	−47 58 02.00	0.028	Sy1.0	60160498002	0.14	19356
2MASXJ21355399+4728217	21 35 54.02	+47 28 21.89	0.025	Sy1.0	60160761002	0.24	18704
Mrk739E	11 36 29.30	+21 35 45.00	0.03	Sy1.0	60260008002	0.12	18547
S52116+81	21 14 01.17	+82 04 48.35	0.084	Sy1.0	60061303002	0.36	18542
3C 206	08 39 50.58	−12 14 34.32	0.198	Sy1.2	60160332002	0.29	17390
3C 227	09 47 45.14	+07 25 20.59	0.086	Sy1.5	60061329002	0.3	17195
IRAS 09149-6206	09 16 09.36	−62 19 29.56	0.057	Sy1.0	90401630002	0.4	112121
NGC 931	02 28 14.46	+31 18 41.46	0.017	Sy1.0	60101002004	0.74	64242
UGC 10120	15 59 09.62	+35 01 47.56	0.031	Sy1.0	60560027002	0.05	62881
MRK 732	11 13 49.75	+09 35 10.58	0.029	Sy1.5	60061208002	0.21	26359
IC 1198	16 08 36.38	+12 19 51.60	0.033	Sy1.5	60361014002	0.11	26973
VII ZW 742	17 46 59.94	+68 36 39.59	0.063	Sy1.0	60160676004	0.05	31393
MRK 885	16 29 48.38	+67 22 41.98	0.025	Sy1.5	60160641002	0.08	28304
Swift J0919.2+5528	09 19 13.20	+55 27 55.02	0.049	Sy1.0	60201036002	0.05	28897
MRK 876	16 13 57.18	+65 43 09.95	0.121	Sy1.0	60160633002	0.1	29969

Continued

Table 2.1 – Following the previous page

Source	α_{2000}	δ_{2000}	z	Type	OBSID	counts/sec	Exposure
NGC 424	01 11 27.64	−38 05 00.42	0.012	Sy1.0	60662007002	0.06	33724
NGC 4507	12 35 36.63	−39 54 33.7	0.012	Sy1.0	60102051004	0.6	34464
SDSS J114921.52+532013.4	11 49 21.53	+53 20 13.29	0.095	Sy1.0	60260009002	0.06	24886
Mrk 334	00 03 09.61	+21 57 36.97	0.022	Sy1.0	60465001002	0.06	32244
2MASXJ23013626-5913210	23 01 36.23	−59 13 21.08	0.15	Sy1.8	60160814002	0.16	19500
2MASXJ23203662+6430452	23 20 36.58	+64 30 44.78	0.072	Sy1.0	60161824002	0.1	21439
UGC03601	06 55 49.53	+40 00 01.12	0.017	Sy1.5	60160278002	0.1	19674
2MASXJ18560128+1538059	18 56 01.28	+15 38 05.90	0.084	Sy1.0	60160701002	0.22	21352
3C 109	04 13 40.34	+11 12 14.78	0.306	Sy1.8	60301011004	0.17	89150
ESO381-G007	12 40 46.96	−33 34 11.84	0.055	Sy1.5	60160508002	0.12	21250
MRK 926	23 04 43.48	−08 41 08.62	0.047	Sy1.5	60201029002	1.53	106201
2E1849.2−7832	18 57 07.76	−78 28 21.21	0.042	Sy1.0	60061290002	0.21	17967
KUG 1141+371	11 44 29.87	+36 53 08.61	0.038	Sy1.0	90601618002	0.28	38562
Ark 241	10 21 40.25	−03 27 13.75	0.041	Sy1.0	60160392002	0.18	20329
3C 332	16 17 42.54	+32 22 34.37	0.151	Sy1.0	60160634002	0.19	20957
MRK 595	02 41 34.87	+07 11 13.85	0.027	Sy1.5	60160119002	0.06	21298
IGR J14471-6414	14 46 28.20	−64 16 24.00	0.053	Sy1.2	60061257002	0.1	15042
FAIRALL 1146	08 38 30.77	−35 59 33.33	0.032	Sy1.5	60061082002	0.34	21278
RBS0770	09 23 43.00	+22 54 32.57	0.033	Sy1.2	60602018002	0.57	42960
NGC 5273	13 42 08.38	+35 39 15.46	0.004	Sy1.9	60061350002	0.46	21117

Continued

Table 2.1 – Following the previous page

Source	α_{2000}	δ_{2000}	z	Type	OBSID	counts/sec	Exposure
ESO 416−G002	02 35 13.45	−29 36 17.25	0.059	Sy1.9	60061340002	0.1	20606
MRK 1310	12 01 14.35	−03 40 41.01	0.02	Sy1.0	60160465002	0.23	21131
PG0804+761	08 10 58.66	+76 02 42.45	0.101	Sy1.0	60160322002	0.18	17315
NGC 5674	14 33 52.28	+05 27 30.11	0.025	Sy1.9	60061337002	0.2	20671
MRK 1392	15 05 56.55	+03 42 26.33	0.036	Sy1.0	60160605002	0.14	21084
NGC 4579	12 37 43.59	+11 49 05.12	0.005	Sy1.9	60201051002	0.18	117843
MRK 205	12 21 44.07	+75 18 38.24	0.071	Sy1.0	60160490002	0.21	20372
2MASXJ11324928+1017473	11 32 49.27	+10 17 47.27	0.044	Sy1.0	60061212002	0.05	20469
2MASXJ04372814−4711298	04 37 28.16	−47 11 29.48	0.053	Sy1.0	30001061002	0.12	73821
MRK 684	14 31 04.78	+28 17 14.12	0.045	Sy1.0	60160586002	0.08	20497
MRK 1239	09 52 19.17	−01 36 44.10	0.02	Sy1.5	60360006002	0.08	21093
RBS 1037	11 49 18.68	−04 16 50.79	0.085	Sy1.0	60061215002	0.1	40679
IRAS04124−0803	04 14 52.66	−07 55 39.68	0.039	Sy1.0	60761001002	0.32	18345

TABLE 2.2: Information on the sources investigated to determine kT_e. The pillars are (1) the source's name, (2) galactic hydrogen column density, N_H^{gal}, in units of 10^{22} atoms cm^{-2} obtained from Willingale et al. (2013), (3) observation ID (4) epoch and (5) date of observation.

Source	N_H^{gal}	OBSID	Epoch	Date
1H0419−577	0.013	60402006002	A	2018-05-15
		60402006004	B	2018-11-13
		60101039002	C	2015-06-03
Mrk 915	0.064	60002060002	A	2014-12-02
		60002060004	B	2014-12-07
		60002060006	C	2014-12-12
3C 111	0.434	60202061002	A	2017-12-26
		60202061004	B	2017-12-29
		60202061006	C	2019-01-04
NGC 3783	0.138	60101110002	A	2016-08-22
		60101110004	B	2016-08-24
		80202006002	C	2016-12-11
		80202006004	D	2016-12-21
NGC 7469	0.052	60101001002	A	2015-06-12
		60101001004	B	2015-11-24
		60101001006	C	2015-12-15
		60101001008	D	2015-12-22
		60101001010	E	2015-12-25
		60101001012	F	2015-12-27
		60101001014	G	2015-12-28
Mrk 110	0.014	60201025002	A	2017-01-23
		60502022002	B	2019-11-16
		60502022004	C	2020-04-05
UGC 06728	0.055	60160450002	A	2016-07-10
		60376007002	B	2017-10-13

Continued

Table 2.2 – Following the previous page

Source	N_H^{gal}	OBSID	Epoch	Date
NGC 4258	0.016	60101046002	A	2015-11-16
		60101046004	B	2016-01-10
KUG 1141+371	0.018	60160449002	A	2019-12-26
		90601618002	B	2020-05-13
MCG-06-30-15	0.047	60001047002	A	2013-01-29
		60001047003	B	2013-01-30
		60001047005	C	2013-02-02
NGC 5506	0.048	60061323002	A	2014-04-01
		60501015002	B	2019-12-28
		60501015004	C	2020-02-09
MCG+08-11-011	0.293	60201027002	A	2016-08-16
		90701640002	B	2021-12-18
GRS 1734-292	0.876	60061279002	A	2014-09-16
		60301010002	B	2018-05-28
Mrk 926	0.125	60201029002	A	2016-11-21
		60761009002	B	2021-07-04
Mrk 841	0.024	60101023002	A	2015-07-14
		80701616002	B	2022-01-09
NGC 5273	0.009	60061350002	A	2014-07-14
		90801618002	B	2022-07-03
NGC 0985	0.035	60061025002	A	2013-08-11
		60761008002	B	2021-09-13
HE 1143−1810	0.033	60302002002	A	2017-12-16
		60302002004	B	2017-12-18
		60302002006	C	2017-12-20
		60302002008	D	2017-12-22
		60302002010	E	2017-12-24

Continued

Table 2.2 – Following the previous page

Source	N_H^{gal}	OBSID	Epoch	Date
NGC 3227	0.021	60202002002	A	09-11-2016
		60202002004	B	25-11-2016
		60202002006	C	29-11-2016
		60202002008	D	01-12-2016
		60202002010	E	05-12-2016
		60202002012	F	09-12-2016
		60202002014	G	21-01-2017
		80502609002	H	15-11-2019
		80502609004	I	05-12-2019
NGC 5548	0.017	60002044002	A	11-07-2013
		60002044003	B	12-07-2013
		60002044005	C	23-07-2013
		60002044006	D	10-09-2013
		60002044008	E	20-12-2013
		90701601002	F	26-01-2021
MR 2251−178	0.027	60102025002	A	18-05-2015
		60102025004	B	17-06-2015
		60102025006	C	10-11-2015
		60102025008	D	11-12-2015
		90601637002	E	16-12-2020

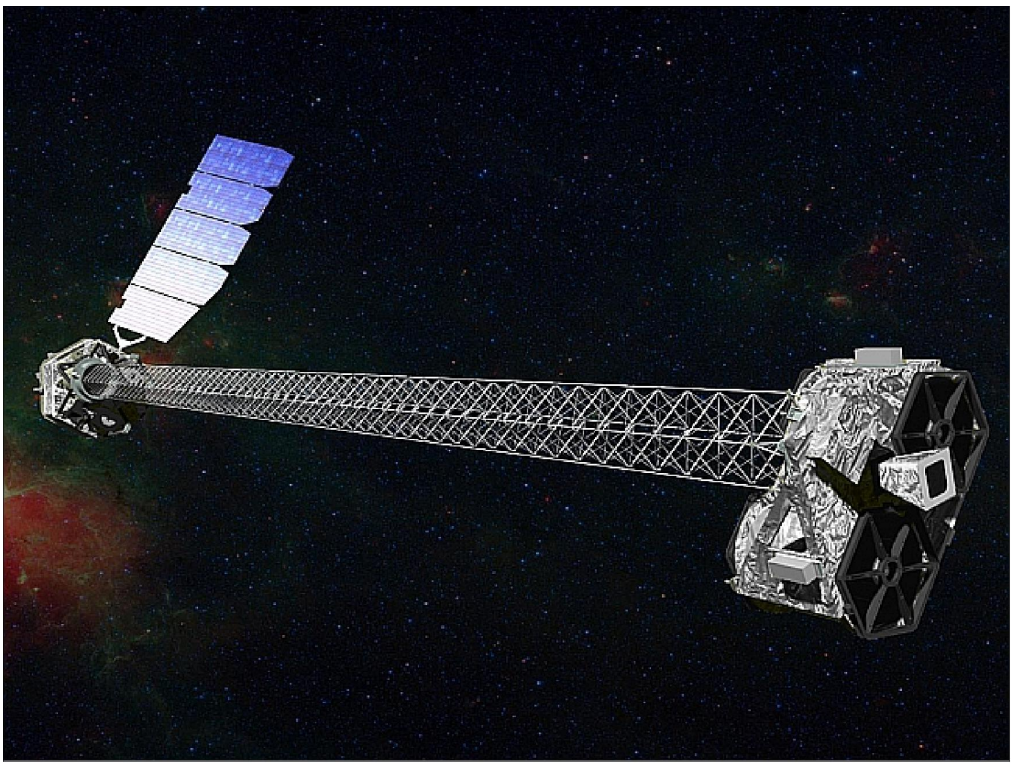

FIGURE 2.2: Artist's representation of *NuSTAR* (image credit: NASA/JPL)

2.2 Observations and Data Reduction

The observations of the sources selected for both the determination of the temperature of the corona and the variation in the temperature of the corona, if any, were from *NuSTAR*. *NuSTAR*, a NASA mission operating in the 3−79 keV band, is the first hard X-ray focussing telescope launched on June 13, 2012. An artist's presentations of the *NuSTAR* spacecraft in orbit is shown in Fig. 2.2. *NuSTAR* is more sensitive and has superior angular resolution than any other hard X-ray equipment currently in use and working in a comparable energy range. (see Fig. 2.3).

We carried out the raw event data reduction taken from the HEASARC archive*, using the standard software NuSTARDAS v1.9.3† distributed by HEASARC within

*https://heasarc.gsfc.nasa.gov/db- perl/W3Browse/w3browse.pl
†https://heasarc.gsfc.nasa.gov/docs/nustar/analysis/nustar swguide.pdf

HEASoft v6.26.1. Using the CALDB release 20190607, all of the event files were created. We generated the calibrated and cleaned event files using the `nupipeline` task. To exclude the periods of elevated background, we selected the filtering options SAACALC=2, SAAMODE=OPTIMIZED and TENTACLE=YES to consider the satellite's passage through the South Atlantic Anomaly (SAA). After the extraction of source and background count rate, all the science products, including energy spectra, auxiliary response files (ARFs) and response matrix files (RMFs), were created using the task `nuproducts` for both the focal plane modules FPMA and FPMB. For spectral analysis, we fitted the background subtracted spectra from FPMA and FPMB simultaneously using XSPEC version 12.10.1 (Arnaud 1996), allowing the cross normalization factor to vary freely during spectral fits. We chose different source and background extraction radii and spectral binning criteria for our work. The choice we made are discussed below. To get an estimate of the model parameters, we used the chi-square (χ^2) statistics. We used the $\chi^2 = 2.71$ criterion to calculate the errors in the model parameters, i.e. 90% confidence range in XSPEC.

The source regions for the 130 Seyfert 1 galaxies were extracted using circular radii between $30'' - 70''$, depending on the source. Similarly, we selected the same circular area on the same chip to extract the background counts. The spectra were binned to have minimum counts of 20 per spectral energy bin.

On reducing the 21 sources with multiple epochs of observations for studies on coronal temperature variation, we chose a circle of radius $70''$ centred around the source. Similarly, to extract the background, we selected a circle of the same radius on the same chip. The background-subtracted source spectra were binned to have a minimum count of 25 in each spectral bin. To extract the source and background counts in NGC 3227, MR 2251−178 and NGC 5548, we chose two circles of radius $60''$ each on the same chip. The spectra were binned to have an S/N greater than

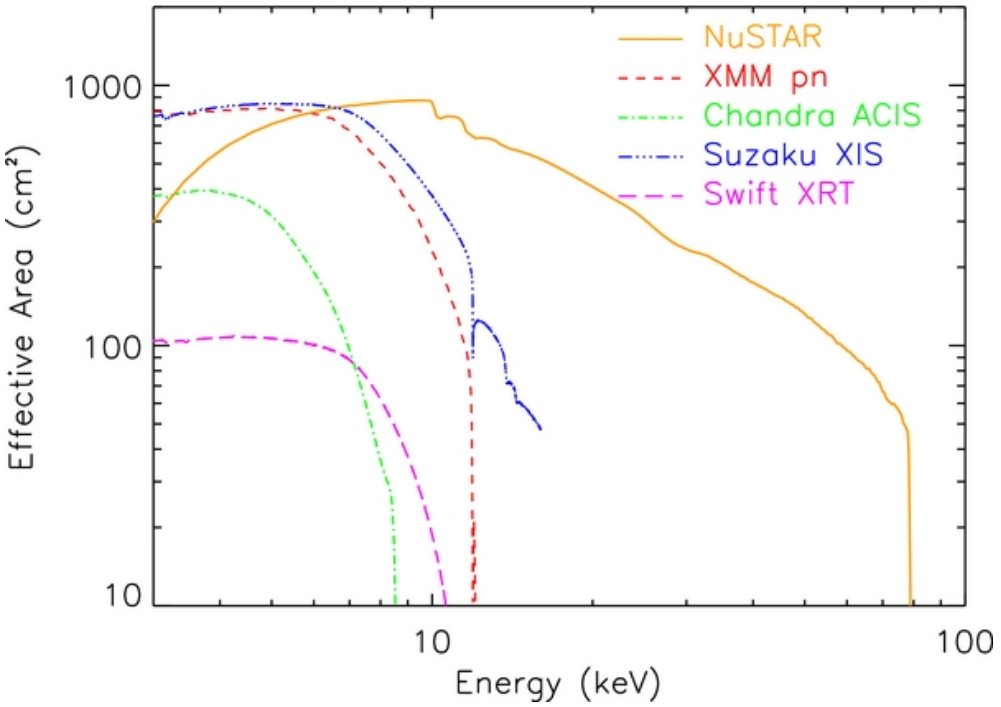

FIGURE 2.3: Effective collecting area of *NuSTAR* compared to selected operating focusing telescopes taken from Harrison et al. (2013).

5 in each spectral channel using the *NuSTAR*-specific Python script *snrgrppha*[‡].

[‡]https://sites.astro.caltech.edu/~mislavb/

Chapter 3

On the properties of corona in type 1 Seyfert galaxies [†]

We carried out an analysis of 130 Seyfert 1 type AGN to determine E_{cut} based on physical model fits to the *NuSTAR* spectra. We could constrain E_{cut} in 75 sources out of the 130 sources. Further, physical model fits were carried out on these 75 sources to constrain kT_e. We could constrain kT_e in 48 sources. Additionally, we attempted to locate these sources on the temperature−compactness ($\theta - l$) diagram and investigated the correlation between different physical parameters obtained from the physical model fits. In this work we adopted the cosmological parameters of $H_0 = 70$ km sec^{-1} Mpc^{-1}, $\Omega_\lambda = 0.7$ and $\Omega_M = 0.3$. All the quoted uncertainties in the deduced parameters were computed with a 90% level of confidence.

[†]The contents of this chapter are from Pal et al. (2023; MNRAS submitted)

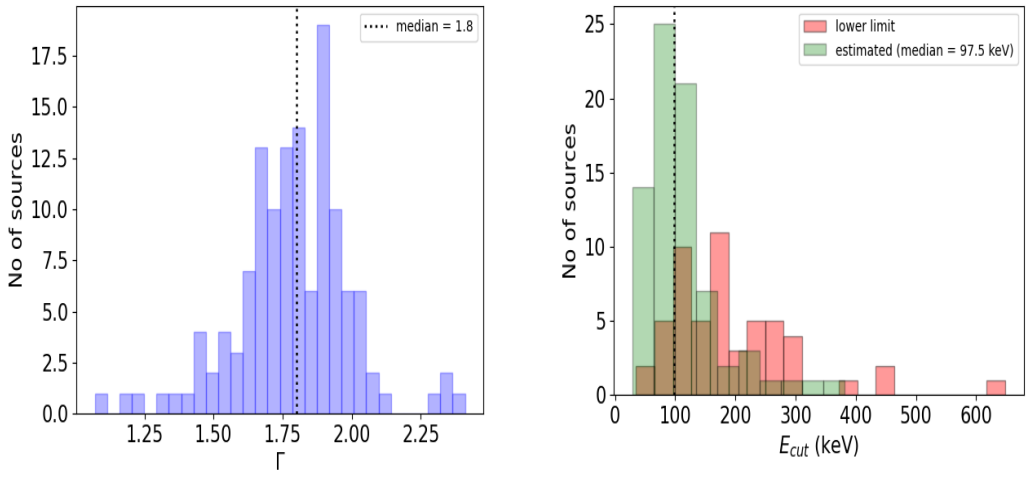

FIGURE 3.1: Left panel: Distribution of Γ obtained from Model−1. Right panel: Distribution of E_{cut} obtained from Model−1 fit to all 130 source spectra. The vertical dotted line in both the plots is the median of the distribution.

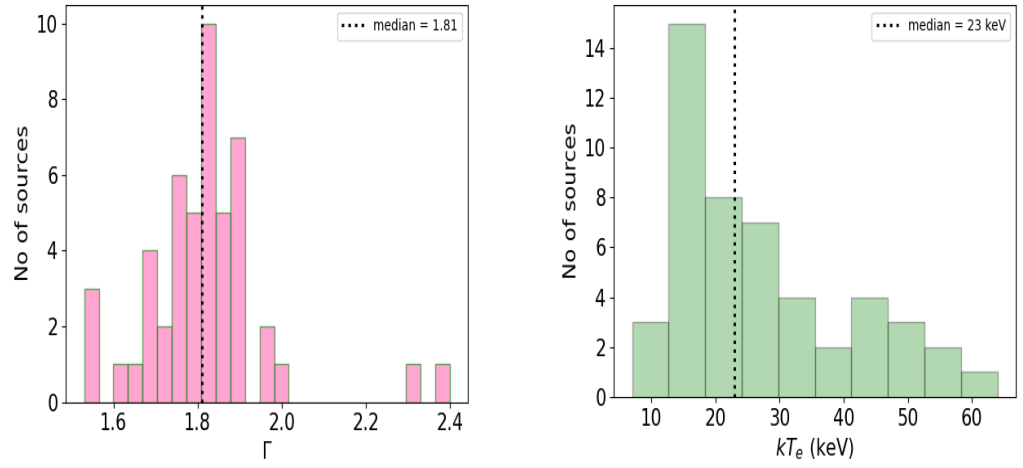

FIGURE 3.2: Distribution of Γ (left panel) and kT_e (right panel) from Model−2 fit for the sample of 49 sources. The black dotted line shows the median of the distribution.

TABLE 3.1: Best-fitted parameters of the Model *const* × *TBabs* × *zTBabs* × *(xillver/relxill/relxill+xillver)* to the source spectra.

Source	Γ	E_{cut} (keV)	χ^2/dof
NGC 3516	$1.90^{+0.02}_{-0.02}$	>448	696/655
MRK 590	$1.68^{+0.02}_{-0.02}$	127^{+33}_{-23}	818/775
MRK 79	$1.89^{+0.01}_{-0.01}$	184^{+49}_{-32}	1008/971
IGRJ19378-0617	$2.11^{+0.07}_{-0.06}$	228^{+419}_{-83}	757/786
ARK 120	$2.02^{+0.01}_{-0.01}$	329^{+102}_{-55}	1182/1148
MRK 817	$1.98^{+0.04}_{-0.04}$	>252	345/321
HE1136−2304	$1.64^{+0.02}_{-0.02}$	86^{+16}_{-12}	718/703
Fairall 51	$1.66^{+0.02}_{-0.01}$	86^{+11}_{-9}	823/764
MKN 6	$1.07^{+0.01}_{-0.02}$	43^{+2}_{-2}	761/842
MRK 279	$1.49^{+0.04}_{-0.05}$	68^{+18}_{-13}	1073/998
NGC 4151	$1.36^{+0.05}_{-0.04}$	105^{+32}_{-55}	2599/2291
NGC 4051	$1.78^{+0.07}_{-0.07}$	>452	1674/1647
MRK 915	$1.65^{+0.04}_{-0.03}$	70^{+12}_{-10}	615/622
MRK 359	$1.91^{+0.03}_{-0.03}$	>163	485/433
MRK 335	$2.03^{+0.02}_{-0.02}$	>394	894/773
IRAS F12397+3333	$2.34^{+0.04}_{-0.04}$	>97	453/399
3C 390.3	$1.77^{+0.01}_{-0.01}$	144^{+34}_{-19}	997/1017
ESO 323−G077	$1.45^{+0.03}_{-0.03}$	89^{+14}_{-13}	409/386
NGC 3783	$1.61^{+0.03}_{-0.04}$	112^{+24}_{-19}	1186/1130
ESO 511−G030	$1.73^{+0.04}_{-0.05}$	65^{+20}_{-12}	309/289
2MASXJ10523297+1036205	$1.16^{+0.04}_{-0.04}$	33^{+4}_{-3}	326/319
MRK 813	$1.96^{+0.04}_{-0.04}$	>228	346/321
PG0052+251	$1.66^{+0.02}_{-0.01}$	>76	167/190
2MASXJ15295830−1300397	$1.79^{+0.05}_{-0.05}$	>201	224/214
MRK 376	$1.98^{+0.06}_{-0.06}$	>222	182/183
ESO 209−G012	$1.90^{+0.04}_{-0.03}$	>260	399/427

Continued

Table 3.1 – Following the previous page

Source	Γ	E_{cut} (keV)	χ^2/dof
MRK 841	$1.80^{+0.03}_{-0.03}$	125^{+49}_{-30}	467/508
RBS0295	$1.73^{+0.06}_{-0.05}$	>91	212/218
NGC 4593	$1.87^{+0.02}_{-0.02}$	>648	523/571
MCG-06-30-15	$1.82^{+0.11}_{-0.09}$	126^{+23}_{-19}	1574/1516
H1821+643	$1.91^{+0.03}_{-0.03}$	229^{+221}_{-77}	450/454
MRK 1148	$1.76^{+0.03}_{-0.03}$	99^{+30}_{-20}	545/532
CGCG229−015	$1.71^{+0.08}_{-0.06}$	46^{+14}_{-8}	164/173
HE0103−3447	$1.54^{+0.12}_{-0.09}$	84^{+64}_{-37}	247/274
IGRJ14552−5133	$1.93^{+0.02}_{-0.02}$	254^{+194}_{-72}	741/775
2MASXJ19380437−5109497	$1.85^{+0.05}_{-0.05}$	102^{+64}_{-29}	243/255
2MASSJ17485512−3254521	$1.61^{+0.04}_{-0.04}$	75^{+18}_{-14}	414/427
MRK 1044	$1.80^{+0.05}_{-0.06}$	381^{+553}_{-179}	1004/1004
UGC 3478	$1.99^{+0.06}_{-0.06}$	>98	212/196
MRK 704	$1.80^{+0.04}_{-0.04}$	207^{+146}_{-64}	374/342
2MASXJ21192912+3332566	$1.80^{+0.04}_{-0.04}$	82^{+33}_{-18}	351/344
1H1934-063	$2.34^{+0.05}_{-0.06}$	>153	780/733
NGC 0985	$1.84^{+0.03}_{-0.03}$	>188	393/469
MRK 110	$1.73^{+0.01}_{-0.01}$	92^{+5}_{-5}	1688/1578
Mrk 509	$1.75^{+0.01}_{-0.01}$	87^{+4}_{-4}	1726/1619
MRK 1383	$1.92^{+0.02}_{-0.02}$	>276	818/768
KUG 1208+386	$1.89^{+0.04}_{-0.04}$	>287	354/342
ESO 031−G008	$2.04^{+0.04}_{-0.04}$	>286	305/354
MRK 1393	$1.95^{+0.04}_{-0.04}$	>295	352/376
ESO 025−G002	$1.67^{+0.04}_{-0.04}$	133^{+93}_{-26}	385/417
VII ZW 653	$2.05^{+0.05}_{-0.05}$	>114	187/213
MCG-01-30-041	$1.80^{+0.06}_{-0.05}$	>201	224/246
MRK 290	$1.59^{+0.04}_{-0.04}$	102^{+46}_{-25}	316/364

Continued

Table 3.1 – Following the previous page

Source	Γ	E_{cut} (keV)	χ^2/dof
IGRJ17476-2253	$1.46^{+0.04}_{-0.04}$	45^{+9}_{-7}	319/319
3C 382	$1.68^{+0.01}_{-0.01}$	112^{+12}_{-10}	1239/1247
2E1739.1-1210	$1.89^{+0.04}_{-0.03}$	>286	443/405
MRK 520	$1.55^{+0.03}_{-0.03}$	60^{+11}_{-9}	356/398
IGR14488-4008	$1.82^{+0.05}_{-0.05}$	>180	254/233
6dFJ1254564-265702	$1.58^{+0.04}_{-0.05}$	>57	164/186
3C 380	$1.66^{+0.06}_{-0.06}$	>217	198/178
IRAS04392-2713	$1.92^{+0.06}_{-0.06}$	>188	172/185
2MASXJ12313717-4758019	$1.88^{+0.06}_{-0.06}$	>112	136/178
2MASXJ21355399+4728217	$1.66^{+0.05}_{-0.04}$	56^{+15}_{-10}	287/292
Mrk739E	$2.07^{+0.07}_{-0.07}$	>241	150/141
S52116+81	$1.75^{+0.04}_{-0.04}$	103^{+40}_{-24}	370/409
3C 206	$1.76^{+0.05}_{-0.05}$	112^{+47}_{-33}	272/264
3C 227	$1.78^{+0.04}_{-0.03}$	>79	264/290
IRAS 09149-6206	$1.83^{+0.01}_{-0.01}$	93^{+9}_{-8}	1134/1008
NGC 931	$1.88^{+0.01}_{-0.01}$	232^{+79}_{-44}	977/954
UGC 10120	$1.91^{+0.07}_{-0.06}$	>225	185/192
MRK 732	$1.78^{+0.04}_{-0.04}$	>279	324/352
IC 1198	$1.75^{+0.06}_{-0.05}$	124^{+107}_{-43}	191/195
VII ZW 742	$1.88^{+0.08}_{-0.08}$	>174	99/108
MRK 885	$1.90^{+0.08}_{-0.06}$	>161	172/151
Swift J0919.2+5528	$2.09^{+0.09}_{-0.08}$	>112	85/90
MRK 876	$1.81^{+0.06}_{-0.06}$	140^{+154}_{-52}	193/187
NGC 424	$1.72^{+0.14}_{-0.69}$	>103	99/71
SDSS J114921.52+532013.4	$1.53^{+0.10}_{-0.10}$	29^{+9}_{-7}	88/75
2MASXJ23203662+6430452	$1.73^{+0.08}_{-0.07}$	93^{+145}_{-37}	120/132
UGC 03601	$1.49^{+0.09}_{-0.08}$	58^{+45}_{-19}	127/109

Continued

Table 3.1 – Following the previous page

Source	Γ	E_{cut} (keV)	χ^2/dof
2MASXJ18560128+1538059	$1.47^{+0.04}_{-0.04}$	41^{+5}_{-5}	287/307
3C 109	$1.64^{+0.03}_{-0.03}$	72^{+10}_{-9}	587/627
ESO381-G007	$1.66^{+0.07}_{-0.07}$	64^{+35}_{-18}	163/161
MRK 926	$1.74^{+0.01}_{-0.01}$	135^{+11}_{-9}	1549/1496
2E1849.2−7832	$1.89^{+0.04}_{-0.04}$	>133	281/267
Ark 241	$1.88^{+0.05}_{-0.05}$	>115	197/214
3C 332	$1.70^{+0.04}_{-0.04}$	>237	279/286
MRK 595	$1.31^{+0.18}_{-0.23}$	>35	104/100
IGR J14471-6414	$2.01^{+0.08}_{-0.08}$	>153	115/106
FAIRALL 1146	$2.03^{+0.03}_{-0.03}$	138^{+73}_{-39}	433/423
RBS0770	$1.77^{+0.02}_{-0.02}$	65^{+8}_{-7}	775/715
NGC 5273	$1.44^{+0.06}_{-0.06}$	68^{+25}_{-16}	593/574
ESO 416−G002	$1.81^{+0.07}_{-0.07}$	>172	119/125
MRK 1310	$1.82^{+0.04}_{-0.04}$	>173	304/293
PG0804+761	$1.94^{+0.05}_{-0.05}$	>269	217/221
NGC 5674	$1.88^{+0.23}_{-0.25}$	>91	269/250
MRK 1392	$1.93^{+0.06}_{-0.05}$	>187	185/193
NGC 4579	$1.73^{+0.06}_{-0.06}$	82^{+49}_{-23}	819/739
MRK 205	$1.92^{+0.05}_{-0.05}$	131^{+122}_{-45}	259/255
2MASXJ11324928+1017473	$2.00^{+0.10}_{-0.10}$	>108	63/58
2MASXJ04372814−4711298	$1.98^{+0.05}_{-0.05}$	116^{+96}_{-38}	272/297
MRK 684	$2.14^{+0.09}_{-0.08}$	>150	99/103
RBS 1037	$2.00^{+0.06}_{-0.06}$	>133	208/200
IRAS04124−0803	$1.53^{+0.04}_{-0.04}$	80^{+21}_{-14}	298/330
MCG+08-11-011	$1.83^{+0.01}_{-0.01}$	153^{+15}_{-13}	1506/1419
ARK 564	$2.41^{+0.04}_{-0.03}$	73^{+30}_{-16}	582/574
NGC 3227	$1.64^{+0.01}_{-0.01}$	94^{+7}_{-6}	1224/1163

Continued

Table 3.1 – Following the previous page

Source	Γ	E_{cut} (keV)	χ^2/dof
NGC 5506	$1.50^{+0.19}_{-0.06}$	81^{+78}_{-10}	1263/1310
SWIFTJ2127.4+5654	$1.89^{+0.01}_{-0.01}$	84^{+6}_{-6}	1094/1089
KUG 1141+371	$1.92^{+0.11}_{-0.14}$	>91	470/514
MRK 1040	$1.88^{+0.01}_{-0.01}$	300^{+108}_{-70}	1025/1007
UGC 06728	$1.62^{+0.005}_{-0.004}$	66^{+7}_{-6}	2402/2081
3C 111	$1.60^{+0.01}_{-0.01}$	128^{+31}_{-21}	910/890
NGC 5548	$1.71^{+0.03}_{-0.01}$	118^{+12}_{-8}	1219/1143
IGRJ21247+5058	$1.61^{+0.05}_{-0.04}$	87^{+18}_{-13}	1336/1279
HE 1143−1810	$1.79^{+0.07}_{-0.06}$	104^{+24}_{-17}	524/617
MR 2251−178	$1.63^{+0.01}_{-0.02}$	96^{+17}_{-9}	818/859
2MASXJ18470283-7831494	$1.91^{+0.04}_{-0.12}$	>182	250/276
NGC 7469	$1.95^{+0.02}_{-0.02}$	122^{+27}_{-21}	647/692
1H 0419-577	$1.67^{+0.03}_{-0.04}$	59^{+8}_{-7}	1138/1096
IC 4329A	$1.77^{+0.01}_{-0.01}$	191^{+14}_{-10}	2211/2088
PG0026+129	$1.82^{+0.02}_{-0.02}$	110^{+20}_{-15}	903/856
3C 120	$1.82^{+0.01}_{-0.01}$	147^{+12}_{-9}	1591/1594
IRAS 05589+2828	$1.83^{+0.11}_{-0.09}$	136^{+109}_{-56}	843/771
GRS 1734-292	$1.67^{+0.02}_{-0.01}$	75^{+6}_{-5}	894/923
2MASXJ23013626-5913210	$1.68^{+0.06}_{-0.06}$	41^{+8}_{-6}	174/179
MCG+05-40-026	$1.77^{+0.07}_{-0.06}$	104^{+151}_{-41}	161/155
2MASS J1830231+731310	$1.69^{+0.04}_{-0.04}$	>107	242/260
2MASXJ1802473-145454	$1.90^{+0.02}_{-0.02}$	>168	578/549
SDSSJ104326.47+110524.2	$1.76^{+0.02}_{-0.04}$	>105	244/248

TABLE 3.2: Best-fitted parameters of the Model *const* × *TBabs* × *zTBabs* × *(xillverCP/relxillCP/relxillCP+xillverCP)* to the 48 source spectra.

Source	N_H^{INT} (10^{22} cm^{-2})	Γ	kT_e (keV)	R	$N_{xillverCP}$ (10^{-4})	$N_{relxillCP}$ (10^{-4})	χ^2/dof	Flux(10^{-11}) (erg $cm^{-2}s^{-1}$)
1H 0419-577	$1.95^{+0.36}_{-0.36}$	$1.82^{+0.01}_{-0.01}$	$14.25^{+01.04}_{-00.89}$	$0.15^{+0.06}_{-0.06}$	$0.79^{+0.01}_{-0.01}$	-	1321/1255	3.48
3C 111	$2.46^{+0.39}_{-0.38}$	$1.84^{+0.01}_{-0.01}$	$37.30^{+34.11}_{-10.36}$	$0.07^{+0.07}_{-0.06}$	$2.46^{+0.03}_{-0.03}$	-	1081/1025	10.57
3C 120	-	$1.85^{+0.01}_{-0.01}$	$45.31^{+18.79}_{-07.82}$	$0.23^{+0.04}_{-0.04}$	-	$2.72^{+0.11}_{-0.08}$	1566/1592	13.09
3C 390.3	$2.29^{+0.37}_{-0.40}$	$1.84^{+0.01}_{-0.01}$	$44.13^{+54.75}_{-12.50}$	$0.15^{+0.08}_{-0.05}$	$2.44^{+0.02}_{-0.03}$	-	1077/1059	10.75
ARK 564	-	$2.40^{+0.02}_{-0.02}$	$24.28^{+09.59}_{-05.68}$	$0.46^{+0.29}_{-0.07}$	<0.08	$0.96^{+0.10}_{-0.26}$	1168/1165	1.98
GRS 1734-292	$3.75^{+0.46}_{-0.44}$	$1.81^{+0.01}_{-0.01}$	$19.86^{+04.33}_{-02.13}$	$0.24^{+0.08}_{-0.09}$	$2.98^{+0.05}_{-0.04}$	-	818/856	14.89
HE 1136-2304	$2.08^{+0.69}_{-0.73}$	$1.78^{+0.03}_{-0.02}$	$27.81^{+78.85}_{-09.30}$	$0.11^{+0.15}_{-0.10}$	$0.53^{+0.01}_{-0.01}$	-	651/649	2.60
HE 1143-1810	-	$1.85^{+0.02}_{-0.02}$	$26.70^{+18.77}_{-07.43}$	$0.26^{+0.15}_{-0.13}$	$1.37^{+0.02}_{-0.02}$	-	534/597	6.73
IC 4329A	$1.89^{+0.11}_{-0.12}$	$1.83^{+0.003}_{-0.003}$	$64.16^{+15.41}_{-11.63}$	$0.30^{+0.03}_{-0.03}$	$6.27^{+0.03}_{-0.04}$	-	2245/2088	30.08
IGR J21247+5058	$2.67^{+0.16}_{-0.16}$	$1.79^{+0.01}_{-0.01}$	$24.70^{+03.79}_{-02.68}$	$0.04^{+0.04}_{-0.03}$	$6.00^{+0.04}_{-0.11}$	-	1466/1378	27.60
IRAS 04124-0803	-	$1.66^{+0.03}_{-0.03}$	$14.88^{+03.70}_{-02.57}$	$0.42^{+0.29}_{-0.30}$	$0.57^{+0.02}_{-0.02}$	-	309/328	3.71
IRAS 09149-6206	-	$1.90^{+0.11}_{-0.09}$	$18.09^{+16.87}_{-04.07}$	$2.04^{+0.68}_{-0.53}$	-	$0.59^{+0.04}_{-0.02}$	989/1007	3.57
IRAS 05589+2828	-	$1.90^{+0.11}_{-0.07}$	$42.90^{+120.46}_{-23.92}$	$1.00^{+1.03}_{-0.40}$	-	$1.19^{+0.14}_{-0.27}$	788/738	7.10
MCG-06-30-15	-	$1.97^{+0.06}_{-0.04}$	$49.63^{+97.84}_{-10.45}$	$0.58^{+0.39}_{-0.12}$	$0.89^{+0.19}_{-0.18}$	$1.71^{+0.31}_{-0.47}$	1572/1516	10.33
MCG+08-11-011	-	$1.88^{+0.01}_{-0.01}$	$55.98^{+26.17}_{-16.01}$	$0.35^{+0.06}_{-0.05}$	$2.92^{+0.02}_{-0.02}$	-	1506/1419	13.96
Mrk 110	-	$1.81^{+0.01}_{-0.01}$	$22.50^{+03.03}_{-02.32}$	$0.10^{+0.03}_{-0.03}$	-	$1.98^{+0.05}_{-0.05}$	1768/1575	9.45
Mrk 509	-	$1.86^{+0.01}_{-0.02}$	$35.78^{+6.78}_{-5.72}$	$0.31^{+0.28}_{-0.21}$	$0.53^{+0.31}_{-0.27}$	$2.34^{+0.08}_{-0.13}$	1646/1591	11.63

Continued

Table 3.2 – Following the previous page

Source	N_H^{INT} (10^{22} cm^{-2})	Γ	kT_e (keV)	R	$N_{xillverCP}$ (10^{-4})	$N_{relxillCP}$ (10^{-4})	χ^2/dof	Flux(10^{-11}) (erg $cm^{-2}s^{-1}$)
Mrk 520	-	$1.63^{+0.03}_{-0.03}$	$15.20^{+4.36}_{-2.77}$	$0.23^{+0.23}_{-0.19}$	$0.61^{+0.02}_{-0.02}$	-	300/328	3.87
Mrk 841	-	$1.88^{+0.02}_{-0.02}$	$33.31^{+21.81}_{-10.50}$	$0.52^{+0.17}_{-0.15}$	$0.80^{+0.01}_{-0.01}$	-	741/744	4.14
Mrk 915	$6.33^{+0.94}_{-0.93}$	$1.83^{+0.03}_{-0.02}$	$28.17^{+50.80}_{-10.91}$	$0.44^{+0.23}_{-0.18}$	$0.35^{+0.01}_{-0.01}$	-	619/622	1.83
NGC 3227	$2.66^{+0.34}_{-0.33}$	$1.76^{+0.01}_{-0.01}$	$26.11^{+05.82}_{-04.12}$	$0.56^{+0.09}_{-0.09}$	$1.89^{+0.02}_{-0.02}$	-	1198/1163	12.01
NGC 3783	-	$1.74^{+0.02}_{-0.02}$	$47.51^{+48.48}_{-09.22}$	$0.41^{+0.20}_{-0.16}$	$0.76^{+0.27}_{-0.26}$	$2.33^{+0.23}_{-0.15}$	1270/1132	14.24
NGC 5273	-	$1.55^{+0.03}_{-0.03}$	$14.71^{+02.72}_{-02.46}$	$0.76^{+0.51}_{-0.34}$	-	$0.68^{+0.12}_{-0.12}$	487/506	5.80
NGC 5506	$2.50^{+0.68}_{-0.63}$	$1.75^{+0.07}_{-0.03}$	$26.54^{+24.87}_{-05.34}$	$0.63^{+0.12}_{-0.09}$	$0.58^{+0.36}_{-0.14}$	$2.69^{+0.15}_{-0.16}$	1254/1310	17.16
NGC 5548	$3.32^{+0.34}_{-0.35}$	$1.81^{+0.01}_{-0.01}$	$34.79^{+09.27}_{-06.79}$	$0.43^{+0.10}_{-0.09}$	$2.23^{+0.07}_{-0.03}$	-	1228/1143	11.90
NGC 7469	-	$2.00^{+0.02}_{-0.02}$	$45.36^{+52.24}_{-17.13}$	$0.74^{+0.20}_{-0.17}$	$1.59^{+0.03}_{-0.03}$	-	650/692	7.52
PG0026+129	-	$1.89^{+0.01}_{-0.01}$	$22.18^{+08.88}_{-04.03}$	$0.30^{+0.12}_{-0.11}$	$0.39^{+0.12}_{-0.11}$	-	899/856	1.66
SWIFTJ2127.4+5654	-	$1.96^{+0.01}_{-0.01}$	$20.70^{+03.36}_{-01.94}$	$0.72^{+0.10}_{-0.10}$	$1.49^{+0.01}_{-0.01}$	-	1084/1089	7.31
UGC 06728	-	$1.73^{+0.07}_{-0.07}$	$16.61^{+24.78}_{-04.93}$	$0.34^{+0.42}_{-0.21}$	-	$0.31^{+0.58}_{-0.39}$	223/239	1.97
IGRJ19378-0617	-	$2.33^{+0.01}_{-0.01}$	$49.35^{+36.94}_{-13.04}$	$0.99^{+0.23}_{-0.18}$	$1.56^{+0.02}_{-0.02}$	-	895/789	3.78
Fairall 51	$11.53^{+0.82}_{-0.80}$	$1.79^{+0.02}_{-0.02}$	$19.48^{+06.54}_{-01.83}$	$1.33^{+0.27}_{-0.24}$	$0.45^{+0.01}_{-0.01}$	-	817/764	3.29
MRK 279	-	$1.68^{+0.02}_{-0.02}$	$16.38^{+01.72}_{-01.55}$	$0.13^{+0.09}_{-0.08}$	$0.29^{+0.02}_{-0.01}$	$0.09^{+0.02}_{-0.02}$	1007/994	1.76
ESO 323−G077	38^{+3}_{-3}	$1.70^{+0.02}_{-0.02}$	$35.21^{+13.02}_{-11.89}$	$2.35^{+0.81}_{-0.66}$	$0.29^{+0.02}_{-0.02}$	-	411/386	2.94
CGCG229−015	-	$1.89^{+0.05}_{-0.04}$	$17.00^{+41.62}_{-05.61}$	$0.82^{+0.83}_{-0.55}$	$0.21^{+0.01}_{-0.01}$	-	168/173	1.18
2MASXJ21355399+4728217	-	$1.81^{+0.03}_{-0.03}$	$15.57^{+12.24}_{-03.90}$	$0.40^{+0.36}_{-0.30}$	$0.43^{+0.02}_{-0.02}$	-	291/292	2.36
2MASXJ18560128+1538059	-	$1.72^{+0.03}_{-0.03}$	$12.32^{+03,12}_{-02.36}$	$0.48^{+0.41}_{-0.36}$	$0.36^{+0.01}_{-0.01}$	-	295/307	2.13

Continued

Table 3.2 – Following the previous page

Source	N_H^{INT} (10^{22} cm^{-2})	Γ	kT_e (keV)	R	$N_{xillverCP}$ (10^{-4})	$N_{relxillCP}$ (10^{-4})	χ^2/dof	Flux(10^{-11}) (erg $cm^{-2}s^{-1}$)
3C 109	-	$1.78^{+0.02}_{-0.02}$	$18.09^{+06.91}_{-02.72}$	$0.26^{+0.17}_{-0.16}$	$0.32^{+0.007}_{-0.007}$	-	591/627	1.34
RBS0770	-	$1.89^{+0.02}_{-0.02}$	$17.71^{+04.30}_{-02.38}$	$0.54^{+0.19}_{-0.17}$	$0.76^{+0.01}_{-0.01}$	-	791/715	3.90
MKN 6	$18.98^{+1.10}_{-1.17}$	$1.53^{+0.01}_{-0.01}$	$14.89^{+01.16}_{-01.12}$	$0.98^{+0.30}_{-0.16}$	$0.43^{+0.01}_{-0.02}$	-	777/842	3.73
3C 382	-	$1.77^{+0.01}_{-0.01}$	$33.07^{+16.81}_{-07.76}$	$0.06^{+0.05}_{-0.05}$	$1.72^{+0.01}_{-0.02}$	-	1279/1247	8.06
HE 0103-3447	-	$1.68^{+0.03}_{-0.03}$	$14.29^{+08.62}_{-03.18}$	<0.17	$0.41^{+0.01}_{-0.02}$	-	256/264	2.20
IGR J17476-2253	-	$1.69^{+0.03}_{-0.03}$	$13.81^{+12.77}_{-3.48}$	<0.37	$0.34^{+0.01}_{-0.01}$	-	303/290	1.87
MR2251−178	-	$1.76^{+0.01}_{-0.01}$	$22.16^{+07.73}_{-03.79}$	<0.02	$2.59^{+0.02}_{-0.02}$	-	835/859	12.31
Mrk 1148	-	$1.86^{+0.02}_{-0.02}$	$25.60^{+83.21}_{-08.24}$	<0.20	$1.04^{+0.02}_{-0.02}$	-	533/534	4.48
Mrk 926	-	$1.80^{+0.01}_{-0.01}$	$54.69^{+43.28}_{-17.50}$	<0.12	$3.40^{+0.02}_{-0.02}$	-	1580/1520	15.03
2MASXJ10523297+1036205	-	$1.54^{+0.03}_{-0.02}$	$10.51^{+02.54}_{-01.57}$	<0.63	$0.20^{+0.08}_{-0.08}$	-	351/319	1.30
SDSS J114921.52+532013.4	-	$1.76^{+0.07}_{-0.07}$	$06.50^{+01.25}_{-00.97}$	<4.72	$0.08^{+0.001}_{-0.001}$	-	88/75	0.49
2MASXJ23013626-5913210	-	$1.87^{+0.04}_{-0.04}$	$13.35^{+06.23}_{-03.48}$	$0.52^{+0.65}_{-0.42}$	$0.30^{+0.02}_{-0.02}$	-	176/179	1.32

TABLE 3.3: Results of the correlation analysis between different parameters. Provided are the slope (m), intercept (c), PCC (r), and the NHPNC (p) from the LLS fit.

	Full sample				Moderately accreting sources				Highly accreting sources			
Relation	m	c	r	p	m	c	r	p	m	c	r	p
$kT_e/\log(\lambda_{Edd})$	1.00±3.01	26.69±3.38	0.12	0.75	9.17±4.26	38.40±5.81	0.73	0.09	−18.96±0.51	22.04±0.12	−0.99	0.02
$R/\log(\lambda_{Edd})$	−0.51±0.14	0.15±0.16	−0.82	0.01	−0.93±0.15	−0.49±0.21	−0.95	0.00	−0.34±0.25	0.35±0.05	−0.81	0.40
kT_e/R	−2.60±1.62	29.68±1.29	−0.55	0.16	–	–	–	–	–	–	–	–
$\Gamma/\log(\lambda_{Edd})$	0.10±0.02	1.90±0.02	0.90	0.00	0.14±0.03	1.95±0.04	0.92	0.01	0.08±0.19	1.88±0.04	0.37	0.76
kT_e/Γ	29.27±9.18	−27.21±17.27	0.85	0.03	–	–	–	–	–	–	–	–
kT_e/τ	−7.59±1.82	56.07±8.02	−0.90	0.01	–	–	–	–	–	–	–	–
$kT_e/\log(\frac{M_{BH}}{M_{Sun}})$	1.68±1.57	14.30±11.13	0.60	0.40	–	–	–	–	–	–	–	–

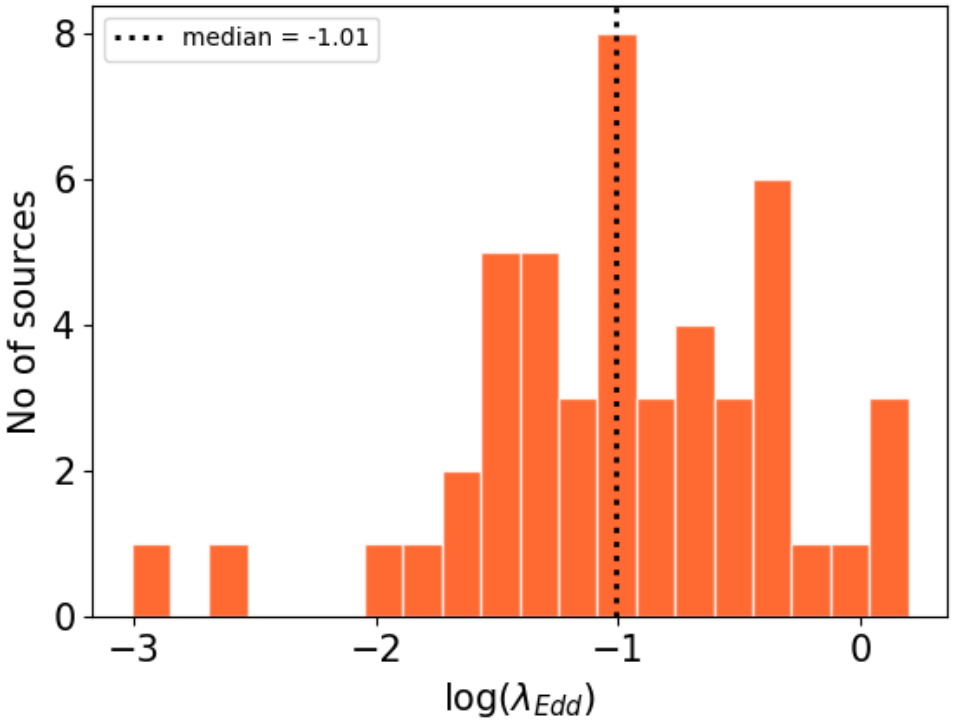

FIGURE 3.3: Eddington ratio distribution for the sources in which we could constrain kT_e with M_{BH} from literature.

3.1 Spectral Analysis

We analysed the spectral data from *NuSTAR* for the 130 sources in the energy range of 3–79 keV, a few of which also have soft X-ray observations. Since these are unobscured Seyfert 1 galaxies, we do not have to deal with the Γ-N_H degeneracy (Marchesi et al. 2018). Therefore, we chose to fit the *NuSTAR* data alone, and we do not expect our results to be significantly affected by the lack of information at energies < 3 keV.

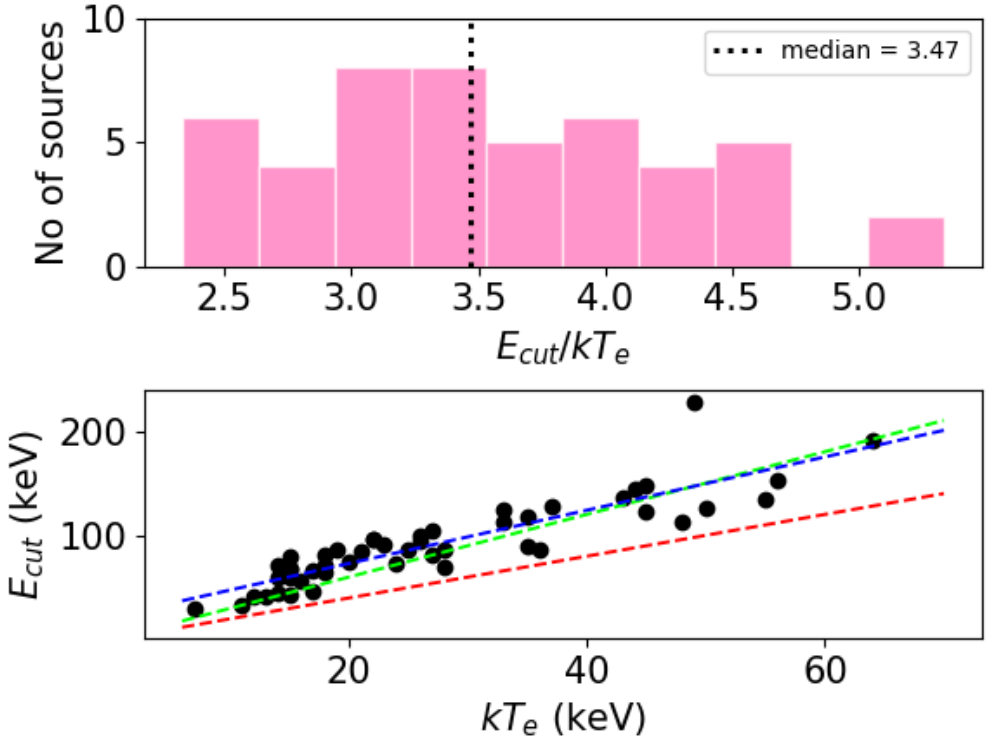

FIGURE 3.4: Distribution of the ratio between E_{cut} to kT_e for the 48 sources with kT_e measurements (top panel). The variation of E_{cut} against kT_e (bottom panel). Here, the red dashed line shows the $E_{cut} = 2kT_e$ relation, the green dashed line shows the $E_{cut} = 3kT_e$ relation and the blue dashed line is the LLS fit to the data.

We used the following two models

- **Model−1:** const × TBabs × zTBabs × (xillver/relxill/(relxill+xillver))
- **Model−2:** const × TBabs × zTBabs × (xillverCP/relxillCP/(relxillCP+xillverCP))

In both the models, *const* represents the offset between the *NuSTAR* focal plane modules. *TBabs* was used to model the Milky Way Galactic hydrogen column density, which was taken from Willingale et al. (2013) for each source. The quantity

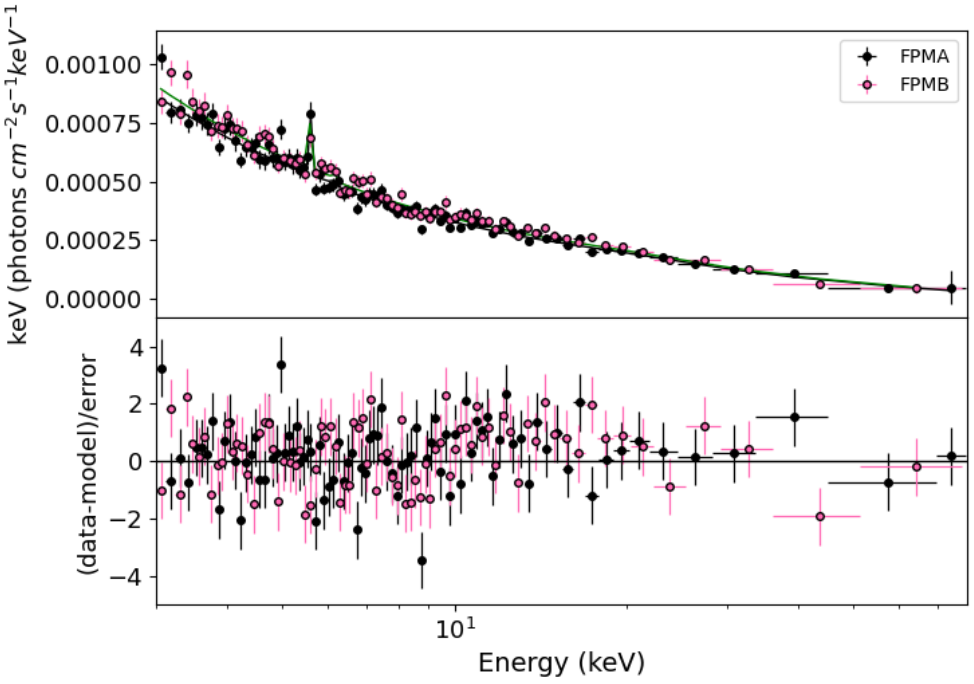

FIGURE 3.5: The best-fitted spectrum of PG0026+129

zTBabs represents the hydrogen column density (N_H^{INT}) of the host galaxy. During the modelling of the source spectrum, the value of N_H^{INT} was allowed to vary freely.

To model the spectrum with an absorbed cut-off power law along with the reflection features present in it we used *relxill/xillver* (García & Kallman 2010; García et al. 2011). In XSPEC Model−1 took the following forms,

- Model−1a: const × TBabs × zTBabs × (xillver)
- Model−1b: const × TBabs × zTBabs × (relxill)
- Model−1c: const × TBabs × zTBabs × (relxill+xillver)

During the fit using Model−1a, the parameters that were kept free were Γ, E_{cut}, R and the normalization ($N_{xillver}$) of the *xillver* component. The reflector was considered neutral; therefore, we fixed the ionization parameter ($log\xi$) to 0.0. The value AF_e was fixed to the solar value (=1.0). We also fixed the inclination angle (θ_i) to 30°.

In Model−1b, we replaced *xillver* with *relxill* to take care of the relativistic smeared Comptonization spectrum for a few sources. In addition to the parameters described in Model−1a, there are a few more additional parameters, such as the inner and outer emissivity indices ($\beta1$ and $\beta2$ respectively), inner radius (r_{in}) and outer radius (r_{out}) of the accretion disk, break radius (r_{br}) between r_{in} and r_{out} and the spin of the black-hole (a_*). During the fit, we tied $\beta1$ and $\beta2$ together and kept them as free parameters. The values of r_{br}, r_{in} and r_{out} were kept frozen to their default values of $15r_g$, $3r_g$ and $400r_g$ respectively. We considered a highly spinning SMBH and fixed a_* to 0.998. AF_e was frozen to the solar value. θ_i was fixed to 30°. The other parameters that were kept free during the fit were Γ, E_{cut}, R, $log\xi$ and the normalization ($N_{relxill}$) of the *relxill* model.

The spectra of a few sources could not be well-fitted using *xillver* or *relxill*. In those cases, we used Model−1c, in which we fitted *relxill* and *xillver* together. Between these two components Γ, kT_e and AF_e were tied together and kept as free parameters during the fitting. The other parameters were treated similarly as described earlier in Model−1a and Model−1b. From the model fits, we could constrain E_{cut} for 75 sources. The summary of the spectral analysis from this model fits to the spectra is given in Table 3.1. The distribution of Γ and E_{cut} (constraints and the lower limits) are given in Fig. 3.1.

As the goal of this particular work is to find kT_e, we carried out physical model fits (Model−2) to these 75 sources for which E_{cut} could be constrained. Using

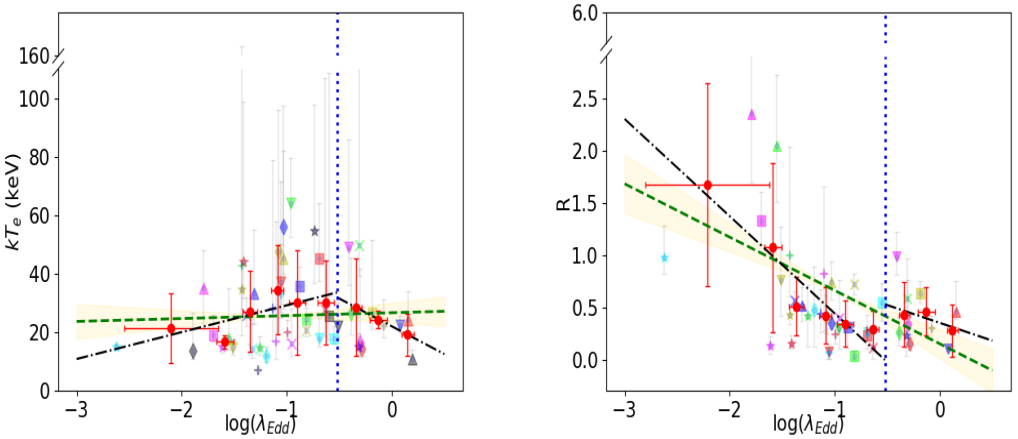

FIGURE 3.6: The relation between kT_e (left panel) and R (right panel) with the Eddington ratio. Sources are marked in different colours and markers as in Table 3.4. The green dashed line represents the ordinary LLS fit for the binned data (red dotted points), and the yellow shaded region is the error in the fit values. The black dashed-dotted lines depict the ordinary LLS fit for the binned data (red dotted points) in two different source distributions separated by the blue dashed vertical lines.

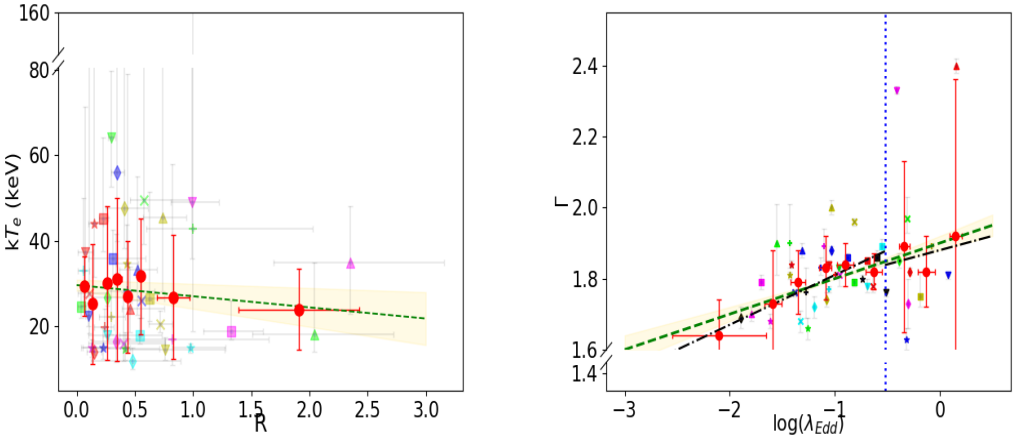

FIGURE 3.7: Left panel: The relation between kT_e and R. Right panel: The relation between Γ and Eddington ratio. The points, lines and shaded regions have the same meaning as given in the caption of Fig. 3.6.

this, we could constrain kT_e for 48 sources. Out of the 48 sources, we used *xillverCP* (García et al. 2014) for 36 sources to estimate different coronal parameters. *xillverCP* is a thermal Comptonization model that also handles the reflection spectrum. A broad emission line was confirmed to be present in 6 out of the 48 Seyferts, and to take care of this, we used *relxillCP* (García et al. 2014; Dauser et al. 2014) model to fit those source spectra. *relxillCP* takes into account the line broadening due to relativistic effects of the reflection spectra. In the other 6 sources, we fitted both *xillverCP* and *relxillCP*, since one model alone could not fit the reflection spectra properly. Both *xillverCP*/*relxillCP* are part of the *xillver*/*relxill* (García & Kallman 2010; García et al. 2011) family and an advanced version of the disk reflection model that takes care of the physical Comptonization continuum. Thus, in XSPEC Model−2 took the following forms,

- Model−2a: const × TBabs × zTBabs × (xillverCP)
- Model−2b: const × TBabs × zTBabs × (relxillCP)
- Model−2c: const × TBabs × zTBabs × (relxillCP+xillverCP)

All the model parameters were handled in a similar fashion as described for Model−1. The best-fitted values of several parameters of the X-ray corona found from fitting the Model−2 to the source spectra are given in Table 3.2. The distribution of Γ and kT_e, as obtained from Model−2, are shown in Fig. 3.2. The distribution of the Eddington ratio (λ_{Edd}) for 47 sources (1 source is excluded since we could not find the black hole mass in literature) is given in Fig. 3.3. In Fig. 3.4 is shown the distribution of E_{cut}/kT_e and the location of the sources in the E_{cut} versus kT_e plane. We show in Fig. 3.5 an example *NuSTAR* spectrum for the source PG0026+129 in our sample for which we measured a kT_e of $22.18^{+8.88}_{-4.03}$ keV.

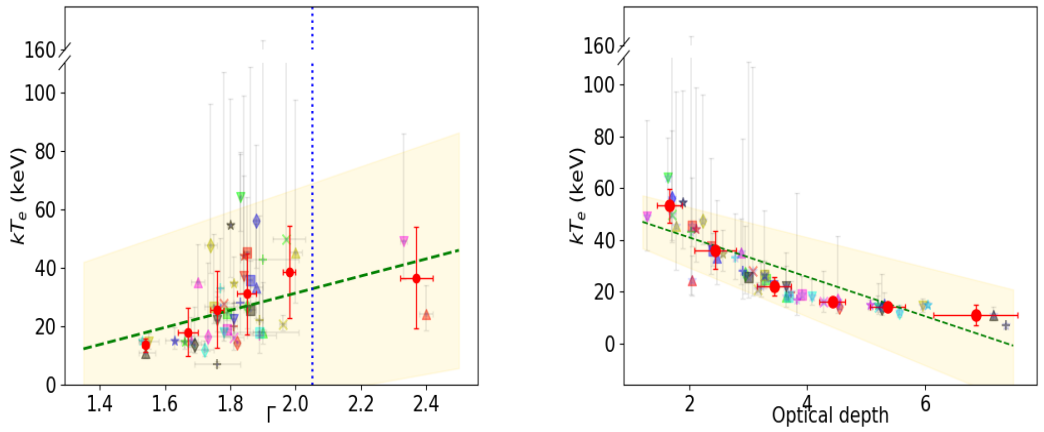

FIGURE 3.8: Left panel: The relation between kT_e and Γ. Right panel: The relation between kT_e and τ. The points, lines and shaded regions have the same meanings as given in the caption of Fig. 3.6.

3.2 Results

Here, we present our findings on the 48 sources for which we obtained kT_e measurements. For completeness, we compared our findings on the E_{cut} measurements for these sources are given in Table A.1 in Appendix A.1. The description of the sources and the previous results on the kT_e analysis found for them in the literature is given in Appendix A.2. We looked for correlations between different physical parameters from the Comptonization model fit. Since we did not find the black hole mass (M_{BH}) for the source 2MASXJ23013626-5913210, we excluded this one from our correlation analysis. Additionally, we showed where these 47 sources are situated on the $l - \theta$ diagram for AGN corona. A summary of all the correlation analyses carried out in this section is given in Table 3.3.

3.2.1 Relation between E_{cut} and kT_e

It is believed that the presence of high energy rollover in the AGN X-ray spectra is related to kT_e as $E_{cut} = 2-3\ kT_e$ (Petrucci et al. 2001). However, recent studies do indicate that this simple relation between E_{cut} and kT_e may not be valid for all sources (Liu et al. 2014; Middei et al. 2019; Pal et al. 2022). We show in the top panel of Fig. 3.4 the distribution of the ratio between E_{cut} to kT_e. We found the ratio to vary between 2.33 and 5.33. In the bottom panel of Fig. 3.4 is shown the distribution of our sources in the E_{cut} versus kT_e plane. Also, as shown in the same figure are the $E_{cut} = 2kT_e$ (red dashed) and $E_{cut} = 3kT_e$ (green dashed) lines. From LLS fit to our sample of sources (blue dashed line in Fig. 3.4), we found

$$E_{cut} = (2.55 \pm 0.20)kT_e + (22.02 \pm 5.99). \tag{3.1}$$

These observations thus indicate that in the sample of sources studied in this work, the generally accepted relation of $E_{cut} = 2-3\ kT_e$ holds good, given the large error bars in E_{cut} and kT_e measurements. Most of our sources lie in the $E_{cut} = 3kT_e$ line.

3.2.2 Correlation between kT_e and λ_{Edd}

We investigated for any relation between kT_e and λ_{Edd}. For getting L_{bol}, we used the intrinsic luminosity calculated in the 2−10 keV band. The observed luminosities were converted to bolometric luminosities using the relation $\log(L_{Bol}) = 20 \times \log(L_{2-10keV})$ (Vasudevan & Fabian 2007). M_{BH} values for the sources were taken from Mejía-Restrepo et al. (2022) except for ARK 564 and IGRJ17476−2253. M_{BH} for these two sources were respectively collected from Denney et al. (2009) and Masetti et al. (2013). From the LLS regression line fit to the binned data

points (see Fig. 3.6), we obtained the best-fitted relation as

$$kT_e = (1.00 \pm 3.01) log(\lambda_{Edd}) + (26.69 \pm 3.38) \tag{3.2}$$

For measuring the strength of the linear correlation, we calculated r and p, and we obtained a r of 0.12 and p of 0.75. We thus noticed that the correlation between $\mathrm{kT_e}$ and λ_{Edd} is insignificant.

The accretion disk of AGN possibly depends on λ_{Edd} (Liu et al. 2021). For AGN with λ_{Edd} between 0.01 and 0.3, the observed spectral energy distribution can be explained by the standard accretion disk (optically thick and geometrically thin). For AGN with higher λ_{Edd}, the accretion disk becomes geometrically thick (Tortosa et al. 2022a). The emergent X-ray spectrum from AGN with thick and thin accretion disks is likely to be different, and hence the accretion disk and corona connection in low and high accreting AGN could be different. To look for any differences in the corona between low and high accreting AGN, we divided our sample into moderately accreting AGN ($\lambda_{Edd} < 0.3$) and highly accreting AGN ($\lambda_{Edd} > 0.3$) and performed LLS fit in the $\mathrm{kT_e}$ v/s λ_{Edd} plane. For the moderately accreting AGN, we found

$$kT_e = (9.17 \pm 4.26) log(\lambda_{Edd}) + (38.40 \pm 5.81) \tag{3.3}$$

with $r = 0.73$ and $p = 0.09$. For the highly accreting sub-sample, we found the best-fitted relation as

$$kT_e = (-18.96 \pm 0.51) log(\lambda_{Edd}) + (22.04 \pm 0.12) \tag{3.4}$$

with a r of -0.99 and a value of $p = 0.02$. Pearson's rank correlation test thus indicates that for moderately accreting systems, the correlation between $\mathrm{kT_e}$ and λ_{Edd} is significant at the 90% level. We also obtained a significant anti-correlation

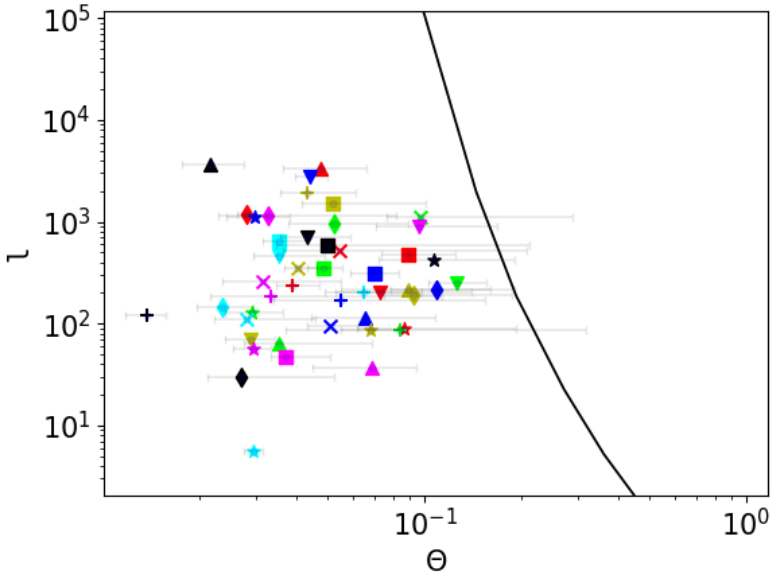

FIGURE 3.9: Location of the sources in the $l - \theta$ diagram.

between these two parameters at the 98% confidence level for the high-accretion system.

Therefore, the different trends noticed between the two accreting systems could point to the difference in the accretion disk−corona connection between these two populations of sources. To validate or deny the trend found in this work, accurate measurements of kT_e on an adequate amount of AGN are required. For the whole sample analysed in this work, we found that there is no correlation between kT_e and λ_{Edd}. This concurs with recent findings in the literature (Tortosa et al. 2018; Molina et al. 2019; Kamraj et al. 2022).

3.2.3 Correlation between R and λ_{Edd}

We show in Fig. 3.6, the correlation between R and λ_{Edd}. We performed a LLS fit for the data and got the relation as

$$R = (-0.51 \pm 0.14) log(\lambda_{Edd}) + (0.15 \pm 0.16) \tag{3.5}$$

with r of -0.82 and a p value of 0.01. For the sources with moderate λ_{Edd}, we found the best-fitted relation as

$$R = (-0.93 \pm 0.15) log(\lambda_{Edd}) + (-0.49 \pm 0.21) \tag{3.6}$$

with a r of -0.95 and a p-value of 0.00. The best-fitted relation for the high Eddington sample is

$$R = (-0.34 \pm 0.25) log(\lambda_{Edd}) + (0.35 \pm 0.05) \tag{3.7}$$

Pearson's correlation test yielded a $r = -0.81$ and a p value of 0.40. Considering our sample of objects and dividing them into two different accreting systems, we found significant anti-correlation for the full and the moderately accreting samples but no significant correlation between R and λ_{Edd} for the relatively higher accreting sources.

3.2.4 Relation between $\mathrm{kT_e}$ and R

We show the relation between $\mathrm{kT_e}$ against R in Fig. 3.7. From LLS fit, we obtained the following best-fitted relation

$$\mathrm{kT_e} = (-2.60 \pm 1.62)\mathrm{R} + (29.68 \pm 1.29) \tag{3.8}$$

We obtained $r = -0.55$ and $p = 0.16$. A mild negative relation is found between kT_e and R at greater than 84% confidence level. Previously, Hinkle & Mushotzky (2021) also established an anti correlation between kT_e and R.

3.2.5 Relation between Γ and λ_{Edd}

We examined the relation between Γ and λ_{Edd} in Fig. 3.7. Considering the whole sample, we noticed a strong positive trend. Pearson's rank test resulted in a significant correlation with $r = 0.90$ and $p = 0.00$. The best-fitted relation is given as

$$\Gamma = (0.10 \pm 0.02) log(\lambda_{Edd}) + (1.90 \pm 0.02) \tag{3.9}$$

For the moderate Eddington sources, we obtained the best-fitted relation as

$$\Gamma = (0.14 \pm 0.03) log(\lambda_{Edd}) + (1.95 \pm 0.04) \tag{3.10}$$

with $r = 0.92$ and $p = 0.01$ For the high Eddington ratio sample, the best-fitted relation is

$$\Gamma = (0.08 \pm 0.19) log(\lambda_{Edd}) + (1.88 \pm 0.04) \tag{3.11}$$

with $r = 0.37$ and a p of 0.76. We discovered a significant positive correlation between Γ and λ_{Edd} for both the entire sample and for the sources with moderate accretion. Prior literature also indicated a positive correlation between these two parameters (Shemmer et al. 2006, 2008; Risaliti et al. 2009; Trakhtenbrot et al. 2017; Ricci et al. 2018).

TABLE 3.4: Description of sources:

Source	Colour	Marker
1H 0419-577	red	diamond
3C 111	red	triangle−down
3C 120	red	square
3C 390.3	red	star
ARK 564	red	triangle−up
GRS 1734-292	red	plus
HE 1136-2304	red	X
HE 1143-1810	green	diamond
IC 4329A	green	triangle−down
IGR J21247+5058	green	square
IRAS 04124-0803	green	star
IRAS 09149-6206	green	triangle−up
IRAS 05589+2828	green	plus
MCG-06-30-15	green	X
MCG+08-11-011	blue	diamond
Mrk 110	blue	triangle−down
Mrk 509	blue	square
Mrk 520	blue	star
Mrk 841	blue	triangle−up
Mrk 915	blue	plus
NGC 3227	blue	X
NGC 3783	yellow	diamond
NGC 5273	yellow	triangle−down
NGC 5506	yellow	square
NGC 5548	yellow	star
NGC 7469	yellow	triangle−up
PG0026+129	yellow	plus

Continued

Table 3.4 – Following the previous page

Source	Colour	Marker
SWIFTJ2127.4+5654	yellow	X
UGC 06728	magenta	diamond
IGRJ19378-0617	magenta	triangle−down
Fairall 51	magenta	square
MRK 279	magenta	star
ESO 323−G077	magenta	triangle−up
CGCG229−015	magenta	plus
2MASXJ21355399+4728217	magenta	X
2MASXJ18560128+1538059	cyan	diamond
3C 109	cyan	triangle−down
RBS0770	cyan	square
MKN 6	cyan	star
3C 382	cyan	plus
HE 0103-3447	cyan	X
IGR J17476-2253	black	diamond
MR2251−178	black	triangle−down
Mrk 1148	black	square
Mrk 926	black	star
2MASXJ10523297+1036205	black	triangle−up
SDSS J114921.52+532013.4	black	plus

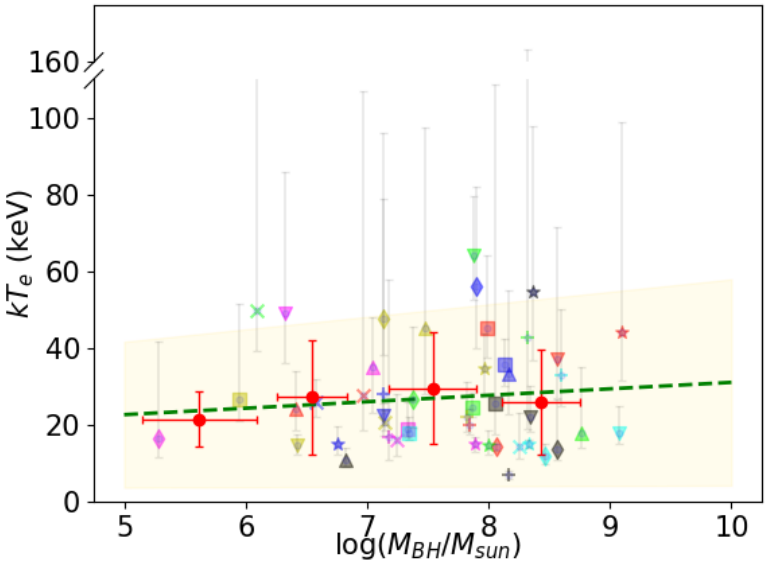

FIGURE 3.10: The relation between kT_e and the logarithm of the black hole mass in the unit of the solar mass. The points, lines and shaded regions have the same meaning as given in the caption of Fig. 3.6.

3.2.6 Correlation between kT_e and Γ

Fig. 3.8 shows the relation between kT_e and Γ. From LLS fit for the data points, we obtained the best-fitted relation as

$$kT_e = (29.27 \pm 9.18)\Gamma + (-27.21 \pm 17.27) \tag{3.12}$$

We obtained $r = 0.85$ and $p = 0.03$. Thus a significant positive relation between these two parameters was found in the analysis. Such studies of the correlation between kT_e and Γ are available in the literature too. From a study of 19 Seyfert galaxies using *NuSTAR* data, Tortosa et al. (2018) found no relation between kT_e and Γ. Molina et al. (2019) reported a positive relation between E_{cut} and Γ based on spectral analysis of 18 Seyfert galaxies using data from *Swift-XRT* and *NuSTAR*. Few recent studies reported positive correlation between E_{cut} and Γ (Kamraj et al. 2018; Hinkle & Mushotzky 2021; Kang & Wang 2022). Of these, Kamraj et al. (2018) analysed a total of 46 Seyfert 1 galaxies, while Hinkle &

Mushotzky (2021) and Kang & Wang (2022) carried out spectral analysis of 33 and 60 sources, respectively. From an analysis of multiple epochs of observations on a source SWIFT J2127.4+5654, Kang et al. (2021a) found a Λ shaped pattern. According to the authors, up to $\Gamma < 2.05$, the source exhibited a steeper when hotter behaviour, while beyond $\Gamma > 2.05$, a harder when cooler behaviour was reported. Though of Kang et al. (2021a) finding is from multiple observations of a single source, we attempted to check the prevalence of such a trend in our sample of sources. Since there are only two sources in our sample with $\Gamma > 2.05$, no statistical test could be performed to check for the said trend. To support this conclusion, a thorough and uniform investigation of quite a few sources is required.

3.2.7 Correlation between $\mathrm{kT_e}$ and τ

We calculated τ using the following equation (Zdziarski et al. 1996)

$$\tau = \sqrt{\frac{9}{4} + \frac{3}{\theta\left[\left(\Gamma + \frac{1}{2}\right)^2 - \frac{9}{4}\right]}} - \frac{3}{2} \tag{3.13}$$

where $\theta = kT_e/m_e c^2$. We found a strong negative correlation between $\mathrm{kT_e}$ and τ (see right panel of Fig. 3.8). From LLS fit to the data we obtained

$$\mathrm{kT_e} = (\text{-}7.59 \pm 1.82)\ \tau + (56.07 \pm 8.02)$$

Pearson's rank correlation analysis yielded $r = -0.90$ and $p = 0.01$. Earlier, Tortosa et al. (2018) also noticed a significant negative correlation between these parameters for slab and spherical geometries.

3.2.8 Position of the sources in l - θ plane

The position of the sources in the compactness temperature diagram is a very important diagnostic tool to understand the physical processes (bremsstrahlung, inverse Compton and pair production) happening in the AGN corona. Fig. 3.9 shows the position of the sources in the $l - \theta$ diagram. We define the compactness l of the AGN corona (Guilbert et al. 1983) as,

$$l = 4\pi \frac{m_p}{m_e} \frac{R_G}{R} \frac{L}{L_E} \tag{3.14}$$

where,

1. m_p = the mass of the protons,
2. m_e = the mass of the electrons,
3. R_G = the gravitational radius,
4. R = the radius of the corona = $10R_G$ (Fabian et al. 2015),
5. L = the luminosity of the sources, and
6. L_{Edd} is the Eddington luminosity of the sources.

Electron temperature (θ) is defined as,

$$\theta = \frac{kT_e}{m_e c^2} \tag{3.15}$$

The theoretical pair line (slab geometry) following Stern et al. (1995) is depicted as a solid black line in Fig. 3.9. All sources are located near the theoretical pair production line. These findings are similar to that found in the literature earlier (Fabian et al. 2015; Ricci et al. 2018; Kamraj et al. 2022). This indicates that the primary X-ray continuum emission of the sources examined in this work appears

to originate in a thermal plasma in corona incapable of pair production. We note that in our analysis, the corona is considered to be homogeneous with a single temperature, while it might not be the case in reality.

3.3 Discussion

We examined the correlation between various coronal properties as well as between the coronal parameters and λ_{Edd} and M_{BH} of the sources. We also examined whether moderately accreting sources have different X-ray emission characteristics relative to the highly accreting sources.

From Table 3.3, we noticed a "hotter-when-softer" (see left panel of Fig. 3.8) and "softer-when-brighter" (see Fig. 3.7) trend for our sample of sources. The second correlation observed in this work is a strong negative relation between R and λ_{Edd} (see right panel of Fig. 3.6). From the analysis of the entire sample, another strong anti-correlation was found between kT_e and τ of the corona (see right panel of Fig. 3.8). Such negative relation between kT_e and τ is already known in literature and is attributed to either the variation in the configuration of the disk-corona or to variation in the intrinsic disk emission (Kang et al. 2021a; Tortosa et al. 2022b). It is possible to constrain the exact cause of this anti-correlation when the coronal geometry (size, shape and location) can be determined. Since the physical mechanism involved in all these correlations are still debatable, it is hard to paint a global picture by examining all these correlations found for the entire sample of sources analyzed in this work. The significant relations observed between different sets of physical parameters here point to the fact that an optically thin corona is needed to sustain a hot corona in its brighter state. Thus a steeper spectrum is expected in this scenario. Sources with flaring corona could move vertically away from the central engine and become optically thin. Thus, the fraction of the

primary emission that falls on the accretion disk reduces, which in turn reduces R.

There is another strong anti-correlation found from examining the LLS results (see Table 3.3) as obtained from the correlation analysis between kT_e and λ_{Edd} for the sources which are accreting with higher Eddington rates. These sources showed a "cooler-when-brighter" behaviour (see Fig. 3.6). On the other hand, the moderate accreting sources showed a "hotter-when-brighter" and "softer-when-brighter" behaviour (see Fig. 3.6 and Fig. 3.7) with R reducing significantly with the increased brightness state of the system (see right panel of Fig. 3.6). We could explain the scenario by considering that as the luminosity of the sources reached a certain level, the corona started interacting more rapidly with the seed photons. This rapid interaction could, in turn, cools the corona down rapidly.

We also plotted kT_e against M_{BH} to check for correlation, if any. Fig. 3.10 shows no correlation between these two parameters. From LLS fit we obtained

$$kT_e = (1.68 \pm 1.57)\log(M_{BH}/M_{\odot}) + (14.30 \pm 11.13) \tag{3.16}$$

with $r = 0.60$ and a p of 0.40. Trakhtenbrot et al. (2017) argued that as M_{BH} decreases, the number of seed photons increases and due to the production of a larger amount of seed photons, the corona interacts with it rapidly, and that in turns cools the corona down. Therefore, based on this argument, one should expect a positive relation between kT_e and M_{BH}. Here, too, there is a hint of a positive relation between kT_e and M_{BH}. However, it is insignificant.

Recently from the X-ray spectral analysis of the source, SWIFT J2127.4+5654, based on 8 epochs of observations Kang et al. (2021a) observed a Λ shaped pattern in the E_{cut} v/s Γ plane. Below $\Gamma < 2.05$, the source showed a "hotter-when-softer" trend, and above $\Gamma > 2.05$, the source showed a "cooler-when-softer" trend.

For our complete sample of sources, we found a "hotter-when-softer" trend and the correlation is significant (see Table 3.3). There are only two sources with $\Gamma > 2.05$, and therefore, no statistically significant consideration could be made. Observations of more sources with $\Gamma > 2.05$ are needed to confirm the trend found by Kang et al. (2021a).

The "hotter-when-softer" trend can be expected in sources that are pair dominated, while a "cooler-when-softer" trend can be shown by sources that are not pair dominated (Kang et al. 2021a). In the l$-\theta$ diagram, all our sample sources lie well below the pair production limit and are thus not pair-dominated.

3.4 Summary

In this study, we analysed the 3$-$79 *NuSTAR* spectra of a sample of 130 Seyfert 1 galaxies, the data for which were publicly available between August 2013 and May 2022 in *NuSTAR* Master Catalog. The goal is to conduct a thorough investigation of the coronal characteristics of Seyfert 1-type AGN. From the physical model fits to the spectrum of 130 source spectra, we could constrain E_{cut} in 75 sources. For these 75 sources, we carried out the physically motivated Comptonization model to fits the spectra to derive various coronal properties as well as investigate the correlation between various parameters of the sources. We could constrain kT_e in 48 sources. Our findings of this study are summarized below:

1. For our sample we noticed E_{cut} is related to kT_e as $E_{cut} = (2.26 \pm 0.18)$ $kT_e + (27.91 \pm 5.45)$. This is in agreement with the notion that the X-ray spectra of AGN are related to the temperature of the corona as $E_{cut} = 2-3kT_e$. For our sample of sources, observations tend to more closely follow the relation: $E_{cut} \sim 3kT_e$.

2. For our entire sample, we found a strong "softer-when-brighter" and "hotter-when-softer" behaviour with a significance greater than 97%.

3. A strong negative correlation was found between R and λ_{Edd} for our complete sample. Dividing the sources into two sub-samples, we found a significant correlation between these parameters in the moderately accreting sources.

4. We found that while the moderately accreting sources showed a "hotter-when-brighter" trend with a significance greater than 90%, the highly accreting sources showed a strong anti-correlation between $\mathrm{kT_e}$ and λ_{Edd}.

5. For the moderately accreting sample, we found a significant correlation between Γ and λ_{Edd} with r=0.92 and p=0.01. Therefore, we conclude that the sources with moderate accretion follow a "softer-when-brighter" behaviour.

6. We found a negative correlation between $\mathrm{kT_e}$ and τ. The best-fitted relation yielded a slope of -7.59 ± 1.82, a linear correlation coefficient of $r = -0.90$ and a p value of 0.01.

7. We obtained a weak negative correlation between $\mathrm{kT_e}$ and R. Pearson's correlation test produced $r = -0.55$ and $p = 0.16$.

8. All these correlations together indicate that an optically thin corona is necessary to sustain a hotter corona with a steeper spectrum. The flaring hot corona could move away vertically from the central part, so the fraction of the reflected emission to the primary emission (R) reduces. After reaching a certain luminosity, the corona could interact with the seed photons rapidly, and that, in turn, cools the corona down.

9. In the $l - \theta$ plane, our source lies below the theoretical pair production line. This indicates that the X-ray emission from corona in our sample seems to generated in a thermal plasma. This is also in agreement with the results that are available in the literature from the other sample of sources (Fabian et al. 2015; Kamraj et al. 2018; Ricci et al. 2018; Kamraj et al. 2022)

A systematic analysis of a large number of sources is definitely needed for firmly establishing the correlation observed between various physical quantities in this study, thereby enhancing our understanding of AGN corona.

Chapter 4

Search for coronal temperature variation in Seyfert galaxies [†]

Our knowledge of the variation in the temperature of the corona in AGN is very limited. For example, in eight sources, namely MCG-5-23-16 (Zoghbi et al. 2017), NGC 4593 (Ursini et al. 2016), NGC 5548 (Ursini et al. 2015), 3C 382 (Ballantyne et al. 2014), Mrk 335 (Keek & Ballantyne 2016), 4C +74.26 (Zhang et al. 2018), SWIFT J2127.4+5654 (Kang et al. 2021b) and NGC 3227 (Kang et al. 2021b) variations in the E_{cut} values are available in the literature. The values of E_{cut} were measured by fitting phenomenological model to the observed X-ray AGN spectra. However, a phenomenological cut-off power law fitting of the data does not permit a singular interpretation due to the numerous complicated explanations for the variance in kT_e (Ursini et al. 2015). Also, from a recent study, Middei et al. (2019) have shown that the typically adopted relation of $E_{cut} = 2{-}3\ kT_e$ (Petrucci et al. 2000) is not valid for all values of τ and kT_e, instead valid for only low values of τ and kT_e. In the case of a non-static corona, such as the one with outflows,

[†]The contents of this chapter are from (a) Pal et al. 2022, A&A, 662A, 78 and (b) Pal & Stalin, 2023, MNRAS, 518, 2529

this conventional relation between E_{cut} and kT_e can be complicated (Liu et al. 2014). Recently, from the physical model fits to the multi-epoch data, Barua et al. (2020) confirmed the change in kT_e in another Seyfert galaxy, namely, Ark 564. Kang et al. (2021b) also reported the variation of kT_e in NGC 3227 and SWIFT J2127.4+5654. Though in ESO 103-035, Barua et al. (2021) found kT_e to increase with the brightness of the source, in Ark 564, Barua et al. (2020) found kT_e to decrease with source brightness. Thus, the limited results in the literature indicate that the variation of kT_e with source brightness may differ among sources. To confirm or refute these findings from limited sources, a systematic and homogenous examination of the variation of kT_e and its association with a variety of physical attributes on a significant number of sources is needed. We looked into the kT_e variation in 21 AGN. The choice of sources is driven by the availability of multiple epochs of data from *NuSTAR*.

4.1 Analysis of spectra

We used XSPEC to fit the *NuSTAR* data in the 3−79 keV band for each source in our sample. We adopted both phenomenological and physical models to fit the source spectra. For the spectral analysis, we used the following four models.

1. const × TBabs × zTBabs × (zpo+zgauss)
2. const × TBabs × zTBabs × (pexrav+zgauss)
3. const × TBabs × zTBabs × (xillver/relxill/relxill+xillver)
4. const × TBabs × zTBabs × (xillverCP/relxillCP/relxillCP+xillverCP)

In all our models that were fit to the observations, *const* (c) represents the cross-calibration between the two focal plane modules (FPMA and FPMB). *TBabs*

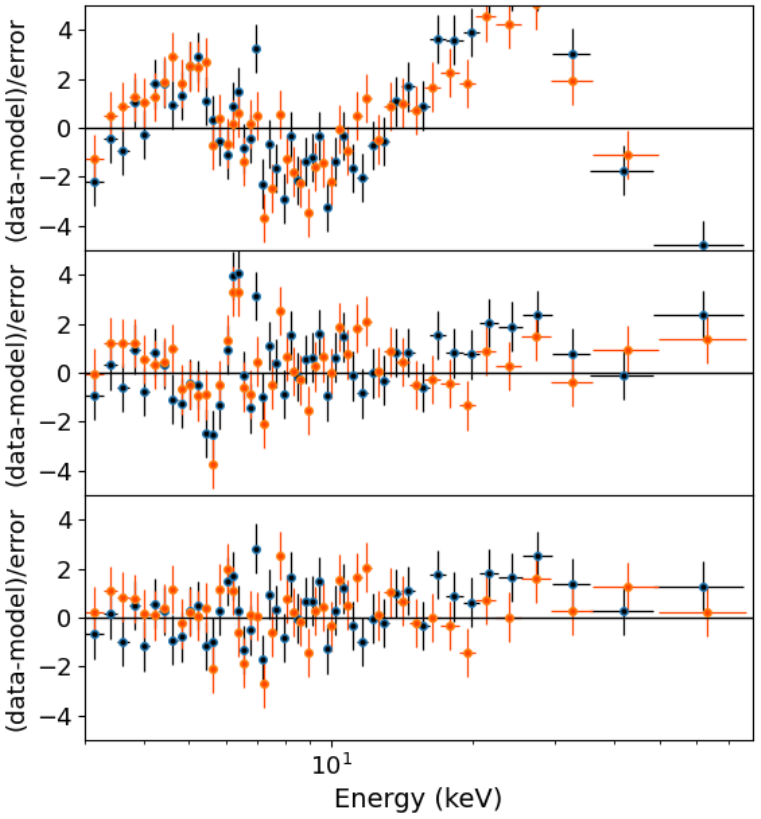

FIGURE 4.1: Upper panel: Ratio of data to the model for the model fits *const* × *TBabs* × *ztbabs* × *(zpo+zgauss)*, Middle panel: *const* × *TBabs* × *ztbabs* × *(relxill)* and Bottom panel: *const* × *TBabs* × *ztbabs* × *(relxill+xillver)* to the FPMA (black dot) and FPMB (orange dot) spectra of ObsID 60501015002 (epoch B) of NGC 5506. The spectra are re-binned for visualization purposes.

accounts for the Milky Way hydrogen column density (N_H^{gal}). The value of N_H^{gal} for each source was obtained from Willingale et al. (2013) and given in Table 2.2. The host galaxy absorption (N_H^{INT}) was taken care of by the *zTBabs* model component in which N_H^{INT} was kept free during the fit of each model.

The conclusion of this study is drawn based on the best-fitted model parameters obtained using the physically motivated Comptonization model const × TBabs × zTBabs × (xillverCP/relxillCP/relxillCP+xillverCP).

4.1.1 Phenomenological model fitting

Our first approach is a simple absorbed power-law model (*zpo*) fit to the data that has the following form in XSPEC,

$$const \times TBabs \times zTBabs \times (zpo + zgauss) \tag{4.1}$$

The parameters that were treated free in the *zpo* model are the Γ and the model normalization (N_{pow}). The data indicated the presence of Fe Kα line emission for the majority of the sources, which was modelled using the *zgauss* component. For most of the observations, the line energy (E), the width (σ) and the normalization (N_{line}) were kept free during the fit. However, in a few cases, we noticed the necessity to freeze either E or σ or both in order to avoid σ getting pegged at very low values during the error calculation. We note that freezing the Fe Kα line parameters significantly affected neither the fit statistics nor the derived physical parameters. Thus in a few cases, we froze E and σ to 6.4 keV and 0.1 keV, respectively. All the model parameters, along with the fit statistic (χ^2/dof), are given in Table 4.1.

Our second approach consisted of fitting the spectra with the widely used exponential cut-off power law along with a neutral reflection part, namely *pexrav* (Magdziarz & Zdziarski 1995). Here too, we used *zgauss* to model the emission line present in the spectra of the sources. In XSPEC, the model takes the form

$$const \times TBabs \times zTBabs \times (pexrav + zgauss) \tag{4.2}$$

This simple model fit could provide us with constraints on important parameters such as Γ, E_{cut} and R. These parameters, along with the model normalization (N_{pexrav}), were treated as free during the fitting. In this model, the accretion disk is considered as a neutral one and for the neutral material, we used solar

abundance. We fixed the inclination to the default of $\cos(\theta_{incl}) = 0.45$. Also, the energy (E) of the emission line within *zgauss* was frozen to the best-fitted numbers obtained from the (*zpo+zgauss*) model and σ was treated as a free parameter in most of the cases. For a few sources, we had to freeze $\sigma = 0.1$ keV to better constrain other parameters, except for Mrk 915 (see Table 4.2), which showed a very narrow emission line. For Mrk 915, fixing σ to 0.001 keV produced an acceptable fit with no significant residue around the line emission region. All the best-fitted model parameters with χ^2/dof are in Table 4.2.

4.1.2 Physical model fitting

To estimate the high energy cut-off, E_{cut} we adopted the physical models *xillver* (García & Kallman 2010; García et al. 2011) and/or *relxill* (García et al. 2014; Dauser et al. 2014). The spectra of 15 sources were fitted using *xillver*, 4 sources were modelled using *relxill* and in 2 sources, both *xillver* and *relxill* were used. These models have the following form in XSPEC,

1. const × TBabs × zTBabs × xillver
2. const × TBabs × zTBabs × relxill
3. const × TBabs × zTBabs × (relxill+xillver)

The best-fitted model parameters are given in Table 4.3.

To estimate kT_e, we did the spectral fitting using *xillverCP* (García et al. 2014) and/or *relxillCP* (García et al. 2014) to take care of the distant and blurred reflection features respectively in the data. These two models are part of the *relxill* and an advanced version of the disk reflection model. The model *xillverCP* (García &

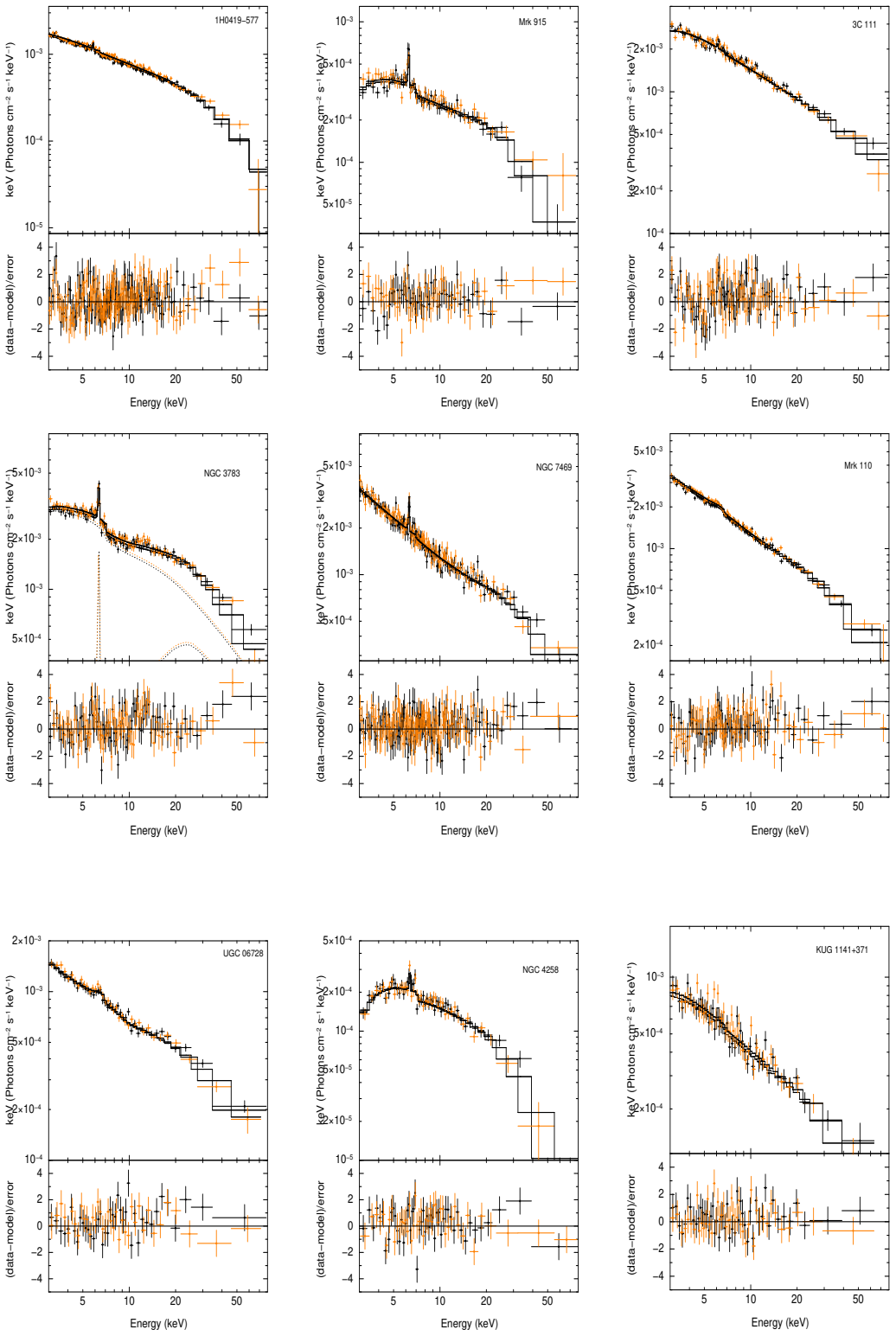

FIGURE 4.2: Upper panel: The spectra and the best-fitted models (*const* × *TBabs* × *ztbabs(xillverCP/relxillCP/relxillCP+xillverCP)*)) along with the residuals (lower panel) of the spectral fitting plots to the sample. Here black points are for FPMA and orange points are for FPMB. The names of the sources are given in the respective panels.

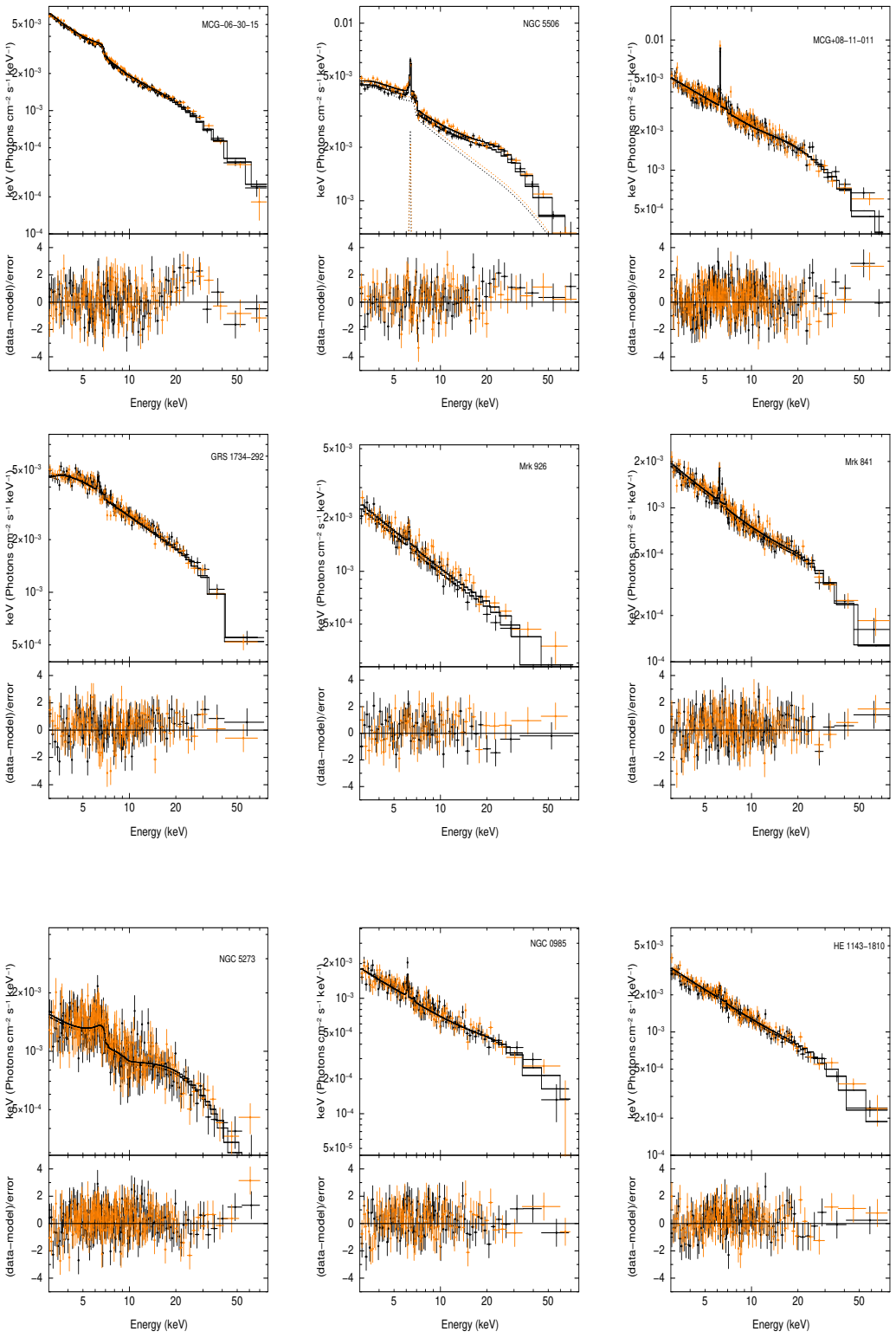

FIGURE 4.3: Upper panel: The spectra and the best-fitted models (*const* × *TBabs* × *ztbabs(xillverCP/relxillCP/relxillCP+xillverCP)*)) along with the residuals (lower panel) of the spectral fitting plots to the sample. Here black points are for FPMA and orange points are for FPMB. The names of the sources are given in the respective panels.

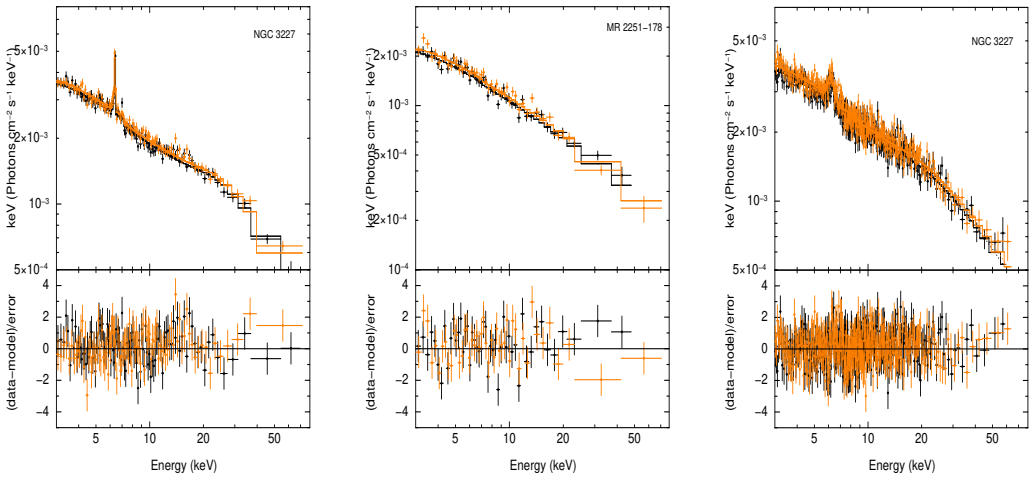

FIGURE 4.4: Upper panel: The spectra and the best-fitted models (*const* × *TBabs* × *ztbabs(xillverCP/relxillCP/relxillCP+xillverCP)*) along with the residuals (lower panel) of the spectral fitting plots to the sample. Here black points are for FPMA and orange points are for FPMB. The names of the sources are given in the respective panels.

Kallman 2010) is an ionized reflector model that takes into account the neutral Fe Kα line at $\sim$ 6.4 keV and Fe Kβ line at $\sim$ 7.07 keV along with the cold reflection component. Of the 21 sources, for 15 sources, *xillverCP* provided good fit statistics properly, taking into account the reflection and emission line components. This model has the following form in XSPEC

$$const \times TBabs \times zTBabs \times xillverCP \tag{4.3}$$

During the fitting we allowed the parameters Γ, kT_e, R and the normalization $N_{xillverCP}$ to vary. We considered the reflective material as neutral and fixed the ionization parameter to 1.0 (i.e $log\xi = 0$). Also, we fixed the inclination (θ_{incl}) to 30° (default value) and adopted solar abundance with AF_e fixed to 1.

For four sources, we found the need for relativistic treatment to take care of the line broadening and the relativistic smearing of the reflected radiation. Therefore for those four sources, we fitted the data with an advanced reflection model *relxillCP*.

In XSPEC the model has the form,

$$const \times TBabs \times zTBabs \times relxillCP \tag{4.4}$$

In this model, we froze a few parameters as it was not feasible to constrain all the parameters due to S/N limitations in the data. The inner radius (r_{in}) and outer radius (r_{out}) of the accretion disk were fixed to 1 ISCO and 400 R_g, respectively. θ_{incl} was fixed to 30°, and we considered a black hole with maximum spin and fixed the spin parameter (a_*) to 0.998. We also considered a continuous disk emission profile and varied only β_1, while β_2 was tied with β_1. Thus here the free parameters were Γ, kT_e, R, AF_e, $log\xi$, β_1 and the normalization $N_{relxillCP}$.

For two sources in our sample, either *xillverCP* or *relxillCP* alone could not take care of the emission region completely (see Fig. 4.1). For those two sources (NGC 3783 and NGC 5506), we considered both models with the following form in XSPEC,

$$const \times TBabs \times zTBabs \times (relxillCP + xillverCP) \tag{4.5}$$

In this model, all the parameters that are common between *relxillCP* and *xillverCP* were tied together except $log\xi$ and the normalization. In *relxillCP*, the accretion disk is assumed to be ionized since it stays closer to the black hole thus, $log\xi$ was kept free; however, within *xillverCP*, the reflection component was assumed to be coming from more distant and neutral ($log\xi = 0$) material. The best-fitted parameters are shown in Table 4.4. The unfolded spectra along the best-fitted models, const × TBabs × zTBabs × (xillverCP/relxillCP/relxillCP+xillverCP) and the residues of the fit for the sample of 21 sources are given in Fig. 4.2, 4.3 and 4.4.

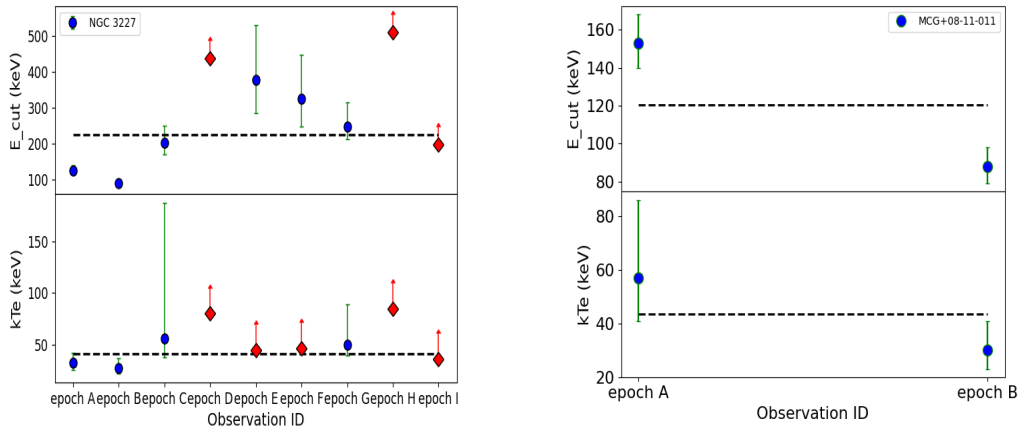

FIGURE 4.5: Upper panel: Variation in E_{cut} and Lower panel: Variation in kT_e with the observation epochs as obtained from the *xillver* and *xillverCP* model fits respectively. The plotted errors were calculated at 90 % confidence level for NGC 3227 (left panel) and MCG+08-11-011 (right panel). The dashed lines in each panel are fits of constant (mean of E_{cut} and kT_e) to the data points.

4.2 Results and Discussion

In this work, we studied the variation in the temperature of the corona in AGN. Our sample consists of 21 sources having a total of 72 epochs of observations. All these observations were analysed in a homogeneous manner. Results for a few OBSIDs in a few sources are the first-time measurements. However, for a few sources in our sample, E_{cut} measurements were available in the literature, either using data from *NuSTAR* in isolation or with the inclusion of data from different instruments along with that from *NuSTAR*. We found that, overall, our results are in line with those reported in the literature (within the bounds of uncertainty). For a significant fraction of the objects, our analysis has provided measurement of kT_e.

For few sources, in this sample, there were indications of kT_e variation; however, due to the large error bars in the derived values, unambiguous claim on the detection of variation in kT_e could not be made, For example, variation in kT_e was detected between epoch A and epoch C of Mrk 915 (see Table 4.4), but as we

could not constrain the best-fitted value of kT_e in epoch A, unambiguous claim on the detection of variation in kT_e in the source could not be made except for two sources, namely NGC 3227 and MCG+08+11-011, where we found variation in kT_e between nine epochs of observations separated by three years in NGC 3227 and two epochs separated by about five years in the case of MCG+08-11-011. However, the variability measured in kT_e between epoch A and epoch B of MCG+08-11-011 is statistically marginal, the measurements being mutually consistent within the 90% confidence level. For both sources, the variation in E_{cut} could also be ascertained from both the *pexrav* and *xillver* model fit to the source spectra. The variation of E_{cut} and kT_e as obtained from the physical model fit (*xillver* and *xillverCP*) with the epochs of observations are plotted in Fig. 4.5 in which the dashed lines in each panel represents the mean value of these two parameters respectively. To understand the reasons behind the change in kT_e, we examined the correlations between Γ against flux, kT_e against flux, R against flux and kT_e against τ. We calculated τ from the following equation (Zdziarski et al. 1996)

$$\tau = \sqrt{\frac{9}{4} + \frac{3}{\theta\left[\left(\Gamma + \frac{1}{2}\right)^2 - \frac{9}{4}\right]}} - \frac{3}{2}$$

where $\theta = kT_e/m_ec^2$. We also estimated the flux for const × TBabs × zTBabs × (xillverCP/relxillCP/relxillCP+xillverCP) in the energy range of 3 to 79 keV using the XSPEC model *cflux*. The values of flux as well as τ are given in Table 4.5. The corresponding errors in flux and τ were calculated at the 90% confidence level. The unfolded epoch A and epoch B FPMA spectra of MCG+08-11-011 along with the best-fitted model, const × TBabs × (xillverCP) and residues of the fit are given in Fig. 4.6.

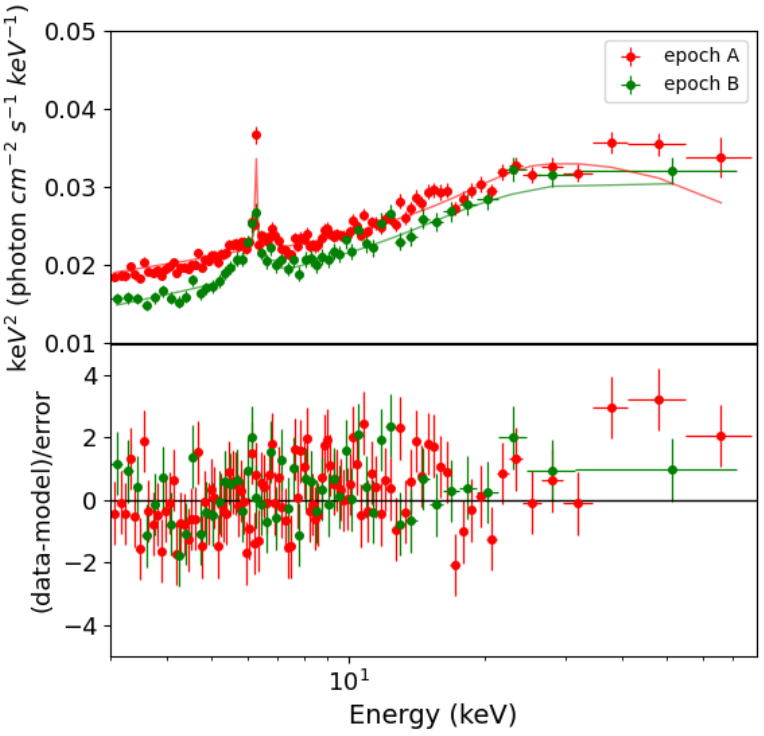

FIGURE 4.6: Upper panel: Unfolded spectra with the best-fitted model *const* × *TBabs* × *(xillverCP)* and Bottom panel: Residue of the fit to the epoch A (red dot) and epoch B (green dot) spectra of MCG+08-11-011. The spectra are re-binned for visualization purpose.

4.2.1 Correlation analysis

We describe below various correlation analyses carried out on two sources, namely, NGC 3227 and MCG+08-11-011, that have shown unambiguous evidence for variation in kT_e.

NGC 3227: We discuss below the correlation between various parameters for NGC 3227. Since the errors in the measured E_{cut} and kT_e values are not symmetric, and there is no conventional way to address such errors during a correlation study, we adopted two procedures to find the correlation between various parameters. In the first case, we neglected the corresponding errors, considered only the best-fitted numbers of the parameters, and performed the ordinary LLS (OLS) fit between

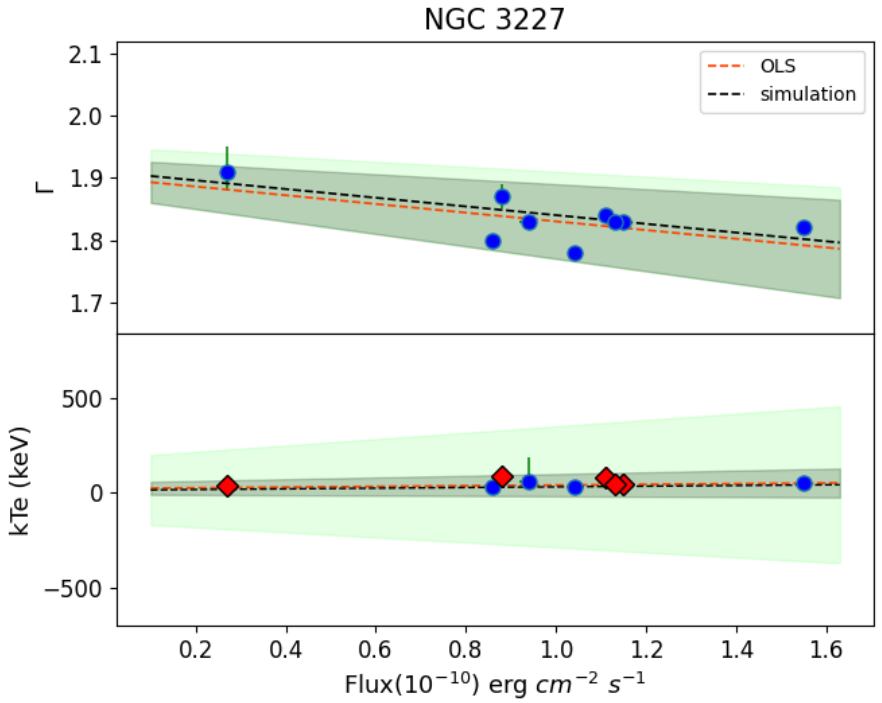

FIGURE 4.7: Upper panel: The correlation between Γ and flux. Lower panel: The relation between kT_e and flux. The dashed orange line is the OLS fit to the data points. The black dashed line is the linear line drawn using the median values of the simulated parameters. The grey-shaded region indicates the upper and lower errors in the fit parameters for OLS, and the green region indicates the errors in the fit parameter obtained from the simulation. In the LLS analysis, epochs in which we were unable to constrain kT_e were dropped (indicated with red point).

them. The PCC (r) and the NHPNC (p) were also estimated. In the second case, to take the non-symmetric errors into account, we simulated 10^5 points from each rectangular box around the best-fitted values (x,y) with x and y boundaries of (x_{low},x_{high}) and (y_{low},y_{high}), respectively. Here x_{low}, y_{low} and x_{high}, y_{high} refer to the lower and upper errors in x and y values. A LLS fit was done 10^5 times, yielding the distribution of the slope (m), the intercept (c), r and p. The median values of the distributions were taken to represent the best-fitted values of the correlation. All the values and the errors for the unweighted correlation as well as for the simulated correlation are given in Table 4.6.

In Seyfert galaxies, the spectra generally appear to be softer with increasing X-ray

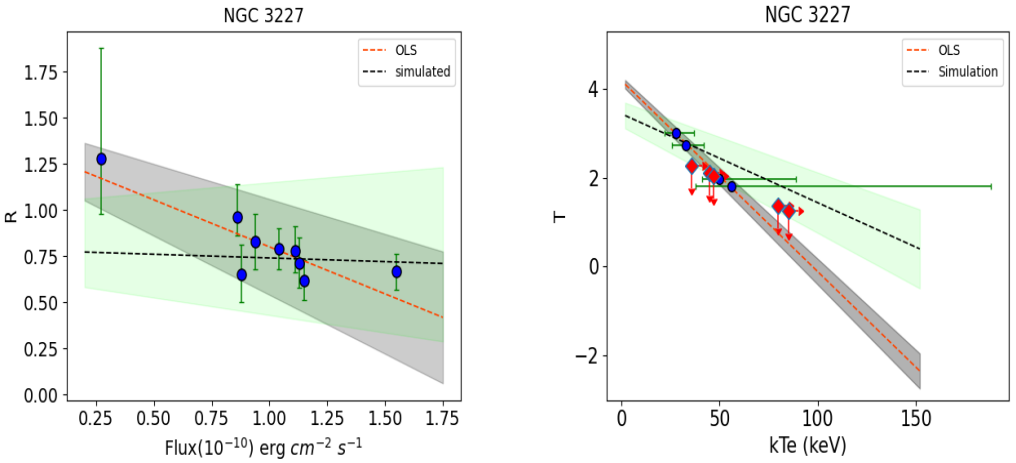

FIGURE 4.8: Left panel: The correlation between R and flux. Right panel: The relation between τ and kT_e. The dashed lines in all the panels are the LLS fit to the data for NGC 3227. The dashed lines, the shaded regions and the red points have the same meaning as in Fig. 4.7.

flux (Markowitz et al. 2003). We show in Fig. 4.7 the correlation between Γ and the brightness of NGC 3227. For the source, each point in the figure corresponds to the Γ, and the flux obtained by *xillverCP* model fits to each epoch of spectra. For NGC 3227, we found an anti-correlation between Γ and flux (see Fig. 4.7 and Table 4.6) between epochs of observation significant at greater than 90% level. Correlations between the changes in the temperature of the corona with apparent brightness and spectral shape of the source spectra, can provide important constraints and enhance our understanding of AGN corona. The correlation between kT_e and flux is shown in Fig. 4.7. Also shown in the figure are the ordinary and simulated LLS fits for the data. No correlation is found between kT_e and flux in NGC 3227. The parameter R is not found to be correlated with flux either (see Fig. 4.8). In NGC 3227, we found an anti correlation between τ and kT_e, with τ decreasing towards higher temperatures (see Fig. 4.8). According to Zdziarski et al. (1996), τ is geometry dependent and equals the radial optical depth in a uniform sphere. The negative correlation between τ and kT_e implies a change in the geometry of the corona (Ballantyne et al. 2014). In NGC 3227 we found no statistically significant correlations between kT_e and flux, between R and flux, and between Γ and flux.

MCG+08-11-011: Like all other bright Seyfert galaxies, MCG+08-11-011 also became softer when it brightened in X-ray (Soldi et al. 2014; Ballantyne et al. 2014). In Fig. 4.9, the *softer-when-brighter* trend is shown for this source. We also found MCG+08-11-011 in its higher flux state ($14.02^{+1.12}_{-0.11} \times 10^{-11} ergcm^{-2}s^{-1}$) on August 2016 (epoch A) with a hotter corona of $kT_e = 57^{+29}_{-16}$ keV. On December 2021 (epoch B), the source was found to have a cooler corona ($kT_e = 30^{+11}_{-7}$ keV) with a lower flux of $12.60^{+0.21}_{-0.21} \times 10^{-11} ergcm^{-2}s^{-1}$ (Fig. 4.6 and Fig. 4.9). The source was optically thinner on August 2016 with $\tau = 1.68$ and τ increased to 2.73 on December 2021. The correlations between kT_e against flux (right panel) and kT_e against τ (right panel) is shown in Fig. 4.9 and 4.10 respectively. Thus, in MCG+08-11-011, we found a "hotter-when-brighter" nature along with the "softer-when-brighter" behaviour. In the brightest epoch, the corona is also found to be optically thinner. The "hotter-when-brighter" and "softer-when-brighter" trend could be understood by the changing nature of the corona. All such correlations point to the Coronal geometry change that, in turn, results in the variation in the heating/cooling of the AGN corona. The possible scenario that can explain such variation is that at the low flux state, the AGN corona lies near to the black hole and remains optically thick. In this position, the fraction of the reflected emission to the primary emission increases, thereby increasing the reflection fraction R. As the source brightens, the corona moves vertically away from the central engine. This vertical movement results in an optically thinner and hotter corona with a lesser amount of reflected emission off the disk. Thus a softer spectrum is expected. The observed correlations among R, flux and τ with kT_e for MCG+08-11-011, shown in Fig. 4.9 and 4.10 are evidences for the *vertically out flowing corona* (Keek & Ballantyne 2016) as a cause of the observed kT_e variation in this source.

Recently, Kang et al. (2021b) found a Λ shaped correlation between E_{cut} and Γ for SWIFT J2127.4+5654. The authors argued for both the *Compton cooling* and *vertically outflowing corona* scenario being responsible for the observed E_{cut}

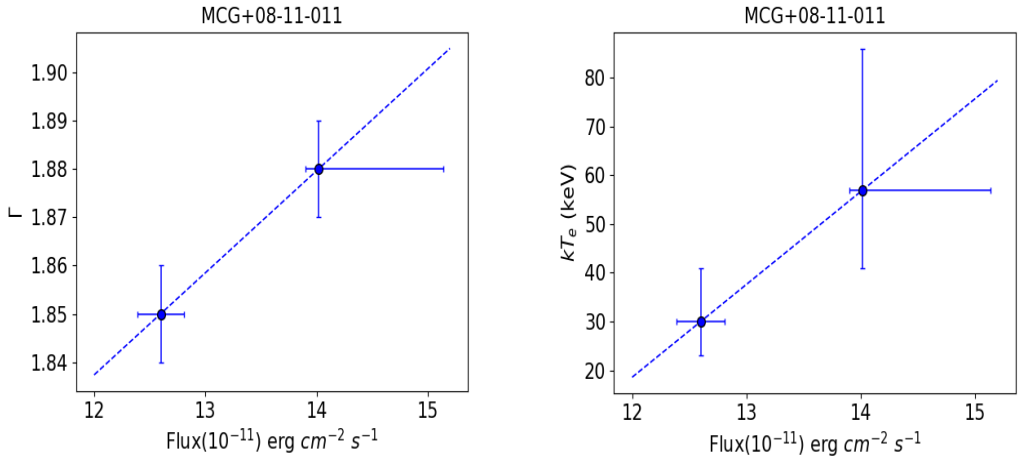

FIGURE 4.9: Left panel: The correlation between Γ and flux. Right panel: The relation between kT_e and flux. The dashed lines in all the panels are the LLS fit to the data for MCG+08-11-011.

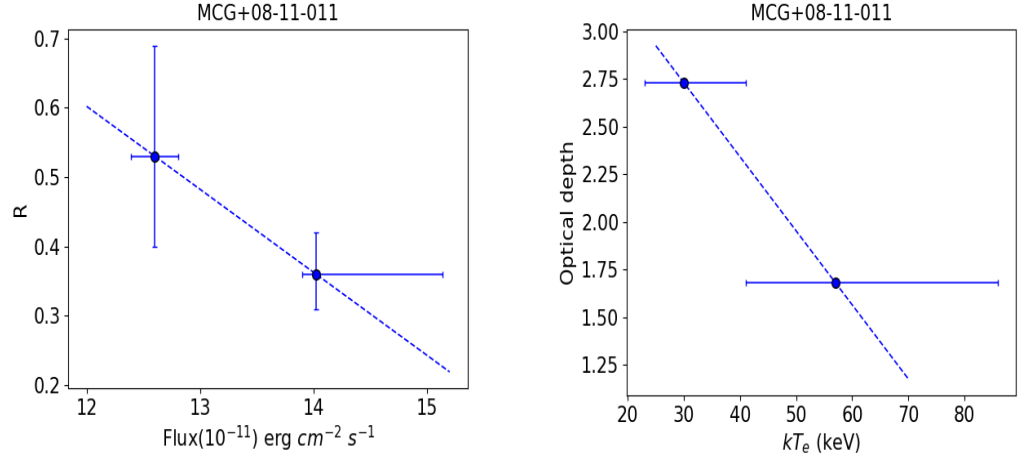

FIGURE 4.10: Left panel: The correlation between R and flux. Right panel: The relation between τ and kT_e. The dashed lines in all the panels are the LLS fit to the data for MCG+08-11-011.

variation in this source. The authors also claimed to have found a break point in Γ ($\gtrsim 2.05$) after which the *Compton cooling* would dominate over the *vertically out flowing corona* scenario. Barua et al. (2021) reported variation of kT_e in a Seyfert 2 galaxy ESO 103-035, wherein they found a positive correlation between kT_e and flux. According to the authors, the "hotter-when-brighter" trend could be due to the AGN variability being driven by coronal heating variation or due to the AGN variability driven by the changes in the seed photon flux. Previously in Ark 564, the same authors (Barua et al. 2020) found evidence of kT_e variation with "cooler-when-brighter" nature. To explain the opposite behaviour of the corona in the two sources, namely ESO 103-035 and Ark 564, the authors pointed to a cut-off in Γ. From the Comptonization model fits to the data, they found $\Gamma < 2.00$ in ESO 103-035 and $\Gamma > 2.00$ in Ark 564. Barua et al. (2021) suggested that the difference in Γ between the two sources is the reason behind the two completely different behaviour observed in them. In the case of NGC 3227 and MCG+08-11-011, too, we found $\Gamma < 2.00$, which could be the driving factor for the "hotter-when-brighter" behaviour observed in both the sources.

We noticed an anti-correlation between τ and kT_e in NGC 3227 and MCG+08-11-011. Tortosa et al. (2018) too, from the analysis of a sample of AGN, found a negative correlation between τ and kT_e. According to the authors, this negative correlation could not be explained with a stable accretion disk-corona connection under radiative balance. The possible explanation for this behaviour could be (a) due to the coronal geometry/position change and/or (b) variation in the fraction of the intrinsic disk emission to the total disk emission. We note that broadband spectral energy distribution fits to simultaneous UV to hard X-ray data alone will be able to provide a strong constraint on τ. This, in turn, can put constraints on the role of accretion disk emission in kT_e changes.

The idea that sources with a positive correlation between kT_e and flux have $\Gamma < 2$, and those with $\Gamma > 2$ show a negative correlation between kT_e and flux needs

to be confirmed, which necessitates detection of kT_e variation and its correlation with flux, in many sources.

TABLE 4.1: Best-fitted parameters of the Model *const* × *TBabs* × *zTBabs* × *(zpo+zgauss)* to the source spectra. he asterisk against entries indicates that they are frozen.

Source	Epoch	N_H^{INT} (10^{22} cm^{-2})	Γ	N_{pow} (10^{-2})	E (keV)	σ (keV)	χ^2/dof	c
1H 0419−577	A	$3.85^{+1.10}_{-1.08}$	$1.84^{+0.03}_{-0.03}$	$0.49^{+0.04}_{-0.04}$	-	-	762/735	$1.06^{+0.02}_{-0.02}$
	B	$3.39^{+1.16}_{-1.14}$	$1.83^{+0.03}_{-0.03}$	$0.55^{+0.05}_{-0.04}$	-	-	671/682	$1.02^{+0.02}_{-0.02}$
	C	$3.53^{+0.61}_{-0.61}$	$1.84^{+0.02}_{-0.02}$	$0.61^{+0.03}_{-0.03}$	6.4*	<0.22	1330/1156	$1.04^{+0.01}_{-0.01}$
Mrk 915	A	$3.09^{+1.04}_{-1.11}$	$1.69^{+0.04}_{-0.04}$	$0.24^{+0.02}_{-0.02}$	6.4*	<0.26	661/650	$1.04^{+0.02}_{-0.02}$
	B	$4.64^{+1.54}_{-1.50}$	$1.65^{+0.05}_{-0.05}$	$0.15^{+0.02}_{-0.02}$	6.4*	<0.46	542/543	$1.05^{+0.03}_{-0.03}$
	C	$6.45^{+1.93}_{-1.95}$	$1.66^{+0.06}_{-0.06}$	$0.13^{+0.02}_{-0.02}$	6.4*	<0.30	426/435	$1.04^{+0.03}_{-0.03}$
3C 111	A	$1.71^{+0.93}_{-0.92}$	$1.81^{+0.03}_{-0.03}$	$1.50^{+0.12}_{-0.11}$	$6.42^{+0.12}_{-0.11}$	0.1*	662/683	$1.01^{+0.02}_{-0.02}$
	B	$2.09^{+0.65}_{-0.64}$	$1.81^{+0.02}_{-0.02}$	$1.39^{+0.07}_{-0.07}$	6.4*	$0.20^{+0.16}_{-0.16}$	976/949	$1.01^{+0.01}_{-0.01}$
	C	$2.17^{+0.73}_{-0.73}$	$1.72^{+0.02}_{-0.02}$	$0.82^{+0.05}_{-0.05}$	$6.47^{+0.09}_{-0.09}$	<0.30	942/898	$1.00^{+0.01}_{-0.01}$
NGC 3783	A	-	$1.57^{+0.01}_{-0.01}$	$0.85^{+0.02}_{-0.02}$	$6.15^{+0.06}_{-0.07}$	$0.34^{+0.08}_{-0.07}$	1163/1040	$1.03^{+0.01}_{-0.01}$
	B	$1.22^{+0.66}_{-0.67}$	$1.52^{+0.02}_{-0.02}$	$0.65^{+0.04}_{-0.04}$	$6.22^{+0.06}_{-0.07}$	$0.28^{+0.10}_{-0.09}$	1220/1004	$1.04^{+0.01}_{-0.01}$
	C	$5.16^{+0.99}_{-0.96}$	$1.46^{+0.03}_{-0.03}$	$0.56^{+0.05}_{-0.04}$	$6.11^{+0.09}_{-0.10}$	$0.38^{+0.12}_{-0.10}$	1068/794	$1.04^{+0.01}_{-0.01}$
	D	$3.86^{+0.84}_{-0.83}$	$1.50^{+0.03}_{-0.03}$	$0.70^{+0.05}_{-0.05}$	6.4*	$0.16^{+0.07}_{-0.07}$	1210/916	$1.02^{+0.02}_{-0.02}$
NGC 7469	A	-	$1.82^{+0.02}_{-0.02}$	$0.96^{+0.04}_{-0.04}$	$6.32^{+0.11}_{-0.09}$	$0.28^{+0.30}_{-0.15}$	631/633	$1.02^{+0.02}_{-0.02}$
	B	-	$1.76^{+0.02}_{-0.02}$	$0.87^{+0.04}_{-0.04}$	$6.39^{+0.66}_{-0.66}$	<0.1	632/629	$1.02^{+0.02}_{-0.02}$
	C	-	$1.75^{+0.02}_{-0.02}$	$0.70^{+0.03}_{-0.03}$	$6.34^{+0.07}_{-0.06}$	$0.18^{+0.10}_{-0.16}$	577/606	$1.00^{+0.02}_{-0.02}$
	D	-	$1.79^{+0.02}_{-0.02}$	$0.83^{+0.04}_{-0.03}$	$6.35^{+0.12}_{-0.22}$	<0.46	666/634	$1.02^{+0.02}_{-0.02}$

Continued

Table 4.1 – Following the previous page

Source	Epoch	N_H^{INT} (10^{22} cm^{-2})	Γ	N_{pow} (10^{-2})	E (keV)	σ (keV)	χ^2/dof	c
	E	-	$1.75^{+0.02}_{-0.02}$	$0.81^{+0.04}_{-0.03}$	$6.32^{+0.06}_{-0.06}$	0.1*	682/620	$1.01^{+0.02}_{-0.02}$
	F	-	$1.73^{+0.02}_{-0.02}$	$0.73^{+0.03}_{-0.03}$	$6.37^{+0.12}_{-0.16}$	$0.29^{+0.18}_{-0.16}$	611/605	$1.00^{+0.02}_{-0.02}$
	G	-	$1.77^{+0.02}_{-0.02}$	$0.93^{+0.04}_{-0.03}$	$6.35^{+0.10}_{-0.10}$	$0.25^{+0.13}_{-0.11}$	679/695	$1.04^{+0.02}_{-0.02}$
Mrk 110	A	-	$1.80^{+0.01}_{-0.01}$	$1.18^{+0.01}_{-0.01}$	$6.4^{+0.07}_{-0.07}$	$0.34^{+0.09}_{-0.08}$	1631/1475	$1.01^{+0.01}_{-0.01}$
	B	-	$1.81^{+0.01}_{-0.01}$	$0.86^{+0.02}_{-0.02}$	$6.34^{+0.11}_{-0.13}$	$0.34^{+0.23}_{-0.16}$	1036/1026	$1.04^{+0.01}_{-0.01}$
	C	-	$1.76^{+0.01}_{-0.01}$	$0.65^{+0.02}_{-0.02}$	$6.35^{+0.09}_{-0.08}$	$0.25^{+0.17}_{-0.15}$	1031/1007	$1.04^{+0.01}_{-0.01}$
UGC 06728	A	-	$1.62^{+0.04}_{-0.04}$	$0.15^{+0.01}_{-0.01}$	$6.32^{+0.27}_{-0.26}$	<0.58	189/198	$1.03^{+0.05}_{-0.05}$
	B	-	$1.64^{+0.02}_{-0.02}$	$0.30^{+0.01}_{-0.01}$	$6.4^{+0.09}_{-0.11}$	<0.28	742/708	$1.01^{+0.02}_{-0.02}$
NGC 4258	A	$13.12^{+2.38}_{-2.26}$	$1.80^{+0.07}_{-0.07}$	$0.13^{+0.03}_{-0.02}$	-	-	264/279	$1.04^{+0.04}_{-0.04}$
	B	$14.51^{+2.05}_{-1.96}$	$1.89^{+0.06}_{-0.06}$	$0.13^{+0.02}_{-0.02}$	$6.4^{+0.26}_{-0.15}$	0.1*	456/408	$0.98^{+0.03}_{-0.03}$
KUG 1141+371	A	$1.57^{+1.28}_{-1.25}$	$1.88^{+0.04}_{-0.04}$	$0.43^{+0.05}_{-0.04}$	-	-	443/487	$1.06^{+0.03}_{-0.03}$
	B	$2.40^{+2.13}_{-2.04}$	$1.76^{+0.07}_{-0.07}$	$0.25^{+0.05}_{-0.04}$	-	-	241/249	$1.05^{+0.04}_{-0.04}$
MCG-06-30-15	A	-	$1.94^{+0.02}_{-0.01}$	$1.68^{+0.05}_{-0.05}$	6.4*	$0.29^{+0.12}_{-0.09}$	785/735	$1.02^{+0.02}_{-0.02}$
	B	-	$1.93^{+0.01}_{-0.01}$	$1.70^{+0.02}_{-0.02}$	6.4*	$0.28^{+0.06}_{-0.06}$	1931/1374	$1.03^{+0.01}_{-0.01}$
	C	-	$1.77^{+0.02}_{-0.02}$	$0.78^{+0.03}_{-0.03}$	6.4*	$0.26^{+0.07}_{-0.07}$	827/743	$1.04^{+0.02}_{-0.02}$
NGC 5506	A	$1.11^{+0.48}_{-0.49}$	$1.58^{+0.02}_{-0.02}$	$1.07^{+0.05}_{-0.05}$	$6.32^{+0.06}_{-0.06}$	$0.45^{+0.08}_{-0.07}$	1493/1231	$1.00^{+0.01}_{-0.01}$
	B	$1.01^{+0.43}_{-0.43}$	$1.56^{+0.01}_{-0.01}$	$1.00^{+0.04}_{-0.04}$	$6.31^{+0.03}_{-0.03}$	$0.30^{+0.04}_{-0.04}$	1621/1313	$1.05^{+0.01}_{-0.01}$
	C	$0.73^{+0.46}_{-0.49}$	$1.59^{+0.02}_{-0.02}$	$1.45^{+0.01}_{-0.01}$	$6.22^{+0.07}_{-0.10}$	$0.50^{+0.11}_{-0.09}$	1539/1296	$1.04^{+0.01}_{-0.01}$
MCG+08-11-011	A	-	$1.77^{+0.01}_{-0.01}$	$1.51^{+0.02}_{-0.02}$	$6.33^{+0.04}_{-0.05}$	$0.27^{+0.07}_{-0.07}$	1301/1315	$1.03^{+0.01}_{-0.01}$

Continued

Table 4.1 – Following the previous page

Source	Epoch	N_H^{INT} (10^{22} cm^{-2})	Γ	N_{pow} (10^{-2})	E (keV)	σ (keV)	χ^2/dof	c
	B	-	$1.70^{+0.02}_{-0.02}$	$1.12^{+0.04}_{-0.04}$	$6.36^{+0.09}_{-0.08}$	$0.36^{+0.11}_{-0.11}$	753/744	$1.01^{+0.02}_{-0.02}$
GRS 1734-292	A	$3.64^{+0.71}_{-0.73}$	$1.83^{+0.02}_{-0.02}$	$2.54^{+0.15}_{-0.15}$	6.4*	<0.41	1018/865	$1.04^{+0.01}_{-0.01}$
	B	$4.13^{+0.74}_{-0.78}$	$1.76^{+0.02}_{-0.02}$	$1.72^{+0.10}_{-0.10}$	$6.07^{+0.15}_{-0.16}$	<0.36	869/855	$0.98^{+0.01}_{-0.01}$
Mrk 926	A	-	$1.76^{+0.01}_{-0.01}$	$1.59^{+0.02}_{-0.02}$	$6.32^{+0.08}_{-0.08}$	$0.38^{+0.10}_{-0.09}$	1453/1467	$1.00^{+0.01}_{-0.01}$
	B	-	$1.69^{+0.03}_{-0.03}$	$0.50^{+0.03}_{-0.03}$	$6.29^{+0.12}_{-0.13}$	<0.29	465/493	$1.06^{+0.03}_{-0.03}$
Mrk 841	A	-	$1.75^{+0.03}_{-0.03}$	$0.48^{+0.03}_{-0.04}$	$6.33^{+0.28}_{-0.85}$	$0.44^{+0.73}_{-0.22}$	477/506	$1.00^{+0.03}_{-0.03}$
	B	-	$1.73^{+0.02}_{-0.02}$	$0.42^{+0.02}_{-0.02}$	$6.33^{+0.16}_{-0.40}$	$0.41^{+0.43}_{-0.17}$	750/743	$1.04^{+0.02}_{-0.02}$
NGC 5273	A	-	$1.54^{+0.02}_{-0.02}$	$0.32^{+0.02}_{-0.02}$	6.4*	$0.32^{+0.22}_{-0.15}$	634/576	$1.07^{+0.03}_{-0.03}$
	B	-	$1.42^{+0.03}_{-0.03}$	$0.24^{+0.01}_{-0.01}$	$6.25^{+0.09}_{-0.09}$	$0.24^{+0.25}_{-0.14}$	483/507	$1.03^{+0.03}_{-0.03}$
NGC 0985	A	$5.22^{+2.73}_{-2.70}$	$1.70^{+0.08}_{-0.08}$	$0.29^{+0.07}_{-0.06}$	6.4*	$0.31^{+0.49}_{-0.27}$	308/266	$1.08^{+0.05}_{-0.04}$
	B	<1.68	$1.74^{+0.03}_{-0.03}$	$0.42^{+0.03}_{-0.03}$	$6.33^{+0.15}_{-0.19}$	$0.24^{+0.19}_{-0.13}$	388/465	$1.00^{+0.03}_{-0.03}$
HE 1143−1810	A	$1.91^{+1.39}_{-1.37}$	$1.82^{+0.04}_{-0.04}$	$0.71^{+0.08}_{-0.08}$	6.4*	<0.99	500/506	$1.03^{+0.03}_{-0.02}$
	B	<2.81	$1.76^{+0.05}_{-0.05}$	$0.60^{+0.08}_{-0.07}$	$6.36^{+0.15}_{-0.16}$	$0.26^{+0.20}_{-0.16}$	466/485	$1.01^{+0.03}_{-0.03}$
	C	-	$1.77^{+0.02}_{-0.02}$	$0.76^{+0.03}_{-0.03}$	$6.24^{+0.17}_{-0.21}$	$3.75^{+2.15}_{-1.55}$	530/594	$1.04^{+0.02}_{-0.02}$
	D	$1.54^{+1.14}_{-1.11}$	$1.82^{+0.04}_{-0.04}$	$0.85^{+0.09}_{-0.08}$	$6.4^{+0.17}_{-0.15}$	0.10*	594/560	$1.04^{+0.02}_{-0.02}$
	E	$1.82^{+1.11}_{-1.08}$	$1.83^{+0.04}_{-0.04}$	$0.86^{+0.08}_{-0.08}$	6.4*	0.10*	597/569	$1.05^{+0.02}_{-0.02}$
NGC 3227	A	-	$1.56^{+0.01}_{-0.01}$	$0.71^{+0.02}_{-0.02}$	$6.35^{+0.03}_{-0.03}$	0.10*	930/826	$1.04^{+0.01}_{-0.01}$
	B	-	$1.55^{+0.01}_{-0.01}$	$0.58^{+0.02}_{-0.02}$	$6.38^{+0.03}_{-0.04}$	0.10*	752/706	$1.02^{+0.01}_{-0.01}$
	C	-	$1.61^{+0.01}_{-0.01}$	$0.73^{+0.02}_{-0.02}$	$6.33^{+0.04}_{-0.04}$	0.10*	834/704	$1.01^{+0.01}_{-0.01}$

Continued

Table 4.1 – Following the previous page

Source	Epoch	N_H^{INT} (10^{22} cm^{-2})	Γ	N_{pow} (10^{-2})	E (keV)	σ (keV)	χ^2/dof	c
	D	-	$1.63^{+0.01}_{-0.01}$	$0.90^{+0.03}_{-0.03}$	$6.32^{+0.04}_{-0.03}$	0.10*	909/777	$1.01^{+0.01}_{-0.01}$
	E	-	$1.66^{+0.01}_{-0.01}$	$1.01^{+0.03}_{-0.03}$	$6.30^{+0.05}_{-0.05}$	0.10*	815/790	$1.02^{+0.01}_{-0.01}$
	F	-	$1.63^{+0.01}_{-0.01}$	$0.92^{+0.03}_{-0.03}$	$6.34^{+0.05}_{-0.05}$	0.10*	684/717	$1.00^{+0.01}_{-0.01}$
	G	$2.91^{+1.04}_{-1.03}$	$1.61^{+0.02}_{-0.02}$	$1.22^{+0.07}_{-0.06}$	$6.23^{+0.04}_{-0.04}$	0.10*	1081/935	$0.99^{+0.01}_{-0.01}$
	H	$4.66^{+1.83}_{-1.80}$	$1.64^{+0.04}_{-0.04}$	$0.76^{+0.08}_{-0.07}$	$6.28^{+0.07}_{-0.07}$	0.10*	600/595	$1.04^{+0.01}_{-0.01}$
	I	$4.57^{+3.73}_{-3.62}$	$1.48^{+0.07}_{-0.07}$	$0.17^{+0.04}_{-0.03}$	$6.38^{+0.05}_{-0.05}$	0.10*	257/247	$1.06^{+0.03}_{-0.03}$
MR 2251−178	A	-	$1.75^{+0.02}_{-0.02}$	$1.42^{+0.05}_{-0.05}$	-	-	583/601	$1.02^{+0.02}_{-0.02}$
	B	-	$1.79^{+0.01}_{-0.01}$	$1.77^{+0.06}_{-0.06}$	-	-	656/633	$1.00^{+0.01}_{-0.01}$
	C	-	$1.79^{+0.02}_{-0.02}$	$1.62^{+0.06}_{-0.06}$	-	-	574/551	$1.03^{+0.02}_{-0.02}$
	D	-	$1.79^{+0.02}_{-0.02}$	$1.62^{+0.06}_{-0.06}$	$6.49^{+0.37}_{-0.27}$	0.10*	516/576	$1.02^{+0.02}_{-0.02}$
	E	$7.82^{+2.99}_{-2.93}$	$1.83^{+0.05}_{-0.05}$	$0.84^{+0.13}_{-0.11}$	-	-	446/400	$1.05^{+0.02}_{-0.02}$
NGC 5548	A	$3.89^{+1.76}_{-1.73}$	$1.62^{+0.03}_{-0.03}$	$1.00^{+0.10}_{-0.09}$	$6.37^{+0.09}_{-0.09}$	0.10*	684/643	$1.02^{+0.02}_{-0.02}$
	B	< 3.21	$1.60^{+0.03}_{-0.03}$	$0.86^{+0.11}_{-0.11}$	$6.33^{+0.08}_{-0.08}$	0.10*	612/634	$1.05^{+0.01}_{-0.01}$
	C	$6.29^{+1.40}_{-1.32}$	$1.59^{+0.02}_{-0.02}$	$0.79^{+0.08}_{-0.08}$	$6.32^{+0.04}_{-0.04}$	0.10*	880/811	$1.02^{+0.01}_{-0.01}$
	D	$2.70^{+1.28}_{-1.27}$	$1.64^{+0.02}_{-0.02}$	$0.93^{+0.07}_{-0.06}$	$6.38^{+0.04}_{-0.04}$	0.10*	890/813	$1.05^{+0.01}_{-0.01}$
	E	$8.97^{+1.65}_{-1.63}$	$1.57^{+0.03}_{-0.02}$	$0.77^{+0.06}_{-0.05}$	$6.66^{+0.04}_{-0.04}$	0.10*	840/810	$1.02^{+0.01}_{-0.01}$
	F	<1.28	$1.57^{+0.03}_{-0.01}$	$0.67^{+0.05}_{-0.02}$	$6.31^{+0.04}_{-0.04}$	0.10*	692/692	$1.05^{+0.01}_{-0.01}$

TABLE 4.2: Best-fitted parameters of the Model *const* × *TBabs* × *zTBabs* × *(pexrav+zgauss)* to the source spectra.

Source	Epoch	N_H^{INT} (10^{22} cm^{-2})	Γ	E_{cut} (keV)	R	N_{pexrav} (10^{-2})	E (keV)	σ (keV)	χ^2/dof
1H 0419−577	A	$2.90^{+1.54}_{-1.54}$	$1.82^{+0.11}_{-0.11}$	94^{+82}_{-31}	$0.46^{+0.30}_{-0.25}$	$0.38^{+0.08}_{-0.06}$	-	-	739/733
	B	$1.96^{+1.66}_{-1.65}$	$1.74^{+0.12}_{-0.12}$	88^{+82}_{-30}	$0.28^{+0.29}_{-0.24}$	$0.39^{+0.08}_{-0.07}$	-	-	657/680
	C	<1.05	$1.62^{+0.07}_{-0.02}$	51^{+9}_{-4}	$0.33^{+0.15}_{-0.11}$	$0.34^{+0.05}_{-0.01}$	6.4*	<0.34	1167/1154
Mrk 915	A	$4.66^{+1.29}_{-1.30}$	$1.87^{+0.10}_{-0.10}$	>667	$0.53^{+0.35}_{-0.30}$	$0.31^{+0.06}_{-0.05}$	6.4*	0.001*	650/649
	B	$3.76^{+2.28}_{-2.25}$	$1.58^{+0.17}_{-0.17}$	112^{+862}_{-55}	<0.62	$0.13^{+0.05}_{-0.03}$	6.4*	0.001*	539/542
	C	$6.33^{+2.76}_{-2.73}$	$1.71^{+0.22}_{-0.22}$	84^{+351}_{-40}	$0.74^{+0.81}_{-0.53}$	$0.13^{+0.06}_{-0.04}$	6.4*	0.001*	419/434
3C 111	A	$1.74^{+0.92}_{-0.69}$	$1.81^{+0.04}_{-0.08}$	>864	<0.11	$1.38^{+0.18}_{-0.18}$	6.42*	<0.20	661/681
	B	$0.73^{+0.81}_{-0.70}$	$1.68^{+0.05}_{-0.05}$	128^{+51}_{-37}	<0.06	$1.04^{+0.10}_{-0.11}$	6.30*	0.1*	957/948
	C	$1.33^{+1.07}_{-1.12}$	$1.65^{+0.06}_{-0.06}$	251^{+513}_{-130}	<0.04	$0.68^{+0.08}_{-0.08}$	6.46*	<0.37	938/897
NGC 3783	A	-	$1.72^{+0.04}_{-0.04}$	245^{+150}_{-70}	$0.86^{+0.21}_{-0.18}$	$1.02^{+0.06}_{-0.06}$	6.15*	$0.33^{+0.07}_{-0.06}$	1049/1039
	B	$3.66^{+0.67}_{-1.07}$	$1.92^{+0.06}_{-0.11}$	>284	$1.83^{+0.41}_{-0.42}$	$1.17^{+0.01}_{-0.02}$	6.21*	$0.20^{+0.07}_{-0.07}$	1030/1003
	C	$7.91^{+0.93}_{-1.82}$	$1.91^{+0.04}_{-0.17}$	>242	$2.00^{+0.53}_{-0.60}$	$1.08^{+0.01}_{-0.03}$	6.11*	$0.31^{+0.08}_{-0.06}$	938/793
	D	$6.85^{+0.82}_{-0.81}$	$1.94^{+0.06}_{-0.06}$	>1225	$1.91^{+0.47}_{-0.42}$	$1.37^{+0.01}_{-0.01}$	6.4*	<0.15	1071/914
NGC 7469	A	-	$1.94^{+0.07}_{-0.06}$	270^{+2404}_{-134}	$0.66^{+0.35}_{-0.28}$	$1.08^{+0.10}_{-0.09}$	6.32*	0.1*	614/633
	B	-	$1.88^{+0.02}_{-0.06}$	>343	$0.46^{+0.30}_{-0.09}$	$0.98^{+0.07}_{-0.08}$	6.39*	0.1*	622/629
	C	-	$1.93^{+0.07}_{-0.07}$	>255	$0.77^{+0.41}_{-0.31}$	$0.86^{+0.08}_{-0.08}$	6.34*	0.1*	533/606
	D	-	$1.98^{+0.05}_{-0.04}$	>890	$0.81^{+0.34}_{-0.28}$	$1.02^{+0.05}_{-0.05}$	6.36*	0.1*	630/635
	E	-	$1.89^{+0.06}_{-0.06}$	>523	$0.57^{+0.33}_{-0.26}$	$0.95^{+0.08}_{-0.08}$	6.33*	0.1*	663/619

Continued

Table 4.2 – Following the previous page

Source	Epoch	N_H^{INT} (10^{22} cm^{-2})	Γ	E_{cut} (keV)	R	N_{pexrav} (10^{-2})	E (keV)	σ (keV)	χ^2/dof
	F	-	$1.86^{+0.07}_{-0.06}$	>867	$0.53^{+0.32}_{-0.24}$	$0.86^{+0.08}_{-0.07}$	6.37*	0.1*	597/605
	G	-	$1.87^{+0.02}_{-0.05}$	>425	$0.38^{+0.24}_{-0.12}$	$1.04^{+0.01}_{-0.07}$	6.35*	0.1*	671/695
Mrk 110	A	-	$1.72^{+0.01}_{-0.01}$	132^{+27}_{-17}	<0.03	$0.99^{+0.02}_{-0.01}$	6.4*	$0.30^{+0.08}_{-0.07}$	1520/1474
	B	-	$1.77^{+0.03}_{-0.03}$	173^{+125}_{-51}	<0.18	$0.77^{+0.03}_{-0.03}$	6.33*	<0.38	1026/1026
	C	-	$1.72^{+0.03}_{-0.03}$	213^{+251}_{-75}	<0.17	$0.59^{+0.03}_{-0.03}$	6.35*	$0.21^{+0.17}_{-0.15}$	1021/1006
UGC 06728	A	-	$1.62^{+0.17}_{-0.15}$	106^{+8766}_{-55}	<1.28	$0.15^{+0.04}_{-0.03}$	6.32*	<0.61	186/197
	B	-	$1.76^{+0.06}_{-0.06}$	295^{+2468}_{-146}	$0.64^{+0.32}_{-0.26}$	$0.65^{+0.03}_{-0.03}$	6.4*	0.1*	719/708
NGC 4258	A	$11.28^{+3.21}_{-3.14}$	$1.68^{+0.25}_{-0.25}$	52^{+123}_{-23}	<1.36	$0.11^{+0.05}_{-0.04}$	-	-	258/277
	B	$10.71^{+2.93}_{-2.89}$	$1.57^{+0.24}_{-0.23}$	32^{+23}_{-9}	<1.10	$0.08^{+0.04}_{-0.03}$	6.4*	<0.35	439/406
KUG 1141+371	A	$2.67^{+1.59}_{-1.74}$	$2.06^{+0.13}_{-0.16}$	>98	$0.75^{+0.663}_{-0.46}$	$0.52^{+0.12}_{-0.12}$	-	-	434/485
	B	$3.76^{+1.82}_{-2.91}$	$1.93^{+0.08}_{-0.23}$	>86	<1.44	$0.30^{+0.10}_{-0.10}$	-	-	238/247
MCG-06-30-15	A	-	$2.25^{+0.09}_{-0.07}$	>210	$1.88^{+0.67}_{-0.49}$	$2.38^{+0.02}_{-0.02}$	6.4*	0.1*	686/734
	B	-	$2.15^{+0.04}_{-0.03}$	>405	$1.17^{+0.27}_{-0.15}$	$2.18^{+0.06}_{-0.07}$	6.4*	$0.37^{+0.40}_{-0.13}$	1541/1372
	C	-	$2.05^{+0.08}_{-0.07}$	>273	$1.49^{+0.51}_{-0.39}$	$1.16^{+0.10}_{-0.09}$	6.4*	$0.27^{+0.09}_{-0.08}$	733/741
NGC 5506	A	$3.11^{+0.50}_{-0.52}$	$1.85^{+0.04}_{-0.04}$	>1389	$0.97^{+0.17}_{-0.16}$	$1.64^{+0.11}_{-0.10}$	6.32*	$0.46^{+0.10}_{-0.10}$	1303/1230
	B	$3.42^{+0.44}_{-0.44}$	$1.90^{+0.03}_{-0.03}$	>2818	$1.30^{+0.19}_{-0.18}$	$1.68^{+0.09}_{-0.08}$	6.31*	$0.22^{+0.05}_{-0.05}$	1302/1312
	C	$3.01^{+0.46}_{-0.49}$	$1.90^{+0.03}_{-0.04}$	>1364	$1.12^{+0.18}_{-0.16}$	$2.35^{+0.14}_{-0.15}$	6.22*	$0.48^{+0.09}_{-0.08}$	1284/1295
MCG+08-11-011	A	-	$1.85^{+0.02}_{-0.02}$	203^{+66}_{-41}	$0.36^{+0.05}_{-0.05}$	$1.64^{+0.05}_{-0.04}$	6.33*	$0.27^{+0.07}_{-0.07}$	1271/1314
	B	-	$1.78^{+0.05}_{-0.05}$	110^{+48}_{-27}	$0.52^{+0.12}_{-0.11}$	$1.24^{+0.08}_{-0.08}$	6.28*	$0.36^{+0.11}_{-0.11}$	742/743

Continued

Table 4.2 – Following the previous page

Source	Epoch	N_H^{INT} (10^{22} cm^{-2})	Γ	E_{cut} (keV)	R	N_{pexrav} (10^{-2})	E (keV)	σ (keV)	χ^2/dof
GRS 1734-292	A	$1.80^{+1.15}_{-1.20}$	$1.74^{+0.10}_{-0.10}$	68^{+23}_{-15}	$0.53^{+0.25}_{-0.22}$	$2.02^{+0.36}_{-0.32}$	6.4*	$0.24^{+0.22}_{-0.17}$	938/863
	B	$3.50^{+1.16}_{-1.27}$	$1.79^{+0.10}_{-0.10}$	108^{+64}_{-31}	$0.65^{+0.26}_{-0.23}$	$1.67^{+0.30}_{-0.28}$	6.06*	<0.35	805/854
Mrk 926	A	-	$1.75^{+0.02}_{-0.02}$	179^{+52}_{-33}	$0.12^{+0.03}_{-0.03}$	$1.52^{+0.04}_{-0.04}$	6.32*	$0.36^{+0.10}_{-0.09}$	1433/1466
	B	-	$1.70^{+0.08}_{-0.08}$	154^{+1367}_{-77}	$0.20^{+0.18}_{-0.15}$	$0.50^{+0.06}_{-0.05}$	6.29*	<0.29	464/493
Mrk 841	A	-	$1.83^{+0.08}_{-0.08}$	185^{+1658}_{-93}	$0.34^{+0.18}_{-0.16}$	$0.51^{+0.06}_{-0.05}$	6.33*	$0.48^{+0.59}_{-0.26}$	470/505
	B	-	$1.84^{+0.05}_{-0.05}$	173^{+213}_{-65}	$0.47^{+0.13}_{-0.12}$	$0.47^{+0.03}_{-0.03}$	6.33*	$0.54^{+0.42}_{-0.28}$	727/742
NGC 5273	A	-	$1.68^{+0.07}_{-0.07}$	182^{+332}_{-77}	$0.55^{+0.19}_{-0.17}$	$0.39^{+0.04}_{-0.04}$	6.4*	$0.42^{+0.41}_{-0.24}$	618/574
	B	-	$1.44^{+0.08}_{-0.08}$	59^{+24}_{-14}	$0.61^{+0.21}_{-0.18}$	$0.25^{+0.03}_{-0.03}$	6.25*	$0.21^{+0.25}_{-0.13}$	462/506
NGC 0985	A	$8.61^{+2.36}_{-3.07}$	$2.15^{+0.55}_{-0.38}$	>176	$1.89^{+0.39}_{-0.79}$	$0.53^{+0.12}_{-0.11}$	6.4*	0.20*	296/266
	B	-	$1.83^{+0.10}_{-0.10}$	>160	$0.37^{+0.47}_{-0.30}$	$0.44^{+0.05}_{-0.06}$	6.33*	$0.26^{+0.22}_{-0.12}$	383/463
HE 1134−1810	A	<3.44	$1.80^{+0.16}_{-0.16}$	95^{+174}_{-39}	$0.43^{+0.47}_{-0.34}$	$0.65^{+0.21}_{-0.15}$	6.4*	0.10*	491/505
	B	<3.37	$1.76^{+0.18}_{-0.13}$	>82	<0.68	$0.56^{+0.21}_{-0.11}$	6.36*	$0.26^{+0.20}_{-0.17}$	462/484
	C	-	$1.76^{+0.07}_{-0.07}$	154^{+239}_{-60}	$0.25^{+0.27}_{-0.22}$	$0.72^{+0.07}_{-0.06}$	6.24*	$0.28^{+0.35}_{-0.22}$	522/595
	D	<3.37	$1.85^{+0.14}_{-0.14}$	>103	$0.27^{+0.36}_{-0.27}$	$0.85^{+0.23}_{-0.18}$	6.4*	0.10*	590/559
	E	$2.27^{+1.64}_{-1.65}$	$1.92^{+0.14}_{-0.14}$	>102	$0.49^{+0.42}_{-0.32}$	$0.92^{+0.24}_{-0.19}$	6.4*	0.10*	588/567
NGC 3227	A	-	$1.68^{+0.05}_{-0.05}$	212^{+140}_{-63}	$0.52^{+0.15}_{-0.13}$	$0.84^{+0.06}_{-0.06}$	$6.35^{+0.03}_{-0.03}$	0.1*	856/824
	B	-	$1.64^{+0.06}_{-0.05}$	163^{+118}_{-50}	$0.48^{+0.18}_{-0.15}$	$0.66^{+0.06}_{-0.05}$	$6.38^{+0.04}_{-0.04}$	0.1*	711/704
	C	-	$1.77^{+0.05}_{-0.05}$	>254	$0.53^{+0.18}_{-0.15}$	$0.91^{+0.08}_{-0.07}$	$6.33^{+0.04}_{-0.04}$	0.1*	784/702
	D	-	$1.83^{+0.04}_{-0.04}$	>1147	$0.55^{+0.16}_{-0.14}$	$1.19^{+0.08}_{-0.07}$	$6.32^{+0.04}_{-0.04}$	0.1*	831/775

Continued

Table 4.2 – Following the previous page

Source	Epoch	N_H^{INT} (10^{22} cm^{-2})	Γ	E_{cut} (keV)	R	N_{pexrav} (10^{-2})	E (keV)	σ (keV)	χ^2/dof
	E	-	$1.88^{+0.05}_{-0.05}$	>411	$0.73^{+0.19}_{-0.17}$	$1.39^{+0.10}_{-0.10}$	$6.31^{+0.06}_{-0.06}$	0.1*	714/788
	F	-	$1.82^{+0.05}_{-0.05}$	>406	$0.55^{+0.18}_{-0.16}$	$1.20^{+0.09}_{-0.09}$	$6.34^{+0.05}_{-0.05}$	0.1*	625/715
	G	$6.43^{+0.92}_{-1.42}$	$1.92^{+0.01}_{-0.07}$	>571	$0.83^{+0.16}_{-0.15}$	$2.07^{+0.19}_{-0.25}$	$6.23^{+0.04}_{-0.04}$	0.1*	920/933
	H	$7.71^{+1.93}_{-1.95}$	$1.85^{+0.08}_{-0.08}$	>775	$0.45^{+0.20}_{-0.18}$	$1.2^{+0.18}_{-0.16}$	$6.28^{+0.07}_{-0.07}$	0.1*	577/593
	I	$8.52^{+4.30}_{-5.18}$	$1.70^{+0.04}_{-0.11}$	>126	$0.38^{+0.49}_{-0.34}$	$0.25^{+0.09}_{-0.09}$	$6.38^{+0.06}_{-0.06}$	0.1*	253/245
MR 2251−178	A	-	$1.65^{+0.05}_{-0.05}$	125^{+96}_{-39}	<0.07	$1.11^{+0.08}_{-0.08}$	-	-	569/599
	B	-	$1.72^{+0.05}_{-0.03}$	185^{+200}_{-69}	<0.11	$1.44^{+0.11}_{-0.06}$	-	-	647/631
	C	-	$1.76^{+0.07}_{-0.07}$	110^{+70}_{-32}	$0.29^{+0.22}_{-0.18}$	$1.39^{+0.15}_{-0.13}$	-	-	552/549
	D	-	$1.79^{+0.06}_{-0.06}$	193^{+417}_{-80}	$0.19^{+0.20}_{-0.17}$	$1.44^{+0.15}_{-0.13}$	$6.48^{+0.67}_{-0.31}$	0.1*	509/574
	E	$7.66^{+3.26}_{-3.02}$	$1.82^{+0.11}_{-0.10}$	>175	<0.23	$0.75^{+0.19}_{-0.14}$	-	-	446/398
NGC 5548	A	$6.06^{+1.58}_{-2.46}$	$1.75^{+0.02}_{-0.10}$	>345	$0.19^{+0.14}_{-0.11}$	$1.26^{+0.07}_{-0.23}$	$6.37^{+0.10}_{-0.10}$	0.1*	675/641
	B	$4.77^{+1.31}_{-2.05}$	$1.81^{+0.02}_{-0.08}$	>502	$0.35^{+0.16}_{-0.14}$	$1.25^{+0.15}_{-0.19}$	$6.32^{+0.09}_{-0.10}$	0.1*	588/632
	C	$5.61^{+2.34}_{-2.36}$	$1.62^{+0.10}_{-0.10}$	152^{+158}_{-54}	$0.28^{+0.11}_{-0.10}$	$0.79^{+0.18}_{-0.15}$	$6.32^{+0.04}_{-0.04}$	0.1*	834/809
	D	$4.46^{+2.13}_{-2.16}$	$1.79^{+0.09}_{-0.09}$	>170	$0.37^{+0.12}_{-0.11}$	$1.18^{+0.23}_{-0.20}$	$6.38^{+0.05}_{-0.05}$	0.1*	840/811
	E	$6.91^{+2.45}_{-2.47}$	$1.61^{+0.10}_{-0.11}$	160^{+178}_{-58}	$0.33^{+0.12}_{-0.10}$	$0.73^{+0.17}_{-0.14}$	$6.35^{+0.04}_{-0.04}$	0.1*	780/808
	F	$3.66^{+1.18}_{-2.10}$	$1.81^{+0.08}_{-0.09}$	>414	$0.42^{+0.14}_{-0.13}$	$1.03^{+0.30}_{-0.17}$	$6.31^{+0.05}_{-0.05}$	0.1*	652/690

TABLE 4.3: Best-fitted parameters of the Model *const* × *TBabs* × *zTBabs* × *(xillver/relxill/(relxill+xillver))* to the source spectra.

Source	Epoch	N_H^{INT} (10^{22} cm^{-2})	Γ	E_{cut} (keV)	R	$log\xi$	AF_e	β_1	$N_{xillver}$ (10^{-4})	$N_{relxill}$ (10^{-4})	χ^2/dof
1H 0419−577	A	$1.59^{+0.67}_{-0.66}$	$1.70^{+0.02}_{-0.03}$	72^{+9}_{-8}	$0.20^{+0.11}_{-0.10}$	-	-	-	$0.64^{+0.10}_{-0.13}$	-	739/733
	B	$1.04^{+0.72}_{-0.70}$	$1.66^{+0.02}_{-0.03}$	72^{+15}_{-8}	$0.13^{+0.11}_{-0.12}$	-	-	-	$0.74^{+0.58}_{-0.16}$	-	657/680
	C	<0.38	$1.59^{+0.02}_{-0.01}$	47^{+2}_{-2}	$0.25^{+0.06}_{-0.06}$	-	-	-	$0.70^{+0.06}_{-0.15}$	-	1173/1156
Mrk 915	A	$5.21^{+0.74}_{-0.74}$	$1.88^{+0.04}_{-0.03}$	>437	$0.46^{+0.17}_{-0.14}$	-	-	-	$0.75^{+0.10}_{-0.02}$	-	653/650
	B	$4.60^{+0.93}_{-0.90}$	$1.65^{+0.03}_{-0.04}$	70^{+15}_{-10}	$0.51^{+0.22}_{-0.21}$	-	-	-	$0.31^{+0.01}_{-0.01}$	-	544/543
	C	$5.84^{+1.13}_{-1.09}$	$1.67^{+0.03}_{-0.04}$	45^{+5}_{-4}	$1.01^{+0.39}_{-0.35}$	-	-	-	$0.21^{+0.07}_{-0.07}$	-	420/435
3C 111	A	$2.50^{+0.58}_{-0.57}$	$1.86^{+0.02}_{-0.02}$	>386	$0.11^{+0.10}_{-0.09}$	-	-	-	$3.81^{+0.11}_{-0.07}$	-	668/683
	B	$1.67^{+0.38}_{-0.39}$	$1.75^{+0.01}_{-0.01}$	133^{+26}_{-20}	$0.11^{+0.07}_{-0.06}$	-	-	-	$2.48^{+0.03}_{-0.01}$	-	974/949
	C	$2.45^{+0.45}_{-0.44}$	$1.72^{+0.02}_{-0.01}$	300^{+170}_{-77}	<0.15	-	-	-	$2.27^{+0.03}_{-0.03}$	-	959/899
NGC 3783	A	-	$1.76^{+0.06}_{-0.10}$	186^{+104}_{-63}	$0.78^{+0.35}_{-0.33}$	$2.75^{+0.31}_{-0.09}$	1.00*	$2.74^{+0.31}_{-0.34}$	$0.95^{+0.41}_{-0.45}$	$2.05^{+0.22}_{-0.28}$	1097/1038
	B	$3.72^{+0.93}_{-0.72}$	$1.95^{+0.03}_{-0.10}$	>363	$1.41^{+0.56}_{-0.43}$	$2.74^{+0.28}_{-0.17}$	1.00*	$3.45^{+0.89}_{-0.45}$	$1.90^{+0.50}_{-0.54}$	$1.83^{+0.23}_{-0.24}$	1033/1002
	C	$8.62^{+1.49}_{-1.12}$	$1.96^{+0.05}_{-0.07}$	>436	$1.49^{+0.85}_{-0.60}$	$2.77^{+0.31}_{-0.40}$	1.00*	$3.22^{+0.85}_{-0.48}$	$2.41^{+0.63}_{-0.71}$	$1.69^{+0.33}_{-0.34}$	937/792
	D	$6.64^{+1.17}_{-0.99}$	$1.94^{+0.05}_{-0.07}$	>441	$1.66^{+0.84}_{-0.59}$	$2.79^{+0.25}_{-0.30}$	1.00*	$3.37^{+0.68}_{-0.45}$	$2.20^{+0.59}_{-0.70}$	$1.91^{+0.37}_{-0.36}$	1048/913
NGC 7469	A	-	$1.94^{+0.02}_{-0.02}$	119^{+26}_{-20}	$0.77^{+0.20}_{-0.17}$	-	-	-	$1.57^{+0.03}_{-0.03}$	-	612/634
	B	-	$1.88^{+0.02}_{-0.02}$	301^{+239}_{-101}	$0.52^{+0.17}_{-0.16}$	-	-	-	$1.87^{+0.03}_{-0.04}$	-	622/630
	C	-	$1.93^{+0.02}_{-0.02}$	163^{+56}_{-33}	$0.93^{+0.20}_{-0.17}$	-	-	-	$1.35^{+0.03}_{-0.03}$	-	562/607
	D	-	$1.94^{+0.02}_{-0.02}$	>463	$0.54^{+0.14}_{-0.14}$	-	-	-	$1.94^{+0.05}_{-0.03}$	-	625/635

Continued

Table 4.3 – Following the previous page

Source	Epoch	N_H^{INT} (10^{22} cm^{-2})	Γ	E_{cut} (keV)	R	$log\xi$	AF_e	β_1	$N_{xillver}$ (10^{-4})	$N_{relxill}$ (10^{-4})	χ^2/dof
	E	-	$1.90^{+0.02}_{-0.02}$	365^{+402}_{-130}	$0.59^{+0.19}_{-0.16}$	-	-	-	$1.84^{+0.03}_{-0.03}$	-	672/620
	F	-	$1.89^{+0.02}_{-0.02}$	>407	$0.56^{+0.17}_{-0.16}$	-	-	-	$2.00^{+0.07}_{-0.04}$	-	599/606
	G	-	$1.88^{+0.02}_{-0.02}$	300^{+200}_{-88}	$0.46^{+0.14}_{-0.13}$	-	-	-	$2.04^{+0.03}_{-0.02}$	-	679/696
Mrk 110	A	-	$1.69^{+0.02}_{-0.02}$	94^{+13}_{-10}	$0.13^{+0.02}_{-0.02}$	$3.00^{+0.04}_{-0.03}$	>8.76	3.0*	-	$2.02^{+0.07}_{-0.06}$	1590/1474
	B	-	$1.72^{+0.03}_{-0.04}$	98^{+30}_{-18}	$0.24^{+0.10}_{-0.09}$	$2.91^{+0.32}_{-0.29}$	>6.44	3.0*	-	$1.43^{+0.10}_{-0.07}$	1027/1025
	C	-	$1.67^{+0.02}_{-0.04}$	112^{+33}_{-24}	$0.22^{+0.10}_{-0.07}$	$3.00^{+0.24}_{-0.29}$	>6.92	3.0*	-	$1.27^{+0.09}_{-0.08}$	1046/1006
UGC 06728	A	-	$1.61^{+0.12}_{-0.06}$	91^{+164}_{-43}	$0.36^{+0.51}_{-0.21}$	<3.07	1.00*	<2.58	-	$0.34^{+0.11}_{-0.07}$	188/197
	B	-	$1.65^{+0.10}_{-0.07}$	252^{+400}_{-88}	$0.54^{+0.34}_{-0.22}$	<3.52	1.00*	<2.69	-	$0.75^{+0.26}_{-0.32}$	718/707
NGC 4258	A	$9.73^{+1.43}_{-1.37}$	$1.56^{+0.05}_{-0.04}$	41^{+5}_{-6}	<0.65	-	-	-	$0.17^{+0.06}_{-0.05}$	-	255/277
	B	$11.17^{+1.18}_{-1.14}$	$1.60^{+0.10}_{-0.04}$	30^{+3}_{-3}	<0.83	-	-	-	$0.13^{+0.05}_{-0.05}$	-	439/408
KUG 1141+371	A	$1.23^{+0.80}_{-0.78}$	$1.91^{+0.03}_{-0.04}$	133^{+64}_{-34}	$0.39^{+0.21}_{-0.19}$	-	-	-	$0.63^{+0.10}_{-0.07}$	-	430/485
	B	$2.69^{+1.33}_{-1.29}$	$1.81^{+0.05}_{-0.05}$	>171	<0.45	-	-	-	$0.66^{+0.24}_{-0.28}$	-	239/247
MCG-06-30-15	A	-	$1.99^{+0.13}_{-0.09}$	>183	$1.76^{+2.58}_{-0.49}$	$3.09^{+0.17}_{-0.18}$	$1.01^{+1.22}_{-0.34}$	$2.83^{+0.28}_{-0.15}$	-	$1.46^{+0.53}_{-0.73}$	647/732
	B	-	$2.06^{+0.02}_{-0.03}$	135^{+20}_{-11}	$1.26^{+0.14}_{-0.13}$	$1.70^{+0.11}_{-0.18}$	$2.89^{+0.58}_{-0.36}$	$2.42^{+0.17}_{-0.12}$	-	$2.42^{+0.03}_{-0.07}$	1416/1371
	C	-	$1.91^{+0.11}_{-0.10}$	114^{+114}_{-30}	$1.55^{+0.49}_{-0.50}$	<2.56	$3.56^{+2.79}_{-1.47}$	$2.52^{+0.45}_{-0.34}$	-	$1.39^{+0.14}_{-0.10}$	705/740
NGC 5506	A	$4.07^{+0.87}_{-0.86}$	$1.83^{+0.09}_{-0.07}$	>143	$0.30^{+0.20}_{-0.16}$	$3.00^{+0.37}_{-0.21}$	$1.28^{+1.02}_{-0.39}$	$2.02^{+0.64}_{-0.65}$	$2.13^{+1.03}_{-1.03}$	$3.55^{+0.45}_{-0.82}$	1240/1228

Continued

Table 4.3 – Following the previous page

Source	Epoch	N_H^{INT} (10^{22} cm^{-2})	Γ	E_{cut} (keV)	R	$log\xi$	AF_e	β_1	$N_{xillver}$ (10^{-4})	$N_{relxill}$ (10^{-4})	χ^2/dof
	B	$0.72^{+1.57}_{-0.68}$	$1.50^{+0.19}_{-0.06}$	81^{+78}_{-10}	$0.66^{+0.10}_{-0.09}$	$2.75^{+0.34}_{-0.29}$	$5.00^{+2.02}_{-2.07}$	$3.31^{+0.21}_{-0.23}$	$0.68^{+0.60}_{-0.14}$	$2.42^{+0.16}_{-0.12}$	1263/1310
	C	<1.94	$1.54^{+0.14}_{-0.11}$	90^{+62}_{-21}	$0.64^{+0.11}_{-0.08}$	$3.00^{+0.10}_{-0.14}$	$5.00^{+4.38}_{-1.55}$	$3.08^{+0.25}_{-0.24}$	$0.56^{+0.35}_{-0.21}$	$3.47^{+0.28}_{-0.25}$	1220/1293
MCG+08-11-011	A	-	$1.83^{+0.01}_{-0.01}$	153^{+15}_{-13}	$0.40^{+0.06}_{-0.05}$	-	-	-	$2.91^{+0.02}_{-0.02}$	-	1368/1316
	B	-	$1.76^{+0.02}_{-0.02}$	88^{+10}_{-9}	$0.63^{+0.15}_{-0.13}$	-	-	-	$2.18^{+0.03}_{-0.03}$	-	781/745
GRS 1734-292	A	$1.43^{+0.45}_{-0.43}$	$1.66^{+0.02}_{-0.02}$	60^{+5}_{-4}	$0.27^{+0.08}_{-0.09}$	-	-	-	$3.46^{+0.08}_{-0.04}$	-	948/865
	B	$2.97^{+0.43}_{-0.47}$	$1.68^{+0.02}_{-0.01}$	87^{+9}_{-5}	$0.27^{+0.11}_{-0.06}$	-	-	-	$3.00^{+0.05}_{-0.08}$	-	825/856
Mrk 926	A	-	$1.75^{+0.01}_{-0.01}$	164^{+17}_{-15}	$0.13^{+0.04}_{-0.04}$	-	-	-	$3.37^{+0.02}_{-0.03}$	-	1519/1468
	B	-	$1.70^{+0.03}_{-0.03}$	136^{+74}_{-36}	<0.44	-	-	-	$1.18^{+0.14}_{-0.04}$	-	475/494
Mrk 841	A	-	$1.80^{+0.03}_{-0.03}$	134^{+60}_{-34}	$0.40^{+0.23}_{-0.19}$	-	-	-	$0.93^{+0.02}_{-0.02}$	-	477/507
	B	-	$1.81^{+0.02}_{-0.02}$	120^{+25}_{-20}	$0.56^{+0.16}_{-0.14}$	-	-	-	$0.81^{+0.01}_{-0.01}$	-	736/744
NGC 5273	A	-	$1.50^{+0.06}_{-0.05}$	71^{+29}_{-17}	$1.06^{+0.35}_{-0.29}$	2.00*	>7.31	$2.78^{+0.26}_{-0.28}$	-	$0.86^{+0.09}_{-0.13}$	594/574
	B	-	$1.23^{+0.07}_{-0.05}$	43^{+14}_{-8}	$0.73^{+0.34}_{-0.21}$	2.00*	>5.35	$2.46^{+0.40}_{-0.73}$	-	$0.80^{+0.09}_{-0.08}$	466/506
NGC 0985	A	$7.65^{+1.56}_{-1.53}$	$1.90^{+0.05}_{-0.04}$	>139	$0.60^{+0.38}_{-0.31}$	-	-	-	$0.70^{+0.03}_{-0.03}$	-	303/267
	B	-	$1.85^{+0.03}_{-0.03}$	184^{+150}_{-58}	$0.54^{+0.27}_{-0.23}$	-	-	-	$0.86^{+0.02}_{-0.02}$	-	390/466
HE 1143−1810	A	$1.00^{+0.77}_{-0.77}$	$1.73^{+0.03}_{-0.03}$	77^{+18}_{-12}	$0.25^{+0.17}_{-0.15}$	-	-	-	$1.07^{+0.09}_{-0.03}$	-	491/506
	B	$2.54^{+0.84}_{-0.81}$	$1.85^{+0.03}_{-0.04}$	141^{+71}_{-33}	$0.42^{+0.21}_{-0.19}$	-	-	-	$1.18^{+0.03}_{-0.02}$	-	469/486

Continued

Table 4.3 – Following the previous page

Source	Epoch	N_H^{INT} (10^{22} cm^{-2})	Γ	E_{cut} (keV)	R	$log\xi$	AF_e	β_1	$N_{xillver}$ (10^{-4})	$N_{relxill}$ (10^{-4})	χ^2/dof
	C	-	$1.77^{+0.02}_{-0.02}$	104^{+24}_{-17}	$0.33^{+0.15}_{-0.14}$	-	-	-	$1.37^{+0.02}_{-0.02}$	-	530/597
	D	$1.85^{+0.71}_{-0.68}$	$1.85^{+0.02}_{-0.02}$	175^{+91}_{-45}	$0.27^{+0.16}_{-0.14}$	-	-	-	$1.56^{+0.03}_{-0.03}$	-	590/561
	E	$1.44^{+0.68}_{-0.67}$	$1.82^{+0.03}_{-0.02}$	155^{+81}_{-36}	$0.20^{+0.15}_{-0.12}$	-	-	-	$1.48^{+0.03}_{-0.03}$	-	590/568
NGC 3227	A	-	$1.69^{+0.01}_{-0.01}$	127^{+14}_{-12}	$0.86^{+0.12}_{-0.12}$	-	-	-	$1.98^{+0.02}_{-0.03}$	-	868/826
	B	-	$1.69^{+0.01}_{-0.01}$	92^{+10}_{-8}	$1.09^{+0.17}_{-0.16}$	-	-	-	$1.46^{+0.02}_{-0.05}$	-	728/706
	C	-	$1.77^{+0.02}_{-0.01}$	204^{+46}_{-34}	$0.85^{+0.14}_{-0.13}$	-	-	-	$2.01^{+0.03}_{-0.03}$	-	785/704
	D	-	$1.83^{+0.01}_{-0.01}$	>439	$0.76^{+0.14}_{-0.12}$	-	-	-	$2.98^{+0.04}_{-0.04}$	-	837/777
	E	-	$1.80^{+0.01}_{-0.01}$	378^{+152}_{-91}	$0.61^{+0.12}_{-0.09}$	-	-	-	$2.97^{+0.03}_{-0.03}$	-	735/790
	F	-	$1.79^{+0.01}_{-0.01}$	326^{+123}_{-78}	$0.71^{+0.14}_{-0.11}$	-	-	-	$2.75^{+0.04}_{-0.04}$	-	627/717
	G	$4.73^{+0.57}_{-0.56}$	$1.77^{+0.01}_{-0.01}$	248^{+67}_{-34}	$0.68^{+0.08}_{-0.08}$	-	-	-	$3.73^{+0.04}_{-0.04}$	-	976/935
	H	$8.58^{+0.98}_{-1.08}$	$1.87^{+0.02}_{-0.02}$	>510	$0.64^{+0.16}_{-0.14}$	-	-	-	$2.72^{+0.03}_{-0.04}$	-	579/595
	I	$12.12^{+1.86}_{-1.82}$	$1.91^{+0.03}_{-0.03}$	>198	$1.36^{+0.47}_{-0.40}$	-	-	-	$0.68^{+0.03}_{-0.03}$	-	260/247
MR 2251−178	A	-	$1.65^{+0.02}_{-0.02}$	124^{+22}_{-18}	<0.10	-	-	-	$2.92^{+0.02}_{-0.04}$	-	569/599
	B	-	$1.72^{+0.02}_{-0.02}$	169^{+45}_{-30}	<0.16	-	-	-	$3.54^{+0.03}_{-0.05}$	-	647/631
	C	-	$1.70^{+0.02}_{-0.02}$	103^{+18}_{-14}	$0.17^{+0.14}_{-0.13}$	-	-	-	$2.79^{+0.05}_{-0.05}$	-	556/549
	D	-	$1.77^{+0.02}_{-0.02}$	163^{+46}_{-30}	$0.22^{+0.15}_{-0.13}$	-	-	-	$3.05^{+0.02}_{-0.05}$	-	510/576
	E	$7.56^{+1.69}_{-1.38}$	$1.82^{+0.02}_{-0.03}$	>366	<0.11	-	-	-	$2.10^{+0.03}_{-0.52}$	-	447/398
NGC 5548	A	$6.47^{+0.98}_{-0.91}$	$1.75^{+0.02}_{-0.02}$	>487	$0.25^{+0.08}_{-0.08}$	-	-	-	$4.35^{+0.10}_{-0.06}$	-	677/643

Continued

Table 4.3 – Following the previous page

Source	Epoch	N_H^{INT} (10^{22} cm^{-2})	Γ	E_{cut} (keV)	R	$log\xi$	AF_e	β_1	$N_{xillver}$ (10^{-4})	$N_{relxill}$ (10^{-4})	χ^2/dof
	B	$4.83^{+0.95}_{-0.91}$	$1.78^{+0.02}_{-0.04}$	>480	$0.36^{+0.10}_{-0.09}$	-	-	-	$3.61^{+0.47}_{-0.14}$	-	595/634
	C	$7.13^{+0.73}_{-0.73}$	$1.68^{+0.02}_{-0.01}$	129^{+15}_{-13}	$0.49^{+0.09}_{-0.08}$	-	-	-	$2.20^{+0.03}_{-0.03}$	-	851/811
	D	$4.52^{+0.69}_{-0.67}$	$1.77^{+0.01}_{-0.01}$	179^{+40}_{-23}	$0.49^{+0.08}_{-0.08}$	-	-	-	$2.47^{+0.03}_{-0.03}$	-	849/813
	E	$8.16^{+0.76}_{-0.75}$	$1.66^{+0.01}_{-0.02}$	133^{+15}_{-13}	$0.51^{+0.09}_{-0.08}$	-	-	-	$2.07^{+0.04}_{-0.04}$	-	792/810
	F	$4.25^{+0.83}_{-0.81}$	$1.81^{+0.01}_{-0.01}$	>395	$0.54^{+0.11}_{-0.10}$	-	-	-	$2.70^{+0.04}_{-0.04}$	-	666/692

TABLE 4.4: Best-fitted parameters of the Model *const* × *TBabs* × *zTBabs* × *(xillverCP/relxillCP/xillverCP+relxillCP)* to the source spectra.

Source	Epoch	N_H^{INT} (10^{22} cm^{-2})	Γ	kT_e (keV)	R	$log\xi$	AF_e	β_1	$N_{xillverCP}$ (10^{-4})	$N_{relxillCP}$ (10^{-4})	χ^2/dof
1H 0419−577	A	$2.61^{+0.68}_{-0.66}$	$1.84^{+0.02}_{-0.02}$	18^{+5}_{-3}	$0.14^{+0.11}_{-0.10}$	-	-	-	$0.66^{+0.03}_{-0.01}$	-	736/733
	B	$2.34^{+0.72}_{-0.71}$	$1.82^{+0.02}_{-0.02}$	19^{+10}_{-4}	<0.17	-	-	-	$0.78^{+0.01}_{-0.01}$	-	659/680
	C	$1.89^{+0.36}_{-0.36}$	$1.82^{+0.01}_{-0.01}$	15^{+1}_{-1}	$0.16^{+0.06}_{-0.06}$	-	-	-	$0.79^{+0.07}_{-0.06}$	-	1180/1156
Mrk 915	A	$5.06^{+0.71}_{-0.71}$	$1.88^{+0.02}_{-0.01}$	>77	$0.46^{+0.17}_{-0.15}$	-	-	-	$0.62^{+0.10}_{-0.02}$	-	655/650
	B	$6.31^{+0.94}_{-0.92}$	$1.82^{+0.02}_{-0.01}$	30^{+124}_{-12}	$0.39^{+0.22}_{-0.17}$	-	-	-	$0.36^{+0.01}_{-0.01}$	-	549/543
	C	$8.00^{+1.10}_{-1.16}$	$1.90^{+0.03}_{-0.03}$	17^{+7}_{-3}	$0.89^{+0.53}_{-0.24}$	-	-	-	$0.25^{+0.01}_{-0.01}$	-	423/435
3C 111	A	$2.43^{+0.60}_{-0.55}$	$1.87^{+0.02}_{-0.02}$	>63	$0.12^{+0.10}_{-0.09}$	-	-	-	$3.13^{+0.51}_{-0.05}$	-	669/683
	B	$2.42^{+0.38}_{-0.39}$	$1.84^{+0.01}_{-0.01}$	40^{+47}_{-12}	$0.08^{+0.07}_{-0.06}$	-	-	-	$2.50^{+0.02}_{-0.02}$	-	981/949
	C	$2.93^{+0.45}_{-0.45}$	$1.77^{+0.02}_{-0.01}$	>50	<0.13	-	-	-	$2.29^{+0.51}_{-0.03}$	-	962/899
NGC 3783	A	-	$1.81^{+0.05}_{-0.04}$	65^{+107}_{-24}	$0.84^{+0.33}_{-0.25}$	$2.75^{+0.16}_{-0.08}$	1.00*	$2.67^{+0.36}_{-0.32}$	$0.62^{+0.39}_{-0.47}$	$2.01^{+0.20}_{-0.18}$	1108/1038
	B	$3.71^{+0.85}_{-0.78}$	$1.87^{+0.04}_{-0.04}$	>100	$1.16^{+0.46}_{-0.36}$	$2.88^{+0.24}_{-0.24}$	1.00*	$3.61^{+0.76}_{-0.60}$	$1.61^{+0.40}_{-0.48}$	$1.59^{+0.23}_{-0.23}$	1037/1002
	C	$8.88^{+1.53}_{-1.30}$	$1.90^{+0.05}_{-0.04}$	>99	$1.22^{+0.79}_{-0.52}$	$3.00^{+0.35}_{-0.32}$	1.00*	$3.56^{+0.71}_{-0.72}$	$2.16^{+0.47}_{-0.60}$	$1.44^{+0.27}_{-0.34}$	940/792
	D	$6.73^{+1.10}_{-1.07}$	$1.88^{+0.05}_{-0.05}$	>95	$1.38^{+0.71}_{-0.51}$	$2.97^{+0.24}_{-0.26}$	1.00*	$3.60^{+0.56}_{-0.59}$	$1.92^{+0.49}_{-0.57}$	$1.64^{+0.29}_{-0.33}$	1052/913
NGC 7469	A	-	$2.00^{+0.02}_{-0.02}$	43^{+42}_{-14}	$0.75^{+0.19}_{-0.18}$	-	-	-	$1.58^{+0.03}_{-0.03}$	-	615/634
	B	-	$1.91^{+0.02}_{-0.02}$	>45	$0.51^{+0.18}_{-0.15}$	-	-	-	$1.82^{+0.04}_{-0.03}$	-	624/630
	C	-	$1.98^{+0.02}_{-0.02}$	>38	$0.93^{+0.23}_{-0.21}$	-	-	-	$1.34^{+0.03}_{-0.03}$	-	565/607

Continued

Table 4.4 – Following the previous page

Source	Epoch	N_H^{INT} (10^{22} cm^{-2})	Γ	kT_e (keV)	R	$log\xi$	AF_e	β_1	$N_{xillverCP}$ (10^{-4})	$N_{relxillCP}$ (10^{-4})	χ^2/dof
	D	-	$1.94^{+0.02}_{-0.02}$	>84	$0.55^{+0.15}_{-0.14}$	-	-	-	$1.64^{+0.03}_{-0.03}$	-	627/635
	E	-	$1.92^{+0.02}_{-0.02}$	>60	$0.60^{+0.19}_{-0.17}$	-	-	-	$1.74^{+0.06}_{-0.03}$	-	674/620
	F	-	$1.89^{+0.02}_{-0.02}$	>81	$0.56^{+0.19}_{-0.16}$	-	-	-	$1.67^{+0.05}_{-0.04}$	-	601/606
	G	-	$1.90^{+0.02}_{-0.02}$	>53	$0.45^{+0.15}_{-0.13}$	-	-	-	$1.99^{+0.05}_{-0.03}$	-	682/696
Mrk 110	A	-	$1.81^{+0.01}_{-0.01}$	23^{+3}_{-2}	$0.10^{+0.03}_{-0.03}$	3.00*	>8.94	3.0*	-	$1.98^{+0.05}_{-0.05}$	1671/1475
	B	-	$1.81^{+0.02}_{-0.02}$	22^{+7}_{-4}	$0.16^{+0.08}_{-0.07}$	$3.10^{+0.30}_{-0.24}$	>7.85	3.0*	-	$1.37^{+0.08}_{-0.08}$	1041/1025
	C	-	$1.77^{+0.01}_{-0.03}$	25^{+9}_{-5}	$0.17^{+0.07}_{-0.08}$	$3.04^{+0.33}_{-0.20}$	>7.76	3.0*	-	$1.20^{+0.08}_{-0.08}$	1061/1006
UGC 06728	A	-	$1.73^{+0.07}_{-0.07}$	17^{+34}_{-5}	$0.33^{+0.41}_{-0.22}$	<3.34	1.00*	<3.98	-	$0.32^{+0.49}_{-0.43}$	188/197
	B	-	$1.70^{+0.07}_{-0.06}$	>23	$0.42^{+1.17}_{-0.17}$	$3.11^{+0.58}_{-0.75}$	1.00*	$2.30^{+0.47}_{-0.97}$	-	$0.67^{+0.20}_{-0.38}$	720/707
NGC 4258	A	$11.73^{+1.69}_{-1.40}$	$1.81^{+0.03}_{-0.03}$	13^{+7}_{-3}	<0.51	-	-	-	$0.20^{+0.18}_{-0.09}$	-	256/277
	B	$13.08^{+1.20}_{-1.15}$	$1.89^{+0.04}_{-0.03}$	9^{+2}_{-1}	<0.93	-	-	-	$0.15^{+0.06}_{-0.05}$	-	438/408
KUG 1141+371	A	$1.64^{+0.79}_{-0.79}$	$1.97^{+0.03}_{-0.03}$	>22	$0.37^{+0.21}_{-0.18}$	-	-	-	$0.64^{+0.16}_{-0.14}$	-	430/485
	B	$2.97^{+1.25}_{-1.38}$	$1.84^{+0.04}_{-0.05}$	>16	<0.44	-	-	-	$0.55^{+0.29}_{-0.37}$	-	239/247
MCG-06-30-15	A	-	$2.00^{+0.08}_{-0.07}$	>50	$1.69^{+2.13}_{-0.47}$	$3.10^{+0.17}_{-0.19}$	$1.01^{+1.47}_{-0.27}$	$2.86^{+0.29}_{-0.21}$	-	$1.43^{+0.43}_{-0.63}$	548/732
	B	-	$2.02^{+0.03}_{-0.03}$	>74	$1.03^{+0.15}_{-0.15}$	$2.84^{+0.09}_{-0.09}$	$3.34^{+0.89}_{-0.64}$	$2.94^{+0.15}_{-0.13}$	-	$2.18^{+0.10}_{-0.11}$	1444/1371
	C	-	$1.88^{+0.07}_{-0.04}$	28^{+59}_{-9}	$1.12^{+0.45}_{-0.22}$	<2.67	>3.05	$2.69^{+0.35}_{-0.47}$	-	$1.39^{+0.08}_{-0.08}$	707/740

Continued

Table 4.4 – Following the previous page

Source	Epoch	N_H^{INT} (10^{22} cm^{-2})	Γ	kT_e (keV)	R	$log\xi$	AF_e	β_1	$N_{xillverCP}$ (10^{-4})	$N_{relxillCP}$ (10^{-4})	χ^2/dof
NGC 5506	A	$4.03^{+0.54}_{-0.97}$	$1.83^{+0.04}_{-0.08}$	>42	$0.27^{+0.13}_{-0.12}$	$3.11^{+0.35}_{-0.24}$	$1.39^{+0.72}_{-0.37}$	$2.08^{+0.57}_{-0.61}$	$1.88^{+0.64}_{-0.64}$	$3.14^{+0.15}_{-0.52}$	1239/1228
	B	$2.50^{+0.68}_{-0.63}$	$1.75^{+0.07}_{-0.03}$	27^{+25}_{-5}	$0.63^{+0.12}_{-0.09}$	$2.43^{+0.35}_{-0.34}$	$4.97^{+2.01}_{-1.36}$	$2.78^{+0.30}_{-0.28}$	$0.58^{+0.36}_{-0.14}$	$2.69^{+0.15}_{-0.16}$	1254/1310
	C	$1.96^{+0.59}_{-0.73}$	$1.71^{+0.05}_{-0.05}$	25^{+19}_{-6}	$0.50^{+0.14}_{-0.08}$	$3.00^{+0.09}_{-0.17}$	$4.61^{+4.80}_{-1.48}$	$2.97^{+0.22}_{-0.24}$	$0.61^{+0.36}_{-0.24}$	$3.54^{+0.21}_{-0.18}$	1218/1293
MCG+08-11-011	A	-	$1.88^{+0.01}_{-0.01}$	57^{+29}_{-16}	$0.36^{+0.06}_{-0.05}$	-	-	-	$2.92^{+0.02}_{-0.02}$	-	1408/1316
	B	-	$1.85^{+0.01}_{-0.01}$	30^{+11}_{-7}	$0.53^{+0.16}_{-0.13}$	-	-	-	$2.30^{+0.03}_{-0.07}$	-	804/745
GRS 1734-292	A	$2.58^{+0.45}_{-0.44}$	$1.83^{+0.01}_{-0.01}$	17^{+2}_{-2}	$0.19^{+0.09}_{-0.08}$	-	-	-	$3.72^{+0.08}_{-0.05}$	-	948/865
	B	$3.75^{+0.46}_{-0.44}$	$1.81^{+0.01}_{-0.01}$	20^{+4}_{-2}	$0.24^{+0.08}_{-0.09}$	-	-	-	$2.98^{+0.05}_{-0.04}$	-	818/856
Mrk 926	A	-	$1.80^{+0.01}_{-0.01}$	45^{+39}_{-9}	<0.12	-	-	-	$3.27^{+0.02}_{-0.02}$	-	1558/1468
	B	-	$1.77^{+0.03}_{-0.03}$	>20	<0.35	-	-	-	$1.19^{+0.03}_{-0.03}$	-	478/494
Mrk 841	A	-	$1.86^{+0.03}_{-0.02}$	>20	$0.35^{+0.23}_{-0.18}$	-	-	-	$0.91^{+0.02}_{-0.02}$	-	479/507
	B	-	$1.88^{+0.02}_{-0.02}$	33^{+22}_{-11}	$0.52^{+0.17}_{-0.15}$	-	-	-	$0.80^{+0.01}_{-0.01}$	-	741/744
NGC 5273	A	-	$1.67^{+0.03}_{-0.03}$	17^{+5}_{-3}	$0.83^{+0.31}_{-0.25}$	2.00*	>7.94	$2.59^{+0.29}_{-0.34}$	-	$0.86^{+0.04}_{-0.06}$	606/574
	B	-	$1.55^{+0.03}_{-0.03}$	15^{+3}_{-3}	$0.76^{+0.51}_{-0.34}$	2.00*	$2.63^{+2.20}_{-1.39}$	$2.80^{+0.36}_{-0.40}$	-	$0.68^{+0.12}_{-0.12}$	487/506
NGC 0985	A	$7.65^{+1.51}_{-1.58}$	$1.93^{+0.04}_{-0.04}$	>23	$0.58^{+0.39}_{-0.30}$	-	-	-	$0.65^{+0.02}_{-0.02}$	-	302/267
	B	-	$1.89^{+0.03}_{-0.03}$	>28	$0.51^{+0.27}_{-0.23}$	-	-	-	$0.86^{+0.02}_{-0.02}$	-	391/466
HE 1143−1810	A	$1.87^{+0.78}_{-0.77}$	$1.86^{+0.02}_{-0.02}$	20^{+13}_{-4}	$0.20^{+0.17}_{-0.15}$	-	-	-	$1.11^{+0.02}_{-0.03}$	-	491/506

Continued

Table 4.4 – Following the previous page

Source	Epoch	N_H^{INT} (10^{22} cm^{-2})	Γ	kT_e (keV)	R	$log\xi$	AF_e	β_1	$N_{xillverCP}$ (10^{-4})	$N_{relxillCP}$ (10^{-4})	χ^2/dof
	B	$3.25^{+0.84}_{-0.82}$	$1.92^{+0.03}_{-0.03}$	>28	$0.39^{+0.21}_{-0.18}$	-	-	-	$1.23^{+0.13}_{-0.03}$	-	470/486
	C	-	$1.85^{+0.02}_{-0.02}$	27^{+19}_{-7}	$0.26^{+0.15}_{-0.13}$	-	-	-	$1.37^{+0.02}_{-0.02}$	-	534/597
	D	$2.26^{+0.71}_{-0.68}$	$1.91^{+0.03}_{-0.02}$	>28	$0.25^{+0.16}_{-0.14}$	-	-	-	$1.52^{+0.15}_{-0.04}$	-	591/561
	E	$1.82^{+0.68}_{-0.68}$	$1.88^{+0.02}_{-0.02}$	37^{+269}_{-15}	$0.18^{+0.15}_{-0.12}$	-	-	-	$1.42^{+0.01}_{-0.03}$	-	590/568
NGC 3227	A	-	$1.78^{+0.01}_{-0.01}$	33^{+9}_{-7}	$0.79+0.11_{-0.11}$		-	-	$1.94^{+0.02}_{-0.02}$	-	881/826
	B	-	$1.80^{+0.01}_{-0.01}$	28^{+9}_{-6}	$0.96^{+0.18}_{-0.10}$	-	-	-	$1.52^{+0.02}_{-0.02}$	-	746/706
	C	-	$1.83^{+0.01}_{-0.01}$	56^{+131}_{-18}	$0.83^{+0.15}_{-0.15}$	-	-	-	$1.89^{+0.03}_{-0.03}$	-	790/704
	D	-	$1.84^{+0.01}_{-0.01}$	>80	$0.78^{+0.13}_{-0.12}$	-	-	-	$2.56^{+0.02}_{-0.03}$	-	838/777
	E	-	$1.83^{+0.01}_{-0.01}$	>45	$0.62^{+0.11}_{-0.11}$	-	-	-	$2.55^{+0.03}_{-0.05}$	-	733/790
	F	-	$1.83^{+0.01}_{-0.01}$	>47	$0.71^{+0.14}_{-0.13}$	-	-	-	$2.50^{+0.04}_{-0.04}$	-	629/717
	G	$4.97^{+0.59}_{-0.55}$	$1.82^{+0.01}_{-0.01}$	50^{+39}_{-10}	$0.67^{+0.09}_{-0.10}$	-	-	-	$3.32^{+0.03}_{-0.07}$	-	970/935
	H	$8.17^{+0.99}_{-0.82}$	$1.87^{+0.02}_{-0.02}$	>85	$0.65^{+0.16}_{-0.15}$	-	-	-	$2.24^{+0.07}_{-0.05}$	-	581/595
	I	$12.21^{+1.73}_{-1.65}$	$1.91^{+0.04}_{-0.03}$	>36	$1.28^{+0.60}_{-0.30}$	-	-	-	$0.66^{+0.02}_{-0.02}$	-	261/247
MR 2251−178	A	-	$1.76^{+0.01}_{-0.01}$	25^{+26}_{-6}	<0.06	-	-	-	$2.68^{+0.02}_{-0.03}$	-	576/599
	B	-	$1.79^{+0.01}_{-0.01}$	35^{+149}_{-11}	<0.11	-	-	-	$3.26^{+0.03}_{-0.05}$	-	650/631
	C	-	$1.80^{+0.02}_{-0.01}$	21^{+8}_{-4}	<0.25	-	-	-	$2.66^{+0.04}_{-0.04}$	-	555/549
	D	-	$1.83^{+0.02}_{-0.01}$	35^{+67}_{-11}	$0.17^{+0.14}_{-0.13}$	-	-	-	$2.85^{+0.04}_{-0.04}$	-	511/576
	E	$7.54^{+1.42}_{-1.45}$	$1.83^{+0.02}_{-0.02}$	>32	<0.09	-	-	-	$1.71^{+0.02}_{-0.04}$	-	447/398

Continued

Table 4.4 – Following the previous page

Source	Epoch	N_H^{INT} (10^{22} cm^{-2})	Γ	kT_e (keV)	R	$log\xi$	AF_e	β_1	$N_{xillverCP}$ (10^{-4})	$N_{relxillCP}$ (10^{-4})	χ^2/dof
NGC 5548	A	$6.47^{+0.99}_{-0.91}$	$1.77^{+0.02}_{-0.02}$	>53	$0.25^{+0.08}_{-0.09}$	-	-	-	$3.46^{+0.05}_{-0.05}$	-	677/643
	B	$4.63^{+0.94}_{-0.92}$	$1.80^{+0.02}_{-0.03}$	>54	$0.35^{+0.11}_{-0.08}$	-	-	-	$2.95^{+0.34}_{-0.04}$	-	595/634
	C	$8.72^{+0.73}_{-0.74}$	$1.79^{+0.01}_{-0.01}$	39^{+14}_{-10}	$0.43^{+0.08}_{-0.08}$	-	-	-	$2.23^{+0.03}_{-0.03}$	-	855/811
	D	$5.66^{+0.69}_{-0.68}$	$1.85^{+0.01}_{-0.01}$	65^{+147}_{-24}	$0.46^{+0.09}_{-0.08}$	-	-	-	$2.46^{+0.03}_{-0.04}$	-	852/813
	E	$9.79^{+0.76}_{-0.75}$	$1.77^{+0.01}_{-0.01}$	38^{+12}_{-9}	$0.45^{+0.08}_{-0.08}$	-	-	-	$2.07^{+0.03}_{-0.03}$	-	795/810
	F	$4.30^{+0.87}_{-0.92}$	$1.84^{+0.01}_{-0.02}$	>65	$0.55^{+0.11}_{-0.11}$	-	-	-	$2.34^{+0.08}_{-0.03}$	-	667/692

TABLE 4.5: Calculated flux and τ.

Source	Epoch	Flux ($10^{-11} ergcm^{-2}s^{-1}$)	τ
MCG-08-11-011	A	$1.40^{+0.11}_{-0.01}$	1.68
	B	$1.26^{+0.02}_{-0.02}$	2.73
NGC 3227	A	$1.04^{+0.02}_{-0.01}$	2.74
	B	$0.86^{+0.01}_{-0.01}$	3.00
	C	$0.94^{+0.01}_{-0.02}$	1.80
	D	$1.11^{+0.01}_{-0.01}$	<1.36
	E	$1.15^{+0.01}_{-0.02}$	<2.10
	F	$1.13^{+0.01}_{-0.01}$	<2.04
	G	$1.55^{+0.01}_{-0.01}$	1.97
	H	$0.88^{+0.01}_{-0.01}$	<1.26
	I	$0.27^{+0.01}_{-0.01}$	<2.27

4.3 Notes on individual sources

Here, we discuss the findings of our spectral analysis from the physical models, const × TBabs × zTBabs × (xillver/relxill/relxill+xillver) (see Table 4.3) and const × TBabs × zTBabs × (xillverCP/relxillCP/relxillCP+xillverCP) (see Table 4.4) for E_{cut} and kT_e measurements respectively. We also make a comparison of the results obtained using these two models in this work with those in the literature if available.

4.3.1 1H 0419−577

This bright Seyfert 1 galaxy is known to have a low temperature corona based on the studies available in literature. The coronal properties of this source have been investigated by several authors using the observations carried out by *NuSTAR* in 2015 (indicated as epoch C in this work). Using *relxill* model, Turner et al. (2018) found $E_{cut} = 63^{+8}_{-9}$ keV. The same authors using *COMPTT* and *nthcomp* models found kT_e values of 15.1±0.8 keV and 13.4±1.0 keV respectively. Similarly, Akylas

& Georgantopoulos (2021) from modelling of the spectra using *pexmon* found a value of $E_{cut} = 54^{+4}_{-4}$ keV. Also, recently, Kang & Wang (2022) from modelling of the spectrum with *pexrav* found a value of $E_{cut} = 54^{+8}_{-6}$ keV. Similarly, from *relxillCP* model fits to the data, Kang & Wang (2022) found a value of kT_e = 16.0±1.0 keV.

In this work, we analysed three epochs of data, of which the results for epochs A and B are reported for the first time. For epoch C we found $E_{cut} = 51^{+9}_{-4}$ keV and 47^{+2}_{-2} keV from *pexrav* and *xillver* fit. From Comptonization model fit to the observations, we found kT_e = 15.0±1.0 keV. Thus for epoch C we are in agreement with that of Turner et al. (2018) and Kang & Wang (2022). For the other two epochs too, we obtained low values for E_{cut} and kT_e. The values of kT_e obtained for the three epochs are in agreement within errors, and thus we did not find variation in kT_e .

4.3.2 Mrk 915

Mrk 915 was observed three times in December 2014. Of these three epochs, the data from epoch A has been analysed earlier by Hinkle & Mushotzky (2021) and Kang & Wang (2022). By jointly fitting *NuSTAR* and *XMM-Newton* observations, Hinkle & Mushotzky (2021) reported a E_{cut} of $57.9^{+11.2}_{-7.4}$ keV. From analysis of *NuSTAR* data, Kang & Wang (2022) obtained a value of $kT_e > 69$ keV. In our analysis too, we obtained a lower limit of 77 keV for kT_e. For epochs B and C, we obtained values of $kT_e = 30^{+124}_{-12}$ keV and 17^{+7}_{-3} keV respectively. Of the three epochs of data, analysis of data from epochs B and C are reported for the first time. Due to large error bars, variation of kT_e if any could not be detected in this source.

TABLE 4.6: Results of the correlation analysis between different parameters for NGC 3227. Provided are the slope (m), intercept (c), PCC (r), and the NHPNC (p) from the OLS fit and the LLS fit from simulated points.

Parameter	OLS				Simulated			
	m	c	r	p	m	c	r	p
Γ/Flux	-0.07±0.03	1.90±0.03	-0.63	0.07	-0.07±0.03	1.91±0.04	-0.64	0.06
kT_e/Flux	18±28	22±31	0.42	0.58	18±150	13±169	0.08	0.52
Γ/kT_e	0.001±0.0006	1.75±0.03	0.86	0.14	0.0005±0.0002	1.78±0.02	0.80	0.20
R/Flux	-0.51±0.13	1.31±0.13	-0.84	0.01	-0.04±0.15	0.78±0.16	-0.09	0.68
τ/kT_e	-0.043±0.002	4.19±0.09	-0.99	0.00	-0.02±0.00	3.44±0.28	-0.97	0.03

4.3.3 3C 111

3C 111 was observed by *NuSTAR* for three epochs, twice in the year 2017 (epochs A and B in this work) and once in the year 2019 (epoch C in this work). The data from epochs A and B were analysed earlier by Kang et al. (2020). who found $E_{cut} > 228$ keV in epoch A and $E_{cut} = 165^{+202}_{-47}$ keV in epoch B. Using *INTEGRAL* data Malizia et al. (2014) obtained a value of $E_{cut} = 136^{+47}_{-29}$ keV for this source. On analysis of the observations obtained in epoch B, Kang & Wang (2022) obtained values of $E_{cut} = 174^{+166}_{-57}$ keV and $kT_e > 35$ keV respectively. Recently, Akylas & Georgantopoulos (2021) performed a spectral fit to the observations in epoch C and obtained $E_{cut} = 148^{+102}_{-43}$ keV. Our results on this source are in agreement with the values available in the literature. Of the three epochs, we obtained lower limits to kT_e of 63 keV and 50 keV for epochs A and C, while for epoch B we obtained a kT_e of 40^{+47}_{-12} keV. We thus conclude that we could not find variation in kT_e in 3C 111.

4.3.4 NGC 3783

This Seyfert type AGN is known for the variable line of sight column density (Mao et al. 2019). It was observed by *NuSTAR* four times between August and December 2016, and we analysed all the observations. Using *INTEGRAL* data Malizia et al. (2014) reported $E_{cut} = 98^{+79}_{-34}$ keV. On analysis of epoch A data, Kang & Wang (2022) found $kT_e > 150$ keV. In this work, we found lower limits to kT_e in epochs B, C and D, while in epoch A we obtained $kT_e = 65^{+107}_{-24}$ keV. As kT_e could not be constrained for three epochs, variation of kT_e if any could not be ascertained in this source.

4.3.5 NGC 7469

We have seven epochs of data from *NuSTAR* observed between June and December, 2015. Of these, using the data for epoch D as reported in this work , Akylas & Georgantopoulos (2021) obtained a value of $E_{cut} > 244$ keV. From our analysis of epoch D data in this work we obtained a lower limt of $E_{cut} > 463$ keV. From joint fitting of the *NuSTAR* and *XMM-Newton* observations in epoch G, Hinkle & Mushotzky (2021) obtained a value of $E_{cut} = 112.8^{+32.8}_{-21.9}$ keV. Using only *NuSTAR* data for the same epoch, Kang & Wang (2022) measured a lower limit of $E_{cut} > 262$ keV. For the same epoch the authors found $kT_e > 77$ keV. Using *BeppoSAX* data Dadina (2007) reported $E_{cut} = 211^{+235}_{-95}$ keV. Though the source was observed seven times by *NuSTAR*, results on only two epochs of observations (epochs D and G) are available in literature. Our analysis of all the seven epochs of data in a homogeneous manner could yield only lower limits to kT_e, except for epoch A, where we found a value of $kT_e = 43^{+42}_{-14}$ keV.

4.3.6 Mrk 110

Mrk 110 was observed three times between 2017 and 2020 by *NuSTAR*. Ezhikode et al. (2020) analysed the epoch A *NuSTAR* spectrum to model the reflection features of the spectrum. The authors reported $E_{cut} = 219.30^{+437.39}_{-112.36}$ keV and $E_{cut} = 219.30^{+412.27}_{-113.95}$ keV for the choice of black hole spin = 0 and 0.998 respectively. From an analysis of epoch A spectrum Akylas & Georgantopoulos (2021) estimated $E_{cut} = 93^{+13}_{-10}$ keV, while Kang & Wang (2022) reported $E_{cut} = 160^{+35}_{-24}$ keV by fitting the same *NuSTAR* spectrum. The authors also found $kT_e = 57^{+54}_{-18}$ keV. All the epochs were analysed recently by Porquet et al. (2021). The author did a broad band X-ray spectral analysis using the simultaneous *XMM-Newton* and *NuSTAR* data. From modelling the source spectra with *relxill* for epochs A, B and C respectively the authors reported $E_{cut} = 117^{+12}_{-17}$ keV, 113^{+28}_{-21} keV and 126^{+35}_{-26} keV. Using the Comptonization model *relxillCP*, the authors obtained $kT_e = 26^{+4}_{-3}$ keV, 26^{+8}_{-5} keV and 26^{+8}_{-5} keV. Our results on kT_e for the three epochs agree with that reported by Porquet et al. (2021).

4.3.7 UGC 06728

UGC 06728 was observed twice by *NuSTAR* between July, 2016 and October, 2017. From an analysis of the data acquired in the year 2017,Akylas & Georgantopoulos (2021) obtained a value of $E_{cut} = 152^{+131}_{-50}$ keV. For the same data set Kang & Wang (2022) obtained E_{cut} values of 230^{+933}_{-108} keV and 183^{+452}_{-62} keV respectively, from fitting two different models to the observations. The same authors using *relxillCP* model fit to the data obtained a lower limit of $kT_e > 26$ keV. Our analysis too yeilded a value of $kT_e > 23$ keV for epoch B. For epoch A, we obtained a value of $kT_e = 17^{+34}_{-5}$keV. Of the two epochs of data available on this source,

we could constrain kT_e only for epoch A, and therefore, the variable nature of the temperature of the corona, if any, could not be established.

4.3.8 NGC 4258

We have *NuSTAR* observations for this source on two epochs observed between November 2015 and January 2016. The findings of the analysis are presented for the first time here. Vasudevan et al. (2013) reported a lower limit of $E_{cut} > 282$ keV using *XMM-Newton* data for this source. We obtained values of $E_{cut} = 41^{+5}_{-6}$ keV and 30^{+3}_{-3} keV respectively for epochs A and B. There is thus an indication of E_{cut} variation in this source. However, from *xillverCP* model fit to both the epochs of observations we found kT_e of 13^{+7}_{-3} keV and 9^{+2}_{-1} keV respectively. Thus, considering the errors, we conclude the temperature of the corona of the source to be non-variable between November 2015 and January 2016.

4.3.9 KUG 1141+371

This source was observed twice by *NuSTAR*, once in December 2019 (epoch A) and again in May 2020 (epoch B). From model fits to the data, we found lower limits of $kT_e > 22$ keV and > 16 keV for epochs A and B respectively. Vasudevan et al. (2013) reported a E_{cut} of $263^{+\infty}_{-212}$ keV using *XMM-Newton* data. From an analysis of the epoch A data, Akylas & Georgantopoulos (2021) obtained $E_{cut} > 79$ keV. From our analysis, while we found a value of $E_{cut} = 133^{+64}_{-34}$ keV for epoch A, and a lower limit for epoch B.

4.3.10 MCG-06-30-15

This source has been studied extensively using *INTEGRAL*, *BeppoSAX*, *Swift-XRT*, *XMM-Newton* and *NuSTAR* data to determine E_{cut}. Dadina (2007) reported a E_{cut} of 190^{+110}_{-66} keV from an analysis of *BeppoSAX* data. Using *INTEGRAL* spectra Malizia et al. (2014) reported $E_{cut} = 63^{+24}_{-15}$ keV for the source. Malizia et al. (2014) reported a $E_{cut} > 110$ keV. This source was observed by *NuSTAR* three times on 29 January 2013 (epoch A), 30 January 2013 (epoch B) and 02 February 2013 (epoch C). Of these three epochs, results are available in the literature on epoch B. Ezhikode et al. (2020) from the fitting of the epoch B spectrum with a combination of *relxill+xillver* model found $E_{cut} = 160.20^{+28.76}_{-18.26}$ keV for $a_* = 0.998$ and $E_{cut} = 149.73^{+31.15}_{-12.46}$ keV for $a_* = 0.0$. From the fitting of same epoch B *NuSTAR* data using *pexrav* and *relxill* Kang & Wang (2022) reported $E_{cut} > 707$ keV and $E_{cut} > 720$ keV respectively. The authors also estimated a lower limit for $kT_e > 280$ keV from the fit of *relxillCP* model. Our analysis of the epoch B *NuSTAR* spectrum yielded a E_{cut} of 135^{+20}_{-11} keV. We obtained $kT_e = 28^{+59}_{-9}$ keV for epoch C, while we obtained lower limits of 50 keV and 74 keV for epochs A and B respectively. Thus, from our analysis, in MCG-06-30-15, we did not discover clear proof of a change in the coronal temperature.

4.3.11 NGC 5506

NuSTAR has observed this source three times on April 2014 (epoch A), December 2019 (epoch B) and February 2020 (epoch C). From joint fit of the epoch A with *Swift XRT*, Matt et al. (2015) found a large $E_{cut} = 720^{+130}_{-190}$ keV. From a reanalysis of the same data set, Tortosa et al. (2018) found $kT_e = 400 \pm 200$ keV. Vasudevan et al. (2013) also obtained a relatively lower value of $E_{cut} = 166^{+107}_{-30}$ keV. Baloković et al. (2020) reported rather lower value of $E_{cut} = 110 \pm 10$ keV. Thus, there are

discrepant results available in the literature on this source. From our analysis, we could constrain both E_{cut} and kT_e on all three epochs, however, we found no variation in the temperature of the corona.

4.3.12 MCG+08-11-011

We have two epochs of observations between August 2016 and December 2021. Using the *INTEGRAL* data Malizia et al. (2014) reported a E_{cut} of 171^{+44}_{-30} keV. Of the two epochs of *NuSTAR* observations, results based on the observations carried out in August 2016 (epoch A) are available in the literature, while analysis of observations acquired in December 2021 (epoch B) has been carried out for the first time. Molina et al. (2019) from joint spectral fit of *Swift XRT* and epoch A data from *NuSTAR* obtained a value of $E_{cut} = 163^{+53}_{-32}$ keV. Similarly, from spectral analysis of the *NuSTAR* data of epoch A, Akylas & Georgantopoulos (2021) found $E_{cut} = 140^{+29}_{-21}$ keV. Analyzing the same epoch of *NuSTAR* observation Tortosa et al. (2018) reported $E_{cut} = 175^{+110}_{-50}$ keV. The authors also found $E_{cut} = 57^{+60}_{-30}$ keV from fitting the source spectrum using *nthcomp*. From our analysis, we found variation in our derived values of both E_{cut} and kT_e between the two epochs. We thus conclude that we have detected kT_e variation in this source at the 90% confidence level.

4.3.13 GRS 1734-292

We have two epochs of observations, namely epoch A in September 2014 and epoch B in May 2018. Of these, results based on epoch A data are available in the literature. From joint analysis of *INTEGRAL*, *XMM* and *BAT* data, Malizia et al. (2014) obtained a value of $E_{cut} = 58^{+24}_{-7}$ keV. From a broadband analysis of

XMM-Newton and *NuSTAR* data obtained during epoch A, Tortosa et al. (2017) found a value of $E_{cut} = 53^{+11}_{-8}$ keV and $kT_e = 11.9^{+1.2}_{-0.9}$ keV. Similarly, from the spectral analysis of *Swift XRT* and epoch A *NuSTAR* data, Molina et al. (2019) obtained a value of $E_{cut} = 53^{+13}_{-9}$ keV. Using only *NuSTAR* data of epoch A, we obtained a value of $E_{cut} = 60^{+5}_{-4}$ keV, which agrees with the value obtained by Tortosa et al. (2017) and Molina et al. (2019). For epoch B, we obtained a value of $E_{cut} = 87^{+9}_{-5}$ keV. There is an indication of variation in E_{cut}, between epochs A and B. However, for epochs A and B, we obtained kT_e of 17^{+2}_{-2} keV and 20^{+4}_{-2} keV respectively, arguing for no coronal temperature variation between the two epochs.

4.3.14 Mrk 926

NuSTAR observed this source two times in November 2016 (epoch A) and July 2021 (epoch B). Hinkle & Mushotzky (2021), from analysis of epoch A *NuSTAR* spectrum reported $E_{cut} = 172.8^{+36.2}_{-26.4}$ keV, while, Kang & Wang (2022) found $E_{cut} = 323^{+241}_{-96}$ keV and $E_{cut} = 292^{+178}_{-87}$ keV from *pexrav* and *relxill* model fit to the epoch A spectrum. The authors also reported a $kT_e > 83$ keV. From an analysis of simultaneous *NuSTAR* epoch A spectra and *XMM-Newton* data Kamraj et al. (2022) reported $E_{cut} = 432^{+435}_{-144}$ keV and $kT_e = 10.01^{+0.15}_{-0.07}$ keV. For epoch A, we obtained a value of $kT_e = 45^{+39}_{-9}$ keV, while for epoch B, we obtained a lower limit of $kT_e > 20$ keV. Results on the analysis of *NuSTAR* data for epoch B are reported for the first time.

4.3.15 Mrk 841

Between 2015 and 2022, Mrk 841 was observed two times by *NuSTAR*. Of these two epochs, results on the analysis of the epoch A spectrum are available in the literature (Kamraj et al. 2018; Akylas & Georgantopoulos 2021; Hinkle & Mushotzky 2021; Kang & Wang 2022; Kamraj et al. 2022), however, results based on the spectrum obtained in epoch B are reported for the first time. For epoch A we found a lower limit to kT_e of 20 keV, while, for epoch B we obtained $kT_e = 33^{+22}_{-11}$ keV. Kang & Wang (2022) too reported a lower limit of $kT_e > 44$ keV during epoch A.

4.3.16 NGC 5273

This source was observed by *NuSTAR* twice, namely July 2014 (epoch A) and July 2022 (epoch B). Of the two data available on this source, epoch A data have been analysed by various authors, while results on epoch B are reported for the first time. Using *NuSTAR* and *Swift/XRT* together for epoch A, Pahari et al. (2017) found $E_{cut} = 143^{+96}_{-40}$ keV and $kT_e = 57^{+18}_{-11}$ keV. For the same data set, Akylas & Georgantopoulos (2021) estimated a value of $E_{cut} = 115^{+91}_{-37}$ keV. Recently, from an analysis of *NuSTAR* and *Swift* spectra jointly, Kamraj et al. (2022) reported a value of $E_{cut} > 220$ keV and $kT_e = 3.58^{+0.16}_{-0.28}$ keV. We found values of $kT_e = 17^{+5}_{-3}$ keV and 15^{+3}_{-3} keV for epoch A and B respectively.

4.3.17 NGC 0985

NuSTAR observed this source two times between 2012 and 2021. The epoch A FPMA/FPMB spectrum was obtained on August, 2013 and the epoch B spectrum was taken on September, 2021. The epoch B spectrum of this source is analysed

for the first time in this work. Previously, Kamraj et al. (2018) reported $E_{cut} > 121$ keV from an analysis of epoch A *NuSTAR* spectrum. For epochs A and B, we obtained lower limit of kT_e of 23 keV and 28 keV respectively.

4.3.18 HE 1143−1810

This source was observed by *NuSTAR* five times in 2017 jointly with *XMM-Newton*. All the observations were analysed by Ursini et al. (2020). From joint spectral fits to *NuSTAR* and *XMM-Newton data*, Ursini et al. (2020) found kT_e of 13^{+7}_{-3}, 13^{+6}_{-3}, 25^{+75}_{-8}, 20^{+80}_{-6} and 20^{+70}_{-6} keV respectively. From our analysis of only *NuSTAR* data we could obtain kT_e for epochs A (20^{+13}_{-4} keV), epoch C (27^{+19}_{-7} keV) and epoch E (37^{+269}_{-15} keV) respectively, while for epochs B and D we could obtain lower limits of kT_e of 28 keV. Our results for epochs A, C and E are in agreement with that of Ursini et al. (2020). Our results are consistent with no variation in kT_e in this source.

4.3.19 NGC 3227

NuSTAR observed this source nine times between November 2016 and December 2019. Of these, results for seven epochs were reported by Kang et al. (2021a), who were able to constrain E_{cut} in three epochs using phenomenological fits and kT_e in two epochs using physical model fits. Here, we report results for two additional epochs and for all nine epochs; we used both phenomenological and physical model fits to model the spectra. The lowest value of E_{cut} of 92^{+10}_{-8} keV was obtained in epoch B, the highest value of E_{cut} was observed in epoch E (378^{+152}_{-91} keV), and intermediate values of E_{cut} were obtained during other epochs. These observed variations in E_{cut} indicate that the coronal temperature of NGC 3227 must be

changing with time. The values of E_{cut} obtained during the first two epochs (A and B) are similar to the value of $E_{cut} = 90 \pm 20$ keV reported by Markowitz et al. (2009). Vasudevan et al. (2013) estimated E_{cut} to lie outside the BAT range at > 636 keV. Recently, Kang et al. (2021a) too reported E_{cut} values for epochs A, B, and G and lower limits for epochs C, D, E, and F from *pexrav* model fits. The values of E_{cut} obtained here using *xillver* for epochs A, B, and G are in agreement with those of Kang et al. (2021a) from the *pexrav* model. Also, our model fits were able to constrain E_{cut} during epochs E and F using *xillver*. Comptonization model fits using *xillverCP* provided values of kT_e that were also found to vary between epochs. We could constrain kT_e for epochs A, B, C, and G and obtain lower limits for epochs D, E, F, H, and I. Kang et al. (2021a), using the same model used here, was only able to constrain kT_e for epochs A and B. Our results for epochs A and B are in agreement with those of Kang et al. (2021a).

4.3.20 MR 2251−178

This source has five epochs of observations that are public and have exposures > 20 ks. In this work, we analysed all of them. To find evidence for the change in kT_e, if any, we carried out fitting of the observations with the physical model, *const*TBabs(xillverCP)*. An examination of the results of the fit shows that the kT_e obtained during all the epochs agree within errors. Though we could not find any signature of kT_e variation with epochs from the *xillverCP* fit, the E_{cut} values obtained from the *xillver* model fit during epochs A, C, and D agree within errors except that of epoch B. This could be due to the quality of the data in epoch B, as the values of E_{cut} and kT_e obtained during that epoch also have large error bars.

4.3.21 NGC 5548

NGC 5548 was observed by *NuSTAR* six times between July 2013 and January 2021. Of these, Zhang et al. (2018) reported results for five epochs. In this work, we carried out both phenomenological and physical model fits for all six epochs. From *xillver* model fits, we could only constrain E_{cut} for epochs C, D, and E, while Zhang et al. (2018) could constrain E_{cut} in the four epochs (A, C, D, and E). For epochs C and D, our values of E_{cut} are in agreement with those of Zhang et al. (2018), but the results do not match for epoch E. Though Zhang et al. (2018) claims to have detected E_{cut} variation in NGC 5548, our analysis could not confirm changes in E_{cut}. This could be due to differences in the choice of binning and the energy ranges used in each work. Ursini et al. (2015) obtained lower limits for E_{cut} in all the epochs except for epoch D. Using the simultaneous *XMM-Newton* and *NuSTAR* data from the 2013 campaign, Cappi et al. (2016) also fitted the 4−79 keV epoch A and B together, epoch D, and epoch E spectra using a cutoff power law and *pexmon*.

4.4 Summary

In this work, we carried out phenomenological and physical model fits to 72 epochs of data from *NuSTAR* on 21 sources. These were carried out to extract important spectral parameters of the sources, such as Γ, kT_e, reflection fraction etc. and investigate for variation in kT_e in these sources. We summarize the results below

1. From the Comptonization model fits to the data, we found that the S/N in the data is sufficient to constrain kT_e and E_{cut} in most of the sources. For a few epochs of observation, we obtained only lower limits.

2. On comparing our results on a few sources to their earlier results in the literature, we found that our results are, in general, consistent with that in the literature.

3. For a few sources, from the spectral analysis, we found variation in E_{cut}; however, variation of kT_e in them could not be confirmed except in NGC 3227 and MCG+08-11-011.

4. In NGC 3227, we found evidence for variation in kT_e. We found no correlation of kT_e, Γ, R, or τ with flux, while τ is found to anti-correlate with kT_e. This could be due to more than one physical process at work in the source causing the change in kT_e.

5. For MCG +08-11-011, we found variation of kT_e at the 90% confidence between two epochs separated by about five years. We also found the source to show a "hotter-when-brighter" and "softer-when-brighter" behaviour. Our observations tend to favour the scenario of change in the position or geometry of the corona leading to variation in the measured kT_e values.

This study has increased the number of sources with known kT_e variation to 11. Among the sources that show kT_e, variation, both "hotter-when-brighter" and "cooler-when-brighter" trend were observed. Thus the observed relation between the temperature of the corona and the source brightness is found to be different among sources. Therefore, it is imperative to find more sources that show variation in the temperature of the corona and it will allow us to explore better correlation of kT_e with various physical properties and provide the needed inputs to enhance our understanding of AGN corona.

Chapter 5

The Compton Thick AGN NGC 1068: Analysis of X-ray data [†]

In the earlier Chapters, we have concentrated on the determination of the temperature of the corona in the Seytfert 1 type of AGN (Chapter 3) and the variation in the temperature of the corona if any (Chapter 4). Here, we focus on a Seyfert 2 AGN, with the objective of characterising the nature of the corona of the source. NGC 1068 is one of the most studied Seyfert 2 galaxies. Situated at a $z = 0.0038$ (Huchra et al. 1999), it is powered by a black hole with $M_{BH} = 1.6 \times 10^7 M_{\odot}$ (Panessa et al. 2006). In X-rays the source is studied in the past (Matt et al. 2004; Bauer et al. 2015; Marinucci et al. 2016; Zaino et al. 2020). NGC 1068 was observed first by *Ginga* in the X-ray band, and that observation revealed the presence of a broad neutral Fe Kα line (Koyama et al. 1989) having an equivalent width of$\sim$1.3 keV. Later *ASCA* observations resolved the Fe lines into neutral and ionized components (Iwasawa et al. 1997). It is known as an emitter of high energy γ-ray radiation in the MeV$-$GeV range (Abdollahi et al. 2020) and also has been reported as a neutrino source (Aartsen et al. 2020). In the past, the hard X-ray

[†]The contents of this chapter are from Pal et al. 2022, MNRAS, 517, 3341

source spectrum was fitted with a two-reflector model (Matt et al. 1997; Guainazzi et al. 1999; Bauer et al. 2015). The central engine of the source is found to be completely obscured by the dusty torus with a column density of $N_H \geq 10^{25}$ cm^{-2} (Matt et al. 2000), therefore, the observer can only see the scattered emission along the line of sight. This scattered emission is commonly believed to be due to two types of reflectors, the "cold" reflector component that arises from Compton scattering off the primary X-ray emission from the neutral circumnuclear matter, while the second "warm" ionized reflector component that arises due to Compton scattering off the heavily ionized material that acts as the "mirror" of the primary emission (Matt et al. 2004).

From the multi-epoch X-ray data Bauer et al. (2015) modelled the data of NGC 1068 using the two reflector model along with different line emission, continuum emission and the off nuclear point source emission. By carrying out the joint fit to the observed *XMM-Newton* and *NuSTAR* high energy ($>$ 4 keV) spectra of NGC 1068 Marinucci et al. (2016) detected excess flux in August 2014 observation above 20 keV by 32$\pm$6 % relative to the observations in December 2012 and February 2015. The excess flux above 20 keV in NGC 1068 spectra was ascribed to a drop in the column density with $N_H > 8.5 \times 10^{24}$ cm^{-2} to (5.9$\pm$0.4) $\times$ 10^{24} cm^{-2} in 2012 spectra. The authors first caught the source during this unrevealing period in which the obscured matter moved from the line of sight, and the source was found to be in its highest flux state. Recently, Zaino et al. (2020) reported the spectral analysis results of the *NuSTAR* data taken between July 2017 and February 2018 to check for spectral variability. From the varying column density found in the timescale of 1 to 6 months, the authors inferred the presence of the clumpy torus structure surrounding the source. Using *Swift* $-$ *XRT* data the authors also detected an ultra-luminous X-ray source at a distance of $\sim$2 kpc from the nuclear region of NGC 1068.

Though the X-ray emission from NGC 1068 has been analysed in the past (Bauer

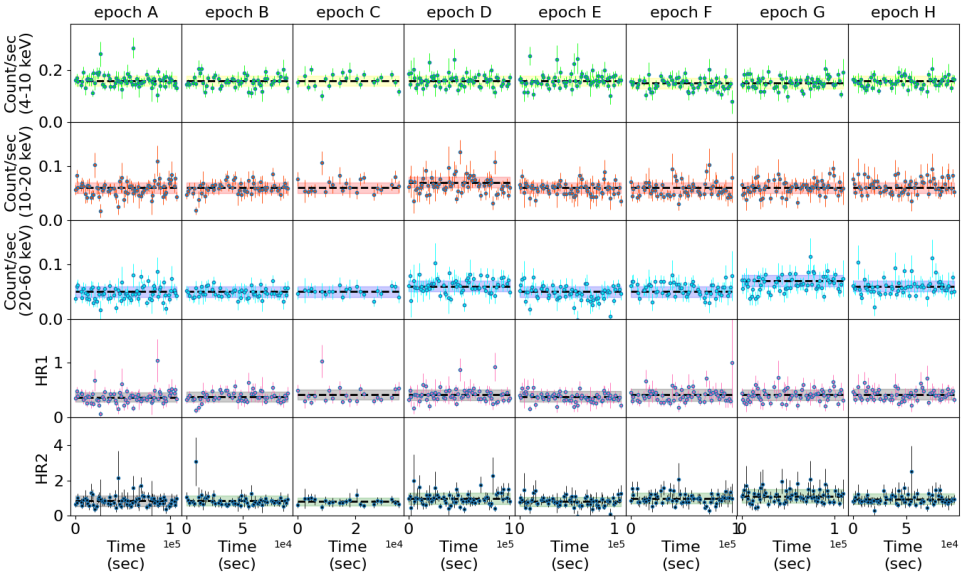

FIGURE 5.1: The *NuSTAR* light curves of NGC 1068 in three energy bands, 4−10 keV (first panel), 10−20 keV (second panel) and 20−60 keV (third panel). The HR1 and HR2 vs time are plotted in the last two panels. The black dashed lines are the mean of the count rate and HR. The shaded region in each panel is the mean errors in the count rate and HR.

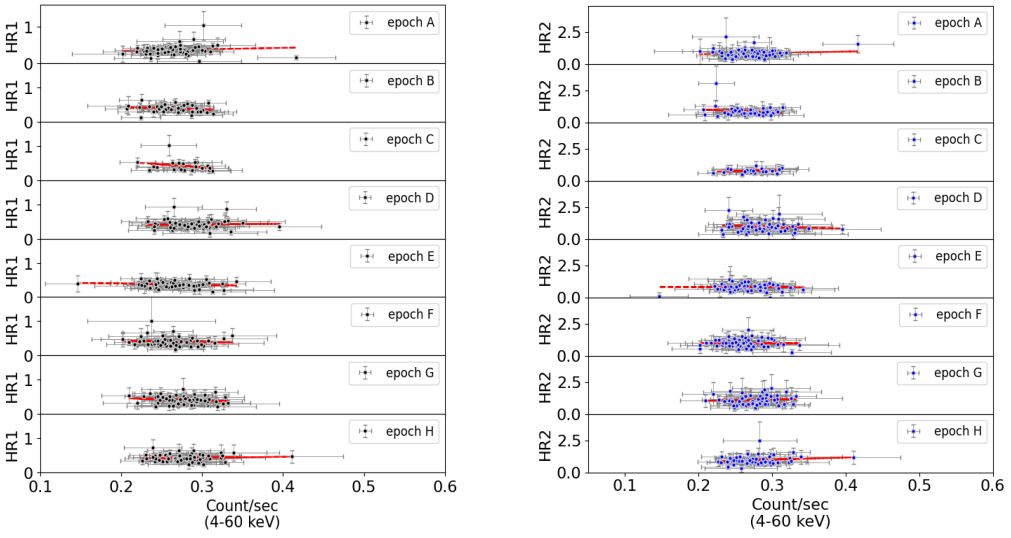

FIGURE 5.2: Left panel: The relation between HR1 and count rate in the 4−60 keV band. Right panel: The relation between HR2 and count rate in the 4−60 keV band. The red dashed lines in both panels are the linear least squares fit to the data.

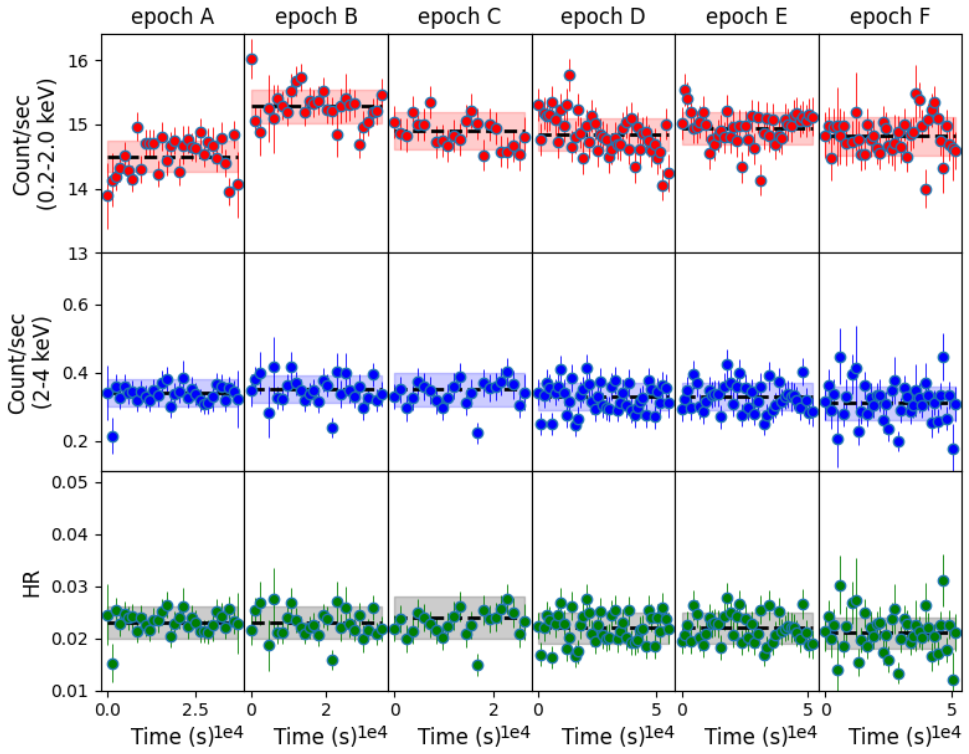

FIGURE 5.3: *XMM-Newton EPIC-PN* light curves of NGC 1068 in two energy bands, 0.2−2 keV (top) and 2−4 keV (middle). The HR vs time is plotted in the bottom panel. The black dashed line and the shaded region in each panel is the mean value of counts/sec or HR and the corresponding errors respectively.

et al. 2015, Marinucci et al. 2016, Zaino et al. 2020), the source has not been studied for variation in the X-ray coronal temperature. Bauer et al. (2015) from a joint fit of 2−195 keV data from different instruments reported a E_{cut} of 128^{+115}_{-44} keV. Recently Hinkle & Mushotzky (2021) jointly fit the *XMM-Newton* (OBSID-0740060401) and *NuSTAR* (OBSID-60002033002) data and reported a E_{cut} of $28.4^{+7.7}_{-4.0}$ keV.

In this thesis, taking advantage of the multiple epochs of data available from *NuSTAR* (along with near-simultaneous *XMM-Newton* data at certain epochs of *NuSTAR* observations), we carried out for the first time an investigation of the variation in the temperature of the corona if any. Also, we present the results of our variability analysis of NGC 1068, from observations carried out by *NuSTAR* between 2012 and 2017. In addition to the spectral analysis of the same *NuSTAR*

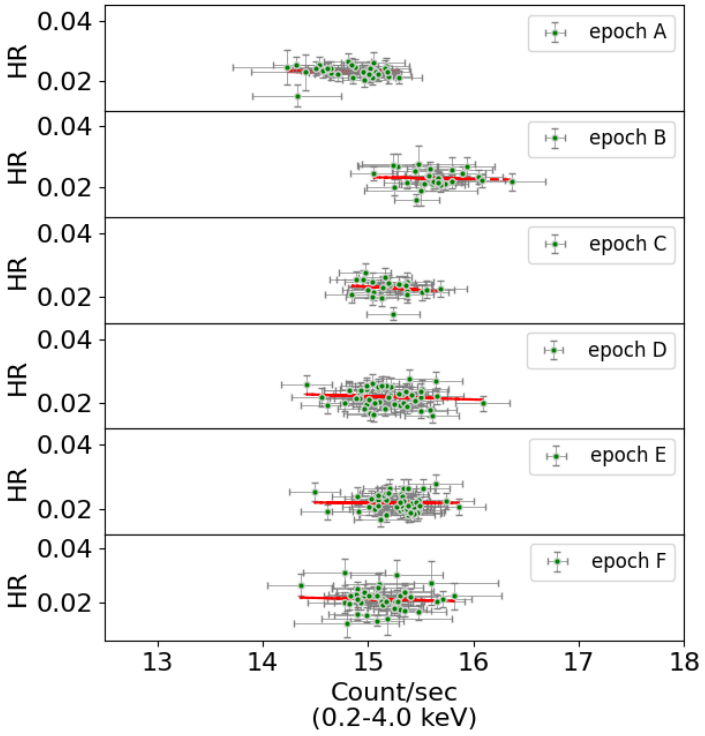

FIGURE 5.4: The relation between HR and count rate in the 0.2−4 keV band. The red dashed lines in both panels are the linear least square fit to the data.

data set in conjunction with observations from *XMM-Netwon*. The aim was to find the temperature of the corona in this source and its variation, if any.

5.1 Reduction of data

5.1.1 *NuSTAR*

We reduced the data of NGC 1068 in the 3−79 keV band using the standard *NuSTAR* data reduction software NuSTARDAS v1.9.7 distributed by HEASARC within HEASoft v6.29. We generated the calibrated event files by running the task

`nupipeline` using the CALDB release 20210701. We chose a circular aperture of 50″ radius around the source to extract the counts from the source. Similarly, to extract the background counts, a circular region of the same radius away from the source on the same chip was chosen to avoid contamination from source photons. We then used the `nuproducts` task to generate energy spectra, response matrix files (RMFs) and auxiliary response files (ARFs), for both the hard X-ray detectors housed inside the detector modules FPMA and FPMB.

5.1.2 *XMM-Newton*

We used the *EPIC-PN* data to extract the source and background spectra of NGC 1068. The log of the OBSIDs used in this work is given in Table 5.1. We used SAS v1.3 for the data reduction. Only single events ("PATTERN==0") with quality flag=0 were selected. Also, we filtered the event files to exclude time ranges with count rates greater than 0.3. Source spectra were extracted from an annular region between the inner and outer radius of 15″ and 30″ centred on the nucleus. Similarly, background spectra were selected from a source-free region of equal area on the same chip as the source. Here we note that for the source extraction, choosing a 30″ circular region produced pile up in the first two OBSIDs. However, pile-up was not noticed in the other four epochs. We extracted the source counts and background counts from an annular region for all six epochs to avoid piling up and maintain uniformity in data reduction. We constructed RMFs and ARFs using the *RMFGEN* and *ARFGEN* tasks for each epoch of observation.

TABLE 5.1: Log of *NuSTAR* and *XMM-Newton* observations.

Telescope	OBSID	Epoch	Date of observation	Exposure time (secs)
NuSTAR	60002030002	A	2012-12-18	57850
	60002030004	B	2012-12-20	48556
	60002030006	C	2012-12-21	19461
	60002033002	D	2014-08-18	52055
	60002033004	E	2015-02-05	53685
	60302003002	F	2017-07-31	49979
	60302003004	G	2017-08-27	52549
	60302003006	H	2017-11-06	49691
XMM − Newton	0111200101	A	2000-07-29	42258
	0111200102	B	2000-07-30	46429
	0740060201	C	2014-07-10	63997
	0740060301	D	2014-07-18	57600
	0740060401	E	2014-08-19	54000
	0740060501	F	2015-02-03	54600

5.2 Timing Analysis

5.2.1 *NuSTAR*

For timing analysis of the source, we utilized the data from *NuSTAR* and generated the background subtracted light curves with multiple corrections (e.g. bad pixel, livetime etc.) applied on the count rate in three energy bands, namely, 4−10 keV, 10−20 keV and 20−60 keV respectively with a bin size of 1.2 ksec. The

TABLE 5.2: Results of the variability analysis in two energy bands of *XMM-Newton*

OBSID	Epoch	Mean count rate		Mean HR	r	p
		0.2−2 keV	2−4 keV			
0111200101	A	14.50±0.24	0.34±0.04	0.023±0.003	-0.03	0.88
0111200201	B	15.28±0.26	0.35±0.04	0.023±0.003	-0.06	0.76
0740060201	C	14.86±0.25	0.34±0.04	0.023±0.003	-0.16	0.45
0740060301	D	14.85±0.25	0.33±0.04	0.022±0.003	-0.11	0.45
0740060401	E	14.94±0.25	0.33±0.04	0.022±0.003	-0.01	0.96
0740060501	F	14.82±0.30	0.31±0.05	0.021±0.003	-0.06	0.71

light curves in different energy bands, along with variations in hardness ratios (HRs) are given in Fig. 5.1. To check for variability in the generated light curves we calculated the fractional root mean square variability amplitude (F_{var};Edelson et al. 2002; Vaughan et al. 2003) for each epoch. F_{var} is defined as $F_{var} = \sqrt{\frac{V^2 - \overline{\sigma^2}}{\overline{x}^2}}$, where, $V^2 = \frac{1}{N-1}(x_i - \overline{x})^2$ is the sample variance and $\overline{\sigma^2} = \frac{1}{N}\sum \sigma_i^2$ is the mean square error in the flux measurements. Here, x_i is the observed value in counts per second, $\overline{x}$ is the arithmetic mean of the x_i measurements, and σ_i is the error in each individual measurement. The error in F_{var} was estimated following Vaughan et al. (2003). For a binning choice of 1.2 ksec the calculated F_{var} values indicate that the source is found not to show any significant variations within epochs. This is also evident in Fig. 5.1. Shown by black dashed lines in Fig. 5.1 is the mean brightness of the source at each epoch determined from the light curves. These mean values are given in Table 5.2. From light curve analysis, the source did not show variation in the 4−10 keV and 10−20 keV energy band during the five years of data analysed in this work. However, variation is detected in the hard band (20−60 keV) (Fig. 5.1).

In the two bottom panels of Figure 5.1, we show the evolution of two hardness ratios, namely HR1 and HR2, for the period analysed in this work. HR1 and HR2 are defined as: HR1 = C(10−20)/C(4−10) and HR2 = C(20−60)/C(10−20), where C(4−10), C(10−20) and C(20−60) are the count rates in 4−10 keV, 10−20 keV, and 20−60 keV, respectively. For each epoch, the mean hardness ratio is

depicted as a black dashed line in Figure 5.1 and the mean values are given in Table 5.2. As the errors are large, no variation in the hardness ratio of the source could be ascertained between epochs. We also looked for a correlation, if any, between the hardness ratios, HR1 and HR2, with count rate in the broad band over 4−60 keV band with a time binning of 1.2 ksec. This is shown in Fig. 5.2. We also show in the same figure the LLS fit to the data. Calculated values of Pearson's rank coefficient (r) and probability for no correlation (p) from the linear least square fit are given in Table 5.2. Analysing those values, we found no variation in hardness ratios with the brightness of the source.

5.2.2 *XMM-Newton*

Using the six epochs of *XMM-Newton EPIC-PN* data from Table 5.1, we generated the light curves in two energy bands, 0.2−2.0 keV and 2.0−4.0 keV using a binning size of 1.2 ksec. The light curves, along with the variation of HR, are shown in Fig. 5.3. Here, we defined HR as the ratio of C(2.0−4.0) to C(0.2−2.0), where C(2.0−4.0) and C(0.2−2.0) are the count rates in 2.0−4.0 keV and 0.2−2.0 keV energy bands respectively. From F_{var} analysis, we found no significant variation within the epochs of observation. The black dashed lines in the first two panels of Fig. 5.3 are the mean values of the count rate in different energy bands. The mean values of the count rate (see Table 5.2) indicate that in the 0.2−2 keV band, NGC 1068 was in its brightest state in epoch B. There is, thus, variation in the soft band, with the source being brighter in epoch B relative to epoch A. However, in the hard band, we did not notice any change in the source brightness between epochs. In the same Table 5.2, the constant values of mean HR between epochs also argue for no variation in the brightness state of the source. In Fig. 5.4, the variation of HR is plotted against the total count rate in the 0.2−4.0 keV energy range. The results of the LLS fit to the data are given in Table 5.2. From the p

values, we conclude no significant correlation is found between HR and the total count rate in NGC 1068.

5.3 Spectral analysis

In addition to characterizing the flux variability of NGC 1068, we also aimed to investigate the variation in the temperature of the corona of the source.

5.3.1 *NuSTAR* only spectral fit

To check for variation in the temperature of the corona in NGC 1068, we first concentrated on the *NuSTAR* data alone. For that, we fitted simultaneous FPMA/FPMB data for the eight epochs of observations available in the *NuSTAR* archive. To avoid the host galaxy contamination we used the *NuSTAR* data in the 4−79 keV energy band (Marinucci et al. 2016). For the analysis of the spectra, with XSPEC version 12.12.0 (Arnaud 1996), we fitted the background subtracted spectra from both the modules, FPMA and FPMB, simultaneously (without combining them) allowing the cross normalization factor to vary freely during spectral fits. We binned the spectra so as to have a minimum 25 counts/energy bin using the task *grppha*. To get an estimate of the model that well describes the observed data, we used the chi-square (χ^2) statistics and for calculating the errors in the model parameters, we used the $\chi^2 = 2.71$ criterion, which corresponds to 90% confidence range in XSPEC.

In all our model fits carried out on the observed spectra, the *const* represents the cross-calibration constant between the two focal plane modules FPMA and FPMB. To model the galactic absorption along the line of sight, we used the

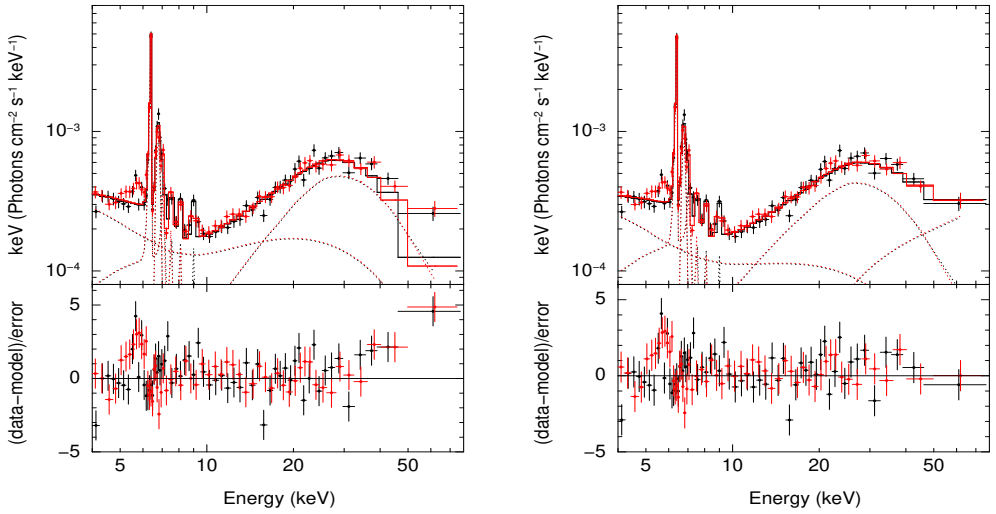

FIGURE 5.5: The best-fitted epoch G (with highest flux) unfolded spectra along with the data to model ratio using Model 1b (left panel) and Model 2b (right panel)

.

component *phabs* for which we froze the neutral hydrogen column density to 3.32×10^{20} atoms cm^{-2} as obtained from Willingale et al. (2013). To take into account the strong emission lines seen in the observed *NuSTAR* spectra, we used four *zgauss* components in XSPEC. In all the *zgauss* models considered to fit the emission lines, the line energies and the normalization were kept free during the fitting while σ was kept frozen to 0.1 keV. The redshift for all the model components was kept fixed to 0.0038 (Véron-Cetty & Véron 2010). We fixed the angle of inclination at 63° (Matt et al. 2004) in all the models.

5.3.1.1 Model 1

NGC 1068 has been extensively studied in the hard X-ray (>3 keV) energy range earlier (Matt et al. 1997, 2004; Bauer et al. 2015; Zaino et al. 2020) mostly using the two component reflector model. The main essence of this model is to fit (a) the cold and distant reflector using *pexrav*/*pexmon*/(*MYTS+MYTL*), and (b) the warm, ionized Compton-scattered component using *power-law*/*cutoff power-law*

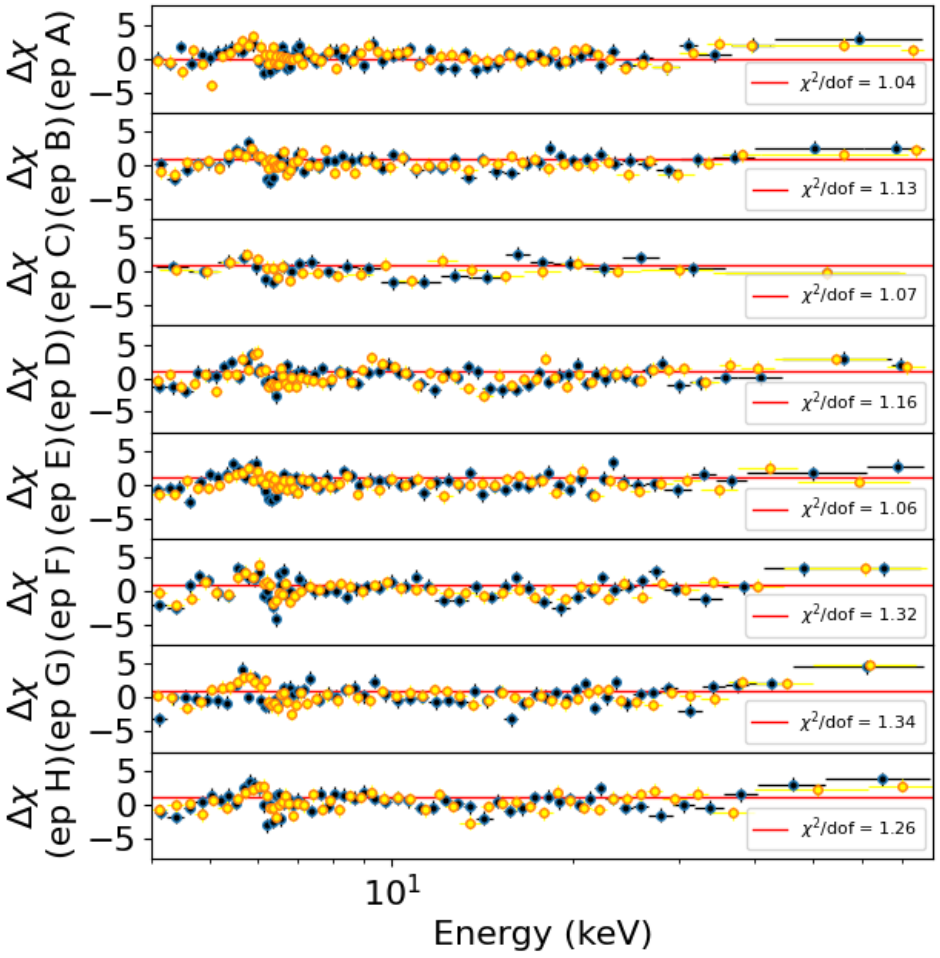

FIGURE 5.6: The ratio of the data to the model for all the eight epochs of *NuSTAR* observations using Model 1b.

with Compton down scattering under the assumption that the electron temperature is much smaller than the photon energy ($m_e c^2$). Few Gaussian components were also used to model various neutral and ionized emission lines present in the source spectra. In this work too, to find the coronal temperature of the source, we modelled the source spectra using two different reflector components.

1. The self-consistent Comptonization model *xillverCP* (García et al. 2014) that takes into account the cold and distant reflector, the Fe kα ($\sim$ 6.4 keV) and

Fe kβ ($\sim$ 7.06 keV) lines.

2. The warm ionized Compton scattered reflection using two models separately. At first, following Poutanen et al. (1996), a Compton scattered component (f_{scat}) for an arbitrary intrinsic continuum (f_{intr}). As an intrinsic continuum, we used a *power-law*, that was modified for Compton down scattering using equation (1) given in Poutanen et al. (1996). Secondly, the self-consistent *xillverCP* model with a high ionization parameter ($log\xi = 4.7$) to model the warm, ionized reflector. Here we note that fixing the ionization parameter to some other values ($log\xi = 3.0$, 3.5 and 4.0) did not produce any significant change in the derived best-fitted values. It only self-consistently added few ionization lines in the model, but, the spectral shape remained unchanged. Using the Compton scattered component in place of a warm mirror may affect the spectra by adding curvature below 2 keV (Bauer et al. 2015), but the spectral modelling of the *NuSTAR* data above 4 keV with or without the inclusion of the Compton down scattering in the warm reflector did not produce any significant effect on the derived best-fitted values. We also arrived at a similar conclusion by using the *XMM-Newton* data and *NuSTAR* data jointly. This is discussed in detail in Section 4.2.

3. Gaussian components to take care of the Fe ionized ($\sim$ 6.57, 6.7 and 6.96 keV), Ni kα ($\sim$ 7.47 keV), Ni kβ ($\sim$ 8.23 keV) and Ni ionized ($\sim$ 7.83 keV) emission lines.

In XSPEC, the two models used in the fitting of the spectra have the following form,

$$Model1a = const * phabs * (f1 * zpo + xillverCP + zgauss + zgauss + zgauss + zgauss)\,, \tag{5.1}$$

and,

$$Model1b = const * phabs * (xillverCP_{warm} + xillverCP_{cold} + zgauss + zgauss + zgauss + zgauss)\,. \tag{5.2}$$

Here, we note that, from the data to model ratio plot we did not find any prominent residuals near the line emission regions, but, in all epochs we noticed residues at around 6.0 keV (see Fig. 5.5 and Fig. 5.6). This feature at 6.0 keV has no physical origin but might appear in the *NuSTAR* data due to calibration issues (Zaino et al. 2020).

Model 1a: For the spectral fit with this model, we used the formula (f1) obtained from Poutanen et al. (1996) to consider the Compton down scattering of the intrinsic continuum (*zpo*). Following Poutanen et al. (1996),

$$f1 \propto \tau_{sc}[1 + \mu^2 + xx_1(1 - \mu)^2] \tag{5.3}$$

In Equation 5.3, $x = h\nu/m_e c^2$ is the dimensionless photon energy μ = cos i, x1 = x/[1- x(1-μ)] and τ_{sc} is the Thompson optical depth of the scattering material. We considered the constant of proportionality $\times$ τ_{sc} as another constant (p1) and kept it as a free parameter in the spectral analysis. During spectral fits Γ and the normalization for the two reflectors was tied together. For the cold reflector, we modelled only the reflection component by fixing the reflection fraction (R) to -1 throughout. The parameters that were kept free are the relative iron abundance (AF_e), kT_e and p1. The constant, p1 was allowed to vary between 0.0 and 10.0 during the fit. To model the cold and neutral reflector the ionization parameter (ξ) was frozen to 1.0 (i.e logξ = 0). The best-fitted values obtained using Model 1a are given in Table 5.3.

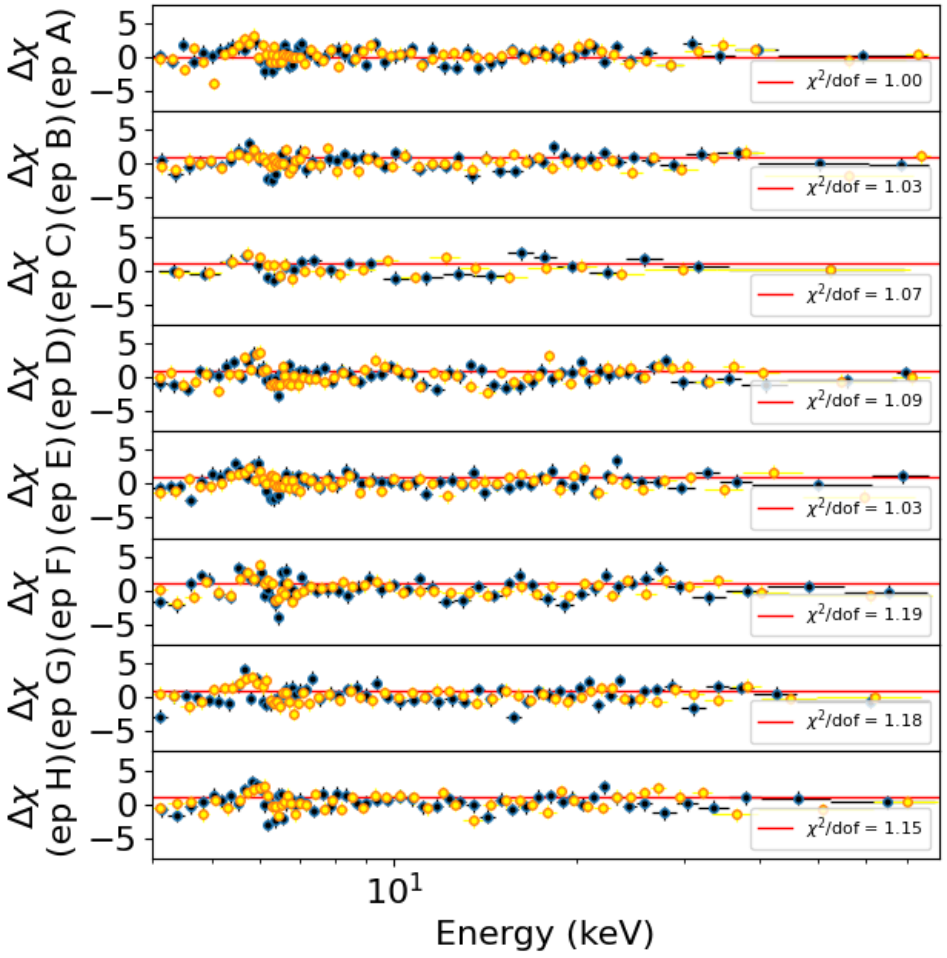

FIGURE 5.7: The ratio of the data to the model for all the eight epochs of *NuSTAR* observations using Model 2b.

Model 1b: Here, we used *xillverCP* twice to model the warm and cold reflections. For the warm and ionized reflector, we used $xillverCP_{warm}$ by fixing the ionization parameter to its highest value ($log\xi = 4.7$) and for the cold and distant reflection ($xillverCP_{cold}$) the reflector was considered as a neutral one with a fixed $log\xi$ of 0.0. In the modelling of the source spectra using Model 1b we tied Γ and kT_e of the two reflectors together. At first, the normalization for the two reflectors was tied together, and the model produced a χ^2 of 637 for 484 degrees of freedom for

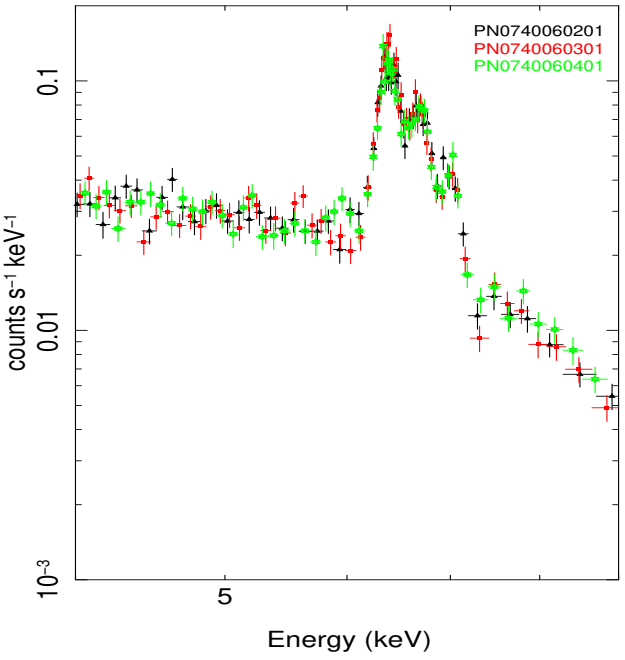

FIGURE 5.8: Three 2014 *EPIC-PN* spectra plotted together in the 4−9 keV band.

epoch A. We then modelled the epoch A spectrum by varying the two normalizations independently and got an improved χ^2 of 504 for 483 degrees of freedom. For the other epochs, we therefore carried out the model fit by leaving the two normalizations untied. For both the reflectors, we fixed R to -1 to consider the reflection components only. During the fitting AF_e between the two reflectors were tied together. The best-fitted unfolded spectra along with the residues of the data to Model 1b fit to the epoch G spectra are given in the left panel of Fig. 5.5. The best-fitted results of Model 1b are given in Table 5.3. For all the epochs, the residuals of the fit are given in the left panel of Fig. 5.6.

5.3.1.2 Model 2

Following Bauer et al. (2015) we then used the "leaky torus" model in which it is assumed that there is a finite probability for the primary emission to escape the medium without scattering or getting absorbed and partially punching through

above $20 - 30$ keV. In a Compton-Thick AGN, the direct transmitted continuum if at all present, is not observable below $\sim$ 10 keV. In Model 2, with the two reflectors, this transmitted or the direct component was taken care of. We assumed that a direct transmitted intrinsic continuum (*zpo*) was attenuated by the line of sight Compton thick absorber having a column density of $N_H = 10^{25}$ atoms cm^{-2} as well as an inclination angle (θ_{incl}) of 90° (for an edge on torus). Here also, we used *xillverCP* with $log\xi = 0.0$ to model the cold reflection, and, either *f1*zpo* (Poutanen et al. 1996) (Model 2a), or *xillverCP* with $log\xi = 4.7$ (Model 2b) to take care of the warm and ionized reflection. In XSPEC the models take the following forms,

$$Model2a = const * phabs * (zpo * MYTZ + f1 * zpo + xillverCP + zgauss + zgauss + zgauss + zgauss)\,, \tag{5.4}$$

and,

$$Model2b = const * phabs * (zpo * MYTZ + xillverCP_{warm} + xillverCP_{cold} + zgauss + zgauss + zgauss + zgauss)\,. \tag{5.5}$$

In both the models, we used the *MYTZ* component from the *MYtorus* set of models (Murphy & Yaqoob 2009; Yaqoob 2012) to fit the zeroth-order continuum. This is often called the "direct" or "transmitted" continuum which is simply a fraction of the intrinsic continuum that leaves the medium without being absorbed or scattered. This energy-dependent zeroth-order component (*MYTZ*) was used as a multiplicative factor to the intrinsic continuum. *MYTZ* is a line-of-sight quantity and does not depend on the geometry and covering fraction of the out-of-sight material. It includes the equivalent column density (N_H), inclination of the obscuring torus to the line of sight (θ_{incl}) and the redshift of the source. During the spectral fits N_H and θ_{incl} were frozen to 10^{25} cm^{-2} and 90° respectively.

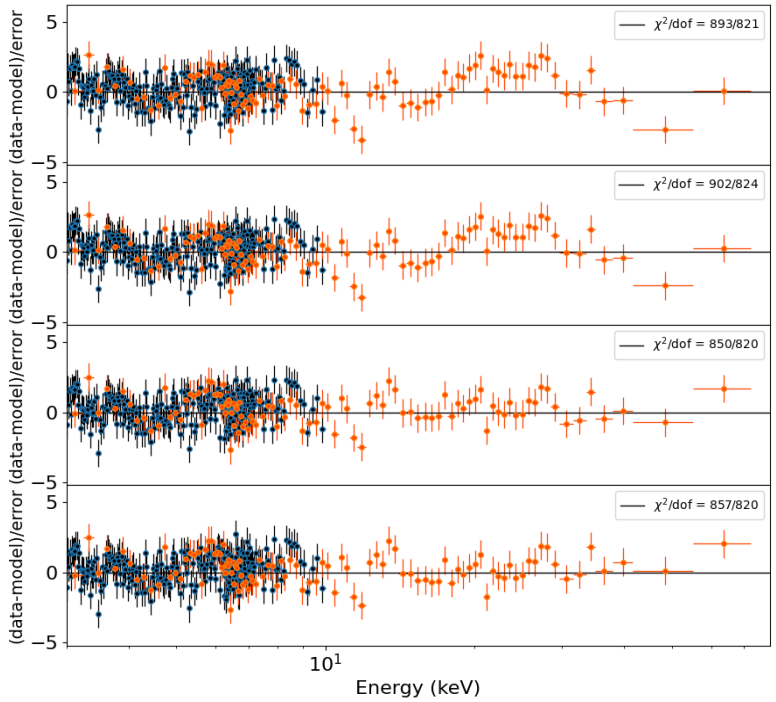

FIGURE 5.9: best-fitted data to the model ratio (from top to bottom) for *constant*phabs*zphabs*(cutoffpl+pexrav)*; *constant*phabs*zphabs(f1*cutoffpl+pexrav)*; *constant*phabs*zphabs(MYTZ*cutoffpl+f1*cutoffpl+pexrav)* and *constant*phabs*zphabs*(zpo*MYTZ+f1*zpo+xillverCP)* to the *XMM-Newton and NuSTAR* (epoch D FPMA) spectra in the 3−79 keV band.

Model 2a: During the spectral fitting with this model, Γ and the normalization for all the transmitted and reflected components were tied together. To model the warm and cold reflectors, we used *f1*zpo* and *xillverCP*, respectively. The parameters for these two models were treated in a similar fashion as described in Model 1a. The best-fitted values obtained from Model 2a fits are given in Table-5.3.

Model 2b: Here, we tied Γ of the transmitted and scattered components together, but we varied the normalization independently to achieve acceptable fit statistics. For the warm and cold reflectors, the model parameters were treated in a similar way as described in Model 1b. Using this model, we obtained better-fit statistics

than Model 1b with no prominent residues present in the hard energy part (see the right panel of Fig. 5.5). The best-fitted values are given in Table 5.3. For Model 2b, we calculated the flux in three energy bands, i.e., 4−10 keV, 10−20 keV and 20−79 keV. The fluxes obtained for the FPMA module (F^{FPMA}) are given in Table 5.3. In the 20−79 keV band on epoch D (August 2014), the source was brighter by about 22% and 28%, respectively, compared to the mean brightness in December 2012 (epoch A, B and C) and February 2015 (epoch E) FPMA spectra. The source brightness again increased in the 20 − 79 keV band on epoch G (August 2017), and it was found to be brighter by about 32% and 36% relative to the December 2012 and February 2015 spectra, respectively. For all the epochs, the best-fitted data to model residues are plotted in the right panel of Fig. 5.6.

TABLE 5.3: Results of Model 1a, Model 1b, Model 2a and Model 2b fits to the simultaneous *NuSTAR* FPMA−FPMB spectra. The kT_e and the line energies (E1, E2, E3 and E4) are in units of keV. Column densities (N_H) are in unit of cm^{-2}. Flux (F) in units of 10^{-11} erg $cm^{-2}s^{-1}$. Normalization of components (N) in different models at 1 keV is in units of photons/keV/cm^2/s. Parameters with the star mark (*) represent the frozen values.

Model	Parameter	Epoch A	Epoch B	Epoch C	Epoch D	Epoch E	Epoch F	Epoch G	Epoch H
1a	Γ	$1.33^{+0.03}_{-0.03}$	$1.30^{+0.03}_{-0.03}$	$1.32^{+0.05}_{-0.06}$	<1.21	$1.32^{+0.03}_{-0.03}$	<1.22	<1.21	<1.22
	A_{Fe}	$4.79^{+0.71}_{-0.37}$	5.00*	$4.87^{+1.50}_{-0.57}$	$4.38^{+0.30}_{-0.32}$	$4.34^{+0.36}_{-0.36}$	$4.93^{+0.47}_{-0.35}$	$4.46^{+0.30}_{-0.30}$	$4.40^{+0.30}_{-0.30}$
	kT_e	$7.60^{+0.47}_{-0.41}$	$7.48^{+0.35}_{-0.32}$	$8.04^{+0.78}_{-0.69}$	$7.44^{+0.28}_{-0.27}$	$6.82^{+0.36}_{-0.32}$	$7.26^{+0.25}_{-0.29}$	$7.60^{+0.29}_{-0.28}$	$7.29^{+0.29}_{-0.28}$
	N $\times(10^{-4})$	$1.31^{+0.10}_{-0.10}$	$1.35^{+0.07}_{-0.08}$	$1.33^{+0.17}_{-0.15}$	$1.60^{+0.08}_{-0.08}$	$1.50^{+0.11}_{-0.10}$	$1.43^{+0.08}_{-0.08}$	$1.61^{+0.09}_{-0.09}$	$1.53^{+0.09}_{-0.09}$
	p1	$1.28^{+0.24}_{-0.20}$	$1.23^{+0.16}_{-0.14}$	$1.31^{+0.35}_{-0.31}$	$0.70^{+0.11}_{-0.10}$	$0.93^{+0.18}_{-0.16}$	$0.76^{+0.10}_{-0.11}$	$0.66^{+0.11}_{-0.10}$	$0.69^{+0.11}_{-0.10}$
	χ^2/dof	468/482	437/421	210/199	483/468	436/452	473/414	528/449	479/429
	E1	$6.75^{+0.03}_{-0.03}$	$6.79^{+0.03}_{-0.03}$	$6.79^{+0.05}_{-0.05}$	$6.77^{+0.03}_{-0.03}$	$6.78^{+0.03}_{-0.03}$	$6.77^{+0.03}_{-0.03}$	$6.80^{+0.03}_{-0.03}$	$6.79^{+0.03}_{-0.03}$
	N_{E1} $\times(10^{-5})$	$3.82^{+0.42}_{-0.47}$	$3.50^{+0.45}_{-0.42}$	$3.61^{+0.37}_{-0.69}$	$3.39^{+0.46}_{-0.43}$	$3.40^{+0.45}_{-0.42}$	$2.64^{+0.44}_{-0.41}$	$2.88^{+0.42}_{-0.40}$	$3.39^{+0.44}_{-0.43}$
	E2	$7.59^{+0.09}_{-0.09}$	$7.58^{+0.16}_{-0.13}$	$7.62^{+0.16}_{-0.15}$	$7.45^{+0.18}_{-0.16}$	$7.51^{+0.14}_{-0.18}$	$7.61^{+0.10}_{-0.09}$	$7.66^{+0.15}_{-0.13}$	$7.55^{+0.09}_{-0.10}$
	N_{E2} $\times(10^{-5})$	$0.81^{+0.21}_{-0.22}$	$0.55^{+0.21}_{-0.21}$	$0.80^{+0.41}_{-0.44}$	$0.46^{+0.23}_{-0.24}$	$0.55^{+0.25}_{-0.28}$	$0.62^{+0.21}_{-0.21}$	$0.56^{+0.21}_{-0.20}$	$0.62^{+0.23}_{-0.23}$
	E3	$8.19^{+0.12}_{-0.16}$	$8.46^{+0.17}_{-0.17}$	$8.07^{+0.16}_{-0.15}$	$7.96^{+0.11}_{-0.11}$	$7.95^{+0.20}_{-0.17}$	$8.33^{+0.13}_{-0.14}$	$8.03^{+0.23}_{-0.21}$	$8.08^{+0.08}_{-0.09}$
	N_{E3} $\times(10^{-5})$	$0.45^{+0.19}_{-0.19}$	$0.48^{+0.19}_{-0.19}$	$0.74^{+0.41}_{-0.41}$	$0.65^{+0.22}_{-0.23}$	$0.43^{+0.26}_{-0.25}$	$0.38^{+0.19}_{-0.18}$	$0.55^{+0.23}_{-0.27}$	$0.56^{+0.21}_{-0.21}$
	E4	$8.77^{+0.11}_{-0.12}$	$8.75^{+0.10}_{-0.11}$	-	$8.63^{+0.18}_{-0.23}$	$8.87^{+0.17}_{-0.36}$	$9.12^{+0.19}_{-0.18}$	$9.00^{+0.14}_{-0.14}$	$9.00^{+0.26}_{-0.29}$
	N_{E4} $\times(10^{-6})$	$3.69^{+1.74}_{-1.79}$	$3.28^{+1.20}_{-1.25}$	-	$2.79^{+1.79}_{-1.79}$	$3.84^{+1.72}_{-1.72}$	$2.15^{+1.69}_{-1.63}$	$4.19^{+1.80}_{-1.79}$	$2.75^{+1.76}_{-1.76}$
	$C_{FPMA/FPMB}$	$1.04^{+0.03}_{-0.03}$	$1.03^{+0.03}_{-0.03}$	$1.01^{+0.05}_{-0.04}$	$1.01^{+0.03}_{-0.03}$	$1.02^{+0.03}_{-0.03}$	$1.00^{+0.03}_{-0.03}$	$1.01^{+0.03}_{-0.03}$	$0.98^{+0.03}_{-0.03}$
1b	Γ	$1.34^{+0.05}_{-0.03}$	$1.26^{+0.08}_{-0.06}$	<1.27	<1.24	$1.31^{+0.04}_{-0.05}$	<1.26	<1.22	<1.26
	A_{Fe}	<7.05	<6.31	>7.29	$5.08^{+1.31}_{-0.23}$	$5.83^{+1.86}_{-1.00}$	$6.82^{+0.95}_{-1.78}$	$5.50^{+0.69}_{-0.59}$	$5.53^{+1.52}_{-0.68}$

Continued

Table 5.3 – Following the previous page

Model	Parameter	Epoch A	Epoch B	Epoch C	Epoch D	Epoch E	Epoch F	Epoch G	Epoch H
	kT_e	$9.10^{+0.13}_{-0.16}$	$8.95^{+0.16}_{-0.20}$	$9.38^{+0.18}_{-0.18}$	$8.75^{+0.16}_{-0.12}$	$8.69^{+0.22}_{-0.25}$	$8.68^{+0.17}_{-0.23}$	$8.77^{+0.13}_{-0.14}$	$8.78^{+0.16}_{-0.16}$
	$N_{xillverCP_{warm}}$ $\times(10^{-5})$	$2.43^{+0.24}_{-0.34}$	$2.29^{+0.36}_{-0.36}$	$2.68^{+0.15}_{-0.49}$	$2.03^{+0.30}_{-0.16}$	$1.90^{+0.35}_{-0.26}$	$1.95^{+0.18}_{-0.35}$	$1.99^{+0.15}_{-0.19}$	$2.02^{+0.31}_{-0.23}$
	$N_{xillverCP_{cold}}$ $\times(10^{-4})$	$1.03^{+0.08}_{-0.06}$	$1.12^{+0.09}_{-0.10}$	$1.00^{+0.11}_{-0.08}$	$1.38^{+0.07}_{-0.09}$	$1.18^{+0.10}_{-0.10}$	$1.22^{+0.10}_{-0.08}$	$1.39^{+0.07}_{-0.07}$	$1.27^{+0.10}_{-0.09}$
	χ^2/dof	504/483	474/420	213/199	545/468	480/452	545/414	600/449	545/431
2a	Γ	$1.32^{+0.03}_{-0.03}$	$1.30^{+0.04}_{-0.04}$	$1.32^{+0.05}_{-0.05}$	<1.22	$1.32^{+0.03}_{-0.03}$	<1.22	<1.21	<1.22
	A_{Fe}	$4.78^{+0.70}_{-0.37}$	$5.50^{+1.14}_{-0.77}$	$4.77^{+1.47}_{-0.60}$	$4.43^{+0.31}_{-0.32}$	$4.32^{+0.38}_{-0.37}$	$5.00^{+0.63}_{-0.37}$	$4.56^{+0.31}_{-0.32}$	$4.33^{+0.37}_{-0.34}$
	kT_e	$7.39^{+0.41}_{-0.69}$	$7.80^{+0.49}_{-0.58}$	$7.28^{+0.86}_{-0.62}$	$7.45^{+0.30}_{-0.29}$	$6.35^{+0.46}_{-0.34}$	$7.51^{+0.33}_{-0.37}$	$7.43^{+0.35}_{-0.55}$	$6.80^{+0.51}_{-0.35}$
	p1	$0.79^{+0.69}_{-0.21}$	$1.34^{+0.20}_{-0.18}$	$0.83^{+0.53}_{-0.35}$	$0.74^{+0.11}_{-0.10}$	$0.53^{+0.25}_{-0.19}$	$0.88^{+0.11}_{-0.11}$	$0.64^{+0.12}_{-0.31}$	$0.72^{+0.10}_{-0.11}$
	χ^2/dof	467/482	421/420	205/199	480/468	431/452	449/414	521/449	476/431
2b	Γ	$1.35^{+0.09}_{-0.07}$	$1.50^{+0.08}_{-0.08}$	$1.49^{+0.13}_{-0.13}$	$1.31^{+0.06}_{-0.04}$	$1.37^{+0.03}_{-0.03}$	$1.35^{+0.04}_{-0.03}$	$1.32^{+0.06}_{-0.05}$	$1.34^{+0.05}_{-0.05}$
	A_{Fe}	$6.09^{+2.43}_{-1.44}$	$4.39^{+0.76}_{-0.70}$	$4.48^{+1.63}_{-0.95}$	$4.98^{+0.56}_{-0.63}$	5.00*	$5.00^{+0.71}_{-0.41}$	$4.43^{+0.72}_{-0.68}$	$4.31^{+0.67}_{-0.66}$
	kT_e	$8.97^{+0.22}_{-0.30}$	$8.51^{+0.49}_{-0.82}$	$9.13^{+0.63}_{-0.98}$	$8.76^{+0.15}_{-0.39}$	$8.55^{+0.17}_{-0.16}$	$8.57^{+0.17}_{-0.32}$	$8.46^{+0.39}_{-0.66}$	$8.30^{+0.45}_{-0.72}$
	χ^2/dof	481/481	433/419	211/198	507/467	464/452	495/415	529/448	496/430
	F^{FPMA}_{4-10}	0.42	0.42	0.43	0.41	0.42	0.38	0.39	0.40
	F^{FPMA}_{10-20}	0.45	0.45	0.48	0.49	0.45	0.42	0.48	0.47
	F^{FPMA}_{20-79}	2.23	2.50	2.55	3.09	2.24	2.92	3.54	2.97

5.3.2 XMM-Newton & NuSTAR Joint fit

Fitting the *NuSTAR* spectra alone could not handle the line emission profiles present in the source spectrum properly. To model the lines we used three *XMM-Newton EPIC-PN* spectra taken in 2014 along with the *NuSTAR* FPMA data. Use of *XMM-Newton* data jointly with *NuSTAR*, the observations of which are not simultaneous requires the source to be non-variable. We show in Fig. 5.8 all three *XMM-Newton PN* spectra taken in 2014. This figure indicates that the source has not shown any noticeable variation in line and continuum flux. Also, in all the eight epochs of *NuSTAR* data accumulated over a period of 5 years, no variation in the soft band (4−10 keV) is observed (see Table 5.2 and Fig. 5.1). Therefore, it is not inappropriate to jointly model the *NuSTAR* and *XMM-Newton* data. We, therefore, combined the three *XMM-Newton EPIC-PN* spectra together using the task *epicspeccombine* and then binned the spectra with 25 counts/bin using the task *specgroup*.

We carried out joint model fits to the 3−10 keV *XMM-Newton* 2014 combined spectra with the 3−79 keV epoch D *NuSTAR* spectrum. To account for both warm and cold reflection, several models were tried. Firstly, we used a *cutoffpl* to model the warm reflector that did not take into account Compton down scattering. For modelling the cold reflector we used *pexrav* (Magdziarz & Zdziarski 1995) with R=−1. We obtained the best-fitted values of $1.59^{+0.09}_{-0.09}$, 95^{+100}_{-47} and $11.22^{+3.51}_{-2.70}$ for Γ, E_{cut} and A_{Fe} respectively with a χ^2/dof of 893/821. Using this model we got reasonably acceptable fit statistics with a mild hump between 20−30 keV band (see top panel of Fig. 5.9). We replaced the *cutoffpl* with *xillver* with a fixed $\log \xi$ = 4.7 to account for the Compton down scattering. We obtained $\Gamma = 1.54^{+0.04}_{-0.04}$, $E_{cut} = 94^{+26}_{-19}$ keV and $A_{Fe} > 9.15$. This fit produced a χ^2/dof of 884/821. We then replaced *xillver* with f1*cutoffpl (for f1, see Equation 5.3) to model the warm reflector and obtained $\Gamma = 1.62^{+0.11}_{-0.11}$, $E_{cut} = 97^{+149}_{-39}$ keV and $A_{Fe} = 11.50^{+4.54}_{-3.11}$ with a χ^2/dof of 902/824. With or without the inclusion of Compton down scattering

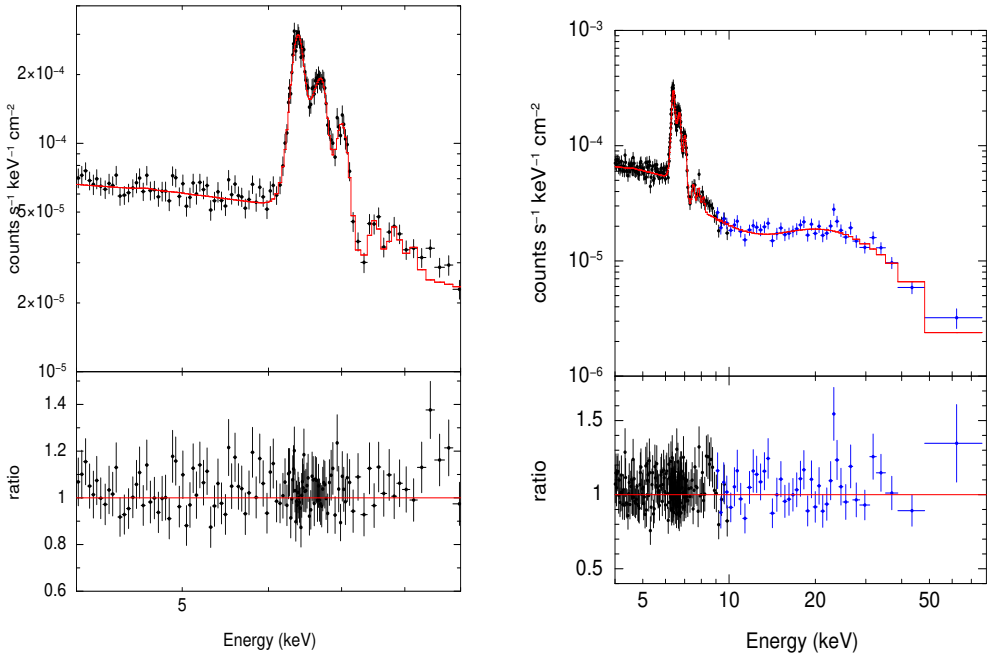

FIGURE 5.10: Left panel: best-fitted *EPIC-PN* combined spectra in the 4−9 keV band. Right panel: *XMM-Newton and NuSTAR* (epoch D FPMA) joint best-fitted spectra in the 4−79 keV band.

in the warm reflector we obtained a similar set of best-fitted values and a hump in the data to model residue plot near 25 keV (see first two panels of Fig. 5.9). We thus conclude that the inclusion of Compton down scattering in the warm reflection has an insignificant effect on the derived parameters.

The spectrum of the Compton-Thick AGN is refection dominated. However, there is a finite probability for the primary emission to be transmitted (above >10 keV) through the Compton thick absorber. Thus, we modified our model to take into account the transmitted primary emission by including the (*MYTZ*cutoffpl*) component into the previously described two reflector models in which the cold reflection was modelled using *pexrav* with R=−1. For the warm reflector, we first used *xillver* with R=−1 and $log\xi$ = 3.1. For the Compton absorber along the line of sight, we assumed a column density of 10^{25} cm^{-2} with an inclination of 90° (Bauer et al. 2015). We obtained Γ <1.28, E_{cut} = 16^{+2}_{-1} keV and A_{Fe} = >7.41 with a χ^2/dof of 847/820. The fit statistics now improved by $\Delta\chi^2$ = 37 over the

TABLE 5.4: best-fitted line energies along with normalization. Here, the line energy (E) is in keV and the normalization (N_E) is in units of 10^{-5} photons keV^{-1} cm^{-2} s^{-1}

Parameter	Line	Value
E1	Fe Be-like Kα	$6.60^{+0.03}_{-0.03}$
N_{E1}		$1.85^{+0.47}_{-0.44}$
E2	Fe He-like Kα	$6.75^{+0.02}_{-0.02}$
N_{E2}		$2.86^{+0.46}_{-0.50}$
E3	Fe H–like Kα	$7.02^{+0.01}_{-0.02}$
N_{E3}		$1.35^{+0.19}_{-0.18}$
E4	Ni Kα	$7.53^{+0.03}_{-0.03}$
N_{E4}		$0.51^{+0.15}_{-0.15}$
E5	Ni ionized He-like Kα	$7.86^{+0.04}_{-0.04}$
N_{E5}		$0.46^{+0.15}_{-0.15}$
E6	Ni Kβ	$8.15^{+0.08}_{-0.08}$
N_{E6}		$0.28^{+0.14}_{-0.14}$

reduction of 1 degree of freedom and the hump around 20−30 keV band was also taken care of. We obtained a similar fit with $\Gamma = 1.37^{+0.18}_{-0.16}$, $E_{cut} = 18^{+4}_{-3}$ keV and $A_{Fe} = 5.68^{+4.20}_{-2.41}$ with a χ^2/dof 850/820 from using *f1*cutoffpl* (see Equation 5.3) as a warm reflector. Inclusion of the transmitted primary emission with the two reflector model described the source spectra well with a harder photon index and lower E_{cut} with no prominent features present in the data to model ratio plot at high energies (see 3rd panel of Fig. 5.9). Previously also, NGC 1068 X-ray spectrum was modelled with a flatter photon index. From a joint analysis of *XMM-Newton* epoch E spectrum with the epoch D *NuSTAR* spectrum Hinkle & Mushotzky (2021) reported $\Gamma = 1.21^{+0.13}_{-0.07}$. From modelling the 0.5−10 keV *ASCA* observation Ueno et al. (1994) found a best-fitted Γ of 1.28±0.14. Replacing *pexrav* with *xillverCP* to model the cold reflector with R=−1 and $log\xi = 0.0$ we obtained $\Gamma = 1.26^{+0.03}_{-0.03}$, $kT_e = 8.59^{+0.40}_{-0.37}$ keV and $A_{Fe} = 4.02^{+0.36}_{-0.33}$ with a $\chi^2 = 857$ for 820 degrees of freedom. The data to the best-fitted model residues are given in Fig. 5.9.

To estimate kT_e we used Model 2b, as described earlier for the *NuSTAR* spectral fit alone. Here the *NuSTAR* FPMA spectra for all the epochs in the 9−79 keV

along with the combined 2014 *XMM-Newton* data in the 4−10 keV band were used to take care of the line emission region carefully. We used six Gaussian components to model all the ionized and neutral lines present in the spectra. The line energies and the normalization were kept free during the fitting while the line widths were frozen to 0.01 keV. The self-consistent $xillverCP_{cold}$ model took care of the neutral Fe kα ($\sim$ 6.4 keV) and kβ ($\sim$ 7.08 keV) lines, wherein the first three Gaussian components were used to model the ionized Fe lines at energies $\sim$ 6.57 keV (Fe Be-like Kα), 6.67 keV (Fe He-like Kα) and 6.96 keV (Fe H–like Kα). The neutral Ni kα ($\sim$ 7.47 keV), Ni kβ ($\sim$ 8.23 keV) and Ni ionized He-like Kα ($\sim$ 7.83 keV) were taken care by the other three Gaussian components. As seen from the Fig. 5.10 (left panel) we did not find any prominent residue in the 4−9 keV band. All the best-fittedted line energies and the normalization are given in Table 5.4. The best-fitted model parameters and their associated errors, are given in Table 5.5. This joint fit produced similar best-fitted values as obtained from *NuSTAR* fit alone. The best-fitted model to the data (the combined *EPIC-PN* data and *NuSTAR* FPMA epoch D spectra) along with the residue is shown in the right panel of Fig 5.10.

TABLE 5.5: Results of the Model 2b fit to the *XMM-Newton* and *NuSTAR* FPMA spectra in the 4−79 keV energy band. kT_e is in unit of keV and column densities (N_H) are in units of cm^{-2}. Normalization of components (N) at 1 keV is in unit of photons/keV/cm^2/s.

Parameter	Epoch A	Epoch B	Epoch C	Epoch D	Epoch E	Epoch F	Epoch G	Epoch H
N_H^{ztbabs}	$9.78^{+2.92}_{-2.96}$	$9.19^{+2.73}_{-2.75}$	$7.09^{+5.04}_{-4.19}$	$9.57^{+2.39}_{-2.60}$	$9.16^{+2.58}_{-2.72}$	$9.72^{+2.37}_{-2.55}$	$9.51^{+2.75}_{-3.15}$	$8.90^{+2.64}_{-2.88}$
Γ	$1.29^{+0.07}_{-0.08}$	$1.33^{+0.15}_{-0.07}$	$1.48^{+0.11}_{-0.25}$	<1.32	$1.33^{+0.10}_{-0.06}$	$1.28^{+0.07}_{-0.05}$	$1.26^{+0.07}_{-0.10}$	$1.30^{+0.07}_{-0.07}$
A_{Fe}	$6.08^{+3.87}_{-1.59}$	$4.89^{+2.89}_{-1.51}$	$3.09^{+4.96}_{-1.08}$	$4.19^{+1.44}_{-0.93}$	$4.75^{+2.19}_{-0.63}$	$4.99^{+1.70}_{-1.10}$	$3.90^{+1.33}_{-1.10}$	$3.81^{+1.27}_{-1.01}$
kT_e	$8.69^{+0.28}_{-0.33}$	$8.62^{+0.33}_{-0.49}$	$8.07^{+0.59}_{-0.75}$	$8.59^{+0.30}_{-0.36}$	$8.60^{+0.34}_{-0.58}$	$8.68^{+0.26}_{-0.38}$	$8.55^{+0.25}_{-0.41}$	$8.48^{+0.35}_{-0.51}$
χ^2/dof	592/584	576/565	516/492	620/586	590/574	613/569	630/584	585/578
$C_{XMM/NuSTAR}$	$0.96^{+0.08}_{-0.08}$	$0.95^{+0.08}_{-0.07}$	$0.94^{+0.11}_{-0.11}$	$0.94^{+0.08}_{-0.08}$	$0.93^{+0.08}_{-0.08}$	$0.98^{+0.08}_{-0.08}$	$0.93^{+0.08}_{-0.08}$	$0.97^{+0.08}_{-0.09}$

5.4 Summary

In this work, we carried out spectral and timing analysis of eight epochs of *NuSTAR* observations performed between December 2012 and November 2017 probing time scales within epochs and between epochs that spans about 5 years. The timing analysis of the six *XMM-Newton* observations between July 2000 and February 2015 was also performed. We also carried out the spectral analysis of the 2014 combined *XMM-Newton EPIC-PN* and *NuSTAR* FPMA data jointly. We summarized the results below

1. We found the source not to show flux variation within each of the eight epochs of *NuSTAR* observation.

2. Between epochs, that span the time-scales from 2012 to 2017, we found variation in the source. Here too, the source did not show variation in the soft energy range. As in agreement with the earlier results by Marinucci et al. (2016) and Zaino et al. (2020), we also found that the observed variations is only due to variation in the energy range beyond 20 keV. This too was noticed in Epoch D (August 2014) and Epoch G (August 2017), when the brightness of the source beyond 20 keV was higher by about 20% and 30% respectively relative to the three *NuSTAR* observations in the year 2012.

3. From timing analysis, we observed no correlation of spectral variation (hardness ratio) with brightness.

4. Fitting physical models to the observed data we could determine the temperature of the corona in NGC 1068 with values ranging from $8.46^{+0.39}_{-0.66}$ keV and $9.13^{+0.63}_{-0.98}$ keV. However, we found no variation in the temperature of the corona during the 8 epochs of observations that span a duration of about 5 years.

5. Based on the timing analysis of six *XMM-Newton EPIC-PN* data we found no significant flux variation both in between and within epochs of observation in the hard band. In the soft band too we found that the source did not show any significant flux variation within epochs but it was brighter in epoch B compared to epoch A.

6. The combined spectral fit of *XMM-Newton* and *NuSTAR* data provided results that are in agreement with those obtained by model fits to the *NuSTAR* data alone.

In NGC 1068, we did not find evidence for variation in the temperature of the corona from the analysis of data that span more than five years. This is evident from the best-fitted values of kT_e from Table 5.3. Also, the results from various models are found to be similar. The values of kT_e found for NGC 1068 also lie in the range of kT_e found in other AGN. Measurements of E_{cut} are available for a large number of AGN consisting of both Seyfert 1 and Seyfert 2 types. However, studies on the variation of E_{cut} or kT_e are limited to less than a dozen AGN (Ballantyne et al. 2014; Ursini et al. 2015, 2016; Keek & Ballantyne 2016; Zoghbi et al. 2017; Zhang et al. 2018; Barua et al. 2020; Kang et al. 2021a; Barua et al. 2021; Pal et al. 2022). Even in sources where E_{cut}/kT_e variations are known, the correlation of the variation of kT_e with various physical properties of the sources are found to be varied among sources (Barua et al. 2020; Barua et al. 2021; Kang et al. 2021a; Pal et al. 2022). These limited observations do indicate that we do not yet understand the complex corona of AGN including its geometry and composition. Investigation of this kind needs to be extended for many AGN to better understand the nature of X-ray corona.

Chapter 6

Spectropolarimetric analysis of IC 4329A using *IXPE* data [†]

Analysis of the X-ray spectra of the Seyfert-type radio-quiet category of AGN using physical model fits to the observations are routinely used to characterise the nature of the corona, such as temperature and optical depth. However, such spectral analyses are insensitive to the shape and location of the corona. The corona of AGN could be either a spherical structure above the black hole (spherical lamp-post; Fabian et al. 2017) or a slab-like structure sandwiching the accretion disk (Haardt & Maraschi 1993) or a conical structure (Ursini et al. 2021). From fitting physical models to the observed high energy spectra of AGN, the kT_e reported in the literature assumes the corona to have either a spherical or a slab geometry (Rani & Stalin 2018a). Also, from the multi-epoch spectral analysis available in the literature, several models of the corona, including changes in the structure of the corona, are proposed to explain the observed changes in kT_e. (Pal et al. 2022;

[†]The contents of this Chapter are from Pal et al. 2023 (submitted to the Journal of Astronomy and Astrophysics)

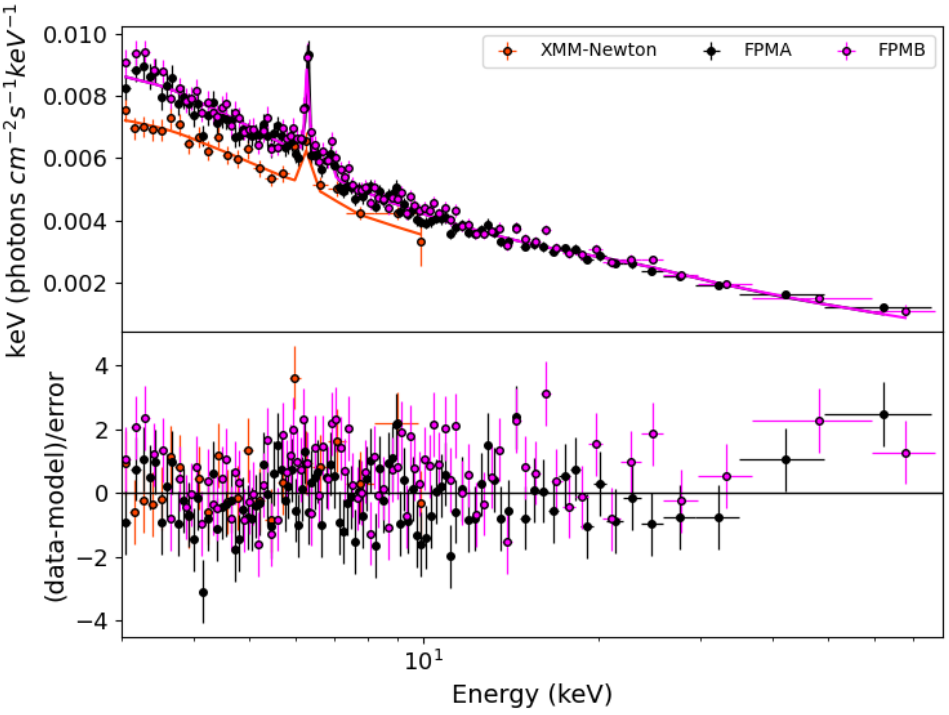

FIGURE 6.1: The *XMM-Newton EPIC-PN*, *NuSTAR* FPMA and FPMB spectra fitted jointly in 3−78 keV energy band using the model *const*×*TBabs*×*zTBabs*×*(xillverCP)*. The observations were taken simultaneously on August 12, 2021.

Pal & Stalin 2023). However, from spectral analysis of AGN, it is difficult to distinguish between different geometrics of corona (Tortosa et al. 2018; Middei et al. 2019). Irrespective of several studies in the literature attempting to characterise the corona in AGN, we still lack knowledge on (i) the origin of the corona, (ii) the cause of its high temperature and (iii) its geometry.

X-ray polarimetric observations on AGN can yield the needed constraints on the geometry of the X-ray-emitting corona in AGN (Matt et al. 1989, 1993b). This is because polarization depends on the geometry of the X-ray emitting region (Tamborra et al. 2018; Zhang et al. 2019). The launch of the *Imaging X-ray Polarimetry Explorer* (*IXPE*; Weisskopf et al. 2022) on December 9, 2021, sensitive in the 2−8 keV band has enabled the studies of X-ray polarization from AGN. As

of now, *IXPE* has observed four radio-quiet AGN, namely MCG-05-23-16, the Circinus galaxy, NGC 4151 and IC 4329A. Of these, a polarization degree $\Pi_X < 4.7\%$ was reported by Marinucci et al. (2022) for MCG-05-23-16. In the case of the Circinus Galaxy, Ursini et al. (2023), reported a high value of $\Pi_X = 28\%$, which is thought to be due to reflection from the torus. For NGC 4151, Gianolli et al. (2023), found values of Π_X and Ψ_X of 4.9 $\pm$1.1% and 86°$\pm$7° respectively, arguing for the corona to have a slab geometry. Here, we report the results of polarization on the fourth radio-quiet AGN, IC 4329A.

IC 4329A is a Seyfert 1.2 galaxy (Véron-Cetty & Véron 2010) at z = 0.016 (Willmer et al. 1991) with a black hole mass of $6.8^{+1.2}_{-1.1} \times 10^7$ $M_\odot$ (Bentz et al. 2023) and an X-ray spectrum having many absorbing systems (Steenbrugge et al. 2005). It is an ideal object to study the intrinsic continuum and reflection from any material surrounding the source. The X-ray timing and spectral properties of IC 4329A has been extensively studied by Dewangan et al. (2021). Observations of IC 4329A in the millimetre were explained as due to synchrotron emission in the hot corona (Inoue & Doi 2018). Using the `COMPPS` model and assuming a spherical corona, Lubiński et al. (2016) obtained a value of $kT_e = 40^{+7}_{-5}$ keV assuming a spherical corona. Alternatively, using the Comptonization model and a slab geometry of the corona, Petrucci et al. (2001) found a value of $kT_e = 170^{+10}_{-5}$ keV. Tortosa et al. (2018) reported $kT_e = 37\pm7$ keV from fitting *compTT* to the source spectrum for slab geometry. Kang & Wang (2022) estimated $kT_e = 71^{+37}_{-15}$ keV using *relxillCP* model. Kamraj et al. (2022) also found $kT_e = 82^{+16}_{-7}$ keV from *xillverCP* fit to the source spectrum. We analyzed the *NuSTAR* spectrum taken in 2012. Fitting the spectrum using *xillverCP*, we found Γ and kT_e of $1.83^{+0.003}_{-0.003}$ and 64^{+15}_{-12} keV respectively (Pal et al. 2023, submitted to MNRAS). From a joint fit of *XMM-Newton EPIC-PN* and *NuSTAR* spectra observed simultaneously on August 12, 2021, we found $\Gamma = 1.88^{+0.01}_{-0.01}$ and $kT_e > 135$ keV. The best-fit model with data and the residues are given in Fig. 6.1. All the spectral fits produced good fit statistics with $\chi^2/dof \sim 1.0$, irrespective of the coronal geometry assumed in the

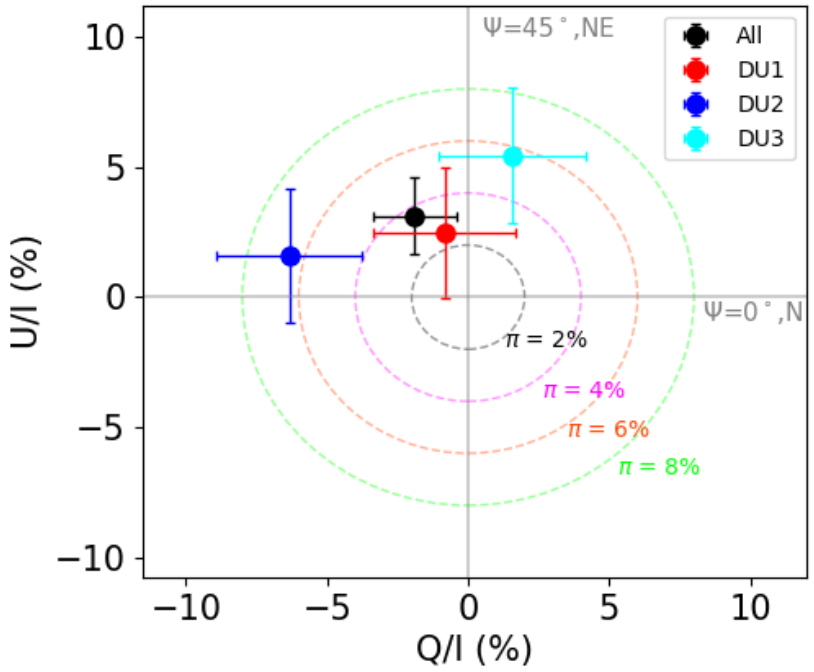

FIGURE 6.2: Normalized U/I and Q/I Stokes parameter in the total 2−8 keV band of *IXPE*. The plotted errors are at the 1σ uncertainties, and the concentric circles correspond to different values of polarization degree.

used models. Thus, from analysis of the AGN X-ray continuum, it is not possible to constrain the geometry of the corona, while X-ray polarimetric observations could provide the needed constraint on the coronal geometry. As part of this thesis, we analysed the first X-ray polarimetric observations carried out on this source by *IXPE*.

6.1 Observations and reduction of data

IC 4329A was observed by *IXPE* (Weisskopf et al. 2022) on January 5, 2023, with a net exposure of about 458 ks with the three detector units (DUs). The log of the *IXPE* observation is given in Table 6.1. The calibrated data were produced by

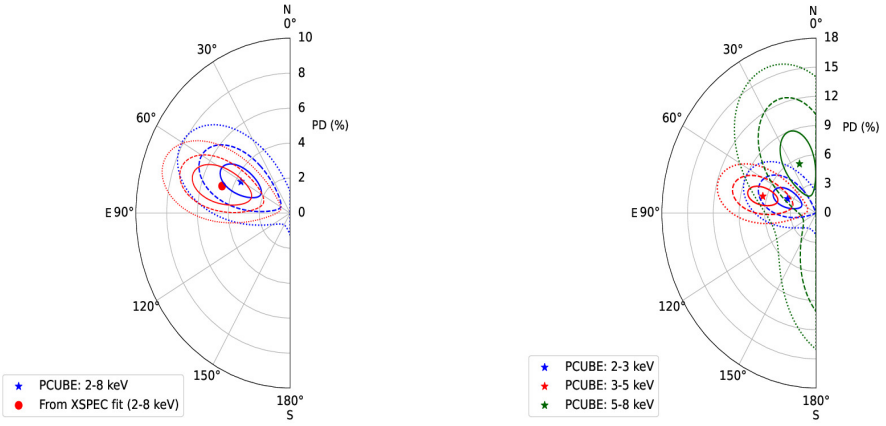

FIGURE 6.3: The 68%, 90% and 99% confidence contours between Π_X and Ψ_X in the 2−8 keV (left panel) band and in three different energy bands (right panel).

TABLE 6.1: Log of *IXPE* observation.

OBSID	Date	Exposure Time (secs)
01003601	2023-01-05	457715

the standard *IXPE* pipeline provided by the Science Operation Center. We used the cleaned and calibrated level 2 data for the scientific analysis.

We analysed the publicly available data on IC 4329A with the software `IXPEOBSSIM` v30.0.0 (Baldini et al. 2022). A count map in sky coordinates was generated using the `CMAP` algorithm within the `xpbin` task. We adopted a circular aperture of 70″ radius for extracting the source counts from the three DUs, and a source-free region with a radius of 100″ was chosen for the background extraction for each DU. We then used the `xpselect` task to generate the filtered source and background regions. For the spectro-polarimetric analysis, the source and background I, Q and U Stokes spectra were generated using the `PHA1`, `PHA1Q` and `PHA1U` algorithm using `xpbin` task within `IXPEOBSSIM` for the three DUs. We used a minimum of 30 counts/bin to bin the I spectra, whereas, in the case of Q and U spectra, we adopted a constant energy binning of 0.2 keV.

6.2 Analysis

6.2.1 Polarimetry

The polarimetric signal from IC 4329A was analysed using the `PCUBE` algorithm in the `xpbin` task. The three polarization cubes for the three DUs were generated to extract information like the I, Q and U Stokes parameters; the minimum detectable polarization (MDP); the polarization degree (Π_X); the polarization angle (Ψ_X) and their associated errors. We first generated the three polarization cubes corresponding to three DUs in the entire 2−8 keV energy band. The combined polarization parameters in the 2−8 keV band from the three DUs are given in Table 6.2. We found $\Pi_X = 3.7\pm1.5\%$, MDP = 4.5% and $\Psi_X = 61°\pm12°$. The normalized values of U/I and Q/I Stokes parameters obtained from the three polarization cubes corresponding to the three DUs and from the combined cube are shown in Fig. 6.2.

To check for the energy dependence of the polarization parameters, we also derived the polarization parameters in three energy bins of 2−3 keV, 3−5 keV and 5−8 keV using the `PCUBE` algorithm. We give in Table 6.2 the values of the derived parameters. The polarization contours for the total 2−8 kev energy range as well as for the different energy ranges are given in Fig. 6.3. From Table 6.2 and Fig. 6.3, it is evident that Π_X and Ψ_X are consistent within errors in the energy range of 2−3, 3−5 and the 2−8 keV, while there is a tendency for a decrease in Ψ_X in the 5−8 keV band. However, the error is so large to arrive at any firm conclusion on the change in Ψ_X at the higher energy band.

Though the values of Π_X in the 2−3, 5−8 and 2−8 keV bands are close to or lower than the MDP values, at 3−5 keV, we found a Π_X of 6.5±1.8%. This exceeds the value of MDP of 5.5%. We thus conclude to have detected significant

X-ray polarization in IC 4329A, and this is the first report of the measurement of the X-ray polarization signal in IC 4329A.

6.2.2 Spectro-polarimetry

We carried out the spectro-polarimetric analysis in the 2−8 keV energy band of the *IXPE* I, Q, U spectra. For spectral fitting, we used an absorbed *powerlaw*, modified by a multiplicative constant polarization model *polconstant* in XSPEC V12.13.0c (Arnaud 1996). This model assumes a constant polarization degree and a constant polarization angle over the specific energy band. In XPSEC the model takes the following form,

$$constant \times TBabs \times zTBabs \times (polconst \times po) \tag{6.1}$$

Here, the *const* represents the inter-calibration constant for each detector, which varies between 0.95 to 1.00. *TBabs* was used to model the Milky-Way Galactic hydrogen column density, which was obtained from Willingale et al. (2013). To model the host galaxy column density, we used *zTBabs* and let the column density (N_H) vary during the fit. This model fits the I, Q, and U spectra well with a reduced chi-square ($\Delta\chi^2$) = 1083/1064. The best fit I, Q and U spectra with the residues are given in Fig. 6.4. The spectro-polarimetric fit produced a Π_X of 4.7±2.2% (larger than the MDP value of 4.5%) and Ψ_X of 71°±14° associated with the primary emission when modelled with a power law of photon index (Γ) of 1.95±0.05. In Fig. 6.3, the contours between Π_X and Ψ_X in 68%, 90% and 99% are plotted along with the contours obtained from the polarimetric analysis. All the model parameters for each of the detectors were tied during the fit. The errors were calculated at the 90% confidence (χ^2 = 2.71 criterion). We give in Table 6.3 the obtained best-fitted parameters. We also performed an MCMC analysis

TABLE 6.2: Polarization parameters in different energy bands.

Energy band keV	$\Pi_X \pm 1\sigma$ %	MDP %	$\Psi_X \pm 1\sigma$ degree
2− 8	3.7±1.5	4.5	61±12
2− 3	3.6±1.8	5.5	66±14
3− 5	6.5±1.8	5.5	74±8
5− 8	5.4±3.5	10.73	21±19

to calculate the errors in 90% confidence associated with the best-fit parameters. The errors from the MCMC analysis are also reported in Table 6.3.

6.3 Discussion

The measured polarised X-ray emission in the radio-quiet category of AGN is believed to be due to the inverse Compton scattering of UV/optical photons from the accretion disk photons by hot electrons in the corona. Therefore, the measured degree of X-ray polarization depends on the geometry of the X-ray corona. We examined the polarimetric properties of the Seyfert 1 galaxy IC 4329A using the *IXPE* data through a model-independent as well as spectro-polarimetric analysis. Using the model-independent approach in the 2−8 keV, we found a polarization angle of 61°±12° and a polarization degree of 3.7±1.5% which is slightly lower than the MDP value of 4.5% (at the 1σ confidence level). From spectro-polarimetric analysis, we found values of Π_X and Ψ_X of 4.7±2.2% (larger than the MDP value of 4.5%) and 71°±14° respectively. Recently, Ursini et al. (2021) simulated polarization signals expected from AGN corona for three different geometries, namely, slab (inner radius $\sim 10R_g$), spherical lamp−post (radius $\sim 10R_g$ and height $\sim 30R_g$ above the accretion disk) and the truncated cone geometry for an outflowing corona (a failed jet with an outflowing velocity of 0.3c and initial radius of $20-30R_g$). The authors claimed that for a slab coronal geometry, the polarization degree goes up to 12%. For the symmetrical nature of a spherical

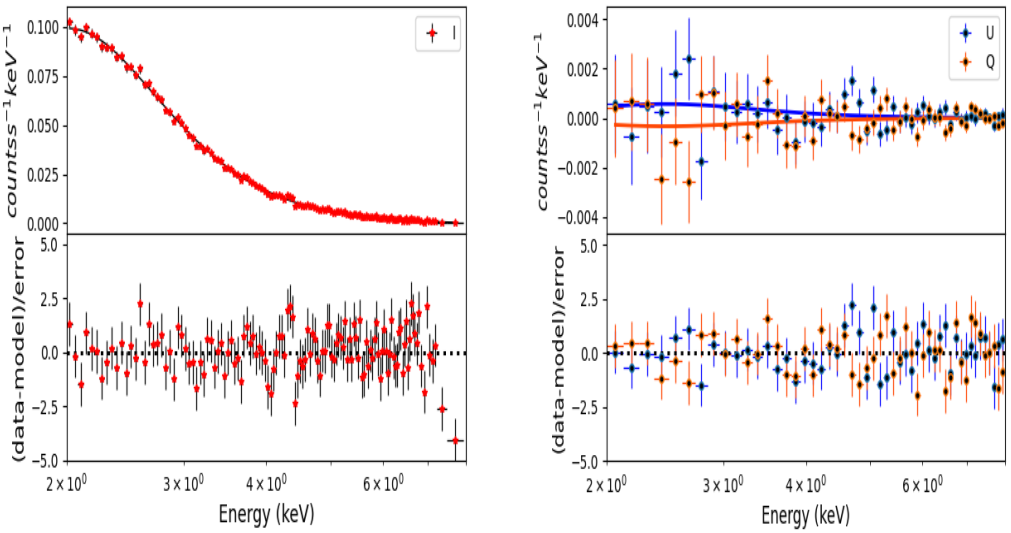

FIGURE 6.4: Left panel: *IXPE* I Stokes best-fitted spectra with residuals. Right panel: The best-fitted Q and U Stokes spectra with residuals.

lamp−post corona, it is expected that the polarization signal received from such sources would be lower than the slab one. For such geometrics, a very low polarization degree ($\sim$ 1−3 %) is expected (Poutanen & Svensson 1996; Tamborra et al. 2018). For the conical corona, the expected polarization could be between the slab and the spherical ones. From their simulation using the `MONK` (Zhang et al. 2019) code, Ursini et al. (2021) also reported that the polarization angle is close to 180° for slab geometry, while for the spherical and conical geometries, it is scattered around 90°. Our measured value of $\Pi_X = 6.5 \pm 1.8\%$ in the 3-5 keV rules out the corona to have a spherical lamp−post geometry. However, compared with the simulations of Ursini et al. (2021), our measured values argue for a conical geometry for the corona in IC 4329A.

6.4 Summary

We carried out the analysis of the first X-ray polarimetric observations using *IXPE* on IC 4329A for a total duration of 458 ksec was taken on 05 January 2023. The findings of the polarimetric study are as follows,

1. From a model-independent analysis, we found a value of $\Pi_X = 3.7 \pm 1.5\%$ and $\Psi_X = 61^\circ \pm 12^\circ$ in the 2−8 keV band. This value of Π_X is slightly lower than the MDP value of 4.5%.

2. From the spectro-polarimetric analysis of model fits to the spectra, we found values of Π_X and Ψ_X of $4.7 \pm 2.2\%$ and $71^\circ \pm 14^\circ$ respectively in the 2−8 keV band. Thus, the polarimetric measurements obtained from both model-independent and spectro-polarimetric analyses agree with each other. Also, the value of Π_X obtained from fitting a model to the observed spectrum is larger than the MDP value of 4.5%.

3. To check for energy-dependent polarization, we derived the polarization parameters in different energy bands. While Π_X is found to be similar within error bars in all the energy bands, the derived values of Ψ_X are found to agree within errors in the 2−3, 3−5 and 2−8 keV bands. There is a tendency for lower values of Ψ_X in the higher energy range of 5−8 keV. However, the error bar is too large in this energy range. Our observations do not find evidence of changes in polarization between energy bands.

4. In the 3−5 keV band, from model-independent analysis, we found a Π_X of $6.5 \pm 1.8\%$. This is greater than the MDP value of 5.5%. Also, from spectro-polarimetric analysis, we found a Π_X of $4.7 \pm 2.2\%$ in the 2−8 keV band, which is larger than the MDP at that energy band. We, therefore, conclude to have detected X-ray polarization in IC 4329A.

TABLE 6.3: Results of spectro-polarimetric analysis.

Parameters	XSPEC analysis	MCMC analysis
N_H	$0.70^{+0.12}_{-0.12}$	$0.70^{+0.12}_{-0.11}$
Π_X (%)	$4.7^{+2.2}_{-2.2}$	$4.7^{+2.0}_{-2.4}$
Ψ_X (°)	71^{+14}_{-14}	71^{+14}_{-15}
Γ	$1.95^{+0.05}_{-0.05}$	$1.95^{+0.05}_{-0.05}$
N	$0.023^{+0.002}_{-0.002}$	$0.023^{+0.002}_{-0.002}$

5. Our observations, when compared with Monte-Carlo simulations in the literature (Ursini et al. 2021), rule out the corona in IC 4329A to have a spherical lamp−post geometry, instead tend to favour a corona with a conical geometry in IC 4329A.

With the results reported in this work, the number of Seyfert type AGN with measured X-ray polarization measurements from *IXPE* observations have increased to four. X-ray polarimetric observations of more Seyfert-type AGN are needed to better constrain the shape of the X-ray corona in AGN. Also, repeated observations of the same source by *IXPE* would enable one to constrain for variations in the geometry of the corona, as has been hinted at from spectral modelling of the observed spectra of AGN in X-rays.

Chapter 7

Summary and Future Prospects

7.1 Summary

This thesis has focussed on characterising the properties of the X-ray corona in the radio-quiet category of AGN, which drives the observed X-ray emission in these objects. The shape of the X-ray continuum in these objects depends on, among other factors, the temperature of the corona (kT_e). The launch of the *NuSTAR* has led to the determination of E_{cut}, and thereby kT_e, in many AGN. Though kT_e are known for many AGN, variation in kT_e is known only in a small number of AGN. This is partly due to the lack of good S/N X-ray spectra covering a wide range of energies. However, *NuSTAR* has provided good quality spectra for a large number of AGN with increased sensitivity beyond 10 keV. This has enabled the determination of kT_e of the corona in many AGN. Though spectral analysis carried out on *NuSTAR* observation could provide the temperature of

the corona, they are insensitive to the geometry and location of the corona. X-ray polarimetric observations could provide the needed constraint on the coronal geometry. Therefore, along with spectral analysis of AGN, we also analysed the first X-ray polarimetric observations on a Seyfert-type source by *IXPE*. The results obtained in this thesis are summarized below,

1. From a uniform and systematic analysis of 130 Seyfert 1 galaxies, the observations of which were carried out by the *NuSTAR* between August 2013 and May 2022, we investigated the nature of the X-ray corona. These sources have a net count rate in the 3−79 keV band larger than 0.1. From the physical model that fits the *NuSTAR* spectra, we could constrain E_{cut} in the high energy X-ray spectra for 75 sources in our sample. For those 75 sources, we fitted the Comptonization model to estimate kT_e of their corona. We could constrain kT_e in 48 sources. We investigated for possible correlations between various properties of the corona obtained from physical model fits to the observed spectra and between various coronal parameters and physical properties of the sources like Eddington ratio and M_{BH}. We found (a) an anti-correlation between kT_e and optical depth (τ), (b) a strong correlation between Γ and Eddington ratio, (c) a correlation between kT_e and photon index (Γ), (d) an anti-correlation between reflection fraction (R) and Eddington ratio, and (e) a negative correlation between kT_e and R at greater than 84% significance level. From the measured kT_e values, we could position our sample of sources in the compactness (l) - temperature (θ) diagram. We found that in the l - θ plane, all the sources are found to lie below the theoretical runaway pair production line suggesting that the primary X-ray coronal emission from the corona is predominantly from thermal processes.

2. To look for variation in kT_e, we performed the X-ray spectral analysis of 21 Seyferts, having more than one epoch of observations. A total of 72 epochs of data were analysed on these 21 AGN. From phenomenological and physical model fits to the multi-epoch data on these 21 sources from *NuSTAR*, we

could constrain the cut-off energy (E_{cut}) in a large fraction of the sources. Also, from Comptonized model fits, we could obtain kT_e for our sample. Of the 21 sources, at the 90% confidence level, evidence for variation in kT_e was found for two sources, namely NGC 3227 and MCG+08-11-011. For NGC 3227, we found no correlation of kT_e, Γ, R, or τ with flux, while τ is found to anti-correlate with kT_e. This could be due to more than one physical process at work in the source causing the change in kT_e. For MCG+08-11-011 between two epochs, separated by about five years, we found kT_e to decrease from 57^{+29}_{-16} keV to 30^{+11}_{-7} keV. During the same period, the flux decreased from (12.60 to 14.02) $\times 10^{-11}$ erg cm^{-2} s^{-1} and the optical depth increased from 1.68 to 2.73. We thus found a positive correlation between flux and coronal temperature with a reduction of about 40% in optical depth. Our observations tend to favour the vertically outflowing corona scenario for the observed variation in kT_e in MCG+08-11-011. Conclusive evidence for the variation in kT_e is not found in the other 19 sources.

3. From an analysis of NGC 1068, a Compton Thick Seyfert 2 galaxy, using *NuSTAR* and *XMM-Newton* for the first time, we calculated kT_e and also checked for variation in kT_e between epochs. The data that is used consists of (a) eight epochs of observations with *NuSTAR* carried out during the period December 2012 to November 2017, and (b) six epochs of observations with *XMM-Newton* carried out during July 2000 to February 2015. From timing analysis of the *NuSTAR* observations, we found the source not to show any variations in the soft band. However, on examination of the flux at energies beyond 20 keV, during August 2014 and August 2017, the source was brighter by about 20% and 30%, respectively, compared to the mean flux of the three 2012 *NuSTAR* observations as in agreement with earlier results in the literature. From an analysis of *XMM-Newton* data, we found no variation in the hard band (2−4 keV) between epochs as well as within epochs. In the soft band (0.2−2 keV), while the source was found to be not variable within epochs, it was found to be brighter in epoch B relative to

epoch A. By fitting physical models, we determined kT_e to range between $8.46^{+0.39}_{-0.66}$ keV and $9.13^{+0.63}_{-0.98}$ keV. From our analysis, we conclude that we found no variation of kT_e in the source.

4. From an analysis of the *IXPE* observations of IC 4329A, we found a polarization degree (Π_X) of 3.7±1.5% and a polarization position angle (Ψ_X) of 61°±12° in the 2−8 keV energy range using a model-independent analysis (at 1σ confidence level). This is found to be similar to the values of Π_X and Ψ_X of 4.7±2.2% and 71° ±14° respectively deduced through spectro-polarimetric analysis of the I, Q and U Stokes spectra in the same energy band at the 90% confidence level. The value of Π_X in the 2−8 keV band obtained from the model-independent analysis is lower than the MDP value of 4.5%. However, Π_X obtained from spectro-polarimetric analysis in the 2−8 keV band is larger than the MDP value. In the 3−5 keV band, we obtained a value of $\Pi_X = 6.5 \pm 1.8$, larger than the MDP value of 5.5%. This is against the value expected from a corona with a spherical lamp post geometry based on simulations. Instead, the deduced values of the degree of polarisation in the 3−5 keV energy range is in agreement with the expected X-ray polarisation signal from a corona with a conical geometry. For IC 4329A, this is the first time measurement of polarised X-rays. We note that with the availability of X-ray polarisation measurements from many AGN, we will be better placed in the future to constrain the shape of the X-ray corona in AGN.

7.2 Future prospects

The X-ray emitting corona is an important component of AGN, and our understanding of its characteristics is extremely important in enhancing our knowledge of the central regions of AGN. In the past, data from several high energy X-ray

missions such as *CGRO*, *BeppoSAX*, *INTEGRAL*, *Swift-BAT*, *Suzaku* etc. were analyzed to understand the coronal physics in AGN, but after the launch of *NuSTAR* a major breakthrough happened in our understanding of the hard X-ray AGN spectra. Due to the instrument's broad spectral coverage (3 to 79 keV), and high sensitivity beyond 10 keV, it has now been possible to constrain several coronal parameters, especially the E_{cut} of the Comptonization spectrum from the analysis of *NuSTAR* data. Importantly, in addition to constraining E_{cut}, there are examples of a few sources in which variation in the spectral shape and kT_e has been reported. Such studies on the variation of the Comptonized spectrum enabled us to study the variable corona in AGN as well. From a study of multi-epoch *NuSTAR* data for a sample of Seyfert galaxies, we found that the physics behind the coronal temperature variation is not the same. Also, there are many sources for which we could not find a variation. This demands deeper studies of AGN for its coronal properties, which might be possible from next-generation X-ray instruments with sensitive broad-band coverage beyond the energy range of NuSTAR.

Though recent observations have succeeded in the determination of various properties of AGN corona, one of the important unknowns in such a study is the geometry of the corona. The most effective way to understand the coronal geometry or its position near the central engine in AGN is the polarization of the X-ray emission. Recently, polarization degree < 4.7 % has been derived in a radio-quiet Sy1.9 type AGN MCG-05-23-16 using *IXPE* (Marinucci et al. 2022). From the analysis of the *IXPE* data of the Circinus Galaxy, Ursini et al. (2023), reported $\Pi_X = 28\%$, which is thought to be due to reflection from the torus. For NGC 4151, Gianolli et al. (2023), found Π_X and Ψ_X of 4.9 $\pm$1.1% and 86°$\pm$7° respectively, arguing for a slab geometry of the corona.

Thus the polarisation observations available as of now point to a complex picture. It is unclear if all AGN have similar coronal geometry or if the coronal geometry

also changes with time. This demands observations of more AGN for X-ray polarisation as well as repeated polarisation observations of sources. I aim to focus on these aspects. In this thesis, I have carried out an investigation of Seyfert type AGN to understand their coronal properties, but such a study on Seyfert 2 type AGN is still missing. In the future, I aim to extend the analysis carried out in this thesis to Seyfert 2 galaxies. By fitting appropriate modern physical models to the source spectra, I plan to characterize the corona in Seyfert 2 type sources and check for the variation of kT_e if any. I aim to investigate several correlations between the coronal parameters and various physical properties of the sources to check for any differences in the X-ray corona between Seyfert 1 and 2 galaxies.

Appendix A

Comparison with existing results in the literature

A.1 Cut-off energy: E_{cut}

Of the 130 sources, analysed in this work (Chapter 3), we could constrain kT_e for 48 sources. In this work, for those 48 sources, E_{cut} measurements were also carried out using physical model fits (*xillver/relxill/(relxill+xillver)*) to the data. For these 48 sources, E_{cut} measurements for 47 sources are available in the literature using phenomenological model (*pexrav/pexmon*) fits to the observed data. A comparison of the E_{cut} measurement is given in Table A.1. In the comparison, we dropped Ark 564 as it is known to host a corona with variable temperature and E_{cut} obtained for the epoch of observation in this work was not analyzed earlier in the literature.

For the majority of the sources in literature, E_{cut} was reported using the broad-band spectral analysis of the *NuSTAR* data in conjunction with the soft X-ray data from several other instruments, such as *XMM-Newton*, *Swift-XRT* etc. (Fabian et al. 2015; Turner et al. 2018; Molina et al. 2019; Porquet et al. 2021; Hinkle & Mushotzky 2021; Kamraj et al. 2022; Diaz et al. 2023). In a few references E_{cut} was obtained from the analysis of the *Swift-BAT*, *BeppoSAX* and *INTEGRAL* broad-band X-ray data (Dadina 2007; Ricci et al. 2017; Molina et al. 2013; Malizia et al. 2014). As seen from Table A.1, our results found from the analysis of only the *NuSTAR* data are in agreement with the previous analysis. Our derived E_{cut} also matches with those already reported in the literature using only the *NuSTAR* data (Tortosa et al. 2018; Kamraj et al. 2018; Baloković et al. 2020; Ezhikode et al. 2020; Kang et al. 2020; Akylas & Georgantopoulos 2021).

For MKN 6, we obtained a very hard spectral index with a lower E_{cut} that best described the source spectrum. Similar results were reported by Molina et al. (2013) and Kamraj et al. (2022). But using the *Swift/XRT-NuSTAR* spectra Molina et al. (2019) found a relatively higher cut-off value of 120^{+51}_{-28} keV by fixing Γ to 1.73. For comparison, we also fixed Γ to 1.73 and obtained a higher cut-off. But this fit could not describe the spectrum well and we obtained significant residues in the lower and higher energy part. Thus, we conclude that a hard spectrum with a lower E_{cut} could explain the source spectrum.

TABLE A.1: Comparison of E_{cut} obtained in this work with those available in the literature. The asterisk marks against the references indicate that E_{cut} was determined only using NuSTAR data,

Source	This work	From literature	References
	E_{cut} (keV)		
1H 0419-577	59^{+8}_{-7}	63^{+8}_{-9}	Turner et al. (2018)
		49^{+7}_{-5}	Kamraj et al. (2022)
3C 111	128^{+31}_{-21}	136^{+47}_{-29}	Malizia et al. (2014)
3C 120	147^{+12}_{-9}	158^{+8}_{-7}	Hinkle & Mushotzky (2021)
3C 390.3	144^{+34}_{-19}	130^{+42}_{-32}	Molina et al. (2019)
		120±20	Tortosa et al. (2018) *
GRS 1734-292	75^{+6}_{-5}	53^{+13}_{-9}	Molina et al. (2019)
		53±10	Tortosa et al. (2018)*
HE 1136-2304	86^{+16}_{-12}	≥63	Ricci et al. (2017)
		97^{+136}_{-77}	Diaz et al. (2023)
HE 1143-1810	104^{+24}_{-17}	183^{+219}_{-59}	Ricci et al. (2017)
IC 4329A	191^{+14}_{-10}	153^{+20}_{-16}	Molina et al. (2019)
		152^{+51}_{-32}	Malizia et al. (2014)
		185±15	Malizia et al. (2014)
IGR J21247+5058	87^{+18}_{-13}	79^{+23}_{-15}	Malizia et al. (2014)
		155^{+157}_{-41}	Molina et al. (2013)

Continued

NuSTAR Ref.

Table A.1 – Following the previous page

Source	This work	From literature	References
	E_{cut} (keV)		
IRAS 04124-0803	80^{+21}_{-14}	$\geq$40	Ricci et al. (2017)
IRAS 09149-6206	81^{+60}_{-26}	$\geq$99	Ricci et al. (2017)
IRAS 05589+2828	136^{+109}_{-56}	71^{+20}_{-14}	Ricci et al. (2017)
MCG-06-30-15	126^{+23}_{-19}	170^{+240}_{-53}	Dadina (2007)
		63^{+24}_{-14}	Malizia et al. (2014)
		>110	Tortosa et al. (2018)*
MCG+08-11-011	153^{+15}_{-13}	163^{+53}_{-32}	Molina et al. (2019)
		171^{+44}_{-30}	Malizia et al. (2014)
		175^{+110}_{-50}	Tortosa et al. (2018)*
Mrk 110	92^{+5}_{-5}	117^{+12}_{-17}	Porquet et al. (2021)
Mrk 509	87^{+4}_{-4}	60^{+71}_{-23}	Dadina (2007)
		102^{+43}_{-19}	Ricci et al. (2017)
Mrk 520	60^{+11}_{-9}	70^{+118}_{-27}	Kamraj et al. (2022)
Mrk 841	125^{+49}_{-30}	139^{+142}_{-49}	Hinkle & Mushotzky (2021)
Mrk 915	70^{+12}_{-10}	58^{+11}_{-7}	Hinkle & Mushotzky (2021)
NGC 3227	94^{+7}_{-6}	60^{+5}_{-4}	Hinkle & Mushotzky (2021)
		87^{+16}_{-12}	Kamraj et al. (2022)

Continued

NuSTAR Ref.

Table A.1 – Following the previous page

Source	This work	From literature	References
	E_{cut} (keV)		
NGC 3783	112^{+24}_{-19}	98^{+79}_{-34}	Fabian et al. (2015)
		77^{+16}_{-11}	Kamraj et al. (2022)
NGC 5273	68^{+25}_{-16}	115^{+91}_{-37}	Akylas & Georgantopoulos (2021)*
		>220	Kamraj et al. (2022)
NGC 5506	81^{+78}_{-10}	110±10	Baloković et al. (2020)*
NGC 5548	118^{+12}_{-8}	70^{+40}_{-10}	Ursini et al. (2015)
NGC 7469	122^{+27}_{-21}	113^{+33}_{-22}	Hinkle & Mushotzky (2021)
PG0026+129	97^{+20}_{-15}	≥45	Ricci et al. (2017)
SWIFTJ2127.4+5654	84^{+6}_{-6}	92^{+26}_{-17}	Kang et al. (2020)*
UGC 06728	66^{+7}_{-6}	63^{+133}_{-25}	Kamraj et al. (2022)
IGRJ19378-0617	228^{+419}_{-83}	241^{+1377}_{-114}	Kamraj et al. (2022)
Fairall 51	86^{+11}_{-9}	>99	Ricci et al. (2017)
MRK 279	68^{+18}_{-13}	≥125	Ricci et al. (2017)
ESO 323−G077	89^{+14}_{-13}	115^{+114}_{-42}	Kamraj et al. (2022)
CGCG229−015	46^{+14}_{-8}	≥35	Ricci et al. (2017)
		54^{+76}_{-22}	Akylas & Georgantopoulos (2021)*
2MASXJ21355399+4728217	56^{+15}_{-10}	67^{+96}_{-23}	Ricci et al. (2017)

Continued

NuSTAR Ref.

Table A.1 – Following the previous page

Source	This work	From literature	References
	E_{cut} (keV)		
		55^{+50}_{-19}	Akylas & Georgantopoulos (2021)*
2MASXJ18560128+1538059	41^{+5}_{-5}	43^{+20}_{-11}	Akylas & Georgantopoulos (2021)*
3C 109	72^{+10}_{-9}	112^{+62}_{-58}	Hinkle & Mushotzky (2021)
RBS0770	65^{+8}_{-7}	$\geq$267	Kamraj et al. (2018)*
		$\geq$256	Ricci et al. (2017)
MKN 6	43^{+2}_{-2}	26^{+6}_{-5}	Kamraj et al. (2022)
		68^{+276}_{-26}	Molina et al. (2013)
3C 382	112^{+12}_{-10}	158^{+39}_{-76}	Kamraj et al. (2022)
		133^{+98}_{-40}	Ezhikode et al. (2020)*
		215^{+150}_{-60}	Tortosa et al. (2018)*
HE 0103-3447	72^{+26}_{-16}	41^{+15}_{-36}	Ricci et al. (2017)
MR2251−178	96^{+17}_{-9}	132^{+130}_{-68}	Dadina (2007)
		138^{+57}_{-38}	Malizia et al. (2014)
		77^{+19}_{-14}	Akylas & Georgantopoulos (2021)*
Mrk 1148	99^{+30}_{-20}	101^{+11}_{-9}	Hinkle & Mushotzky (2021)
Mrk 926	135^{+11}_{-9}	211^{+235}_{-95}	Dadina (2007)
		320^{+166}_{-79}	Ricci et al. (2017)

Continued

NuSTAR Ref.

Table A.1 – Following the previous page

Source	This work	From literature	References
	E_{cut} (keV)		
2MASXJ10523297+1036205	33^{+4}_{-3}	$\geq$35	Ricci et al. (2017)
SDSS J114921.52+532013.4	29^{+9}_{-7}	47^{+86}_{-14}	Ricci et al. (2017)
2MASXJ23013626-5913210	41^{+8}_{-6}	59^{+150}_{-26}	Kamraj et al. (2022)

A.2 Temperature of the corona: kT_e

In this section, we discuss the results obtained from the spectral analysis using the model const × tbabs × ztbabs × (xillverCP/relxillCP/relxillCP+xillverCP). We also compare the best-fit values of our analysis with the previously measured values of kT_e from the literature, if available. Among the 48 sources for which we could constrain kT_e, 17 sources were already discussed by us earlier in Chapter 4. Therefore, here we give details on the rest of the 31 sources.

2MASXJ23013626-5913210: This source at a redshift $z = 0.150$ was observed by *NuSTAR* once in 2017. We used Model−2a (see Chapter 3) to estimate the coronal properties of the source. We found the source spectra to be well described with $\Gamma = 1.87^{+0.04}_{-0.04}$ and $kT_e = 13.35^{+06.23}_{-03.48}$ keV. Previously, using similar Comptonization model Kamraj et al. (2022) found a value of $\Gamma = 1.78^{+0.14}_{-0.11}$ and $kT_e = 11.10^{+12.22}_{-02.87}$ keV. Our results are thus in agreement with Kamraj et al. (2022).

2MASXJ19301380+3410495: This source is situated at z=0.0629 and was observed by *NuSTAR* twice between July 2016 and October 2017. Here we report the analysis of the spectrum taken in 2017 as it satisfied our criteria of count rate > 0.1. From spectral fits to the data using Model−2b (see Chapter 3), we found that a high intrinsic hydrogen column density was needed to take care of the absorption in the low energy part of the spectrum (see Table 3.2). During the spectral fit, we had to freeze the ionization parameter and the inner and outer emissivity indices (by tying these two indices together) to 2.0 and 3.0, respectively. From the spectral analysis we found $\Gamma = 1.72^{+0.13}_{-0.35}$ and $kT_e = 09.97^{+04.09}_{-05.08}$ keV which is similar to the value of $\Gamma = 1.87^{+0.44}_{-0.24}$ found by Kamraj et al. (2022). While we could constrain kT_e, Kamraj et al. (2022) obtained a lower limit of $kT_e > 13.74$ keV using *xillverCP* model.

3C 120: This is a radio-loud Seyfert 1 galaxy at z=0.033. *NuSTAR* observed

the source two times on the same day in February 2013. Of the two observations, we analysed the spectrum with the highest exposure time using Model−2b (see Chapter 3). We obtained values of $\Gamma = 1.85^{+0.01}_{-0.01}$ and $kT_e = 45.31^{+18.79}_{-07.82}$ keV respectively. Kang & Wang (2022) analysing the same data using *relxillCP* found a lower limit of $kT_e > 91$ keV.

3C 390.3: This radio-loud Seyfert 1 galaxy at z=0.05613 was observed twice by *NuSTAR* on the same day in May 2013. From spectral analysis of the data using Model−2a (see Chapter 3) we obtained $\Gamma = 1.84^{+0.01}_{-0.01}$ and $kT_e = 44.13^{+54.75}_{-12.50}$ keV. For the same data set Kang & Wang (2022) and Kamraj et al. (2022) reported lower limits of $kT_e > 46$ keV and $kT_e > 49.86$ keV respectively.

ARK 564: This source was observed by *NuSTAR* two times between May 2015 and November 2018. Of these, results on the observation done by *NuSTAR* is reported in this work for the first time. Fitting the observed data with Model−2c (see Chapter 3), we obtained $\Gamma = 2.40^{+0.02}_{-0.02}$ and $kT_e = 24.28^{+13.60}_{-04.29}$ keV respectively. From analysis of the data acquired by *NuSTAR* in 2015, Kara et al. (2017) determined $kT_e = 15 \pm 2$ keV arguing the source to have the coolest corona. Also, based on two epochs of data, Barua et al. (2020) reported variation in the temperature of the corona.

HE 0103−3447: This Seyfert 1 galaxy at z=0.057 was observed by *NuSTAR* once in February, 2019. Results on spectral analysis are reported for the first time. Using Model−2a (see Chapter 3) we found that the Comptonized spectrum was well described with $\Gamma = 1.68^{+0.03}_{-0.03}$ and $kT_e = 14.29^{+08.62}_{-03.18}$ keV. We also found a very weak reflection component with an upper limit of R<0.17.

HE 1136−2304: This Seyfert galaxy is a changing look AGN. It was found to change its optical spectral nature from Type 2 in 1993 to type 1.5 in 2014 (Parker et al. 2016). It was observed by *NuSTAR* twice on the same day in July 2014. Of

the two, we analysed the spectrum with maximum exposure. The best fit values obtained from fitting Model−2a (see Chapter 3) to the source spectrum were $\Gamma = 1.78^{+0.03}_{-0.02}$ and $kT_e = 27.81^{+78.85}_{-09.30}$ keV. From an analysis of same *NuSTAR* spectrum using *relxillCP* Kang & Wang (2022) obtained a lower limit of $kT_e > 21$ keV.

IC 4329A: This Seyfert 1 galaxy was observed six times by *NuSTAR*, once in 2012 and the others during August 2021. We analysed here the *NuSTAR* spectrum taken in 2012. Fitting the spectrum using Model−2a (see Chapter 3) we obtained best fit values of Γ and kT_e as $1.83^{+0.003}_{-0.003}$ and $64.16^{+15.41}_{-11.63}$ keV respectively. This source has been studied extensively in the past. For example, Tortosa et al. (2018) reported $kT_e = 37\pm7$ keV from fitting *compTT* for a slab geometry. Kang & Wang (2022) estimated $kT_e = 71^{+37}_{-15}$ keV using *relxillCP* model. Kamraj et al. (2022) also found $kT_e = 82^{+16}_{-7}$ keV from *xillverCP* fit to the source spectrum.

IGR J17476−2253: The source is classified as a Seyfert 1 galaxy and is at z=0.047. It has not been studied for its coronal properties before, and the temperature of its coronal has been reported for the first time. From fitting Model−2a (see Chapter 3) to the source spectrum we obtained $\Gamma = 1.69^{+0.03}_{-0.03}$ and $kT_e = 13.81^{+12.77}_{-03.48}$ keV.

IGR J21247+5058: This Seyfert 1 galaxy was observed by *NuSTAR* two times between December 2014 and January 2018. Both the data sets were analysed by Buisson et al. (2018) and from *xillverCP* model fit to the source spectra the authors reported $kT_e = 19^{+3}_{-2}$ keV and $kT_e = 20^{+3}_{-2}$ keV in the year 2014 and 2018 respectively. We analysed the *NuSTAR* data of the source observed in January 2018 using Model−2a (see Chapter 3). We obtained best-fit values of $\Gamma = 1.79^{+0.01}_{-0.01}$ and $kT_e = 24.70^{+03.79}_{-02.68}$ keV. Recently, Kang & Wang (2022) also reported $kT_e = 26^{+6}_{-3}$ keV from an analysis of 2018 *NuSTAR* spectra. The results obtained from these sources are thus in agreement with the results recently reported in the literature.

2MASXJ21355399+4728217: This Seyfert galaxy was observed by *NuSTAR* on September 2019. From the analysis of the source spectrum Akylas & Georgantopoulos (2021) reported $E_{cut} = 55^{+50}_{-19}$ keV. We analysed the same observation ID using Model−2a (see Chapter 3) and found $kT_e = 15.57^{+12.24}_{-03.90}$ keV.

IRAS 04124-0803: Analysis of the *NuSTAR* observations (done in September 2021) on this source is carried out for the first time. From fitting Model−2a (see Chapter 3) to the source spectrum, we obtained the best fit values of $\Gamma = 1.66^{+0.03}_{-0.03}$ and $kT_e = 14.88^{+03.70}_{-02.57}$ keV.

IRAS 09149-6206: Results on *NuSTAR* observations of this source are reported for the first time. This source was observed by *NuSTAR* twice between July and August, 2018. We modelled the Comptonized spectrum (observed on August 2018) and estimated the best-fit value of kT_e using Model−2b (see Chapter 3). From the model fit to the spectrum we obtained $\Gamma = 1.90^{+0.11}_{-0.09}$ and $kT_e = 18.09^{+16.87}_{-04.07}$ keV.

IRAS 05589+2828: This Seyfert 1 galaxy situated at z=0.02940 was observed by *NuSTAR* in April 2020. The temperature of the corona of the source is reported for the first time. From the physical model fit to the observed spectrum we found values of $\Gamma = 1.90^{+0.11}_{-0.07}$ and $kT_e = 42.90^{+120.46}_{-23.92}$ keV (see Chapter 3).

Mrk 1148: This Seyfert 1 galaxy was observed by *NuSTAR* in January, 2018. We carried out the spectral analysis using Model−2a (see Chapter 3). The best-fit values obtained using the model fit to the spectrum are $\Gamma = 1.86^{+0.02}_{-0.02}$ and $kT_e = 24.04^{+19.81}_{-06.76}$ keV. Recently, analysing the same spectrum, both Kamraj et al. (2022) and Kang & Wang (2022) found values of $kT_e > 18$ keV.

Mrk 509: *NuSTAR* observed the source two times between April and June 2015. In this work, we analysed the spectrum taken on April 2015. From fitting

Model−2c (see Chapter 3) to the observed spectrum we obtained $\Gamma = 1.86^{+0.01}_{-0.02}$ and $kT_e = 35.78^{+06.78}_{-05.72}$ keV. On analysis of same spectrum using *relxillCP* model Kang & Wang (2022) reported relatively smaller value of $kT_e = 24 \pm 2$ keV.

2MASXJ18560128+1538059: This Seyfert 1 galaxy was observed by *NuSTAR* in 2017, and from the analysis of the source spectrum using our Model−2a (see Chapter 3), we found $kT_e = 12.32^{+3.12}_{-2.36}$ keV. Using the same observation ID Akylas & Georgantopoulos (2021) reported $E_{cut} = 43^{+20}_{-11}$ keV.

Mrk 520: This Seyfert 1 galaxy was observed by *NuSTAR* once in May, 2017. In this work, we report an estimate of the temperature of the corona of the source for the first time. By fitting Model−2a (see Chapter 3) to the observed spectrum, we obtained $\Gamma = 1.63^{+0.03}_{-0.03}$ and $kT_e = 15.20^{+04.36}_{-02.77}$ keV.

PG 0026+129: *NuSTAR* observed the Seyfert 1 galaxy once in January 2021 and results on the analysis of the observation is reported for the first time. From Model−2a (see Chapter 3) fit to the observed spectrum we obtained best fit values of $\Gamma = 1.89^{+0.01}_{-0.01}$ and $kT_e = 22.18^{+08.88}_{-04.03}$ keV.

SWIFTJ2127.4+5654: This source classified as a narrow line Seyfert 1 galaxy, was observed by *NuSTAR* nine times between September 2012 and December 2018. We analysed the observations carried out by *NuSTAR* in September 2012 as it has the maximum exposure time. By fitting the observed spectrum using Model−2a (see Chapter 3), we obtained $\Gamma = 1.96^{+0.01}_{-0.01}$ and $kT_e = 20.70^{+03.36}_{-01.94}$ keV. From an analysis of the same spectrum, Kang et al. (2021a) reported a kT_e of 21^{+2}_{-2} keV.

IGRJ19378−0617: This source is situated at z=0.0103. It was classified as a Seyfert 1 galaxy, observed six times by *NuSTAR* between 2015 and 2022. From fitting the source spectrum using Model−2a (see Chapter 3), we found $kT_e = 49.35^{+36.94}_{-13.04}$ keV. From the spectral analysis of the source spectrum Kamraj et al.

(2022) reported $kT_e > 122$ keV.

Fairall 51: *NuSTAR* observed this Seyfert 1 galaxy 4 times between 2018 and 2021. We analysed the *NuSTAR* spectrum observed in June 2018. From fitting the source spectrum using Model−2a (see Chapter 3), we found $kT_e = 19.48^{+6.54}_{-1.83}$ keV.

Mrk 279: This Seyfert 1 galaxy was observed 4 times by *NuSTAR* between 2019 and 2020. We analysed the August 2020 spectrum using Model−2c (see Chapter 3) and found $kT_e = 16.38^{+1.72}_{-1.55}$ keV. By analysing the source spectrum taken in October 2019, Kang & Wang (2022) reported $E_{cut} > 231$ keV and $kT_e > 84$ keV.

ESO 323−G077: This source is classified as a Seyfer 1.5 galaxy (Winkler 1992), situated at z = 0.0155. *NuSTAR* observed this source six times between August 2016 to February 2017. We analyzed January 2017 *NuSTAR* data. From the Model−2a (see Chapter 3) fit to the source spectrum, we obtained $kT_e = 35.21^{+13.02}_{-11.89}$ keV.

3C 109: This Seyfert galaxy was observed by *NuSTAR* twice in August 2017. We analysed the one with the maximum exposure time. By fitting Model−2a (see Chapter 3) to the source spectrum, we found $kT_e = 18.09^{+6.91}_{-2.72}$ keV.

RBS0770: This source was observed four times between 2012 and 2021 by *NuSTAR*. From the analysis of the same observation, Kamraj et al. (2022) reported a lower limit for $kT_e > 24$ keV. By fitting Model−2a (see Chapter 3) to the source spectrum we found $kT_e = 17.71^{+4.30}_{-2.38}$ keV.

CGCG229−015: This nearby Seyfert 1 galaxy was observed once by *NuSTAR* on February 2018. From an analysis of the same observation ID Akylas & Georgantopoulos (2021) reported $E_{cut} = 54^{+13.02}_{-11.89}$ keV. From the Model−2a (see Chapter

3) fit to the source spectrum, we obtained $kT_e = 17.00^{+41.62}_{-5.61}$ keV.

MKN 6: *NuSTAR* observed this source two times in 2015. We analysed the source spectrum taken on April 2015. From the analysis of this spectrum using Model−2a (see Chapter 3) we found $kT_e = 14.89^{+1.16}_{-1.12}$ keV. By fitting *xillver* to the source spectrum Kamraj et al. (2022) reported $kT_e > 143$ keV.

3C 382: This Seyfert galaxy was observed 7 times between 2012 and 2016. We analysed the 2013 spectrum and reported $kT_e = 33.07^{+16.81}_{-7.76}$ keV (see Chapter 3). From the analysis of the same observation Ezhikode et al. (2020) reported $E_{cut} = 132.75^{+98.32}_{-39.98}$ keV.

SDSS J114921.52+532013.4: This Seyfert 1 galaxy was observed once in 2016. From the Model−2a (see Chapter 3) fit to the source spectrum, we found $kT_e = 6.50^{+1.25}_{-0.97}$ keV.

2MASXJ10523297+1036205: *NuSTAR* observed this source once in 2017. From the analysis using Model−2a (see Chapter 3) we found $kT_e = 13.35^{+6.23}_{-3.48}$ keV.

Bibliography

Aartsen, M. G., Ackermann, M., Adams, J., et al. 2020, *Phys. Rev. Lett.*, 124, 051103, doi: 10.1103/PhysRevLett.124.051103

Abdollahi, S., Acero, F., Ackermann, M., et al. 2020, *Astrophys. J. Suppl.*, 247, 33, doi: 10.3847/1538-4365/ab6bcb

Akylas, A., & Georgantopoulos, I. 2021, *Astron. Astrophys.*, 655, A60, doi: 10.1051/0004-6361/202141186

Antonucci, R. 1993, *Ann. Rev. Astron. Astrophys.*, 31, 473, doi: 10.1146/annurev.aa.31.090193.002353

Antonucci, R. R. J., & Miller, J. S. 1985, *Astrophys. J.*, 297, 621, doi: 10.1086/163559

Arnaud, K. A. 1996, Astronomical Society of the Pacific Conference Series, Vol. 101, XSPEC: The First Ten Years, ed. G. H. Jacoby & J. Barnes, 17

Awaki, H., Koyama, K., Inoue, H., & Halpern, J. P. 1991, *Pub. Astron. Soc. Japan*, 43, 195

Baldini, L., Bucciantini, N., Lalla, N. D., et al. 2022, SoftwareX, 19, 101194, doi: https://doi.org/10.1016/j.softx.2022.101194

Ballantyne, D. R. 2020, *Mon. Not. Roy. Astron. Soc.*, 491, 3553, doi: 10.1093/mnras/stz3294

Ballantyne, D. R., & Xiang, X. 2020, *Mon. Not. Roy. Astron. Soc.*, 496, 4255, doi: 10.1093/mnras/staa1866

Ballantyne, D. R., Bollenbacher, J. M., Brenneman, L. W., et al. 2014, *Astrophys. J.*, 794, 62, doi: 10.1088/0004-637X/794/1/62

Baloković, M., Harrison, F. A., Madejski, G., et al. 2020, *Astrophys. J.*, 905, 41, doi: 10.3847/1538-4357/abc342

Barua, S., Jithesh, V., Misra, R., et al. 2020, *Mon. Not. Roy. Astron. Soc.*, 492, 3041, doi: 10.1093/mnras/staa067

—. 2021, *Astrophys. J.*, 921, 46, doi: 10.3847/1538-4357/ac1c74

Barua, S., Jithesh, V., Misra, R., et al. 2021, The Astrophysical Journal, 921, 46, doi: 10.3847/1538-4357/ac1c74

Bauer, F. E., Arévalo, P., Walton, D. J., et al. 2015, The Astrophysical Journal, 812, 116, doi: 10.1088/0004-637x/812/2/116

Bentz, M. C., Onken, C. A., Street, R., & Valluri, M. 2023, The Astrophysical Journal, 944, 29, doi: 10.3847/1538-4357/acab62

Bianchi, S., Guainazzi, M., Matt, G., Fonseca Bonilla, N., & Ponti, G. 2009, *Astron. Astrophys.*, 495, 421, doi: 10.1051/0004-6361:200810620

Blandford, R. D., & Königl, A. 1979, *Astrophys. J.*, 232, 34, doi: 10.1086/157262

Buisson, D. J. K., Fabian, A. C., & Lohfink, A. M. 2018, *Mon. Not. Roy. Astron. Soc.*, 481, 4419, doi: 10.1093/mnras/sty2609

Cappi, M., De Marco, B., Ponti, G., et al. 2016, *Astron. Astrophys.*, 592, A27, doi: 10.1051/0004-6361/201628464

Crummy, J., Fabian, A. C., Gallo, L., & Ross, R. R. 2006, *Mon. Not. Roy. Astron. Soc.*, 365, 1067, doi: 10.1111/j.1365-2966.2005.09844.x

Dadina, M. 2007, *Astron. Astrophys.*, 461, 1209, doi: 10.1051/0004-6361:20065734

Dauser, T., Garcia, J., Parker, M. L., Fabian, A. C., & Wilms, J. 2014, *Mon. Not. Roy. Astron. Soc.*, 444, L100, doi: 10.1093/mnrasl/slu125

Denney, K. D., Watson, L. C., Peterson, B. M., et al. 2009, *Astrophys. J.*, 702, 1353, doi: 10.1088/0004-637X/702/2/1353

Dewangan, G. C., Tripathi, P., Papadakis, I. E., & Singh, K. P. 2021, Monthly Notices of the Royal Astronomical Society, 504, 4015, doi: 10.1093/mnras/stab1113

Diaz, Y., Hernàndez-García, L., Arévalo, P., et al. 2023, *Astron. Astrophys.*, 669, A114, doi: 10.1051/0004-6361/202244678

Done, C., Davis, S. W., Jin, C., Blaes, O., & Ward, M. 2012, *Mon. Not. Roy. Astron. Soc.*, 420, 1848, doi: 10.1111/j.1365-2966.2011.19779.x

Edelson, R., Turner, T. J., Pounds, K., et al. 2002, *Astrophys. J.*, 568, 610, doi: 10.1086/323779

Edge, D. O., Shakeshaft, J. R., McAdam, W. B., Baldwin, J. E., & Archer, S. 1959, Mem. R. Astron, 68, 37

Ezhikode, S. H., Dewangan, G. C., Misra, R., & Philip, N. S. 2020, *Mon. Not. Roy. Astron. Soc.*, 495, 3373, doi: 10.1093/mnras/staa1288

Ezhikode, S. H., Dewangan, G. C., Misra, R., & Philip, N. S. 2020, Monthly Notices of the Royal Astronomical Society, 495, 3373, doi: 10.1093/mnras/staa1288

Fabian, A. C., Ballantyne, D. R., Merloni, A., et al. 2002, *Mon. Not. Roy. Astron. Soc.*, 331, L35, doi: 10.1046/j.1365-8711.2002.05419.x

Fabian, A. C., Lohfink, A., Belmont, R., Malzac, J., & Coppi, P. 2017, *Mon. Not. Roy. Astron. Soc.*, 467, 2566, doi: 10.1093/mnras/stx221

Fabian, A. C., Lohfink, A., Kara, E., et al. 2015, *Mon. Not. Roy. Astron. Soc.*, 451, 4375, doi: 10.1093/mnras/stv1218

Fabian, A. C., Zoghbi, A., Ross, R. R., et al. 2009, *Nature*, 459, 540, doi: 10.1038/nature08007

Fanaroff, B. L., & Riley, J. M. 1974, *Mon. Not. Roy. Astron. Soc.*, 167, 31P, doi: 10.1093/mnras/167.1.31P

Fath, E. A. 1909, Lick Observatory Bulletin, 149, 71, doi: 10.5479/ADS/bib/1909LicOB.5.71F

García, J., & Kallman, T. R. 2010, *Astrophys. J.*, 718, 695, doi: 10.1088/0004-637X/718/2/695

García, J., Kallman, T. R., & Mushotzky, R. F. 2011, The Astrophysical Journal, 731, 131, doi: 10.1088/0004-637x/731/2/131

García, J., Dauser, T., Lohfink, A., et al. 2014, *Astrophys. J.*, 782, 76, doi: 10.1088/0004-637X/782/2/76

George, I. M., & Fabian, A. C. 1991, *Mon. Not. Roy. Astron. Soc.*, 249, 352, doi: 10.1093/mnras/249.2.352

Gianolli, V. E., Kim, D. E., Bianchi, S., et al. 2023, arXiv e-prints, arXiv:2303.12541, doi: 10.48550/arXiv.2303.12541

Gliozzi, M., & Williams, J. K. 2020, *Mon. Not. Roy. Astron. Soc.*, 491, 532, doi: 10.1093/mnras/stz3005

Grupe, D., Komossa, S., Leighly, K. M., & Page, K. L. 2010, The Astrophysical Journal Supplement Series, 187, 64, doi: 10.1088/0067-0049/187/1/64

Guainazzi, M., Matt, G., Antonelli, L. A., et al. 1999, *Mon. Not. Roy. Astron. Soc.*, 310, 10, doi: 10.1046/j.1365-8711.1999.02803.x

Guilbert, P. W., Fabian, A. C., & Rees, M. J. 1983, *Mon. Not. Roy. Astron. Soc.*, 205, 593, doi: 10.1093/mnras/205.3.593

Haardt, F., & Maraschi, L. 1991, *Astrophys. J. Lett.*, 380, L51, doi: 10.1086/186171

—. 1993, *Astrophys. J.*, 413, 507, doi: 10.1086/173020

Haardt, F., Maraschi, L., & Ghisellini, G. 1994, *Astrophys. J. Lett.*, 432, L95, doi: 10.1086/187520

Harrison, F. A., Craig, W. W., Christensen, F. E., et al. 2013, *Astrophys. J.*, 770, 103, doi: 10.1088/0004-637X/770/2/103

Hazard, C., Mackey, M. B., & Shimmins, A. J. 1963, *Nature*, 197, 1037, doi: 10.1038/1971037a0

Hinkle, J. T., & Mushotzky, R. 2021, *Mon. Not. Roy. Astron. Soc.*, 506, 4960, doi: 10.1093/mnras/stab1976

Ho, L. C. 2008, *Ann. Rev. Astron. Astrophys.*, 46, 475, doi: 10.1146/annurev.astro.45.051806.110546

Huchra, J. P., Vogeley, M. S., & Geller, M. J. 1999, *Astrophys. J. Suppl.*, 121, 287, doi: 10.1086/313194

Inoue, Y., & Doi, A. 2018, *Astrophys. J.*, 869, 114, doi: 10.3847/1538-4357/aaeb95

Iwasawa, K., Fabian, A. C., & Matt, G. 1997, *Mon. Not. Roy. Astron. Soc.*, 289, 443, doi: 10.1093/mnras/289.2.443

Jin, C., Ward, M., & Done, C. 2012, *Mon. Not. Roy. Astron. Soc.*, 425, 907, doi: 10.1111/j.1365-2966.2012.21272.x

Johnson, W. N., McNaron-Brown, K., Kurfess, J. D., et al. 1997, *Astrophys. J.*, 482, 173, doi: 10.1086/304148

Kamraj, N., Harrison, F. A., Baloković, M., Lohfink, A., & Brightman, M. 2018, *Astrophys. J.*, 866, 124, doi: 10.3847/1538-4357/aadd0d

Kamraj, N., Brightman, M., Harrison, F. A., et al. 2022, *Astrophys. J.*, 927, 42, doi: 10.3847/1538-4357/ac45f6

Kang, J., Wang, J., & Kang, W. 2020, *Astrophys. J.*, 901, 111, doi: 10.3847/1538-4357/abadf5

Kang, J.-L., & Wang, J.-X. 2022, The Astrophysical Journal, 929, 141, doi: 10.3847/1538-4357/ac5d49

Kang, J.-L., Wang, J.-X., & Kang, W.-Y. 2021a, *Mon. Not. Roy. Astron. Soc.*, 502, 80, doi: 10.1093/mnras/stab039

—. 2021b, *Mon. Not. Roy. Astron. Soc.*, doi: 10.1093/mnras/stab039

Kara, E., García, J. A., Lohfink, A., et al. 2017, *Mon. Not. Roy. Astron. Soc.*, 468, 3489, doi: 10.1093/mnras/stx792

Keek, L., & Ballantyne, D. R. 2016, *Mon. Not. Roy. Astron. Soc.*, 456, 2722, doi: 10.1093/mnras/stv2882

Kellermann, K. I., Sramek, R., Schmidt, M., Shaffer, D. B., & Green, R. 1989, *Astron. J.*, 98, 1195, doi: 10.1086/115207

Khachikian, E. Y., & Weedman, D. W. 1974, *Astrophys. J.*, 192, 581, doi: 10.1086/153093

Koyama, K., Inoue, H., Tanaka, Y., et al. 1989, *Pub. Astron. Soc. Japan*, 41, 731

Lanzuisi, G., Gilli, R., Cappi, M., et al. 2019, *Astrophys. J. Lett.*, 875, L20, doi: 10.3847/2041-8213/ab15dc

Liu, H., Luo, B., Brandt, W. N., et al. 2021, *Astrophys. J.*, 910, 103, doi: 10.3847/1538-4357/abe37f

Liu, T., Wang, J.-X., Yang, H., Zhu, F.-F., & Zhou, Y.-Y. 2014, *Astrophys. J.*, 783, 106, doi: 10.1088/0004-637X/783/2/106

Lubiński, P., Zdziarski, A. A., Walter, R., et al. 2010, *Mon. Not. Roy. Astron. Soc.*, 408, 1851, doi: 10.1111/j.1365-2966.2010.17251.x

Lubiński, P., Beckmann, V., Gibaud, L., et al. 2016, *Mon. Not. Roy. Astron. Soc.*, 458, 2454, doi: 10.1093/mnras/stw454

Lynden-Bell, D. 1969, *Nature*, 223, 690, doi: 10.1038/223690a0

Magdziarz, P., Blaes, O. M., Zdziarski, A. A., Johnson, W. N., & Smith, D. A. 1998, *Mon. Not. Roy. Astron. Soc.*, 301, 179, doi: 10.1046/j.1365-8711.1998.02015.x

Magdziarz, P., & Zdziarski, A. A. 1995, *Mon. Not. Roy. Astron. Soc.*, 273, 837, doi: 10.1093/mnras/273.3.837

Magdziarz, P., & Zdziarski, A. A. 1995, Monthly Notices of the Royal Astronomical Society, 273, 837, doi: 10.1093/mnras/273.3.837

Malizia, A., Molina, M., Bassani, L., et al. 2014, *Astrophys. J. Lett.*, 782, L25, doi: 10.1088/2041-8205/782/2/L25

Malkan, M. A., & Sargent, W. L. W. 1982, *Astrophys. J.*, 254, 22, doi: 10.1086/159701

Mao, J., Mehdipour, M., Kaastra, J. S., et al. 2019, *Astron. Astrophys.*, 621, A99, doi: 10.1051/0004-6361/201833191

Marchesi, S., Ajello, M., Marcotulli, L., et al. 2018, *Astrophys. J.*, 854, 49, doi: 10.3847/1538-4357/aaa410

Marinucci, A., Bianchi, S., Matt, G., et al. 2016, *Mon. Not. Roy. Astron. Soc.*, 456, L94, doi: 10.1093/mnrasl/slv178

Marinucci, A., Muleri, F., Dovciak, M., et al. 2022, *Mon. Not. Roy. Astron. Soc.*, 516, 5907, doi: 10.1093/mnras/stac2634

Markoff, S., Nowak, M. A., & Wilms, J. 2005, *Astrophys. J.*, 635, 1203, doi: 10.1086/497628

Markowitz, A., Reeves, J. N., George, I. M., et al. 2009, *Astrophys. J.*, 691, 922, doi: 10.1088/0004-637X/691/2/922

Markowitz, A., Edelson, R., Vaughan, S., et al. 2003, *Astrophys. J.*, 593, 96, doi: 10.1086/375330

Masetti, N., Parisi, P., Palazzi, E., et al. 2013, *Astron. Astrophys.*, 556, A120, doi: 10.1051/0004-6361/201322026

Matt, G., Bianchi, S., Guainazzi, M., & Molendi, S. 2004, *Astron. Astrophys.*, 414, 155, doi: 10.1051/0004-6361:20031635

Matt, G., Fabian, A. C., Guainazzi, M., et al. 2000, *Mon. Not. Roy. Astron. Soc.*, 318, 173, doi: 10.1046/j.1365-8711.2000.03721.x

Matt, G., Fabian, A. C., & Ross, R. R. 1993a, *Mon. Not. Roy. Astron. Soc.*, 262, 179, doi: 10.1093/mnras/262.1.179

—. 1993b, *Mon. Not. Roy. Astron. Soc.*, 264, 839, doi: 10.1093/mnras/264.4.839

Matt, G., Perola, G. C., Costa, E., & Piro, L. 1989, in ESA Special Publication, Vol. 296, Two Topics in X-Ray Astronomy, Volume 1: X Ray Binaries. Volume 2: AGN and the X Ray Background, ed. J. Hunt & B. Battrick, 991–993

Matt, G., Guainazzi, M., Frontera, F., et al. 1997, *Astron. Astrophys.*, 325, L13. https://arxiv.org/abs/astro-ph/9707065

Matt, G., Baloković, M., Marinucci, A., et al. 2015, *Mon. Not. Roy. Astron. Soc.*, 447, 3029, doi: 10.1093/mnras/stu2653

Matzeu, G. A., Nardini, E., Parker, M. L., et al. 2020, *Mon. Not. Roy. Astron. Soc.*, 497, 2352, doi: 10.1093/mnras/staa2076

Mejía-Restrepo, J. E., Trakhtenbrot, B., Koss, M. J., et al. 2022, *Astrophys. J. Suppl.*, 261, 5, doi: 10.3847/1538-4365/ac660210.48550/arXiv.2204.05321

Middei, R., Bianchi, S., Marinucci, A., et al. 2019, *Astron. Astrophys.*, 630, A131, doi: 10.1051/0004-6361/201935881

Middei, R., Petrucci, P. O., Bianchi, S., et al. 2020, *Astron. Astrophys.*, 640, A99, doi: 10.1051/0004-6361/202038112

Molina, M., Bassani, L., Malizia, A., et al. 2013, *Mon. Not. Roy. Astron. Soc.*, 433, 1687, doi: 10.1093/mnras/stt844

Molina, M., Malizia, A., Bassani, L., et al. 2019, *Mon. Not. Roy. Astron. Soc.*, 484, 2735, doi: 10.1093/mnras/stz156

Murphy, K. D., & Yaqoob, T. 2009, *Mon. Not. Roy. Astron. Soc.*, 397, 1549, doi: 10.1111/j.1365-2966.2009.15025.x

Nicastro, F., Piro, L., De Rosa, A., et al. 2000, *Astrophys. J.*, 536, 718, doi: 10.1086/308950

Osterbrock, D. E., & Pogge, R. W. 1985, *Astrophys. J.*, 297, 166, doi: 10.1086/163513

Pahari, M., McHardy, I. M., Mallick, L., Dewangan, G. C., & Misra, R. 2017, *Mon. Not. Roy. Astron. Soc.*, 470, 3239, doi: 10.1093/mnras/stx1455

Pal, I., & Stalin, C. S. 2023, *Mon. Not. Roy. Astron. Soc.*, 518, 2529, doi: 10.1093/mnras/stac3254

Pal, I., Stalin, C. S., Mallick, L., & Rani, P. 2022, *Astron. Astrophys.*, 662, A78, doi: 10.1051/0004-6361/202142386

Panessa, F., Bassani, L., Cappi, M., et al. 2006, *Astron. Astrophys.*, 455, 173, doi: 10.1051/0004-6361:20064894

Parker, M. L., Komossa, S., Kollatschny, W., et al. 2016, *Mon. Not. Roy. Astron. Soc.*, 461, 1927, doi: 10.1093/mnras/stw1449

Petrucci, P. O., Ursini, F., De Rosa, A., et al. 2018, *Astron. Astrophys.*, 611, A59, doi: 10.1051/0004-6361/201731580

Petrucci, P. O., Haardt, F., Maraschi, L., et al. 2000, *Astrophys. J.*, 540, 131, doi: 10.1086/309319

—. 2001, *Astrophys. J.*, 556, 716, doi: 10.1086/321629

Petrucci, P. O., Paltani, S., Malzac, J., et al. 2013, *Astron. Astrophys.*, 549, A73, doi: 10.1051/0004-6361/201219956

Petrucci, P. O., Gronkiewicz, D., Rozanska, A., et al. 2020, *Astron. Astrophys.*, 634, A85, doi: 10.1051/0004-6361/201937011

Porquet, D., Reeves, J. N., Grosso, N., Braito, V., & Lobban, A. 2021, *Astron. Astrophys.*, 654, A89, doi: 10.1051/0004-6361/202141577

Porquet, D., Reeves, J. N., Matt, G., et al. 2018, *Astron. Astrophys.*, 609, A42, doi: 10.1051/0004-6361/201731290

Poutanen, J., Sikora, M., Begelman, M. C., & Magdziarz, P. 1996, The Astrophysical Journal, 465, L107, doi: 10.1086/310149

Poutanen, J., & Svensson, R. 1996, *Astrophys. J.*, 470, 249, doi: 10.1086/177865

Rani, P., & Stalin, C. S. 2018a, *Astrophys. J.*, 856, 120, doi: 10.3847/1538-4357/aab356

—. 2018b, Journal of Astrophysics and Astronomy, 39, 15, doi: 10.1007/s12036-017-9502-5

Rani, P., Stalin, C. S., & Goswami, K. D. 2019, *Mon. Not. Roy. Astron. Soc.*, 484, 5113, doi: 10.1093/mnras/stz275

Rees, M. J. 1984, *Ann. Rev. Astron. Astrophys.*, 22, 471, doi: 10.1146/annurev.aa.22.090184.002351

Reeves, J. N., Braito, V., Porquet, D., et al. 2021, *Mon. Not. Roy. Astron. Soc.*, 500, 1974, doi: 10.1093/mnras/staa3377

Ricci, C., Walter, R., Courvoisier, T. J. L., & Paltani, S. 2011, *Astron. Astrophys.*, 532, A102, doi: 10.1051/0004-6361/201016409

Ricci, C., Trakhtenbrot, B., Koss, M. J., et al. 2017, *Astrophys. J. Suppl.*, 233, 17, doi: 10.3847/1538-4365/aa96ad

Ricci, C., Trakhtenbrot, B., Koss, M. J., et al. 2017, The Astrophysical Journal Supplement Series, 233, 17, doi: 10.3847/1538-4365/aa96ad

Ricci, C., Ho, L. C., Fabian, A. C., et al. 2018, *Mon. Not. Roy. Astron. Soc.*, 480, 1819, doi: 10.1093/mnras/sty1879

Risaliti, G., Young, M., & Elvis, M. 2009, *Astrophys. J. Lett.*, 700, L6, doi: 10.1088/0004-637X/700/1/L6

Różańska, A., Malzac, J., Belmont, R., Czerny, B., & Petrucci, P. O. 2015, *Astron. Astrophys.*, 580, A77, doi: 10.1051/0004-6361/201526288

Salpeter, E. E. 1964, *Astrophys. J.*, 140, 796, doi: 10.1086/147973

Sandage, A., Véron, P., & Wyndham, J. D. 1965, *Astrophys. J.*, 142, 1307, doi: 10.1086/148415

Schmidt, M. 1963, *Nature*, 197, 1040, doi: 10.1038/1971040a0

Schmidt, M., & Green, R. F. 1983, *Astrophys. J.*, 269, 352, doi: 10.1086/161048

Seyfert, C. K. 1943, *Astrophys. J.*, 97, 28, doi: 10.1086/144488

Shakura, N. I., & Sunyaev, R. A. 1973, *Astron. Astrophys.*, 500, 33

Shemmer, O., Brandt, W. N., Netzer, H., Maiolino, R., & Kaspi, S. 2006, *Astrophys. J. Lett.*, 646, L29, doi: 10.1086/506911

—. 2008, *Astrophys. J.*, 682, 81, doi: 10.1086/588776

Shields, G. A. 1978, *Nature*, 272, 706, doi: 10.1038/272706a0

Slipher, V. M. 1917, Lowell Observatory Bulletin, 3, 59

Soldi, S., Beckmann, V., Baumgartner, W. H., et al. 2014, *Astron. Astrophys.*, 563, A57, doi: 10.1051/0004-6361/201322653

Steenbrugge, K. C., Kaastra, J. S., Sako, M., et al. 2005, *Astron. Astrophys.*, 432, 453, doi: 10.1051/0004-6361:20041542

Stern, B. E., Poutanen, J., Svensson, R., Sikora, M., & Begelman, M. C. 1995, The Astrophysical Journal, 449, L13, doi: 10.1086/309617

Sun, W.-H., & Malkan, M. A. 1989, *Astrophys. J.*, 346, 68, doi: 10.1086/167986

Tamborra, F., Matt, G., Bianchi, S., & Dovčiak, M. 2018, *Astron. Astrophys.*, 619, A105, doi: 10.1051/0004-6361/201732023

Tazaki, F., Ueda, Y., Terashima, Y., & Mushotzky, R. F. 2011, *Astrophys. J.*, 738, 70, doi: 10.1088/0004-637X/738/1/70

Tortosa, A., Bianchi, S., Marinucci, A., Matt, G., & Petrucci, P. O. 2018, *Astron. Astrophys.*, 614, A37, doi: 10.1051/0004-6361/201732382

Tortosa, A., Marinucci, A., Matt, G., et al. 2017, *Mon. Not. Roy. Astron. Soc.*, 466, 4193, doi: 10.1093/mnras/stw3301

Tortosa, A., Ricci, C., Tombesi, F., et al. 2022a, *Mon. Not. Roy. Astron. Soc.*, 509, 3599, doi: 10.1093/mnras/stab3152

Tortosa, A., Ricci, C., Ho, L. C., et al. 2022b, arXiv e-prints, arXiv:2212.06183. https://arxiv.org/abs/2212.06183

Trakhtenbrot, B., Ricci, C., Koss, M. J., et al. 2017, *Mon. Not. Roy. Astron. Soc.*, 470, 800, doi: 10.1093/mnras/stx1117

Turner, T. J., Reeves, J. N., Braito, V., & Costa, M. 2018, *Mon. Not. Roy. Astron. Soc.*, 476, 1258, doi: 10.1093/mnras/sty318

Ueno, S., Mushotzky, R. F., Koyama, K., et al. 1994, *Pub. Astron. Soc. Japan*, 46, L71

Urry, C. M., & Padovani, P. 1995, *Pub. Astron. Soc. Pac.*, 107, 803, doi: 10.1086/133630

Ursini, F., Matt, G., Bianchi, S., et al. 2022, *Mon. Not. Roy. Astron. Soc.*, 510, 3674, doi: 10.1093/mnras/stab3745

Ursini, F., Matt, G., Bianchi, S., et al. 2021, Monthly Notices of the Royal Astronomical Society, 510, 3674, doi: 10.1093/mnras/stab3745

Ursini, F., Boissay, R., Petrucci, P. O., et al. 2015, *Astron. Astrophys.*, 577, A38, doi: 10.1051/0004-6361/201425401

Ursini, F., Petrucci, P. O., Matt, G., et al. 2016, *Mon. Not. Roy. Astron. Soc.*, 463, 382, doi: 10.1093/mnras/stw2022

Ursini, F., Petrucci, P. O., Bianchi, S., et al. 2020, *Astron. Astrophys.*, 634, A92, doi: 10.1051/0004-6361/201936486

Ursini, F., Marinucci, A., Matt, G., et al. 2023, *Mon. Not. Roy. Astron. Soc.*, 519, 50, doi: 10.1093/mnras/stac3189

Vasudevan, R. V., Brandt, W. N., Mushotzky, R. F., et al. 2013, *Astrophys. J.*, 763, 111, doi: 10.1088/0004-637X/763/2/111

Vasudevan, R. V., & Fabian, A. C. 2007, Monthly Notices of the Royal Astronomical Society, 381, 1235, doi: 10.1111/j.1365-2966.2007.12328.x

Vaughan, S., Edelson, R., Warwick, R. S., & Uttley, P. 2003, *Mon. Not. Roy. Astron. Soc.*, 345, 1271, doi: 10.1046/j.1365-2966.2003.07042.x

Véron-Cetty, M. P., & Véron, P. 2010, *Astron. Astrophys.*, 518, A10, doi: 10.1051/0004-6361/201014188

Wagner, S. J., & Witzel, A. 1995, *Ann. Rev. Astron. Astrophys.*, 33, 163, doi: 10.1146/annurev.aa.33.090195.001115

Weisskopf, M. C., Soffitta, P., Baldini, L., et al. 2022, Journal of Astronomical Telescopes, Instruments, and Systems, 8, 026002, doi: 10.1117/1.JATIS.8.2.026002

Wilkins, D. R., & Fabian, A. C. 2012, *Mon. Not. Roy. Astron. Soc.*, 424, 1284, doi: 10.1111/j.1365-2966.2012.21308.x

Willingale, R., Starling, R. L. C., Beardmore, A. P., Tanvir, N. R., & O'Brien, P. T. 2013, *Mon. Not. Roy. Astron. Soc.*, 431, 394, doi: 10.1093/mnras/stt175

Willmer, C. N. A., Focardi, P., Chan, R., Pellegrini, P. S., & da Costa, N. L. 1991, *Astron. J.*, 101, 57, doi: 10.1086/115665

Winkler, H. 1992, *Mon. Not. Roy. Astron. Soc.*, 257, 677, doi: 10.1093/mnras/257.4.677

Yaqoob, T. 2012, *Mon. Not. Roy. Astron. Soc.*, 423, 3360, doi: 10.1111/j.1365-2966.2012.21129.x

Zaino, A., Bianchi, S., Marinucci, A., et al. 2020, *Mon. Not. Roy. Astron. Soc.*, 492, 3872, doi: 10.1093/mnras/staa107

Zdziarski, A. A., Johnson, W. N., & Magdziarz, P. 1996, *Mon. Not. Roy. Astron. Soc.*, 283, 193, doi: 10.1093/mnras/283.1.193

Zdziarski, A. A., Poutanen, J., & Johnson, W. N. 2000, *Astrophys. J.*, 542, 703, doi: 10.1086/317046

Zhang, J.-X., Wang, J.-X., & Zhu, F.-F. 2018, *Astrophys. J.*, 863, 71, doi: 10.3847/1538-4357/aacf92

Zhang, W., Dovčiak, M., & Bursa, M. 2019, The Astrophysical Journal, 875, 148, doi: 10.3847/1538-4357/ab1261

Zoghbi, A., Fabian, A. C., Reynolds, C. S., & Cackett, E. M. 2012, *Mon. Not. Roy. Astron. Soc.*, 422, 129, doi: 10.1111/j.1365-2966.2012.20587.x

Zoghbi, A., Matt, G., Miller, J. M., et al. 2017, *Astrophys. J.*, 836, 2, doi: 10.3847/1538-4357/aa582c